הטכניון
מכון טכנולוגי לישראל
TECHNION
Israel Institute of Technology

ספריות הטכניון
The Technion Libraries

בית הספר ללימודי מוסמכים ע"ש ארווין וג'ואן ג'ייקובס
Irwin and Joan Jacobs Graduate School

Experimental study of thermally driven anabatic flows

Research thesis in Partial Fulfillment of
the Requirements for the
Degree of Doctor of Philosophy

Roni Goldshmid

Submitted to the Senate of the Technion –
Israel Institute of Technology.
Tishre 5781, Haifa, September 2020

The research thesis was completed under the supervision of
Associate Professor Dan Liberzon
in the Faculty of Civil and Environmental Engineering.

The generous financial support of the
Technion-Israel Institute of Technology,
United States-Israel Binational Science Fund,
and Israel Science Foundation
are gratefully acknowledged.

List of Publications:

1. Goldshmid RH, Liberzon D. (2020) Automated identification and characterization of turbulent bursting from single-point records of the velocity field. *Meas. Sci. Technol.* doi: 10.1088/1361-6501/ab912b.
   Quartile: Q1 in Engineering. Impact Factor: 1.861. (Dissertation Chapter 5).
2. Hilel Goldshmid R, Bardoel SL, Hocut CM, Zhong Q, Liberzon D, Fernando HJS (2018) Separation of Upslope Flow over a Plateau. *Atmosphere*, *9*, 165.
   Quartile: Q2 in Environmental Science. Impact Factor: 2.046. (Dissertation Chapter 3.1).

List of symposia reports

3. Goldshmid RH, Liberzon D (2019) Automatic identification and characterization of bursting periods in a turbulent velocity field. 72nd annual APS DFD conference. Seattle, WA, USA. (Dissertation Chapter 5).
4. Shani-Zerbib Almog, Goldshmid RH, Liberzon D (2019) Observations of water waves and wind-wave interactions in the Gulf of Aqaba (Eilat). 72nd annual APS DFD conference. Seattle, WA, USA. (Dissertation Chapter 4.1).
5. De Serio F, Armenio E, Badin G, Di Leonardo A, Goldshmid RH, Liberzon D, et al. (2019) Jets interacting with vegetation in the rotating LEGI platform. EGU 2019 conference. Vienna, Austria. (Not in this dissertation).
6. Hilel Goldshmid R, Liberzon D (2018) Experimental investigation of upslope flow separation on smooth and rough symmetric slopes. ISEH 2018 conference. Notre Dame, IN, USA. (Dissertation Chapter 3.2).
7. Hilel R, Liberzon D (2017) Experimental study of thermally driven anabatic flows. First PhD department seminar at the Technion-Israel Institute of Technology. (Dissertation Chapter 3.2).

Acknowledgements

I would like to express my most sincere gratitude to Associate Professor Dan Liberzon. Your consistent support, guidance, encouragement, and knowledge provided me with so many tools that brought me to where I am today. I am truly happy I chose to complete my graduate studies at your lab. You are, and will continue to be, a big role model and a great inspiration. Dan, thank you for everything and for making T-SAIL my second family.

I gratefully acknowledge the generous financial support of the Technion-Israel Institute of Technology, United States-Israel Binational Science Fund (Grant #2014075), and Israel Science Foundation (Grant #2063/19).

My dear husband, Itay, thank you for always being supportive and the best life partner I could ask for. My dear family and friends, thank you for always believing in me. My fellow T-SAIL lab mates, thank you for the support and for making these years such a wonderful experience; our friendship will always stay strong. My final sincere thank you goes to the Civil and Environmental Engineering Faculty at the Technion, thank you for being my home away from home.

Table of Contents

Table of Contents (continued)

Table of Figures

Table of Figures (continued)

Table of Figures (continued)

Table of Figures (continued)

Table of Figures (continued)

Table of Figures (continued)

Table of Figures (continued)

Table of Figures (continued)

Table of Figures (continued)

Table of Figures (continued)

Table of Figures (continued)

Table of Figures (continued)

Table of Figures (continued)

Table of Figures (continued)

Table of Figures (continued)

Table of Tables

Abstract

The lack of understanding of slope flows is one of the major reasons of misinforming and inaccurate weather/climate forecasts. Upslope flows, or anabatic flows, influence microclimates and are responsible for transport of scalars such as dust/pollution which directly affect daily human activities. Slope flows are characterized as turbulent boundary layer (BL) flows, and in absence of synoptic forcing, these are driven purely by the diurnal heating/cooling cycles. Characterization of such flows is cumbersome due to their highly turbulent and transient nature, explaining the small number of field and laboratory research currently available in the literature. This study presents the findings of both laboratory and field work conducted to characterize both large and fine scale properties of anabatic flows.

In the laboratory, we have conducted experiments simulating naturally occurring anabatic flows on slopes of various angles, heat fluxes, and subject to two geometric features: single slopes topped off by a plateau and symmetric double slopes. *First*, we expanded the recently developed flow separation prediction model developed by Hocut et. al. (2015) by incorporating the existence of a plateau. An effective angle incorporating the plateau width revealed a quantitative similarity to the previous model. Predictions for the dependence of the separation location were presented. *Next*, we characterized large scale BL properties of anabatic flows developing on symmetric double slopes, with a much larger tank. The velocity profiles, Reynolds stress profiles, and vorticity estimate patterns revealed the transient 3D nature of the flow. Further examination of the instantaneous flow behavior highlighted the importance of the three-dimensionality of the flow and revealed the limitations of the previously adopted 2D models. *Finally*, we conducted several qualitative experiments to examine the 3D nature of the flow. Coherent structures resembling a helical shape were observed, confirming the suspicions of their existence. These experiments strengthened the significance of the flow three-dimensionality and suggested future studies to perform quantitative examinations of the structure and mean behavior.

In the field, a collocated sonic-hotfilm (combo) probe was previously shown to have the capability of sensing anabatic flow that developed on a moderate slope. The probe, however, was only able to sense flow in a 120° range, and we present the mechanical development that enables 360° sensing. The combo was tested in an open sea environment and was shown to operate properly and automatically, without human intervention, for several days or weeks at a time. Later, we automated the combo

calibration procedure using deep artificial neural networks along with the low-pass filtered combo data.

The last part presents the development of an automated method capable of accurately identifying bursting periods in point measurements. The combo sensed fine-scale turbulent bursts in anabatic BL flow. After separating the bursts from the background flow, the background turbulence was found to highly resemble the Kolmogorov theory, while the bursting periods varied significantly. This enables future studies to better characterize bursts and their generation mechanism. Both the fine and large-scale findings of this research can be incorporated into existing forecasting models to potentially improve their performance.

Nomenclature

Γ	Empirical constant
Π	Scaling constant
Φ	Diffusive term of heat equation
Ω	angular frequency of planetary rotation
A	Slope/boundary/flat plate area
D	Plateau width
H	Shape factor
I	Electric current
L	Representative length along the slope
P	Power density of velocity fluctuations
Q	Heat flux
T	Instantaneous temperature
V	Voltage
W	Width of plate/slope
b	Baroclinic torque
f	Frequency
g	Gravitational acceleration
h	Convective heat-transfer coefficient
k	Thermal conductivity constant
n	Slope normal coordinate (in slope coordinate system
p	Pressure
s	Along slope coordinate (in slope coordinate system)
t	Time
u	Streamwise velocity component
uvw	3 component sub-probe of the 4-wire probe
v	Transverse velocity component
w	Perpendicular velocity component
x	Streamwise coordinate
y	Transverse coordinate (in slope coordinate system)
y	Transverse coordinate
z	Perpendicular coordinate
α	Thermal diffusivity
β	Slope angle
γ	empirical proportionality constant
δ	Boundary layer height/thickness
η	Kolmogorov length scale
θ	Scalar dissipation rate
λ	Taylor length scale
μ	Dynamic viscosity
ν	Kinematic viscosity
ρ	Density
τ	Shear stress
ψ	Arbitrary parameter
ϕ	Altitude

Subscripts

D_i	Molecular diffusivity of species i
$E_{1,1}$	Voltage reading from film (wire) 1 of probe 1
$E_{1,2}$	Voltage reading from film (wire) 2 of probe 1
$E_{2,1}$	Voltage reading from film (wire) 2 of probe 1
$E_{2,2}$	Voltage reading from film (wire) 2 of probe2
F_b	Buoyancy force
H_0	Slope height
H_s	Significant wave height
L_0	Length of slope/boundary/flat plate
L_H	Horizontal length scale
L_s	Separation length
L_w	Plume width
T_∞	Temperature outside the BL
T_N	Normalized temperature
T_w	Temperature at the wall/ boundary
U_{10}	Mean velocity at 10 m above mean sea level
U_N	Normalized streamwise velocity
U_s	Streamwise velocity at separation point
c_i	Concentration of species i
c_p	Specific heat capacity
d_P	Diameter f particle
f_c	Coriolis force
q_0	Buoyancy flux
sk_B	Streamwise velocity derivative skewness of background flow
sk_I	Streamwise velocity derivative skewness of intermediate period
sk_{TB}	Streamwise velocity derivative skewness of turbulent bursting periods
t_s	Experimental duration of quasi-steady flow
u_*	Friction velocity

u_0	Representative streamwise velocity
u_∞	Streamwise velocity outside the BL
u_e	Near-field entrainment velocity
u_p	Probe obtained streamwise velocity
u_s	Sonic obtained streamwise velocity
u_s	Streamwise velocity at separation
w_P	Particle settling velocity
α_1	Entrainment coefficient
β_0	Coefficient of thermal expansion
β_c	Critical slope angle
β_e	Effective slope angle
δ_{ABL}	Height of anabatic BL
δ_{lam}	Height of equivalent laminar BL
δ_s	Boundary layer height at the point of separation
δ_u	Streamwise delta error
δ_v	Transverse delta error
δ_w	Perpendicular delta error
ε_H	Eddy diffusivity of heat
ε_N	Normalized instantaneous TKE dissipation rate
ε_T	Threshold of normalized TKE dissipation rate
ε_m	Eddy diffusivity of momentum
θ_N	Normalized scalar dissipation rate
λ_B	Taylor scale of background flow
λ_I	Taylor scale of intermediate period
λ_{TB}	Talyor scale of turbulent bursting periods
ν_f	Kinematic viscosity of fluid
ρ_0	Reference density
ρ_∞	Density outside the BL
ρ_P	Density of particle
ρ_f	Density of fluid
τ_{ATB}	Approximated bursting duration
τ_{TB}	Detected bursting duration
τ_{min}	Minimum window length
τ_w	Wall shear stress
τ_λ	Taylor time scale
ω_y	Vorticity parallel to y axis in the along-slope coordinates

Superscripts

$\overline{\ }$	Ensemble average
$\bar{\rho}$	ratio of particle to fluid density
$'$	Fluctuating component
$*$	Dimensionless parameters
$\bar{\varepsilon}$	Mean TKE dissipation rate
$\bar{\delta}$	Average delta error

Operators

∂	Partial derivative
Δ	Difference/change in
∇	Nabla

Dimensionless numbers

Gr	Grashof number
Nu	Nusselt number
Nu_{L_0}	Nusselt number based on slope length
Nu_x	Nusselt number based on distance along the slope
Nu_N	Nusselt number of natural convection
Nu_F	Nusselt number of forced convection
Pr	Prandtl number
Pr_t	Turbulent Prandtl number
Ra_{L_0}	Raleigh number based on slope length
Re	Reynolds number
Re_{L_0}	Reynolds number using the slope length
Re_x	Reynolds number using the distance along the slope
Ri	Richardson number
Ro	Rossby number

Chapter 1: Introduction

Complex mountainous topography characterizes more than 70% of urban areas and greatly influences microclimates and local weather. Daily human activities are impacted by complex terrain weather and have significant health, safety, and economic implications such as pollution transfer in urban centers, formation of clouds, accurate weather forecasting, safety of civil and military aviation operations, sustainable and health aware urban planning, and operation of recreational centers. Flow characteristics of local wind systems in mountainous regions change depending on the balance between thermal circulation flows (up/down-slope and up/down valley) and external flows (synoptic scale forcing). During the past decades substantial progress has been made in understanding synoptic scale, mean flow, approaching mountains and driven by large-scale pressure gradients [1–4], while significantly less progress has been made in understanding thermally driven flows. These flows result from thermal forcing due to the diurnal solar heating/cooling cycle of the slopes and are characterized as turbulent flows. The turbulent slope flows are broken down into two type of flows: up slope and down slope flows. A large amount of publications is available on katabatic (down-slope) flow configurations due to the relatively more stable conditions than those of anabatic (up-slope) flow. Anabatic flow is more difficult to investigate because of the inhomogeneity, instability, and non-stationary nature of the flow especially in changing field conditions including mean wind velocity, temperature, and humidity. Structure of its turbulent boundary layer (BL) and flow separation along the slope are of great significance governing apex plume formation and entrainment

of flow outside of the BL, which influences pollution transfer, cloud formation and consequently precipitation regimes in the region [5–8].

Experimental investigation of highly turbulent and unstable anabatic flows is cumbersome and limited by the temporal and spatial resolution of the available field and laboratory scale instruments and data processing techniques. The current state of field work available in the literature mainly presents the use of slow or insufficient spatial resolution instruments such as ultrasonic anemometers (sonic) or LIDARS (Light Detection and Ranging). It, therefore, lacks the necessary and important information about the fine scale turbulence, actual dissipation rates, mixing lengths, and heat transfer rates. These can be obtained using the hot wire/film anemometry but the need of constant re-calibration of the sensors due to the changing field conditions and degradation of the films/wires is impractical. A recently developed instrument, the combo probe which consists of collocated sonic and hot film sensors (hotfilm), offers a solution for the calibration challenges associated with field measurements of turbulent flows [9–11]. In the combo, hotfilm sensors effectively sense and capture the fine scale turbulence, while the much slower records of the sonic are used for continuous *in-situ* calibration of the hotfilm (using Neural Networks) and their re-alignment along the mean-flow direction. A recent field experiment (conducted by the author and her supervisor) was staged on a moderate slope (5.7°) on the southwestern side of Nofit, a communal village located ~15 km from Haifa, Israel [12]. It reported on fine scale turbulence statistics of anabatic flow. The combo probe collected anabatic flow velocity data at 2 kHz continuously for 8 days. Eventually turbulence statistics of the flow, fully resolved spectra of velocity field components, and empirical correlations of many important parameters were obtained.

Although field experiments are valuable, modeling turbulent slope flows in the lab is advantageous for different aims such as to capture flow separation, quantify transfer of pollutants, improve space-time resolution of prediction models, and specify boundary conditions for which rapid spatial and temporal variability is required. The laboratory offers a highly controlled environment, possibility for higher accuracy measurements, and allows repeatability, which is particularly important for deriving empirical relations of various parameters governing the flow. Water tanks are commonly used in the lab for modeling of convective/slope flows [13, 14] and other atmosphere-related experiments [15, 16]. This calls for an accurate and comprehensive experimental study that would address the challenges in modelling/forecasting weather and climate conditions associated with anabatic turbulent flows.

The first part of this dissertation will present the highly controlled laboratory model experiments. The second part will focus on the development of field measurement techniques. Finally, the third will present a newly developed automated detection method of turbulent bursting periods, allowing effective separation and individual examination of the background turbulence and the intermittent turbulent bursts in anabatic flows and other turbulent BL flows.

Chapter 2: Scientific background

The first part of this study focuses on the mean boundary layer (BL) behavior while the second and third parts focus on BL turbulent and on other fine-scale characteristics. The development of a comprehensive model of anabatic turbulent BL flow requires the consideration of all governing equations and dimensionless numbers, which will enable comparison between different flow scales and different fluids.

When a BL develops on an object, in this case the mountain slope, the height/thickness (δ) of the BL is much smaller than the length of object. The thickness of the hydrodynamic BL is defined as the height at which the streamwise velocity still behaves as a BL. It is commonly defined as the height where $u = 0.99u_{\infty}$, where the subscript ∞ denotes a point outside the BL. The thickness of the thermal BL is similarly defined as the height at which the temperature still behaves as a BL. It is commonly defined as $(T_w - T)/(T_w - T_{\infty}) = 0.99$, T_w is the temperature at the interface between the solid and the fluid [17]. Given δ is small in comparison to boundary length scale, both temperature and velocity gradients inside BL must be large to maintain continuity on the boundaries. The *boundary layer approximation*, therefore, assumes that changes in the streamwise direction $\partial/\partial x$ are much smaller than the changes in the direction perpendicular to the solid surface $\partial/\partial z$; this approximation is common for BL problems. Under the assumption that the flow is homogeneous in the transverse, y, direction, a two-dimensional cut is used to analyze the flow [18, 19].

Neglection of Coriolis forces is valid for Rossby numbers $Ro = \frac{\bar{u}}{f_C L_0} \gg 1$. Where $f_C = 2\Omega sin\phi$ is the Coriolis frequency, $\Omega = 7.3 \times 10^{-5}\ rads\ s^{-1}$ is the angular

frequency of planetary rotation, and ϕ is the altitude. It is typically proper to neglect Coriolis forces for mountain winds; for example, a mountain with slope length $L_0 \sim O(1)\, km$, average wind speed of $\bar{u} \sim O(10)\, m\, s^{-1}$, at the mid-altitudes $f \sim O(10^{-4})\, rads\, s^{-1}$, the planetary rotation frequency, yields $Ro \sim O(100)$ [18, 20].

The governing, along flat boundary/plate, equations of a two-dimensional problem of hydrodynamics, temperature, and concentration of species in a fluid without chemical reactions and electro migration are,

$$\frac{\partial \rho}{\partial t} + \frac{\partial (\rho u)}{\partial x} + \frac{\partial (\rho w)}{\partial z} = 0, \tag{2.1}$$

$$\frac{\partial (\rho u)}{\partial t} + u\frac{\partial (\rho u)}{\partial x} + w\frac{\partial (\rho u)}{\partial z} = -\frac{\partial p}{\partial x} + \frac{\partial}{\partial x}\left(\mu \frac{\partial u}{\partial x}\right) + \frac{\partial}{\partial z}\left(\mu \frac{\partial u}{\partial z}\right) - \rho g sin(\beta), \tag{2.2}$$

$$\frac{\partial (\rho w)}{\partial t} + u\frac{\partial (\rho w)}{\partial x} + w\frac{\partial (\rho w)}{\partial z} = -\frac{\partial p}{\partial z} + \frac{\partial}{\partial x}\left(\mu \frac{\partial w}{\partial x}\right) + \frac{\partial}{\partial z}\left(\mu \frac{\partial w}{\partial z}\right) - \rho g cos(\beta), \tag{2.3}$$

$$\frac{\partial \left(T\rho c_p\right)}{\partial t} + u\frac{\partial \left(T\rho c_p\right)}{\partial x} + w\frac{\partial \left(T\rho c_p\right)}{\partial z} = \frac{\partial}{\partial x}\left(k\frac{\partial T}{\partial x}\right) + \frac{\partial}{\partial z}\left(k\frac{\partial T}{\partial z}\right) + \mu\Phi, \tag{2.4}$$

$$\frac{\partial c_i}{\partial t} + u\frac{\partial c_i}{\partial x} + w\frac{\partial c_i}{\partial z} = \frac{\partial}{\partial x}\left(D_i\frac{\partial c_i}{\partial x}\right) + \frac{\partial}{\partial z}\left(D_i\frac{\partial c_i}{\partial z}\right). \tag{2.5}$$

Here, ρ is the density, u, w are the along the slope and normal to the slope x, z components of velocity, μ is the viscosity, T is the temperature, c_p is the specific heat capacity,k is the thermal conductivity constant, β is the slope angle with respect to the horizontal, D_i is the diffusivity coefficient, and c_i is the concentration of species in the fluid. Equation (2.1) is the continuity equation, (2.2) and (2.3) are the x and z-direction conservation of momentum, (2.4) is the thermal energy equation where the viscous dissipation terms , Φ, are denoted in (2.6)

$$\Phi = \left(\frac{\partial u}{\partial z} + \frac{\partial w}{\partial x}\right)^2 + 2\left(\left[\frac{\partial u}{\partial x}\right]^2 + \left[\frac{\partial w}{\partial z}\right]^2\right). \tag{2.6}$$

Finally, (2.5) is the conservation of species equation. When considering the following assumptions of steady state, incompressible flow, constant properties, i.e. k, c_p, μ, D_i are constant, and without additional external sources of heat into the system, the system of governing equations can be reduced to [19],

$$\frac{\partial u}{\partial x} + \frac{\partial w}{\partial z} = 0\,, \tag{2.7}$$

$$\frac{\partial u}{\partial t} + u\frac{\partial u}{\partial x} + w\frac{\partial u}{\partial z} = -\frac{1}{\rho}\frac{\partial p}{\partial x} + \nu\left(\frac{\partial^2 u}{\partial x^2} + \frac{\partial^2 u}{\partial z^2}\right) - sin(\beta)g\,, \tag{2.8}$$

$$\frac{\partial w}{\partial t} + u\frac{\partial w}{\partial x} + w\frac{\partial w}{\partial z} = -\frac{1}{\rho}\frac{\partial p}{\partial z} + \nu\left(\frac{\partial^2 w}{\partial x^2} + \frac{\partial^2 w}{\partial z^2}\right) - cos(\beta)g\,, \tag{2.9}$$

$$\frac{\partial T}{\partial t} + u\frac{\partial T}{\partial x} + w\frac{\partial T}{\partial z} = \alpha\left(\frac{\partial^2 T}{\partial x^2} + \frac{\partial^2 T}{\partial z^2}\right) + \mu\Phi\,, \tag{2.10}$$

$$\frac{\partial c_i}{\partial t} + u\frac{\partial c_i}{\partial x} + w\frac{\partial c_i}{\partial z} = D_i\left(\frac{\partial^2 c_i}{\partial x^2} + \frac{\partial^2 c_i}{\partial z^2}\right). \tag{2.11}$$

For further simplification, let us first study the simplest case of natural/free convection. Consider a long flat horizontal plate of length L_0 with constant upward facing heat flux. Assuming steady state, laminar BL flow driven solely by buoyancy forces, and assuming the boundary layer approximation is valid, (2.9) reduces to

$$u\frac{\partial w}{\partial x} + w\frac{\partial w}{\partial z} = -\frac{1}{\rho}\frac{\partial p_\infty}{\partial z} + \nu\left(\frac{\partial^2 w}{\partial z^2}\right) - g\,. \tag{2.12}$$

Assuming that there is no external flow, $u_\infty, w_\infty = 0$ the vertical pressure gradient becomes

$$\frac{\partial p_\infty}{\partial z} = -\rho_\infty g\,, \tag{2.13}$$

and substituting (2.12) into (2.13) then yields

$$u\frac{\partial w}{\partial x} + w\frac{\partial w}{\partial z} = \frac{(\rho_\infty - \rho)}{\rho}\,g\, + \nu\left(\frac{\partial^2 w}{\partial z^2}\right). \tag{2.14}$$

This expression must apply in every point of the free convection laminar BL; the first term on the right is the buoyancy term that describes the origin of the flow due to density variations. Assuming these variations are only due to temperature gradient, we can relate this term to the volumetric thermal expansion fluid property at constant pressure, $\beta_0 = \frac{1}{\rho}\frac{\partial \rho}{\partial T} \approx -\frac{1}{\rho}\frac{\Delta \rho}{\Delta T} = -\frac{1}{\rho}\frac{\rho_\infty - \rho}{T_\infty - T}$. It provides that $\rho_\infty - \rho \approx \rho\beta_0(T - T_\infty)$ and therefore,

$$u\frac{\partial w}{\partial x} + w\frac{\partial w}{\partial z} = \beta_0(T - T_\infty)g \quad + \nu\left(\frac{\partial^2 w}{\partial z^2}\right). \tag{2.15}$$

This is the commonly applied *Boussinesq Approximation,* demonstrating temperature gradient acting as the driving force of the flow. This approximation couples the z-momentum equation with the thermal energy equation (2.15).

We begin with a stable case or positive stratification, i.e. the less dense particles are atop the denser ones, without an imposed pressure gradient or mean flow. The acceptance of the BL approximation implies $\frac{\partial}{\partial x} \ll \frac{\partial}{\partial z}$ and $\frac{\partial^2}{\partial x^2} \ll \frac{\partial^2}{\partial z^2}$. For simplicity, we assume steady state and no mass transfer and that the viscous dissipation term in the heat equation is negligible compared to the buoyancy term, and our governing equations are

$$\frac{\partial u}{\partial x} + \frac{\partial w}{\partial z} = 0\,, \tag{2.16}$$

$$u\frac{\partial u}{\partial x} + w\frac{\partial u}{\partial z} = \nu\left(\frac{\partial^2 u}{\partial z^2}\right), \tag{2.17}$$

$$u\frac{\partial w}{\partial x} + w\frac{\partial w}{\partial z} = \beta(T - T_\infty)g \quad + \nu\left(\frac{\partial^2 w}{\partial z^2}\right), \tag{2.18}$$

$$u\frac{\partial T}{\partial x} + w\frac{\partial T}{\partial z} = \alpha\left(\frac{\partial^2 T}{\partial z^2}\right), \tag{2.19}$$

These equations are complex, and we typically approach this problem using a similarity solution. First, we must introduce similarity variables defining non-dimensional normalized length, velocity, and temperature scales

$$x^* \equiv \frac{x}{L_0} \qquad y^* \equiv \frac{y}{L_0} \qquad u^* \equiv \frac{u}{u_0} \qquad w^* \equiv \frac{w}{u_0} \qquad T^* \equiv \frac{T - T_\infty}{T_w - T_\infty}, \tag{2.20}$$

where u_0 is the representative velocity defined below. Applying (2.20) transforms the governing equations into

$$\frac{\partial u^*}{\partial x^*} + \frac{\partial w^*}{\partial z^*} = 0\,, \tag{2.21}$$

$$u^* \frac{\partial u^*}{\partial x^*} + w^* \frac{\partial u^*}{\partial z^*} = \frac{1}{Re_L}\left(\frac{\partial^2 u^*}{\partial z^{*2}}\right), \tag{2.22}$$

$$u^* \frac{\partial w^*}{\partial x^*} + w^* \frac{\partial w^*}{\partial z^*} = \frac{g\beta L(T_w - T_\infty)}{u_0^2} T^* + \frac{1}{Re_{L_0}}\left(\frac{\partial^2 w^*}{\partial z^{*2}}\right), \tag{2.23}$$

$$u^* \frac{\partial T^*}{\partial x^*} + w^* \frac{\partial T^*}{\partial z^*} = \frac{1}{Re_{L_0} Pr}\left(\frac{\partial^2 T^*}{\partial z^{*2}}\right)\,. \tag{2.24}$$

As a result of non-dimensionalization of governing equations we have derived relationships of several parameters that are known to us as characteristic dimensionless numbers. Dimensionless numbers characterize important relations between governing parameters of the flow and allow comparison of flows in different regimes and at different scales. For example, Reynolds number describes the ratio between inertial and viscous forces in the flow by comparing the order of magnitude of inertia/advection from the momentum equation $u\frac{\partial u}{\partial x} \sim \frac{u^2}{L_0}$to the order of magnitude of viscous dissipation $\frac{\mu}{\rho}\frac{\partial^2 u}{\partial x^2} \sim \frac{\mu}{\rho}\frac{u}{L_0^2}$.

$$\frac{u^2/L_0}{\mu u/\rho L_0^2} = \frac{uL_0}{\nu} \equiv Re_{L_0}, \tag{2.25}$$

L_0 being the characteristic length scale of the problem. When inertial forces dominate, $Re_{L_0} \gg 1$. In the same manner, Prandtl number is the ratio between momentum ν and thermal diffusivities,

$$Pr \equiv \frac{\nu}{\alpha} . \tag{2.26}$$

Here, $\alpha = k/(c_p \rho)$ is the thermal diffusivity.

The first term on the right side of (2.23) is the buoyancy force term; since there is no free stream velocity in this example, a representative velocity may be defined as $u_0^2 = g\beta_0 L_0 (T_w - T_\infty)$ to make the term multiplying T^* equal unity. This representative velocity is used to calculate Re_{L_0} in natural convection, providing $Re_{L_0} = [g\beta_0 L_0 (T_w - T_\infty)]^{\frac{1}{2}} L_0/\nu$ and since the Grashof number is the square of Re_{L_0}, we have

$$Gr \equiv Re_{L_0}^2 = \frac{g\beta_0 (T_w - T_\infty) L_0^3}{\nu^2} . \tag{2.27}$$

Grashof number measures the ratio of the buoyancy to viscous forces acting on the fluid. Another important dimensionless number of our problem is the Nusselt number. It is the ratio between the convective and conductive heat transfer rates. The convective heat flux from one side of a plate is $Q = h\Delta T$ $[W\ m^{-2}]$, where ΔT is the temperature difference between the plate and a reference temperature, and h $[W\ K^{-1}\ m^{-2}]$ is the conductance of the surface, which is actually a function of the surface temperature, shape, roughness, orientation, and fluid velocity above the surface. Fourier's law $Q = -k\nabla \mathrm{T}$ describes the conductive heat flux; k in $[W\ K^{-1}\ m^{-1}]$ is the thermal conductivity constant. The ratio between the heat fluxes is then

$$Nu \equiv \frac{Q_{convective}}{Q_{conductive}} = \frac{h\Delta T}{\frac{k\Delta T}{L_0}} = \frac{hL_0}{k}, \tag{2.28}$$

with L_0 being a characteristic length.

Another important finding from the governing equations are the functional dependences of dimensionless parameters: $u^* = f\left(x^*, z^*, Re_{L_0}\right)$, $w^* = f\left(x^*, z^*, Re_{L_0}, Gr, T^*\right)$, and $T^* = f(x^*, z^*, Re_{L_0}, Pr)$. These are useful for deriving empirical correlations/models from laboratory measurements for when the set of governing equations is complex and does not have an analytical solution. Over the years, experimental data provided such empirical correlations as a solution to the horizontal flat plate free convection with constant heat flux [21]

$$\overline{Nu_{L_0}} = 0.54 Ra_{L_0}^{1/4} \quad \forall\ 10^4 < Ra_{L_0} < 10^7\ , \tag{2.29}$$

$$\overline{Nu_{L_0}} = 0.15 Ra_{L_0}^{1/3} \quad \forall\ 10^7 < Ra_{L_0} < 10^{11}\ . \tag{2.30}$$

The Rayleigh number, Ra_{L_0}, is the product of Grashof and Prandtl numbers measuring the instability of a layer of fluid due to temperature and density gradient.

In the case of forced convection, however, the choice of the representative velocity for nondimensionalization is different; it is that of the free stream $u_0 = u_\infty$. Providing forced convection equations as

$$\frac{\partial u^*}{\partial x^*} + \frac{\partial w^*}{\partial z^*} = 0\ , \tag{2.31}$$

$$u^* \frac{\partial u^*}{\partial x^*} + w^* \frac{\partial u^*}{\partial z^*} = \frac{1}{Re_{L_0}} \left(\frac{\partial^2 u^*}{\partial z^{*2}} \right)\ , \tag{2.32}$$

$$u^* \frac{\partial w^*}{\partial x^*} + w^* \frac{\partial w^*}{\partial z^*} = \frac{Gr}{Re_{L_0}^2} T^* + \frac{1}{Re_{L_0}} \left(\frac{\partial^2 w^*}{\partial z^{*2}} \right), \tag{2.33}$$

$$u^* \frac{\partial T^*}{\partial x^*} + w^* \frac{\partial T^*}{\partial z^*} = \frac{1}{Re_{L_0} Pr} \left(\frac{\partial^2 T^*}{\partial z^{*2}} \right). \tag{2.34}$$

The ratio between free and forced convection is the ratio multiplying the first term on the right side of (2.33), and is known as the Richardson number, $Ri \equiv Gr/Re_{L_0}^2$. Depending on Richardson number, we may turn this problem into one of three cases:

- *Case 1:* when $Ri \ll 1$ natural convection is negligible. This simplifies the problem such that (2.34) is not coupled with (2.31)-(2.33) anymore. If the boundary conditions for (2.33) and (2.34) are the same and Pr ~1, i.e. the thermal and hydrodynamic BL would have the same influence on the flow, then the mathematical solution for the two equations would be the same. Using Blasius method, which follows a similarity solution using the stream function, provides the velocity field analytical solution. It is then used for the solution of the thermal equation for laminar flow [21, 22],

$$Nu_x = 0.453 Re_x^{1/2} Pr^{1/3} \qquad \forall\, Pr > 0.6\ . \tag{2.35}$$

- *Case 2:* When $Ri \gg 1$ forced convection is negligible, and the solution would be the same as the previously discussed solution in (2.29)-(2.30).
- *Case 3:* However, when Ri~1, the problem becomes much more complex due to comparable contributions of both free and forced convection. The effect of buoyancy on the forced convection solution is highly dependent on the direction of buoyancy force relative to the flow direction. The three extensively studied cases are when the buoyancy force is parallel to the direction of the flow, when it is perpendicular, and when it is antiparallel. These cases are known as *assisting*, *opposing*, and *transverse.* Given a specific geometry, it is common to take each of the Nusselt numbers of the forced, Nu_F, and natural, Nu_N, conditions separately (i.e. the results from *Case 1* and *Case 2* independently) and superimpose them as in (2.36). For example, in the case of a flat plate with surface area, perimeter, and

representative length scale, $L = Area/Perimeter$, buoyancy acts to increase the heat transfer rate. For this specific geometry of interest, the best correlation found is [21]

$$Nu^{7/2} = Nu_F^{7/2} + Nu_N^{7/2}. \tag{2.36}$$

It was also found that the enhancement of buoyancy forces above a horizontal plate is negligible for turbulent flow conditions vs. laminar [21, 23].

Upslope flows in nature correspond to the third case. This is because buoyant forces develop with heating of the slope surface which initiates the flow (*Case 2*) that eventually transforms into a forced flow combined with natural convection (*Case 3*). In nature, it is also common to find synoptic systems in the background, i.e. mean flow as an addition to the existing thermally driven flow. This work examines thermally driven flows in the absence of background synoptic forcing.

The next adjustment to the existing governing equations is that the flow inside the BL is turbulent. The governing equations of turbulent flows are modified such that the flow components are decomposed into the mean and fluctuating components,

$$u(x,z,t) = \bar{u} + u', \tag{2.37}$$

$$w(x,z,t) = \bar{w} + w' . \tag{2.38}$$

The decomposition is used to replace the instantaneous velocities of the BL governing equations (2.16)-(2.19). Since turbulent flows are chaotic, the ensemble average is taken (a process called Reynolds averaging) to simplify the equations to

$$\frac{\partial \bar{u}}{\partial x} + \frac{\partial \bar{w}}{\partial z} = 0 , \tag{2.39}$$

$$\bar{u}\frac{\partial \bar{u}}{\partial x} + \bar{w}\frac{\partial \bar{u}}{\partial z} = \frac{\partial}{\partial z}\left(\nu \frac{\partial \bar{u}}{\partial z} - \overline{u'w'}\right), \tag{2.40}$$

$$\bar{u}\frac{\partial \bar{w}}{\partial x}+\bar{w}\frac{\partial \bar{w}}{\partial z}=\beta_0(\bar{T}-T_\infty)g \quad +\frac{\partial}{\partial z}\left(\nu\frac{\partial \bar{w}}{\partial z}-\overline{u'w'}\right), \tag{2.41}$$

$$\bar{u}\frac{\partial \bar{T}}{\partial x}+\bar{w}\frac{\partial \bar{T}}{\partial z}=\frac{\partial}{\partial z}\left(\alpha\frac{\partial \bar{T}}{\partial z}-\overline{T'w'}\right). \tag{2.42}$$

The averaged product of fluctuating velocities and temperature are the Reynolds stresses and the turbulent buoyancy heat flux. They are significant because they quantify the transport of momentum and energy that occurs through eddies.

The system of four equations (2.39)-(2.42) has six unknowns, two of which are unknown correlations of fluctuating velocity components and temperature, known as the closure problem. To close the system of equations we must add more equations or use one of the many turbulence models available in literature expressing the fluctuations products in terms of averaged quantities. These closure models are based on assumptions, and therefore they are only approximations. These approximations are typically compared/confirmed using experimental data. One of the methods for closure, for example, is the eddy viscosity model. It assumes that both terms on the right sides of (2.40)-(2.42) should be proportional to the respective mean quantity gradient, and therefore [22]

$$\overline{u'w'}=\varepsilon_m(z)\frac{\partial \bar{u}}{\partial z}, \tag{2.43}$$

$$\overline{T'w'}=\varepsilon_H(z)\frac{\partial \bar{T}}{\partial z}, \tag{2.44}$$

where, $\varepsilon_m, \varepsilon_H$ denote the eddy diffusivity of momentum and heat, respectively. They are functions of z because eddies are larger further away from the wall. The mixing length model is based on empirical results and provides a relationship between the eddy diffusivity to the molecular viscosity. The heat flux model is based on the mixing length model and the turbulent Prandtl number defined as $Pr_t=\varepsilon_m/\varepsilon_H$.

The $Pr_t \sim O(1)$ since eddies transport momentum and heat simultaneously, ultimately providing enough information to close the system.

In addition to the closure problem, complex terrain flows are typically on slopes rather than flat terrains, and so the specific geometry is different than that of a flat plate. One of the early studies of inclined plates heat transfer suggested that the convection coefficient can be determined from vertical plate correlations, since there is an analytical solution for natural convection heat transfer on vertical plates. However, these are only true in cases where the plate bounds the instable part of the flow to prevent separation, i.e. fluid flow below a heated plate or fluid flow above a cooled plate, which does not lie in our range of interest [21]. Additionally, it is important to mention that the governing equations that we considered up to now are for steady state, while natural anabatic flows are transient, meaning changes with respect to time are not negligible.

The lack of an analytical solution for upslope thermally driven flows motivated a few groups over the years to conduct studies to model such flows [11, 24]. The model developed in 2003 by Hunt et al. [24] focused on the mean flow, averaged over an hour, of slopes with angles $\beta < 0.1$, small mean velocities, and accounts for changes over time. In this model, a slope-aligned coordinate system is adopted, and the buoyancy term is translated to the slope coordinate system. The slope was small enough and the density/temperature profiles are such that the flow does not separate. Assuming that the pressure is constant because the flow begins with stable stratification and there is no pressure gradient to drive the flow, density is only a function of temperature. The temperature changes of air considered are $< 10\ ^{\circ}C$, and $\rho/\rho_{\infty} \sim 1$ allowing us to assume ρ, T are *relatively* constant. If we use this in the volumetric thermal expansion definition, $\beta_0 = -\frac{1}{\rho}\frac{\rho}{T} = -\frac{1}{T}$. Additionally, on

the right side of (2.19), the conduction term may be replaced with Fourier's law of conduction: $Q = -k\frac{\partial T}{\partial z}$ and by defining the specific buoyancy as $F_b = Q/\rho c_p$, (2.16)-(2.19) are now

$$\frac{\partial u}{\partial x} + \frac{\partial w}{\partial z} = 0\,, \tag{2.45}$$

$$\frac{\partial u}{\partial t} + u\frac{\partial u}{\partial x} + w\frac{\partial u}{\partial z} = \nu\left(\frac{\partial^2 u}{\partial z^2}\right), \tag{2.46}$$

$$\frac{\partial w}{\partial t} + u\frac{\partial w}{\partial x} + w\frac{\partial w}{\partial z} = -\frac{(T - T_\infty)}{T_\infty}g \;\; + \nu\left(\frac{\partial^2 w}{\partial z^2}\right), \tag{2.47}$$

$$\frac{\partial T}{\partial t} + u\frac{\partial T}{\partial x} + w\frac{\partial T}{\partial z} = -\frac{\partial F_b}{\partial z}\,, \tag{2.48}$$

By defining characteristic length scales as the ones in (2.20) and comparing the ratios of different forces governing the flow, the equations reduce to

$$\frac{\partial u}{\partial x} + \frac{\partial w}{\partial z} = 0\,, \tag{2.49}$$

$$\frac{\partial u}{\partial t} = \nu\left(\frac{\partial^2 u}{\partial z^2}\right), \tag{2.50}$$

$$\frac{\partial w}{\partial t} = -\frac{(T - T_\infty)}{T_\infty}g \;\; + \nu\left(\frac{\partial^2 w}{\partial z^2}\right), \tag{2.51}$$

$$\frac{\partial T}{\partial t} = -\frac{\partial F_b}{\partial z}\,, \tag{2.52}$$

Eventually, simplified solutions were derived for three different layers within the BL, referred to as the surface layer, the mixed/middle layer, and the inversion layer. The surface layer is the layer that is most influenced by the wall, the mixed layer is dominated by turbulent mixing which makes buoyancy forces relatively negligible, and in the inversion layer the buoyancy forces, inertial forces, and shear stresses are significant.

This model is a good start but is not sufficient because it lacks consideration of the separation point and only represents very gentle slopes. Separation point is

commonly defined as the point where the wall shear stress vanishes, it is defined such that $\tau_w = \mu \frac{\partial u}{\partial z}\Big|_{z=0} = 0$ [25]. Figure 2.1b demonstrates that at the point of separation, S, the boundary layer is no longer attached to the boundary but begins flowing in the transverse direction. The fluid flow at $x > S$ therefore flows in the negative x direction to comply with continuity. This may be useful to detect the location of the separation point.

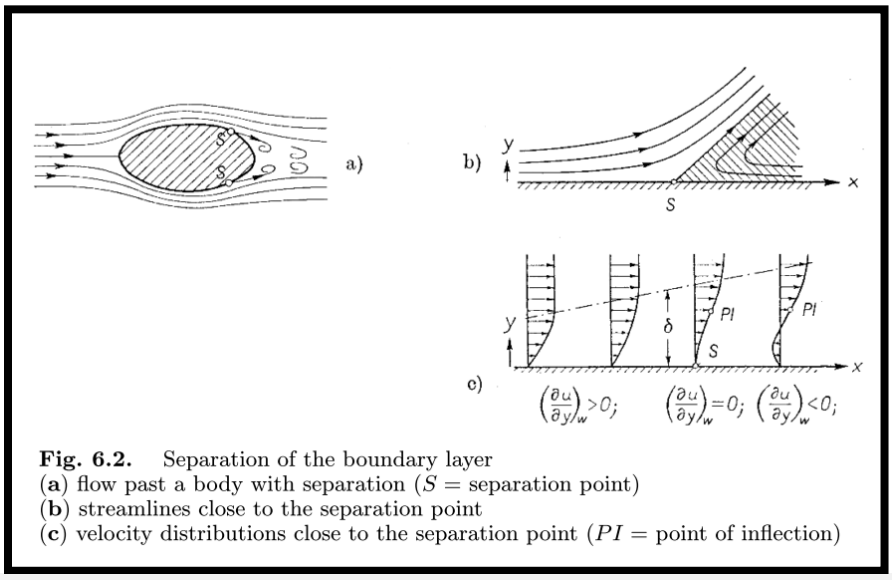

Fig. 6.2. Separation of the boundary layer
(**a**) flow past a body with separation (S = separation point)
(**b**) streamlines close to the separation point
(**c**) velocity distributions close to the separation point (PI = point of inflection)

Figure 2.1 Visual representation of the boundary layer separation, taken from [25].

The very recent experimental study by Hocut et al. [11] delved into flow separation in mountainous terrain. It showed great correspondence between the water tank model and field measurements. Although separation is a common occurrence in typical laboratory studies dealing with diurnal heating in complex topography [26], no other studies have been reported hitherto on flow separation and apex plume formation. In their model, they obtain a representative velocity scale from dimensional analysis of the velocity-vorticity form of the Navier Stokes equations.

$$u_S \sim (q_0 L_s \cos\beta)^{1/3} \ , \tag{2.53}$$

where u_s, L_s are the representative velocity, and length along the slope at the separation point respectively, and the buoyancy flux is $q_0 = \frac{g\alpha Q}{\rho c_p}$. In their study, Hocut et al. [11] compared their derived velocity scale to the one derived in Hunt et al. [24] $u_s \sim (q_0 \delta \sin\beta)^{1/3}$ and found it is valid only until the point of separation although also for larger slope angles than considered in [24]. Equating the two at the point of separation a relationship $L_s/\delta_s \sim \tan\beta$ was obtained. Which in turn allowed derivation [11] of the expected separation length along the slope

$$\frac{L_s}{L_0} = \left[1 + \Pi \frac{\sin^{\frac{1}{4}} 2\beta}{\sin\beta} \right]^{-1} \ , \tag{2.54}$$

where $\Pi = 0.35$ is a constant from scaling and L_0 is the slope length. This suggests that the separation point is independent of Re_H, which is in agreement with [25], and this finding agrees with their laboratory experimental results for slope angles larger than 20°. This is promising because the Re numbers in the lab cannot be matched with the ones observed in the field.

The water tank model used in that study [11], however, had limited dimensions of $125\ cm$ [L] × $30\ cm$ [W] × $30\ cm$ [H] which prevented the flow from maintaining its stability for periods longer than several minutes. The first part of this dissertation, Chapter 3, will present three types of extensions to the model: an addition of a plateau to the smaller tank configuration [27], experiments on a double slope configuration in a much larger tank, and consideration of the three dimensionality of the flow eventually invoking revision of the accepted model from [11].

The second core part of this dissertation, Chapter 4, demonstrates two advancements of the up-to-date available fine-scale field measurement instrumentation and techniques: new combo probe design and an automated calibration procedure. These advancements were built off of the recent study conducted during my Master's degree [12, 28] that detailed the first-ever field measurements of an anabatic flow field on a moderate slope. The point measurements of the flow were conducted using the novel collocated sonic-hotfilms combo anemometer. The combo uses the slow data from the ultrasonic anemometer and the simultaneously sampled and low pass-filtered data from the hotfilms to train hourly in-situ neural networks that provide the voltage to velocity functional dependencies. The combo continuously realigns the hotfilm sensors with the mean flow. However, the previously used combo was geometrically constrained and was only able to follow the flow in a yaw-rotation range of 120°. The newly developed design of the combo probe (Combo 10.0) eliminates this limitation and enables the combo to realign the hotwires in any desirable angle of attack, i.e. a complete 360° yaw rotation. The calibration procedure of the combo probe consisted of manually selecting suitable minutes to use for the construction of each hourly training set. Here, an alternative approach is proposed, effectively converting the calibration to an automated procedure. Enabling the capture of real-time fine-scale turbulent field measurements to be obtained anywhere and possibly used for in-situ weather prediction models. Finally, the third core part of this dissertation, Chapter 5, presents a novel and automated method for detection of the naturally occurring fine-scale phenomenon in turbulent flows, the turbulent bursting phenomenon [29]. An accurate detection of bursting periods effectively allows separation between the

latter and the background turbulence, facilitating both the independent analysis of both flow regimes and investigation of bursts generation mechanisms.

Chapter 3: Laboratory scale modelling

Complex terrain, which includes slopes, valleys, canyons, escarpments, gullies, and buttes covers about 70% of the land surface on Earth [30]. Many of the urban areas have been built in complex terrain because of its association with water resources. Slope and valley flows are important characteristics of complex terrain in the absence of synoptic effects, with downslope (katabatic) and down valley flows occurring at night, and upslope (anabatic) and up valley flows occurring during the day [5, 31]. During the night, the downslope winds blow through the gaps and canyons [32], which separate out from the slope as intrusions [33] and collide with each other. During the morning transition, when the nocturnal stable boundary layer breaks down and the daytime convective boundary layer is developed, the downslope flow reverses to form an upslope flow, due to the heating of the slope. The vorticity of the upslope flow is countered by the baroclinic generation of vorticity (baroclinic torque), which facilitates flow separation [34]. In the case of flow separation, a thermal plume is formed, and deep convective clouds can often be observed directly over the mountain peak [11, 35].

In complex terrain weather prediction, the excessive precipitation over steep and high mountains, in both mesoscale and climate models, has been attributed to the difficulties of parameterizing flow separation over sloping boundaries, in particular the sub-grid heat ventilation that is separated by upslope flows [36]. The combination of an overestimated heat flux and excessive moisture transport leads to false precipitation predictions. In the context of urban fluid mechanics, the presence or absence of flow separation appears to determine the fate of pollution. The meteorological and chemical measurements that were made during the 1997 Azteca experiment over the southern mountain range of Mexico City, the largest

metropolitan area in North America, with a population of about 20 million [37–40], indicated that the upslope flows transported pollutants out of the city to higher elevations during the day, and the downslope flows transported a portion of the pollutants back towards the city at night [41, 42]. Further investigation showed that the pollutants had lofted to regional flow or formed elevated recirculating flows within the convective boundary layer when the flow separated from the slope [31, 33, 43–47], and when it did not, the pollutants typically returned to the urban valley at night [31, 48]. The complex terrain therein can be approximated by a truncated structure with a slope and a plateau [37–40].

Despite its importance, research on the upslope flow separation over sloping boundaries has received little attention [24, 47]. Though laboratory studies are advantageous, as they allow repetitive and well controlled measurements of high accuracy to deduce the important relations, only a few studies have been performed in such a controlled environment [6, 43, 44]. Recently, Hocut et al. [11] conducted laboratory experiments on flow separation over a smooth heated slope. The study was performed without background stratification, which represents the case of the upslope flow after the morning transition. Three flow regimes were identified in their study. In the first regime, at slope angles β larger than a critical value of $\beta_c \approx 20°$, the separated flow generated a plume—a warmer bulk of fluid, rising inside colder surrounding fluid—that was fed solely by the upslope flow. For this regime, the location of the separation point was successfully predicted by a model, which was based on the balance between the opposing vorticities of baroclinicity and shear. The second regime occurred when $10° < \beta \leq \beta_c$, in which case the rising plume was fed by both the upslope flow and the entrainment of ambient fluid. In the third

regime, $\beta \leq 10°$, the plume had almost entirely covered the slope, like a buoyant plume emanating from a source of finite dimensions.

Hocut et al. [11] focused on the flow over a uniform smooth slope. Terrain in nature, however, is more complex, as the natural topography includes breaking slopes, convex/concave slopes, roughness gradients because of the varying vegetation density, slopes topped with a plateau, and more. Hence, the next step was to moderately increase the complexity of the terrain that was used by Hocut et al. [11], toward a representation of more realistic cases: e.g. a single slope topped off by a plateau, symmetric double slopes, and eventually introduction of roughness to the slopes .

3.1 Introducing higher complexity: incorporation of a plateau

The first part will delve into the incorporation of a plateau to the existing model of Hocut et al [11]. More specifically, the case of a uniformly smooth slope with a plateau at the top, as observed in several natural settings [37]. This section will detail my second publication during my PhD [27]. The experiments themselves were conducted at Notre Dame University and I led the data analysis and development of the extended model. The presented outcomes include: the separation location, the mean upslope velocity at the point of separation, and their dependence on the plateau width, slope angle, and buoyancy flux.

3.1.1 Experimental setup

The experiments were carried out using a model of the slope and plateau setup, situated in a water tank. Both the slope and the plateau surface were heated using electrical heaters and simulated the natural solar heating of the slope and

plateau land surface on a clear sky day. The same glass tank that was used by Hocut et al. [11], with a rectangular cross-section base ($125\ cm \times 30\ cm$), was used here. It was filled with deionized water to a depth of $35\ cm$. To ensure the two-dimensionality (2D) of the flow, the heat leakage to ambient air was minimized using water at room temperature, by encasing the tank with 5 cm thick Styrofoam thermal insulation, and by adopting long circulation stabilization times. A removable window in the insulation provided optical access to the flow. Two custom manufactured $15.6\ cm \times 30\ cm$ heating elements were used to heat the slope and plateau. Both units consisted of densely packed heating wires that were embedded in silicon rubber, which constituted a smooth upper surface. The units were fully insulated on the bottom. Constant DC current was used to heat up the heating units, which provided heat fluxes of up to $9.6\ \mathrm{kW\ m^{-2}}$. The heat flux was estimated as $Q = IV/A$, with V being the applied voltage, I being the applied DC current, and A being the surface area of a single heating unit. The calibration techniques that were described in Hunt et al. [24] were used to verify this estimate.

A schematic representation of the experimental design is shown in Figure 3.1. The slope–plateau configuration was placed abutting the wall of the tank. A vertically placed acrylic glass (Polymethyl Methacrylate [PMMA]) plate, which isolated the flow in the cavity between the plate and end wall, was used to vary the plateau width. As in Hocut et al. [11], the no-slip condition at the wall played a lesser role in the overall plume dynamics, and hence, the flow separation was assumed to be unaffected by the vertical wall.

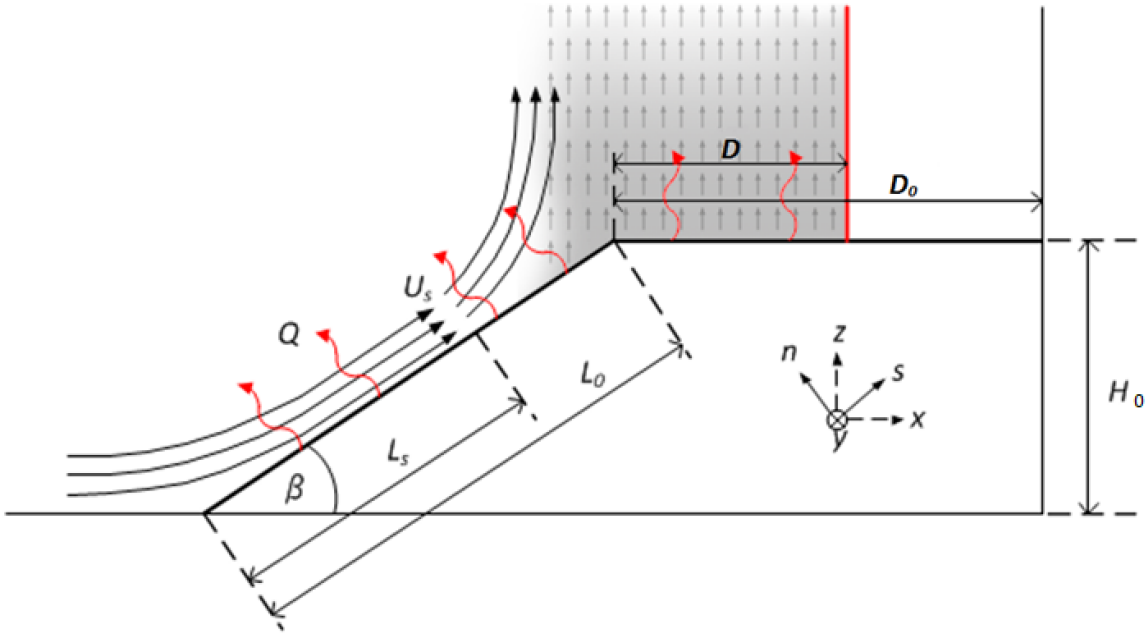

Figure 3.1 A schematic of the experimental configuration. The width of the plateau (D) was varied by moving the vertical wall indicated in red.

Prior to each experiment, the water tank would settle for two-hours to allow the residual motion to decay, after which a prescribed current was applied to the two heating units. Four slope angles, $\beta = 15°, 25°, 35°$, and $45°$, and five plateau widths, $D = L_0, \frac{3}{4}L_0, \frac{1}{2}L_0, \frac{1}{4}L_0$, and 0, were used, where $L_0 = 15.6$ cm was the full width of the heating unit and hence the width of the slope. The heat flux was varied between 0.50 W m^{-2} and 9.6 kW m^{-2}.

As in the work of Hocut et al. [11], the flow velocities were measured using the Particle Tracking Velocimetry (PTV). A vertical cross-section of the flow in the middle of the tank was illuminated by a 3 mm thick argon laser sheet (wavelength ~532 nm) through a vertical slit in the insulation. Orange polyethylene microspheres, which were 90– 106 μm in diameter and had a density of $\rho \approx 1\ g\ cm^{-3}$, were used to seed the flow. The particle motion was recorded at 5 frames per second (fps), using a 2 Megapixel CCD camera, that was positioned in front of the observation

window. The recorded videos were converted into individual frames and processed by in-house-developed PTV software. In post processing, the image quality was first improved by applying an image enhancement and a spatial filter. The image enhancements included adjusting the contrast and filtering the possible noise, while the spatial band-pass filter was applied to filter out any features of the dimensions below and above those of the used particles. As a result, the PTV algorithm was fed with images of a high contrast, of low noise level, and that included only the seeded particles on a black background; this process was used to ease the identification of each particle in the frame and to prevent false detections. Next, the individual particles were detected, which facilitated the reconstruction of 2D particle tracks. Afterwards, the velocity components were calculated using the track information. Additional PTV algorithm details can be found in Hocut et al. [11] and Liberzon and Shemer [49].

Similar to Hocut et al. [11], the separation distance, L_s, was determined by visually examining the PTV particle tracks and identifying the locations of the first visible separating track. In addition, the Feature Tracking Visualizations (FTV) that provided a time history of the flow, by color mapping and animating the particle tracks according to the track length and/or velocity, were used to verify, and if necessary, correct the determined separation point location. In unison, this method allowed for the detection of L_s with confidence. The mean along the slope velocity at the point of separation, U_s, was then obtained by ensemble averaging the velocities that were near the separation point. The measurement uncertainties were estimated using the technique of Kline and McClintock [50].

3.1.2 Expansion of existing model

After the initiation of heating, small-scale convective roll structures appeared on the slope and rolled up, to form a well-defined upslope flow that eventually separated and rose vertically to the water surface as a plume. Upon reaching the upper boundary (i.e., the water surface), the plume was deflected and propagated horizontally as an intrusion towards the distant end wall. This transient period had a maximum duration of about 200 s and varied based on the experimental parameters, (i.e., longer for the lower buoyancy fluxes). The transition period was followed by a quasi-steady period of 80– 130 s, depending on the set buoyancy flux and slope angle values, during which the upslope flow and the rising plume experienced minimal end wall influence, as the intrusion was propagated. The typical quasi-steady period lasted for about five minutes, with small variations based on the prescribed buoyancy flux and plateau width feeding the plume after the detachment of the upslope flow. The higher values of the buoyancy flux and plateau width formed larger plumes, which resulted in shorter quasi-steady periods. The measurements were performed for $t_s = 80– 120\ s$ during this quasi-steady period and were concluded when the plume intrusion reached the end wall. The quasi-steady upslope flow was achieved at a range of buoyancy fluxes, $q_0 = g\alpha Q/\rho_0 c_p$, which are elaborated in Table 3-1. Here, ρ_0 was a reference density, α was the thermal expansion coefficient, and c_p was the specific heat capacity. As observed by Hocut et al. [11], below this range of q_0, the flow either developed eddies that rolled up the slope (similar to laminar convection on slopes [51]) or formed a counterclockwise rotating single stationary eddy, of a size that was approximately equal to the depth of the tank. When it was quasi-steady, the upslope flow was parallel to the slope, with the entrainment at the top of the upslope boundary layer, and the flow was separated at a distance, L_s, from the bottom.

Important experimental parameters, including the buoyancy flux and the quasi-steady period length, are listed in Table 3-1.

Table 3-1 Experimental parameters examined in this setup.

$\boldsymbol{\beta}$ (degrees)	$\boldsymbol{D/L_0}$ (-)	$\boldsymbol{\beta_e}$ (degrees)	$\boldsymbol{q_0}$ (m²/s³)	$\boldsymbol{t_s}$ (s)
15	$0, \frac{1}{4}, \frac{1}{2}, \frac{3}{4}, 1$	$15, 18.75, 22.5, 30$	9.94×10^{-8} 1.49×10^{-7} 1.98×10^{-7}	$50, 80, 120$
25	$0, \frac{1}{6}, \frac{1}{3}, \frac{1}{2}, \frac{2}{3}, \frac{5}{6}, 1$	$25, 29.17, 33.33,$ $37.5, 41.67, 45.83, 50$	4.93×10^{-9} 1.5×10^{-8} 2.5×10^{-8} 3.5×10^{-8}	100
35	$0, \frac{1}{8}, \frac{1}{4}, \frac{1}{2}, \frac{3}{4}, 1$	$35, 39.38, 43.75,$ $52.5, 61.25, 70$	5×10^{-8} 2.45×10^{-7} 1.3×10^{-7} 1.3×10^{-7}	50
45	$0, \frac{1}{8}, \frac{1}{4}, \frac{1}{2}, \frac{3}{4}, 1$	$45, 50.63, 56.25,$ $67.5, 78.75, 90$	6.4×10^{-8} 9.6×10^{-8} 1.28×10^{-7}	$50, 80$

The separation length, L_s, was detected by the method that was described in the previous section. Figure 3.2 shows the PTV track maps of three example experiments, with white arrows marking the separation point. The error of the separation distance detection was estimated as the distance that was travelled by a particle during three consecutive frames, described by Hocut et al. [11], that is, $\Delta L_s = \pm 3 \Delta t U_s$, Δt being the time between two frames, which was the reciprocal of the frame rate (5 fps).

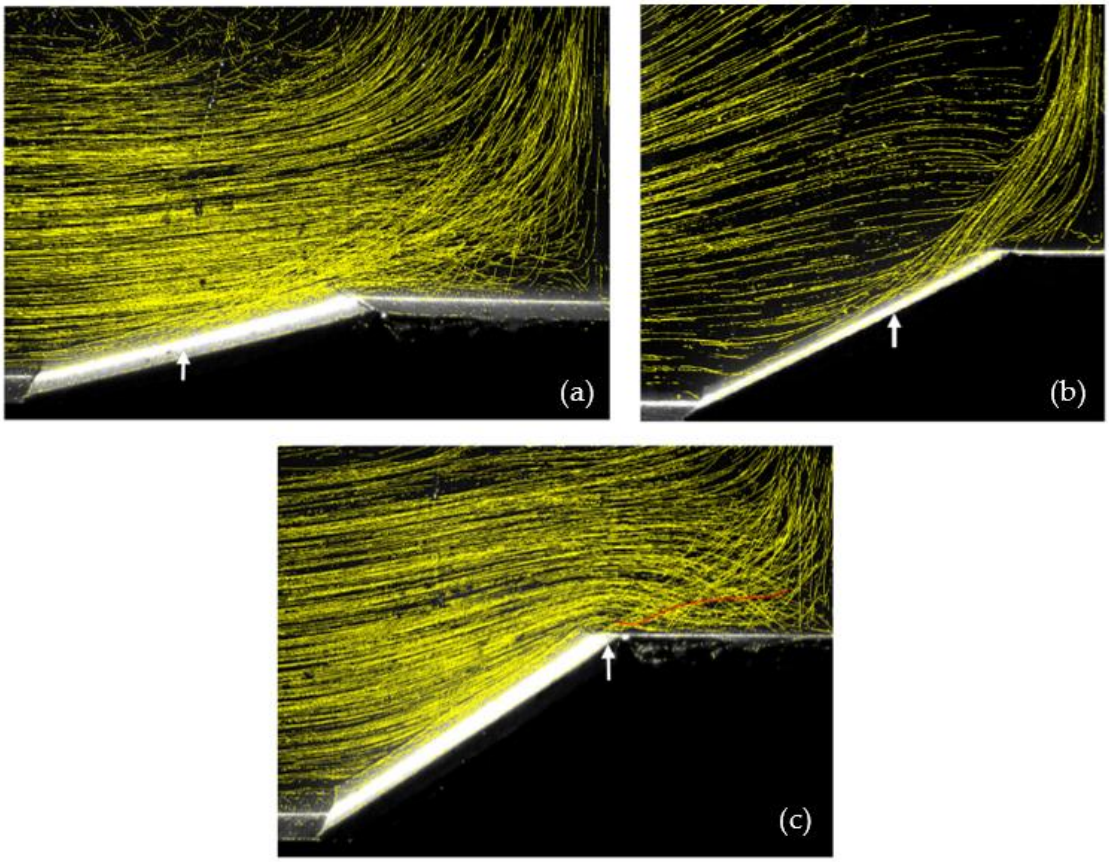

Figure 3.2 Three Particle Tracking Velocimetry (PTV) track maps: (a) $\beta = 15°$ and $D = \frac{3}{4}L_0$, (b) $\beta = 25°$ and $D = \frac{1}{3}L_0$, and (c) $\beta = 35°$ and $D = \frac{3}{4}L_0$, illustrating the path lines of the fluid parcels over the slope and plateau. The separation locations are marked by white arrows. In (a,c), where the plateau is large, there are many fluid parcels from the slope penetrating the plume over the plateau, which is illustrated by the red particle track in (c). In (b) there is much less penetration into the plume core.

Hocut et al. [11] found that the nondimensional separation length L_s/L_0 was independent of the buoyancy flux. They then proposed, using scaling arguments, its dependence on the geometric angle, β (see Equation. 5.8), which took the form of $L_s/L_0 = \left[1 + \Pi \cdot \left(\sin^{\frac{1}{4}} 2\beta \,/\, \sin\beta\right)\right]^{-1}$, where L_0 is the slope length and Π is an empirical constant. In the present work, however, it was observed that for a given slope angle, the presence of a plateau resulted in an increased separation length, compared with the case without the plateau present. Moreover, the separation length had increased with the increasing width of the plateau, mimicking the

behavior of steeper slopes. Hence, an empirical effective slope angle $\beta_e = \beta \cdot (1 + D/L_0)$ was developed to represent the effects of the plateau presence and width. In other words, using the effective angle, we represented the influence of a plateau that was analogous to a slope without plateau. This allowed a direct comparison of the results with the previous work of Hocut et al. [11].

Figure 3.3 shows the dimensionless separation distance, L_s/L_0, as a function of β_e. The estimated errors of the L_s/L_0 were $\sim 3 - 5.5\%$, with the error bars omitted from the figure for the sake of clarity. At least three different buoyancy fluxes were used for each prescribed angle and plateau width, and Figure 3.3 shows that the L_s/L_0 varies only slightly for different buoyancy fluxes when the flow is quasi-steady; which indicated the Reynolds number independence, as observed in Hocut et al. [11] (see their Figure 5). The data for $D = 0$ was taken from Hocut et al. [11]. Therefore, L_s/L_0 was taken as a constant for a given effective angle (i.e., for a combination of the geometric angle and normalized plateau width) within the experimental error. The exceptions were data obtained at the $\beta = 35°$ slope angle, where a larger scatter was observed with variations in both the plateau width and buoyancy flux.

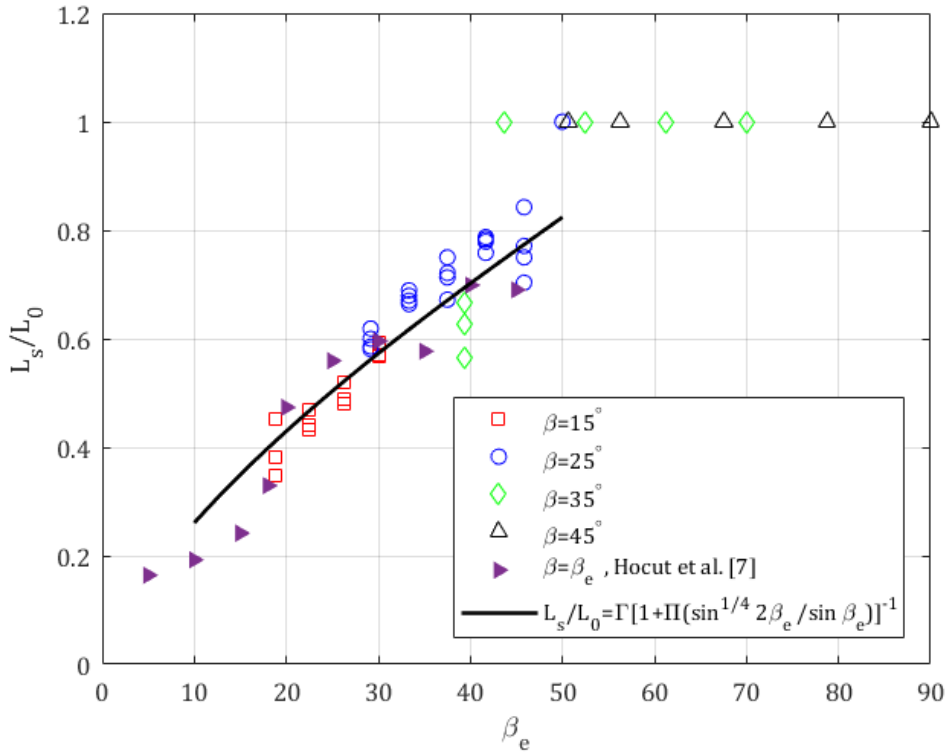

Figure 3.3 The dimensionless flow separation distance L_s/L_0 as a function of the effective angle β_e, which incorporates the plateau with $\Pi = 7.4$ and $\Gamma = 8.8$. The data of no plateau $D = 0$, is taken from Hocut et al. [11].

Next, we compared the fit of Hocut et al. [11] with the present data, in order to estimate the expected dimensionless separation length as a function of β_e in the range $10° < \beta_e < 45°$. That fit was derived for the cases of no plateau, with a significant upslope flow and separation, here β was replaced by β_e, as follows:

$$\frac{L_s}{L_0} = \Gamma \cdot \left[1 + \Pi \cdot \frac{\sin^{\frac{1}{4}} 2\beta_e}{\sin \beta_e}\right]^{-1}, \tag{3.1}$$

where the modification of the Hocut et al. parameterization accounts for the plateau effects. After introducing an additional constant Γ, so as to allow for an extra degree of freedom for the fitting algorithm, an excellent fit was obtained using the least squares that were fitted for the tightly collapsed data ($\Pi = 7.4$ and $\Gamma = 8.8$) in the range $17° < \beta_e < 45°$, which included the data taken from Hocut et al. [11] in this

range. In the range $17° < \beta_e < 45°$, as was expected from dimensional considerations, the separation length L_s was dependent on β_e but independent on the heat flux. For $\beta_e \gtrsim 45°$, the flow separation was generally suppressed and occurred at the slope apex. The fit curve was also plotted down to $\beta_e = 10°$, as in the previous work of Hocut et al. [11]. A different behavior was observed for the slope angles that were less than 20°, and the comparison was less favorable for these slope angle values.

It was also interesting to note there was a sub-regime for the slope angle $\beta \sim 15°$, in which the fluid parcels penetrated the plume near the separation point (Figure 3.2). This was very similar to the case $\beta \leq 10°$ without a plateau, as observed in Hocut et al. [11], where there was a substantial lateral penetration as the flow approached the case of a plume from a uniformly heated source with an infinite width of L_w. The scaling for the buoyancy b, vertical velocity w, and near-field entrainment velocity u_e for the horizontal plume source of finite dimensions L_w, driven by a buoyancy flux q_0, were proposed by Colomer et al. [27]. For 2D horizontal sources of finite source dimensions, the analogous 2D near-field scaling becomes the following:

$$b \sim \frac{(q_0 L_w)^{2/3}}{L_w}, \quad w \sim (q_0 L_w)^{1/3} \quad \text{and} \quad u_e \sim (q_0 L_w)^{1/3}. \tag{3.2}$$

The separation distance L_s can be estimated using the vertical momentum equation, by considering a balance of the buoyancy forces due to heating of the entrainment flow and the vertical inertia forces, as follows:

$$b \sim \frac{\mathrm{D}w}{\mathrm{D}t} \sim u\frac{\partial w}{\partial x} \sim \frac{u_e w}{L_s} \sim \frac{\alpha_1 w^2}{L_s}, \tag{3.3}$$

where w is the vertical velocity outside the thermal boundary layer and α_1 is the entrainment coefficient for 2D plumes (according to Rouse et al. [52], for 2D line-source plumes, $\alpha_1 \approx 0.25$). Together, Equations (3.2) and (3.3) give the following:

$$L_s \sim \alpha_1 L_w, \tag{3.4}$$

that should be valid for slope angles of $\beta < 20°$. In our case, the width of the plume was given by $L_w = D + (L_0 - L_s)\cos\beta$. Figure 3.4 shows the L_s/L_w ratio as a function of D/L_0. For $\beta = 15°$ the ratio of L_s/L_w is approximately constant attaining value of ≈ 0.29, independent on the width of the plateau, and with the entrainment value $\alpha_1 \approx 0.25$. For slope angles larger than 15° the ratio is not constant and changes with the plateau width.

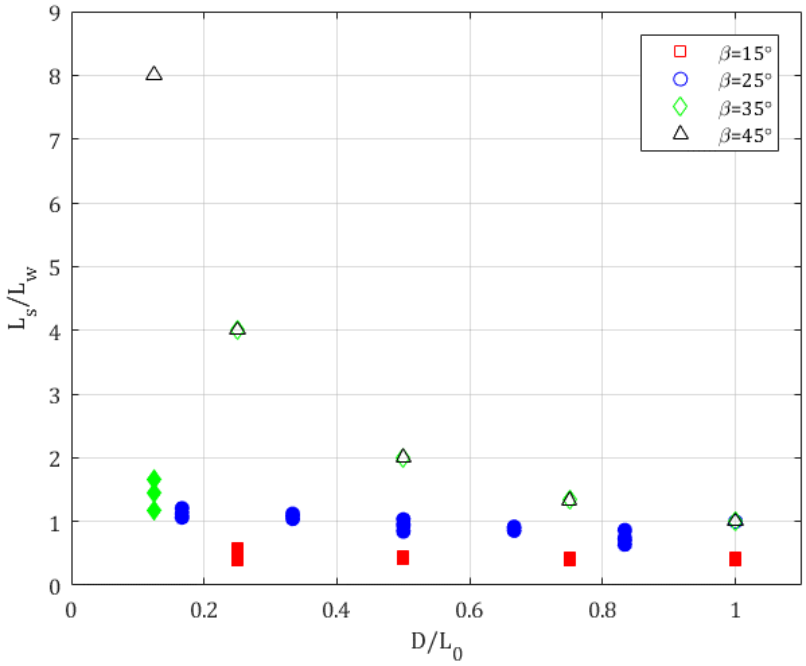

Figure 3.4 The ratio L_s/L_w, where L_s is the separation length and L_w the width of the plume. For $\beta = 15°$, the ratio has the constant value of ≈ 0.29, while for $\beta = 25°$, the ratio is of $O(1)$. The filled in markers represent data with separation $L_s/L_0 < 1$, and empty markers represent cases with separation at the apex.

For each of the examined cases, the PTV data were used to determine the local mean upslope velocity at the separation point U_s. This was done by selecting a small

rectangular interrogation area ($\sim 1 \times 1\ \mathrm{cm}^2$) around the detected separation point. The area dimensions were chosen by examining the upslope velocity magnitude values distribution, and eventually the dimensions at which the distribution best resembled a normal distribution were chosen. The particle velocities were calculated in this interrogation area by dividing the digitized track lengths between two consecutive frames by Δt. The rectangular interrogation area was placed, such that it included a small portion of the slope itself, in order to ensure that the near-slope boundary layer was included. Out of all the velocity magnitude values that were detected in the area, only those that oriented along the slope were considered, and their distribution histograms were plotted and examined. The values that were outside of the main distribution range, low values contributed by on slope particles high values contributed by outside the BL or the erroneous detections particles, were taken out of the ensemble. A representative histogram of the calculated velocity magnitudes at the point of separation from the case $\beta = 25°$ and $D = \frac{1}{3}L_0$, is shown in Figure 3.5.

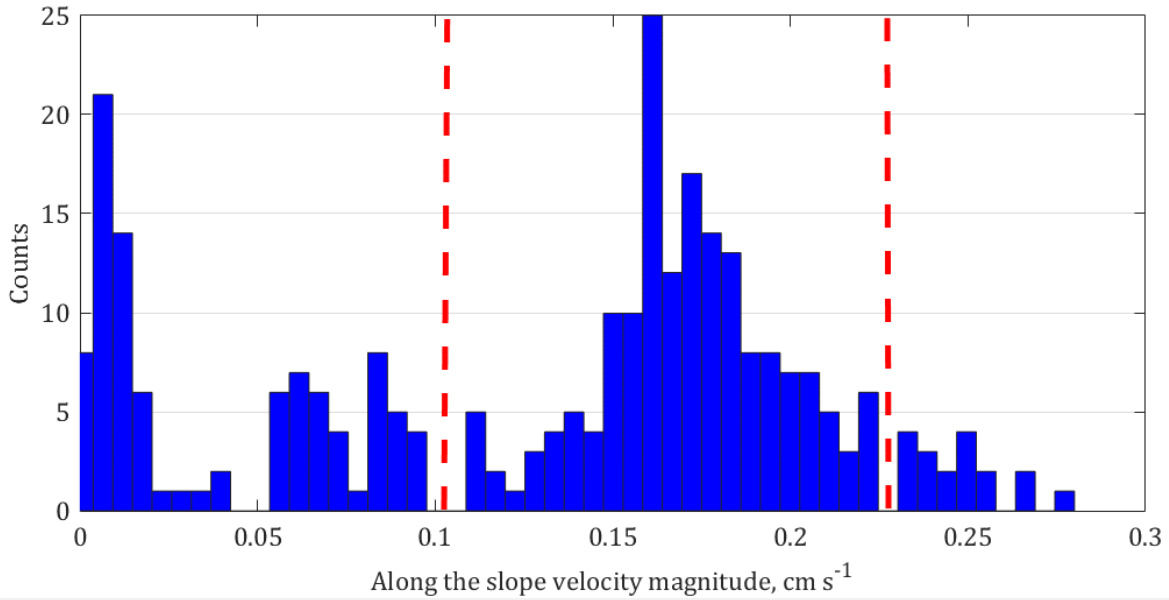

Figure 3.5 The distribution of magnitudes of the upslope-oriented velocity at the flow separation point ($\beta = 25°$ and $D = \frac{1}{3}L_0$). The red dashed lines mark the limits of the ensemble taken for averaging.

The local mean upslope velocity magnitude U_s was then determined by averaging the remaining ensemble. The error of the mean velocity was determined by considering a particle position detection accuracy of $\pm 0.5\, pixels$, spatial resolution of 32– 51 $pixel\ cm^{-1}$, and a frame rate of 5 fps.

Figure 3.6 shows the local mean upslope velocity, U_s, at the separation point. Hocut et al. [11] derived a velocity scale for the upslope velocity at the flow separation, given by the following:

$$U_s = \gamma \cdot (q_0 L_s \cos\beta)^{1/3}, \tag{3.5}$$

γ is a proportionality constant. This was derived by balancing the vorticities of the baroclinic torque and the shear flow, which was estimated from the vorticity equation, and it was expected to be valid up to the flow separation point on the slope. In the present study, using the effective angle β_e, a proportionality constant $\gamma = 1.3$ was found, as shown by the black line in Figure 3.6. The data for cases with

separation before the apex followed the line accurately, while there was an evident larger scatter for cases with separation at the apex (see these cases in Figure 3.3). Although the separation length L_s was dependent on the geometric parameters only, U_s was found to be depended on buoyancy flux q_0 as well.

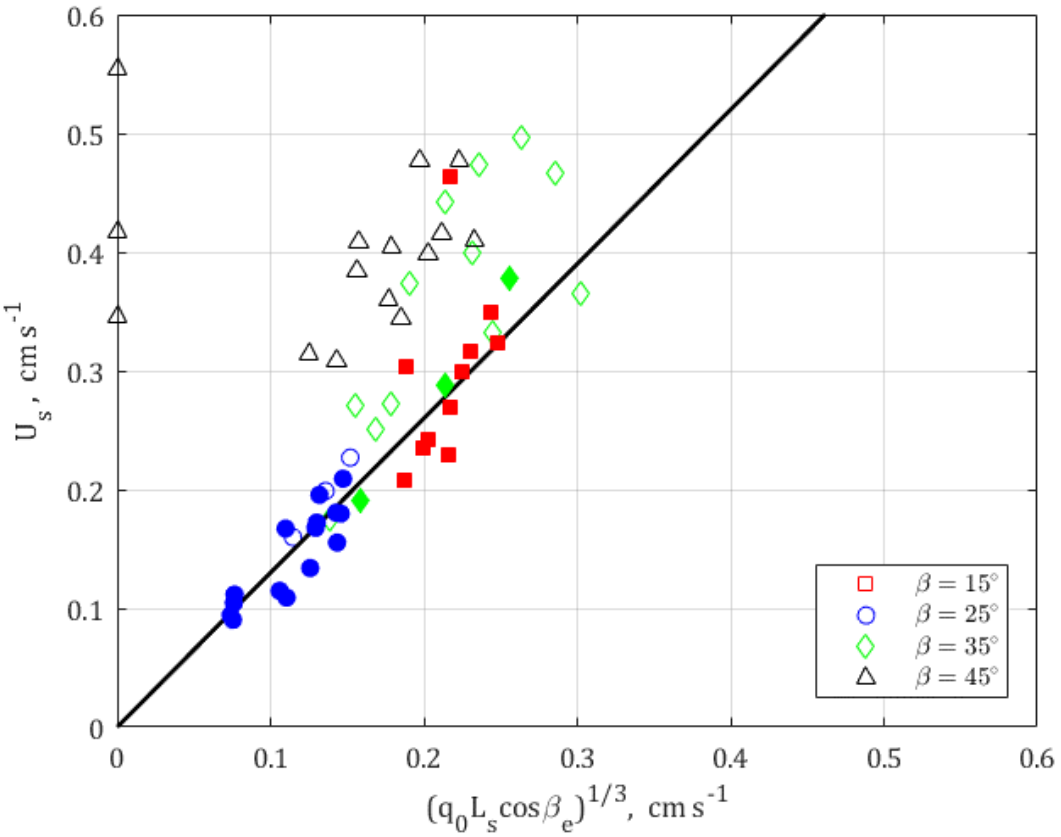

Figure 3.6 Local mean upslope velocity, U_s, at the flow separation point. The filled in markers represent data with separation along the slope, $L_s/L_0 < 1$, and empty markers represent cases with separation at the apex. The solid line is a linear fit of Equation (3.5) for the cases with separation before the apex where the proportionality constant $\gamma = U_s/(q_0 L_s \cos\beta_e)^{1/3} = 1.3$, using the effective slope angle.

3.1.3 Conclusions and limitations

The behavior of the upslope flow developing over natural slopes depends on numerous topography features. Natural slopes come in a variety of shapes, such as concave, convex, varied slope angles, and more. Another factor that is present in nature is the roughness of the slope: it can be relatively uniform, moderately vary in

magnitude, or exhibit a significant gradient along the slope (e.g., a forest canopy often becomes sparse with increasing altitude). Another important factor is the presence of a plateau at the apex of the slope. The diurnal heating/cooling cycle of the slope and of the plateau surface then influence the thermal circulations along the slope that form (up- and down-slope flows that are developing correspondingly during the day and night hours) under clear sky quiescent conditions. These are of significance for climate studies, local and meso-scale weather prediction models, and studies of pollution transport and prevention. This study is an extension of the previous work that was reported in Hocut et al. [11], where the flows over a smooth slope were examined. It represents a step toward increasing the complexity of the laboratory model, to better represent the natural complex terrain with the addition of a heated plateau.

Laboratory experiments were conducted to study the separation of the thermally driven upslope flow on a 2D slope that was topped by a plateau, which resembled the shape of a truncated pyramid. The topographical model was uniformly heated to mimic the solar heating during daytime hours. Water was used as a model fluid, and a neutrally stratified water tank provided quiescent neutral background conditions. A range of slope angles, plateau widths, and buoyancy fluxes were used for the experiments. Particle Tracking Velocimetry (PTV) and Feature Tracking Visualization (FTV) were employed to determine the upslope flow separation point and mean upslope velocity at the point of separation. The measurements were conducted under quasi-steady conditions with minimal end wall influence. During the experiments, the rising warmer fluid deflected at the top of the water level and was propagated away from the slope region, while the

upslope flow and the separated plume were quasi-steady. Major findings are summarized below.

1. Given that the slope is topped by a plateau of finite width (D), the influence of the plateau on the upslope flow could be expressed in terms of an effective slope angle $\beta_e = \beta \cdot \left(1 + \frac{D}{L_0}\right)$, *w*here L_0 is the slope length and β is the physical slope angle. For effective angles of $17° < \beta_e < 45°$, the separation length L_s increases with β_e. When $\beta_e \gtrsim 45°$, the upslope flow reached the apex and did not separate, which is independent of the plateau width. In this configuration, the upslope flow is insufficient to feed the plume that has formed on the plateau, thus requiring additional horizontal entrainment of the ambient fluid to the plume.
2. When $\beta \sim 15°$, there exists a sub-regime, in which the fluid parcels horizontally penetrate the plume near the separation point. The flow approaches that of a plume that is emanating from a uniformly heated horizontal source of finite width. The relationship between the separation length and the width of the plume for this case is observed to be $\frac{L_s}{L_w} \approx 0.29$.
3. The mean upslope velocity at the separation point (U_s) is dependent on the buoyancy flux, the effective slope angle, and the separation length. The upslope flow velocity scale that was proposed by Hocut et al. [7], was shown to also be valid in the present study, if the effects that are induced by the plateau are incorporated, using the effective angle definition.

This research incorporated the influence of a heated plateau to a previously introduced model of thermally driven upslope flow separation. The introduction of the effective slope angle β_e, which encompasses the plateau influence in terms of the slope angle shows a direct similarity to the previously examined cases in the absence

of a plateau. The results included the upslope flow separation location and the upslope velocity at the point of separation. Together, the upslope velocity scaling and the separation length parametrization could quantify similar complex topography flows. The next logical step is the examination of slope roughness and its variation along the slope to mimic realistic natural flows.

In conclusion, this first part of the chapter presented the empirical findings of thermally driven upslope flow in the presence of a plateau. We presented the empirical models of the separation of the upslope flow from the slope and the associated upslope velocity at the point of separation. In the second part of the chapter we expand the laboratory scale modelling to a much larger volume, aiming to observe the flow behavior in longer durations, the three dimensionality of the flow, and the effect of roughness on the slopes.

3.2 Introducing higher complexity: symmetric double slopes

Although the empirical findings from the previous section provide a basis for the understanding of mean anabatic flow behavior, the water tank used was not large enough for the examination of the periodic flow patterns. Only the first quasi-steady period was examined, until the plume started recirculating and breaking the BL, lasting for several minutes. The finite size of that tank was also found to limit the flow behavior to 2D as the changes in the transverse axis appeared negligible.

The second section of this chapter will delve into the investigation of symmetric double slopes in a much larger water tank. The motivation was to increase the duration of the experiments, examining the steadiness of highly turbulent and potentially separating boundary layer flow. While examining the results, it was discovered that the flow in a much larger tank was mainly governed

by 3D behavior, introducing high level of intermittency in both mean and fluctuating parameters. The presented outcomes include: the separation location comparison with the previous model, boundary layer characteristics, velocity profiles, temperature profiles, the baroclinic torque to vorticity ratio, three-dimensionality of the flow, and BL behavior with roughness introduced. The combined results provide a deeper understanding of the flow patterns expected to be observed on a symmetric mountain.

3.2.1 Experimental setup

This laboratory work was conducted in the T-SAIL (Technion-Sea Atmosphere Interactions research Laboratory) facility, which consists of a larger water tank with dimensions of $200\ cm$ [L] $\times$ $60\ cm$ [W] $\times$ $120\ cm$ [H], as in Figure 3.7, to allow for longer persistent flow periods of anabatic flow developing on a double slope. The experimental setup consisted of two 1.23 MP cameras sampled at $5\ fps$, a grid of 32 k-type thermocouples to sample temperature, continuous $400\ mW$ argon green laser, and electric heating to model the symmetric double slope geometry. Visualization of the flow was performed using neutrally buoyant fluorescent particles with diameters of $27-32\ \mu m$. Temperature measurements were obtained using a grid of thermocouples on one side of the slope, as illustrated in Figure 3.7. The thermocouples locations along the slope are presented in Figure 3.10.

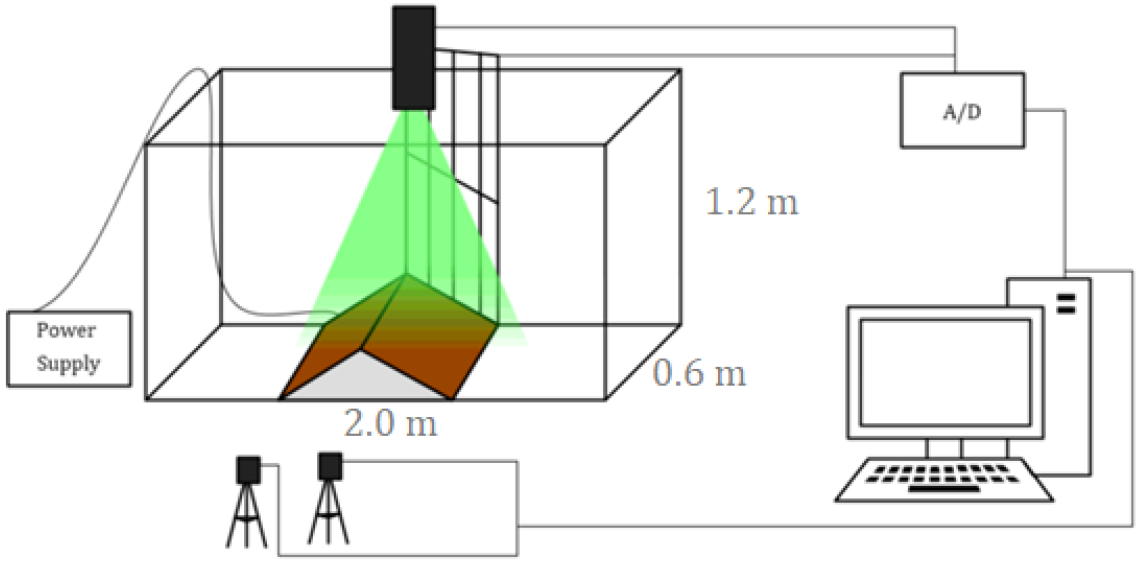

Figure 3.7 Experimental setup in laboratory consisting of a water tank, a green laser sheet, single and double-sided slope/s, camera/s, computer, A/D cards, and thermocouples.

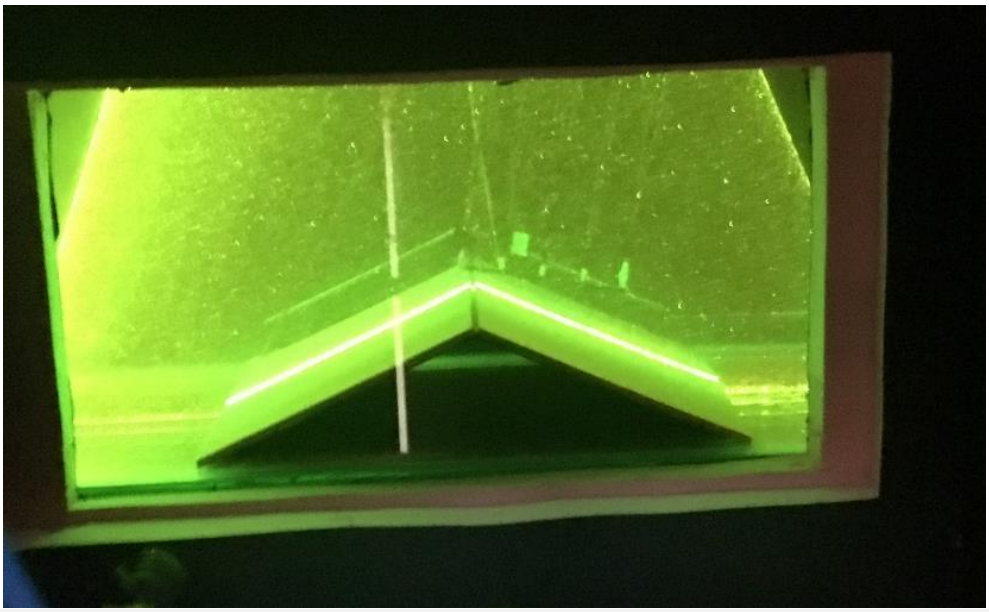

Figure 3.8 The experimental setup as observed from the window designed for optical access. The cameras are placed in a Styrofoam enclosure to prevent heat leakage to the environment and to enclose additional lighting to prevent noise.

The flow visualization method of choice is 2-D Particle Image Velocimetry (PIV). This Eularian approach is less costly computationally, than its Lagrangian counterpart (PTV) and provides a vector map where each vector is representative of the most probable fluid-parcel movement within an interrogation window. In more detail, PIV *refers to a class of methods used in experimental fluid mechanics to determine instantaneous fields of the vector velocity by measuring the displacement of numerous particles that accurately follow the motion of the fluid* [53]. A laser sheet is used to illuminate the particles in the cross section of the control volume and a camera placed perpendicular to the laser sheet captures the movement of the particles. Solid particles are more advantageous than dye because they do not diffuse or deform and they produce a better image due to better light scattering [53, 54]. The laser light scattered from the particles is recorded on camera/s with a predefined frame rate. To calculate velocities, each image pair is divided into interrogation windows and cross-correlation determines the average particle displacement within an interrogation window by means of using the correlation peak. The measured displacement and time difference between the frames provide a velocity vector map. Calibration is simply done by taking an image of an object with a known size inside the laser sheet, i.e. the length of the slope.

The large dimensions of the water tank and thermal insulation allowed for experimental durations of more than two-hours. Selection of the particle size was based on the desired initial experimental conditions and dimensions of the tank. The desired initial conditions are complete stand still of the water in the tank and its uniform temperature to isolate the anabatic flow phenomenon from external/mean flow. Stabilization times of such conditions were found to be roughly $12-24$ hours, depending on initial tank condition (i.e. mixing/seeding the particles and

arrangement of the setup). The waiting time for stabilization began after the particles are seeded. The particles must not sink nor float during that time so that when the experiment starts these can be used to trace the flow. Commercially available particles have a density of $\rho_P = 0.99 - 1.01\ g/cc$, while the water at laboratory temperature of $22° - 28\ °$ has a density of $\rho_f = 0.998 - 0.996\ g/cc$. The settling velocity is then calculated by

$$w_P = \frac{\bar{\rho} - 1}{\bar{\rho}} \frac{t_0 g}{\phi_1}\ , \tag{3.6}$$

where ϕ_1 is the constant shear stress condition and is evaluated at 1 according to [53], $\bar{\rho} = \rho_P/\rho_f$, and $t_0 = \rho_P d_P^2/18\nu_f\rho_f$. For example, the settling velocity for the above mentioned properties with particle diameter of $200\ \mu m$ are $73.6 - 75.1\ \mu m/s$. In other words, it would take the suspended particles approximately 1 hour to sink/float a distance of $23\ cm$, whereas for particles of $30\ \mu m$ it would take about 1.5 days to sink or float the same distance; this length was chosen as an example since it is the height of the region of interest filmed by the cameras. Hence, taking into consideration the explained above requirements for 24 hours waiting period to achieve still water conditions explains the selection of particle diameter not exceeding $30\ \mu m$. The selected particles are fluorescent, and a bandpass filter was placed on the camera lenses to reduce noise in the images. This assisted in preventing excess noise from entering the frame, i.e. the background was pitch black (including the laser sheet itself) and the only light captured by the camera was the light from the fluorescent particles.

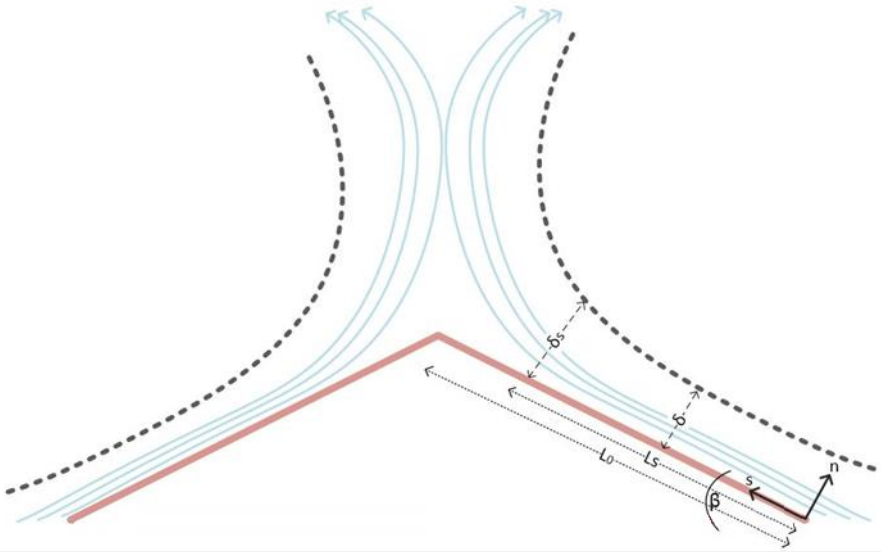

Figure 3.9 Coordinate system along the slope. This coordinate system is defined separately for each slope, the right slope and left slope. β is the angle of the slope, L_0 is the slope length, L_s is the length at the point of separation, δ is the height of the BL, δ_s is the height of the BL at separation, and s and n are the along slope and normal coordinates.

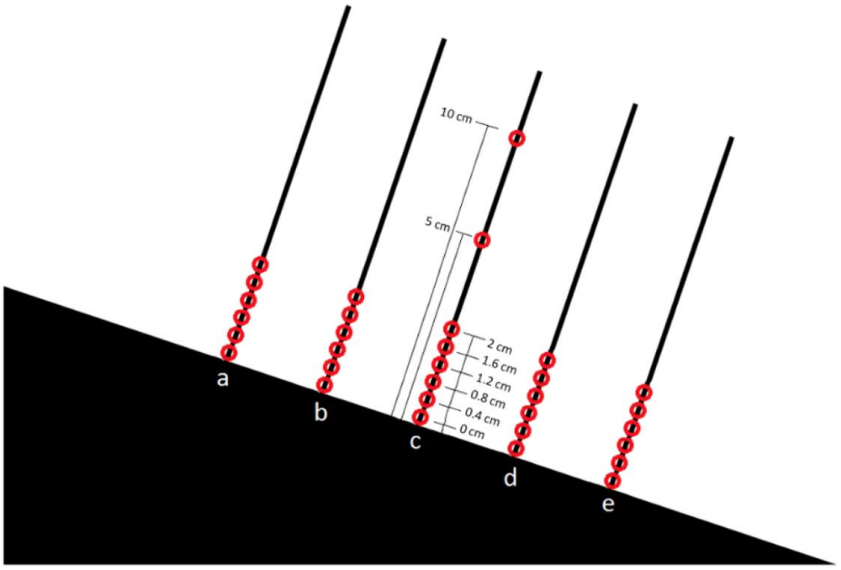

Figure 3.10 The grid of $k-type$ thermocouples placed on the center of the slope. The distance between each rod is 5 cm.

The entire tank was covered with 5 cm styrofoam to prevent heat leakage to the environment. A rectangular section was cut out to enable camera access. The cameras themselves were placed in another enclosure to block out external light (noise) and heat leakage. An example of a single frame can be seen below in Figure 3.38. The conducted experiments ranged on slope angles $\beta = 5.7°, 10°, 15°, 20°, 25°, 30°, 35°, 40°, 45°$ at various heat fluxes in the range of $Q = 40 - 1000\ W/m^2$, and are clearly presented in Figure 3.11. These correspond to buoyancy fluxes in the range of $2 \times 10^{-8}\ m^2 s^{-3}\ to\ 5 \times 10^{-7}\ m^2 s^{-3}$. All experiments were run for two-hours with a sampling frequency of 5 Hz and a camera resolution of $40 - 45\ pixels/cm$. All results presented in the next section are in the slope coordinate system.

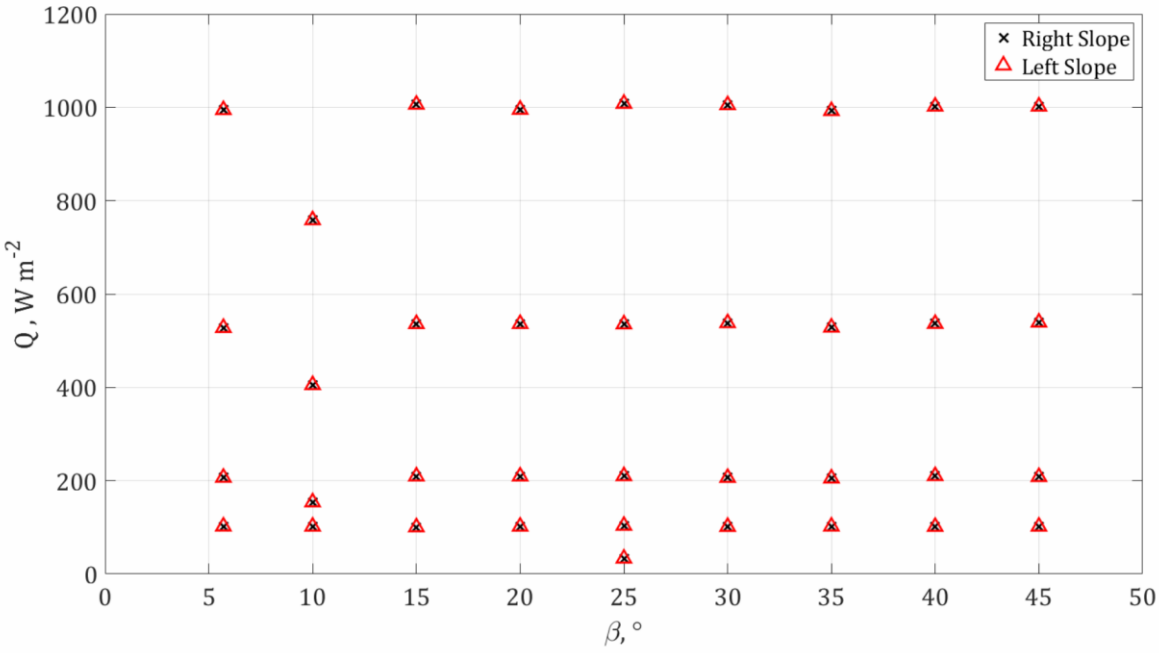

Figure 3.11 All experiments conducted in the water tank with a double slope configuration. The range of angles and heat fluxes are presented above and the differentiation between the slopes is indicated by a black "x" or a red "Δ" for the right and left slopes, respectively.

3.2.2 Mean boundary layer properties

Four-minute average velocity profiles are provided below. They follow a similar pattern with a constant variance at all heights. These points along the slope were selected as they correspond to the locations of the temperature measurements available. Below are three sample profiles for $\beta = 15°, 25°, 35°$ presented in Figure 3.12-3.14. Observation of the temperature profiles suggests that the used temperature sensors grid was too coarse and, in several cases, did not even cover the entire boundary layer. It is recommended to use a significantly finer grid, an infrared camera, or thermochromic particles in future experiments. The four-minute mean velocity and temperature profiles collapsed well for the entire duration of the experiment and the collapse of all experiments with the same geometric configuration and all heat-flux variations is examined in Figures 3.15-3.23. The normalized average profiles also follow a similar pattern between the different experiments of similar geometry. The velocity normalization is defined as $U_N = u/u_{max}$ where u_{max} is the maximum along slope velocity observed for each profile. The temperature normalization is defined as $T_N = \frac{T-T_\infty}{T_w-T_\infty}$, where T_w is the temperature on the slope and T_∞ is the background and initial fluid temperature.

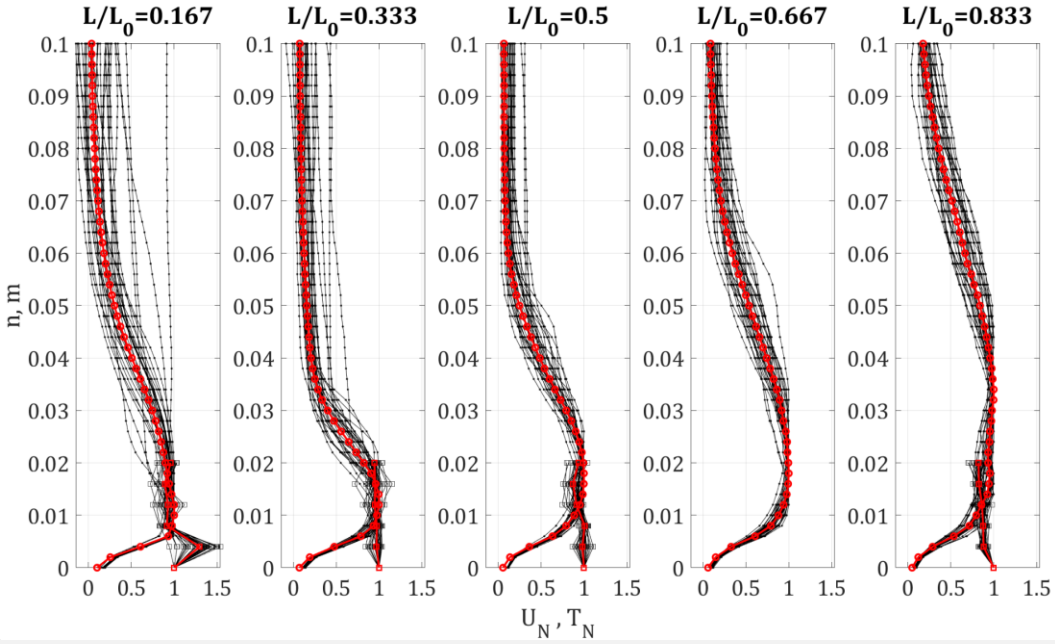

Figure 3.12 Along slope normalized velocity profiles at five cross sections along the slope. The representative experiment presented here is of slope angle of $\beta = 15°$ and the highest heat flux examined, $Q = 1000\ W/m^2$. Each black curve represents a four-minute average. The velocity is marked with circle markers and temperatures are marked by squares. The red curves represent the two-hour average, i.e. the entire experiment.

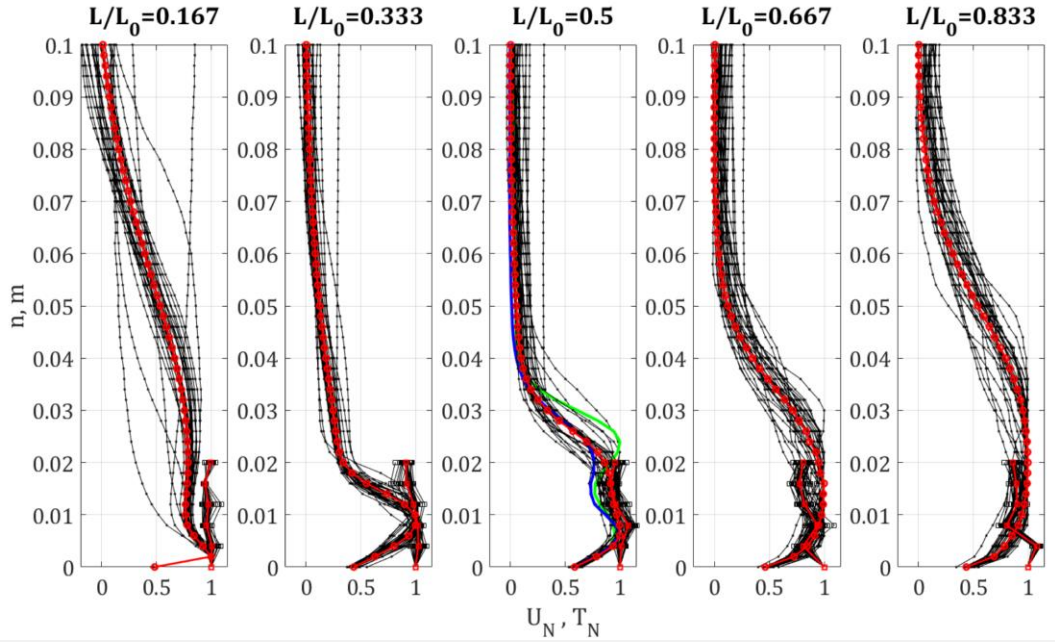

Figure 3.13 Along slope normalized velocity profiles at five cross sections along the slope. The representative experiment presented here is of slope angle of $\beta = 25°$ and the highest heat flux examined, $Q = 1000\ W/m^2$. Each black curve represents a four-minute average. The velocity is marked with circle markers and temperatures are marked by squares. The red curves represent the two-hour average, i.e. the entire experiment. The blue and green curves are references to *Clue#1* discussed below, representative of the "B-shaped" profile.

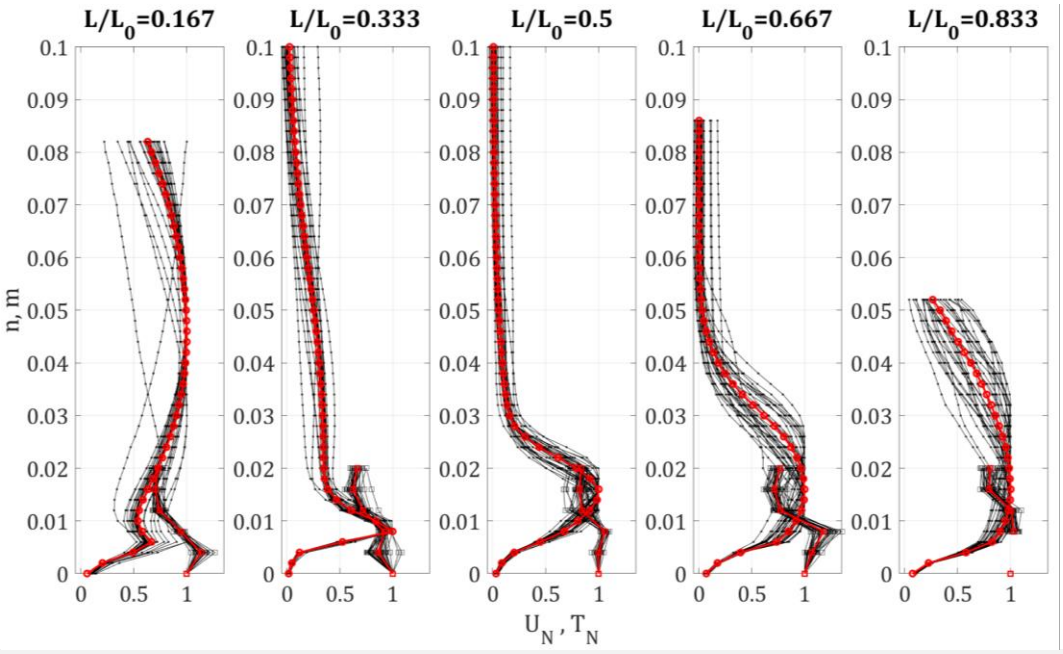

Figure 3.14 Along slope normalized velocity profiles at five cross sections along the slope. The representative experiment presented here is of slope angle of $\beta = 35°$ and the highest heat flux examined, $Q = 1000\ W/m^2$. Each black curve represents a four-minute average. The velocity is marked with circle markers and temperatures are marked by squares. The red curves represent the two-hour average, i.e. the entire experiment.

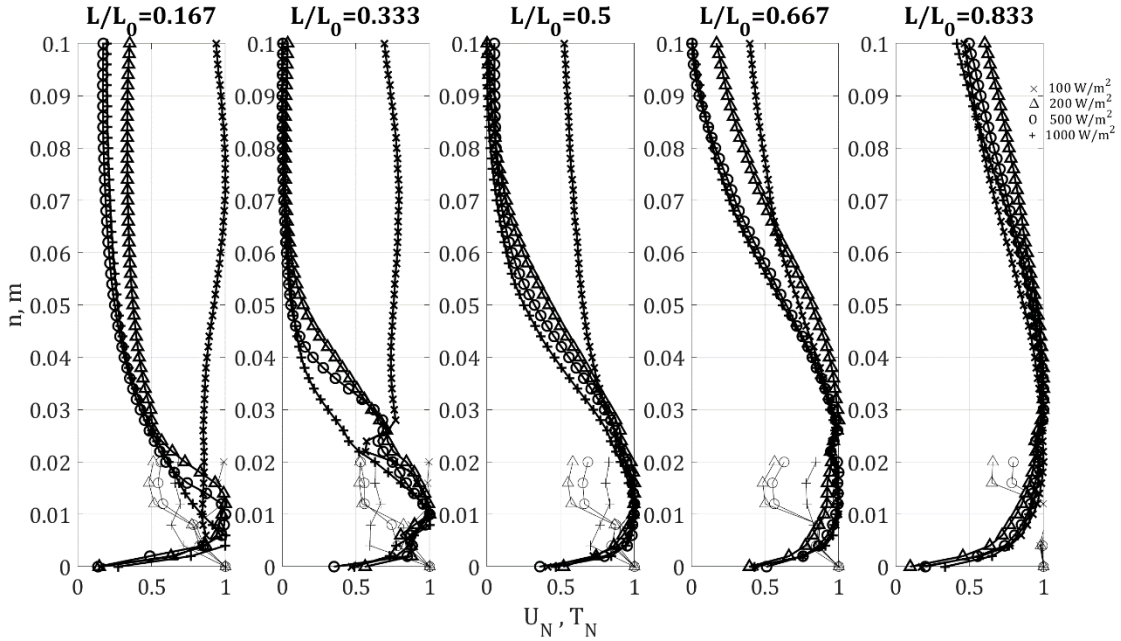

Figure 3.15 The two-hour normalized average velocity and temperature profiles of the double slope configuration of $\beta = 5.7°$ for all heat fluxes examined.

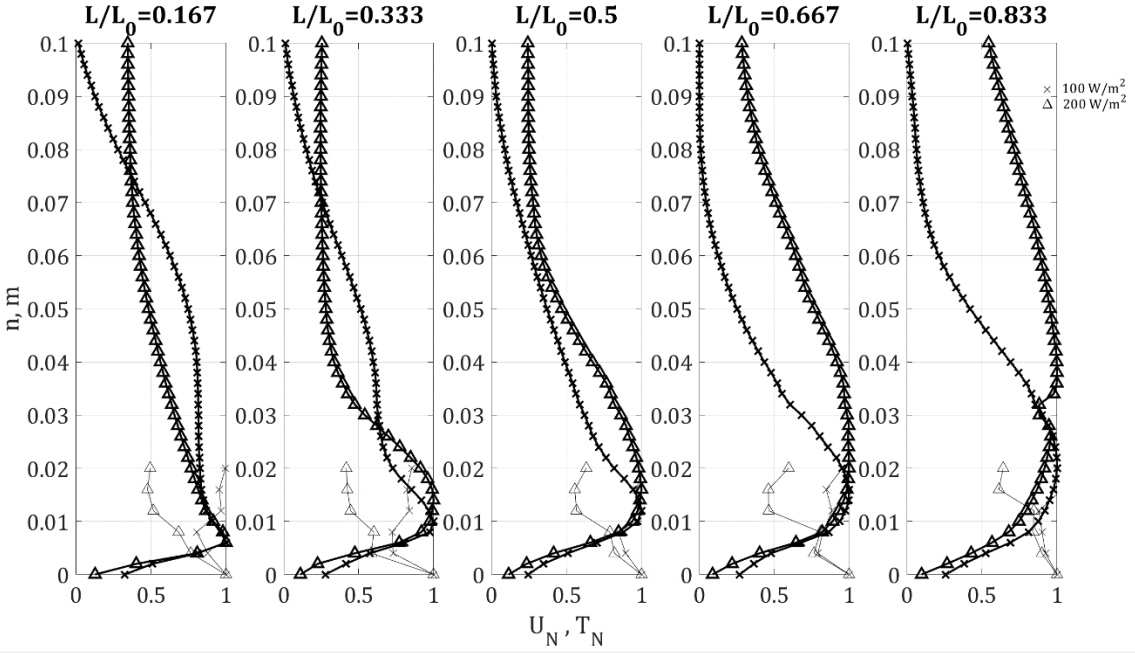

Figure 3.16 The two-hour normalized average velocity and temperature profiles of the double slope configuration of $\beta = 10°$ for all heat fluxes examined.

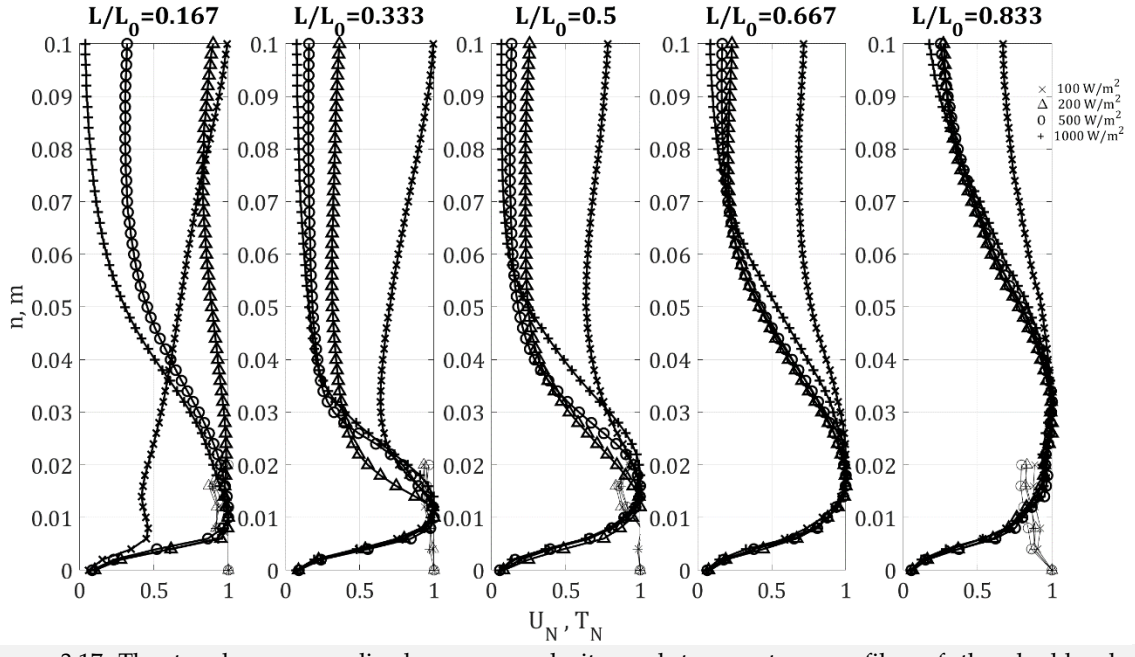

Figure 3.17 The two-hour normalized average velocity and temperature profiles of the double slope configuration of $\beta = 15°$ for all heat fluxes examined.

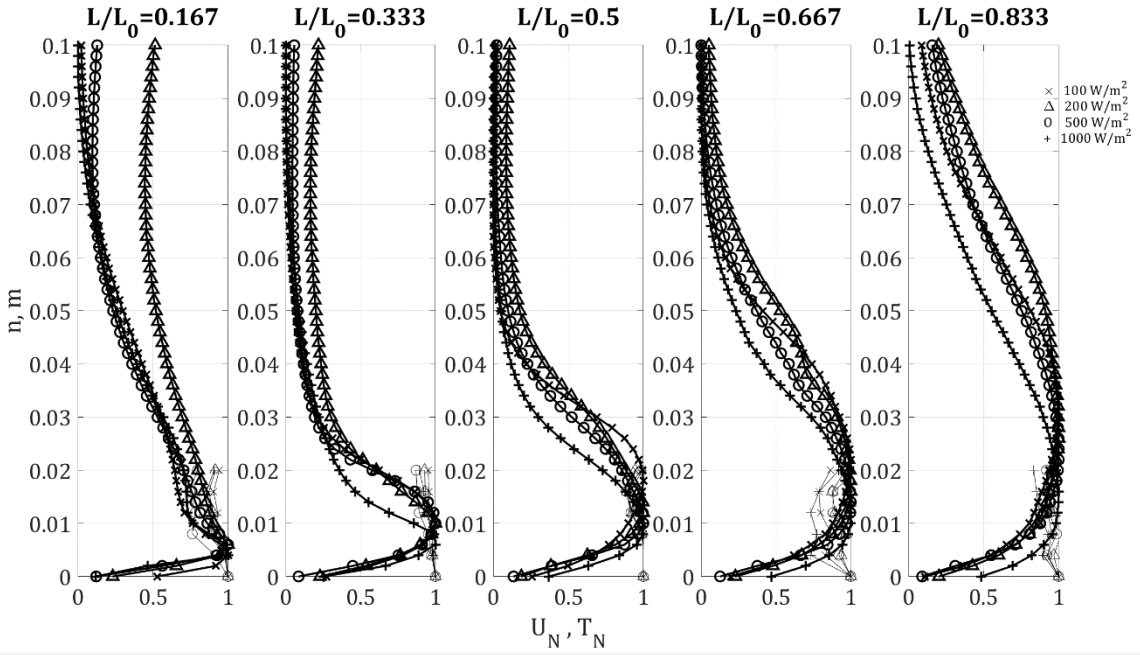

Figure 3.18 The two-hour normalized average velocity and temperature profiles of the double slope configuration of $\beta = 20°$ for all heat fluxes examined.

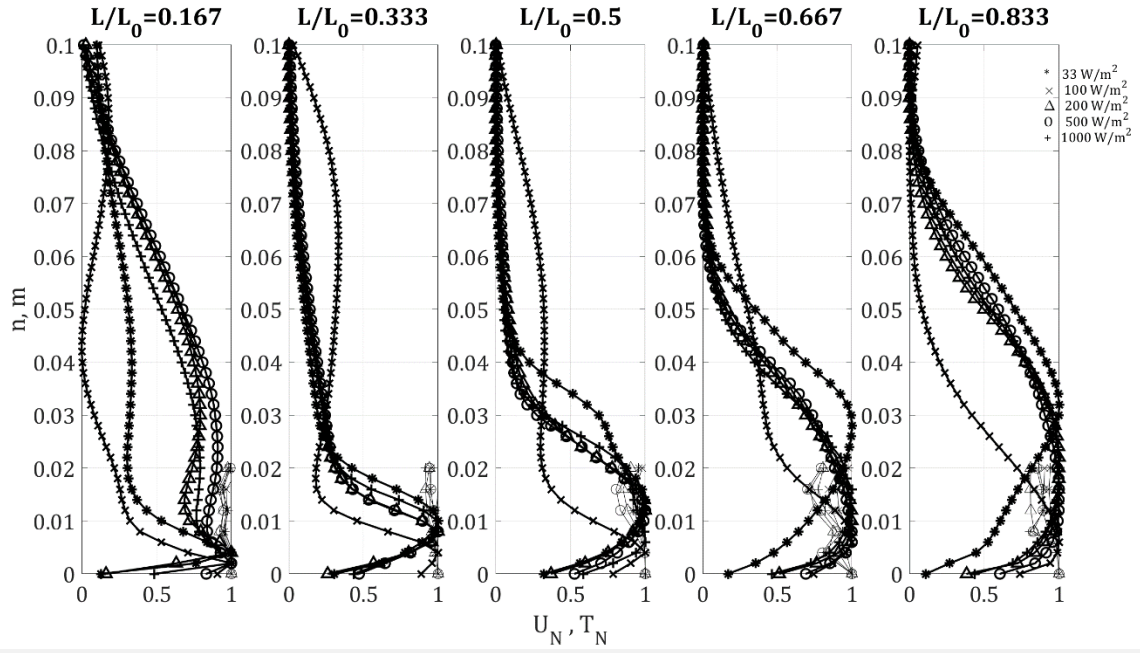

Figure 3.19 The two-hour normalized average velocity and temperature profiles of the double slope configuration of $\beta = 25°$ for all heat fluxes examined..

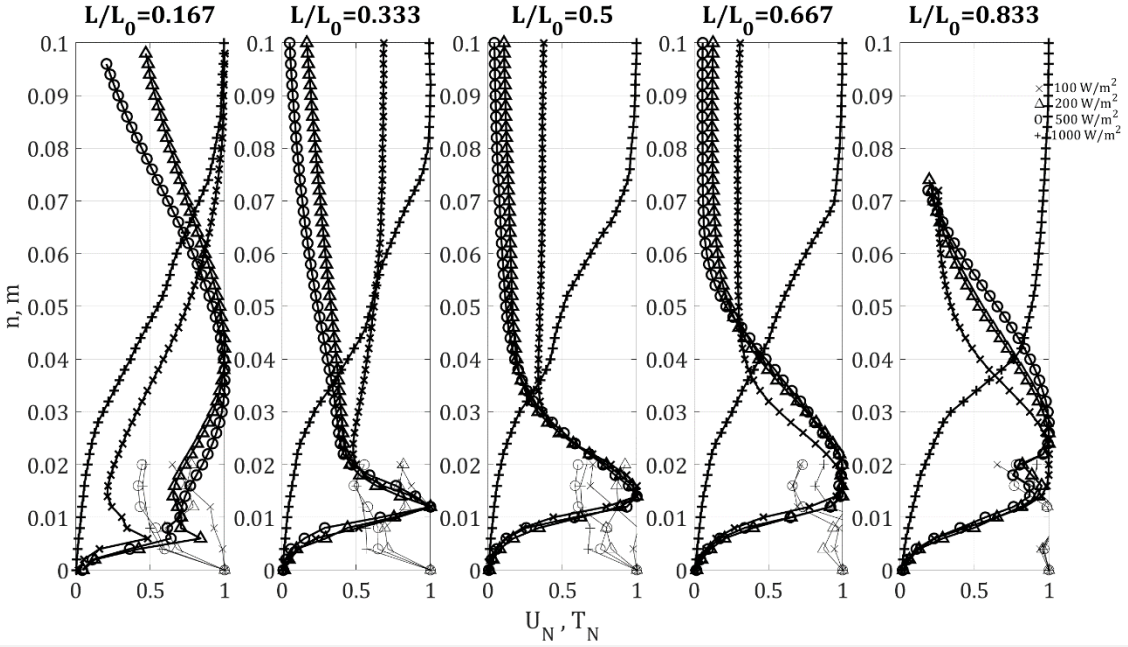

Figure 3.20 The two-hour normalized average velocity and temperature profiles of the double slope configuration of $\beta = 30°$ for all heat fluxes examined.

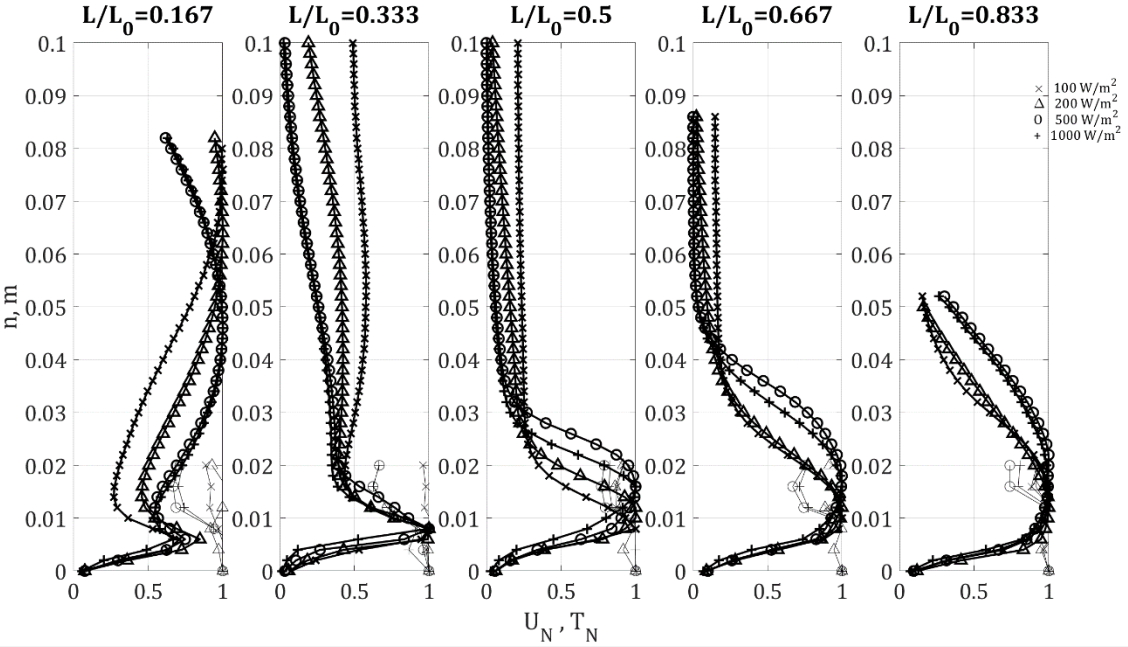

Figure 3.21 The two-hour normalized average velocity and temperature profiles of the double slope configuration of $\beta = 35°$ for all heat fluxes examined.

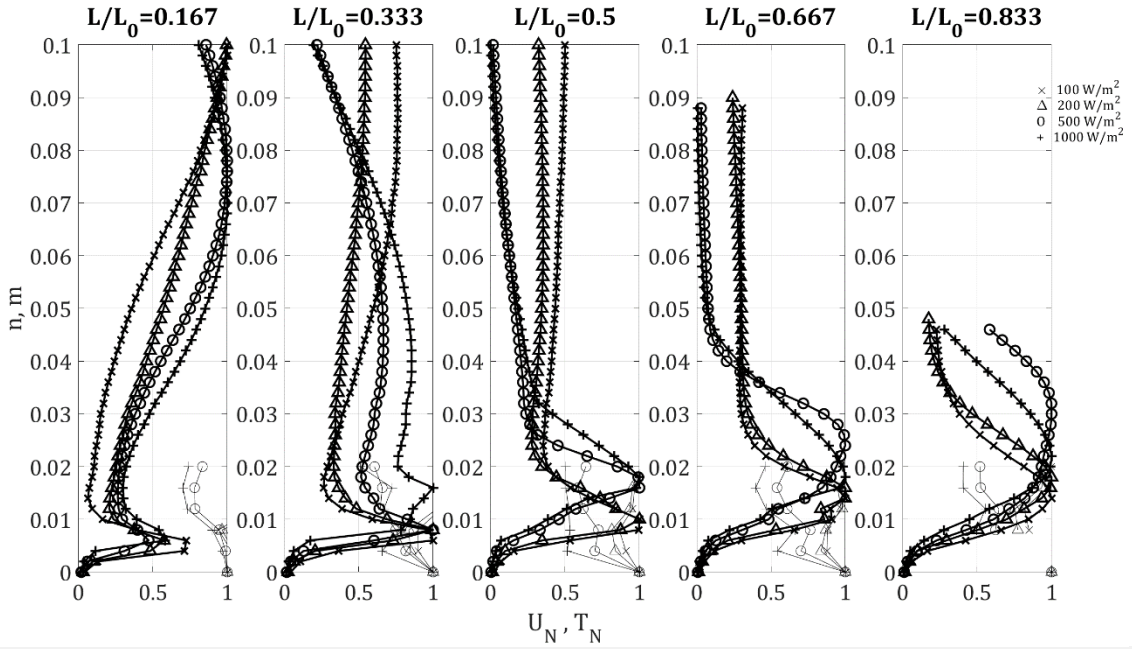

Figure 3.22 The two-hour normalized average velocity and temperature profiles of the double slope configuration of $\beta = 40°$ for all heat fluxes examined.

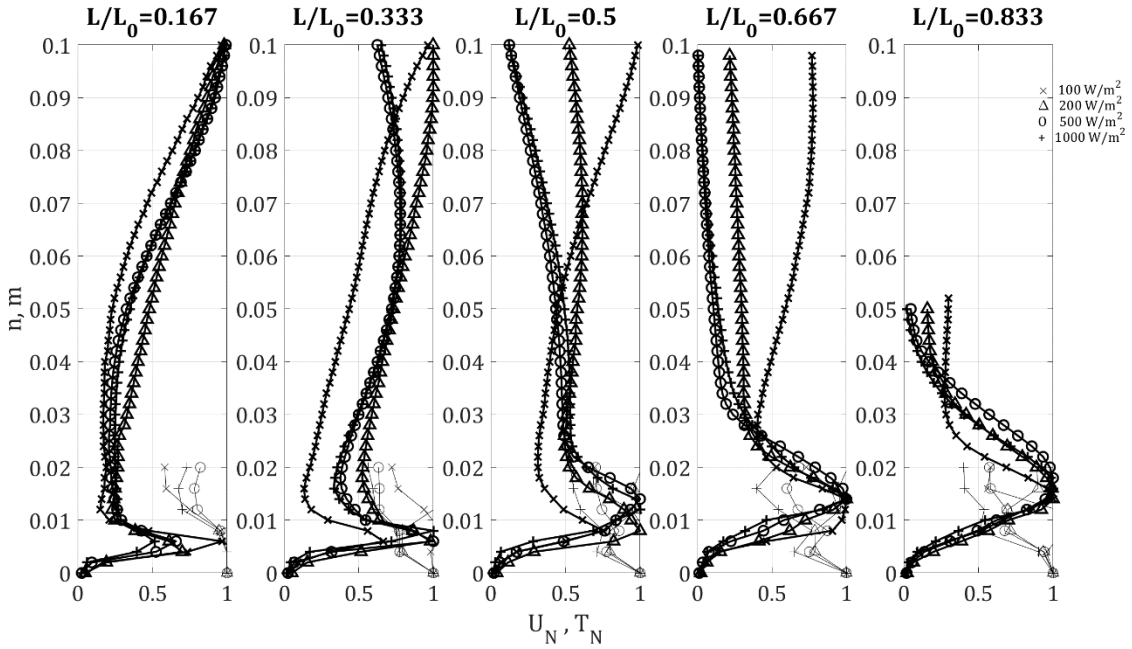

Figure 3.23 The two-hour normalized average velocity and temperature profiles of the double slope configuration of $\beta = 45°$ for all heat fluxes examined.

For a more accurate comparison with the results obtained from the smaller tank [11, 27], an experiment was staged with the double slope configuration and a wall placed between the two slopes at $\beta = 25°$. This configuration mimics the single slope previously studied [11] yet in a much larger volume. The normalized velocity and temperature profiles from the "single" slope configuration are presented in Figure 3.24.

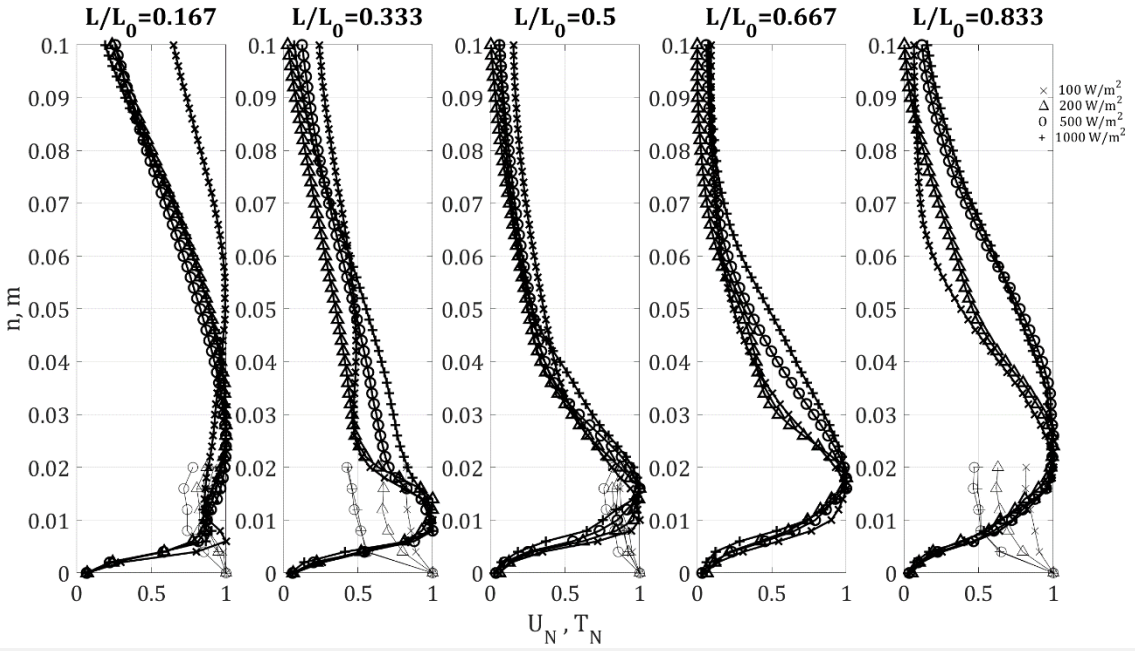

Figure 3.24 The two-hour normalized average velocity and temperature profiles of the "single" slope configuration of $\beta = 25°$ for all heat fluxes examined. The single slope configuration was accomplished by using the same double slope configuration as the previously discussed experiments and adding a vertical wall at the apex, therefore preventing flow from transferring from one side to another. These experiments were conducted for a more direct comparison with the Hocut et al [11] setup.

Selection of the maximum along the slope velocity for the normalization of the profiles, instead of the commonly used parameter u_*, was made due to the coarse spatial resolution of the velocity field near the boundary. The brightness of the laser sheet reflected on the slope itself and reflected light on particles in front of the laser sheet, increasing the measurement error closer to the boundary/the slope. Future

measurements should also consider increasing the spatial resolution as the experiments had at most four points in the lower log-layer of the velocity profiles. Using these noisier points can introduce a large error in attempt to obtaining u_* using a curve fitting method. It is, therefore, recommended that future experiments increase the camera resolution by a factor of at least two.

Another important finding is some of the 4-minute mean profile shapes in Figure 3.13. We also call those the first clue, *Clue#1,* which alludes to the importance of the transient nature and 3D structure of the flow. It is pronounced as "B-shaped" profiles, i.e. consisting of two distinct bumps instead of the expected "D-shaped" profiles consisting of one larger bump.

Below are three representative cases of the turbulent flux profiles, $\overline{u'w'}$. All four-minute mean turbulent flux profiles exhibited a constant variation between the profiles for the entire two-hour duration, as in Figures 3.25-3.27. For a more extensive comparison, the two-hour mean turbulent flux profiles at all heat fluxes corresponding to the same geometric configuration were plotted together in Figures 3.28-3.37. These profiles also indicate that a similar pattern of the flow is observed, except for several examples with the repeated "B-shaped" profiles, an example is Figure 3.32 and it will be referred to as *Clue#2*.

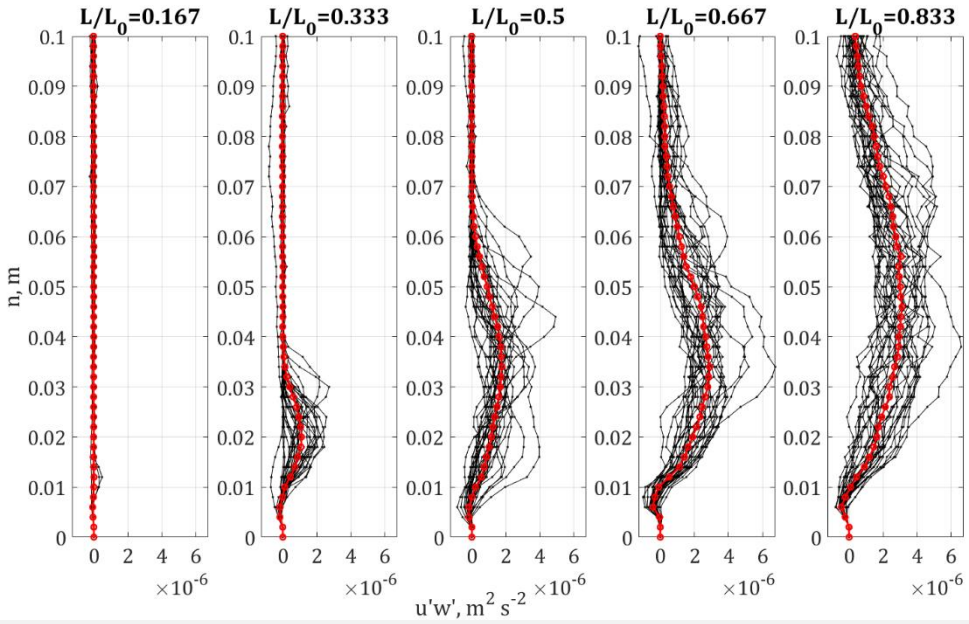

Figure 3.25 Along slope turbulent flux $\overline{u'w'}$ profiles at five cross sections along the slope. The representative experiment presented here is of slope angle of $\beta = 15°$ and the highest heat flux examined, $Q = 1000\, W/m^2$. Each black curve represents a four-minute average. The red curves represent the two-hour average, i.e. the entire experiment.

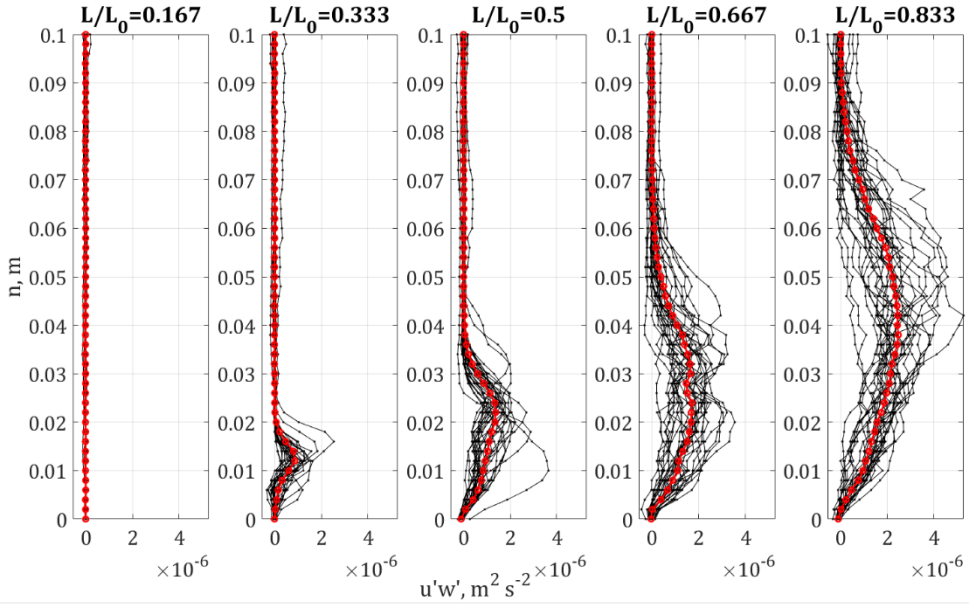

Figure 3.26 Along slope turbulent flux $\overline{u'w'}$ profiles at five cross sections along the slope. The representative experiment presented here is of slope angle of $\beta = 25°$ and the highest heat flux examined, $Q = 1000\, W/m^2$. Each black curve represents a four-minute average. The red curves represent the two-hour average, i.e. the entire experiment.

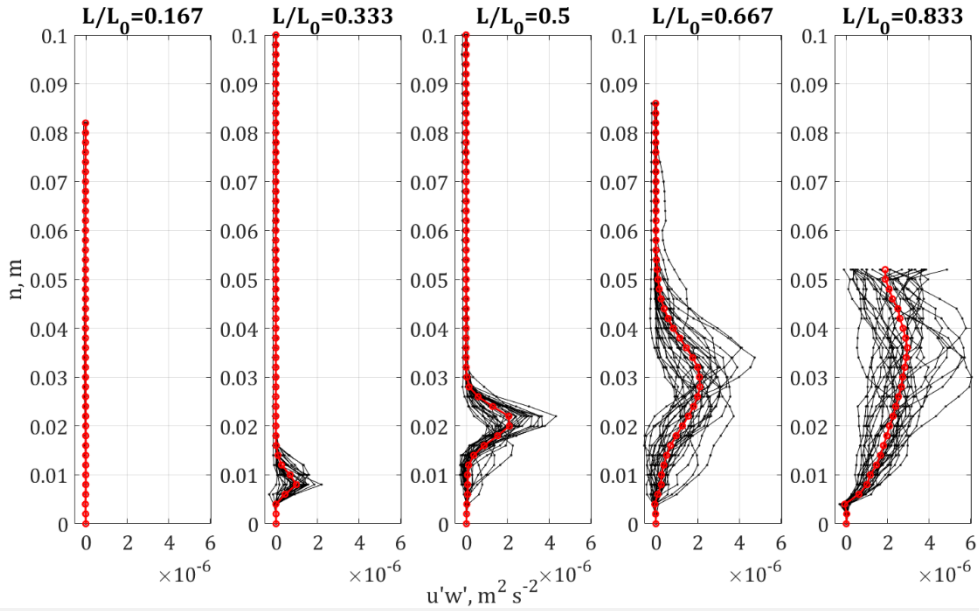

Figure 3.27 Along slope turbulent flux $\overline{u'w'}$ profiles at five cross sections along the slope. The representative experiment presented here is of slope angle of $\beta = 35°$ and the highest heat flux examined, $Q = 1000\ W/m^2$. Each black curve represents a four-minute average. The red curves represent the two-hour average, i.e. the entire experiment.

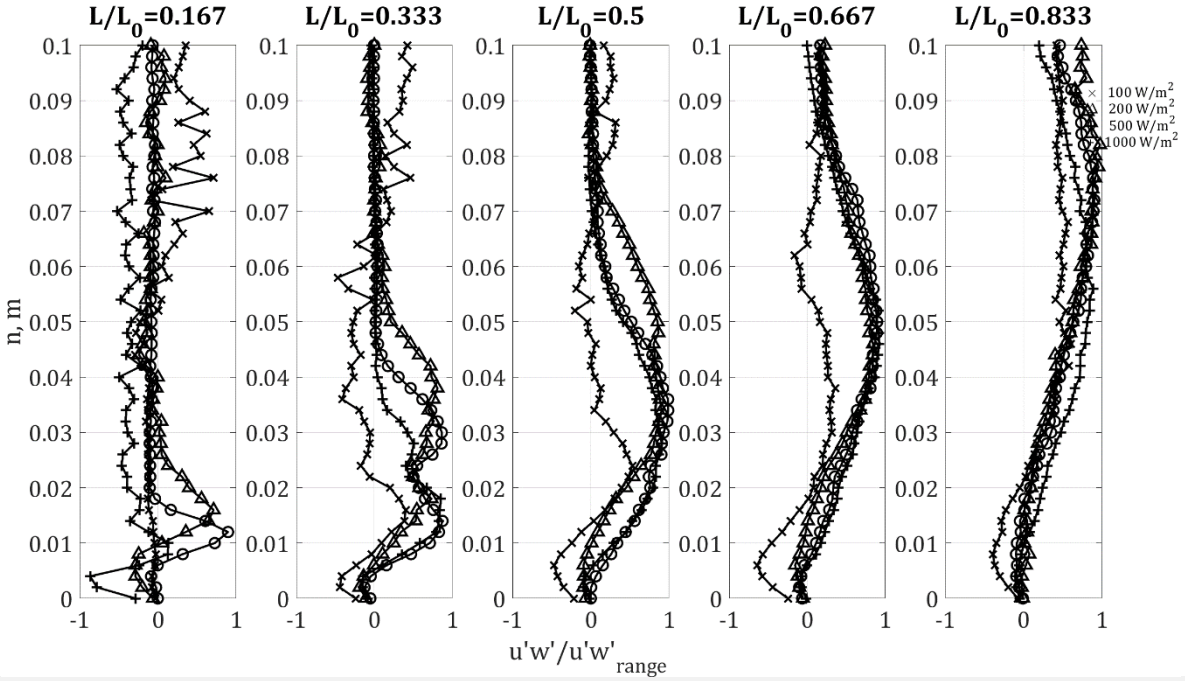

Figure 3.28 The two-hour normalized average turbulent flux $\overline{u'w'}$ profiles of the double slope configuration of $\beta = 5.7°$ for all heat fluxes examined.

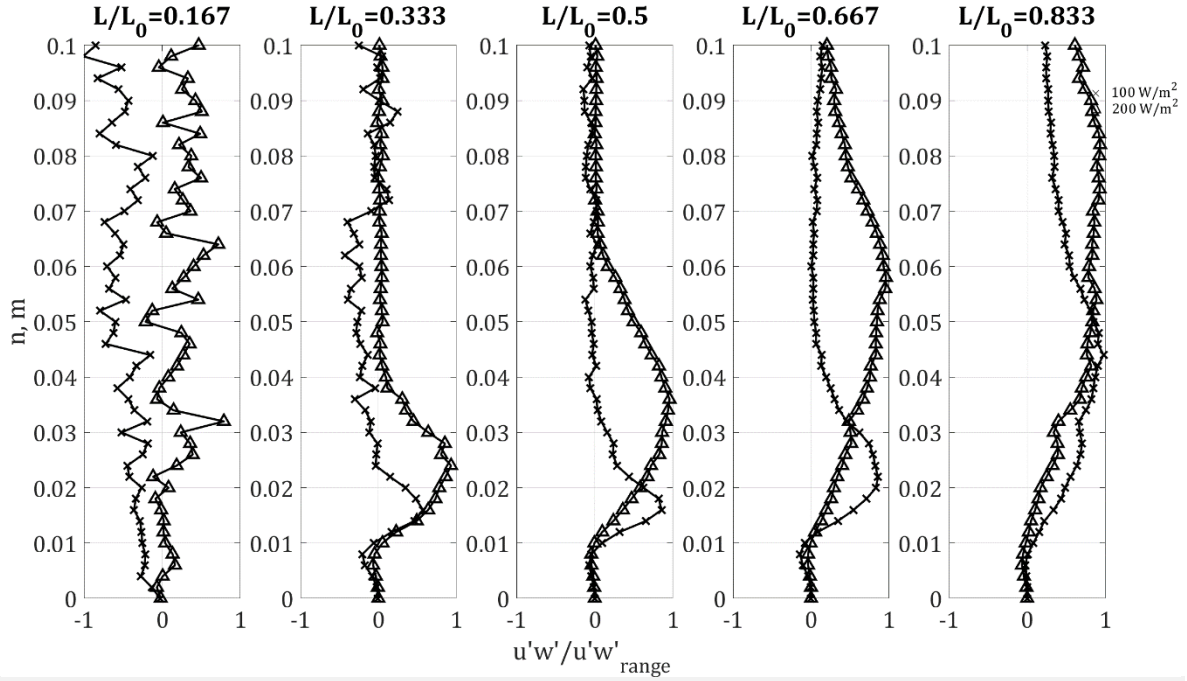

Figure 3.29 The two-hour normalized average turbulent flux $\overline{u'w'}$ profiles of the double slope configuration of $\beta = 10°$ for all heat fluxes examined.

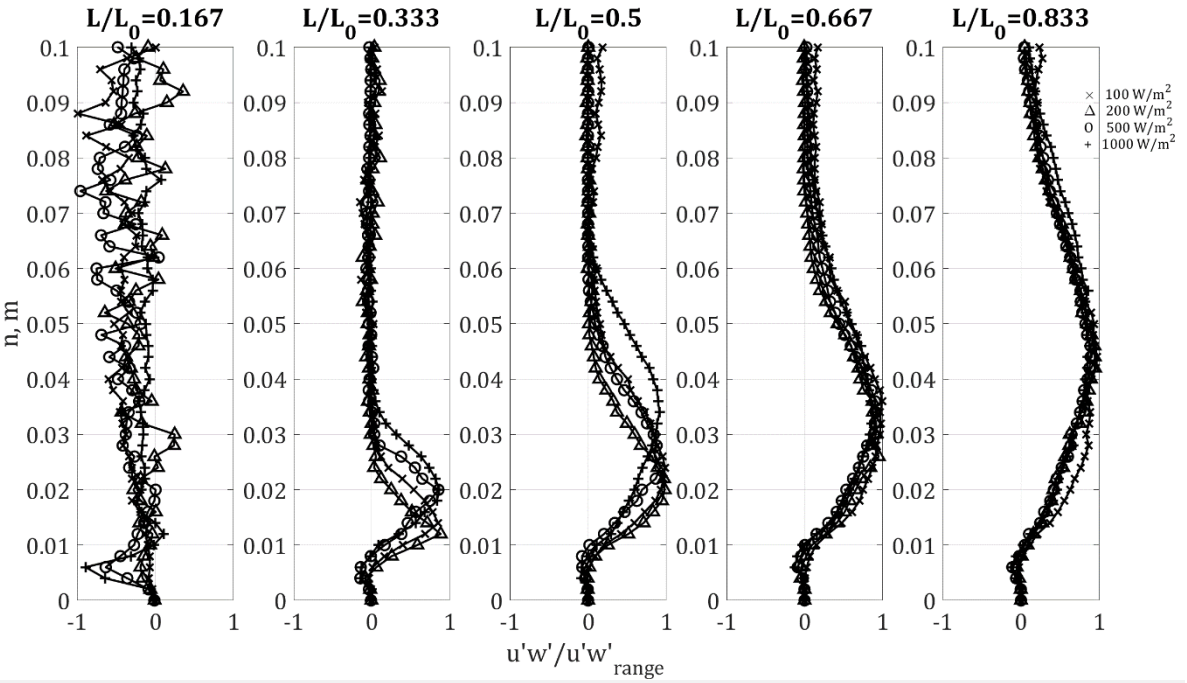

Figure 3.30 The two-hour normalized average turbulent flux $\overline{u'w'}$ profiles of the double slope configuration of $\beta = 15°$ for all heat fluxes examined.

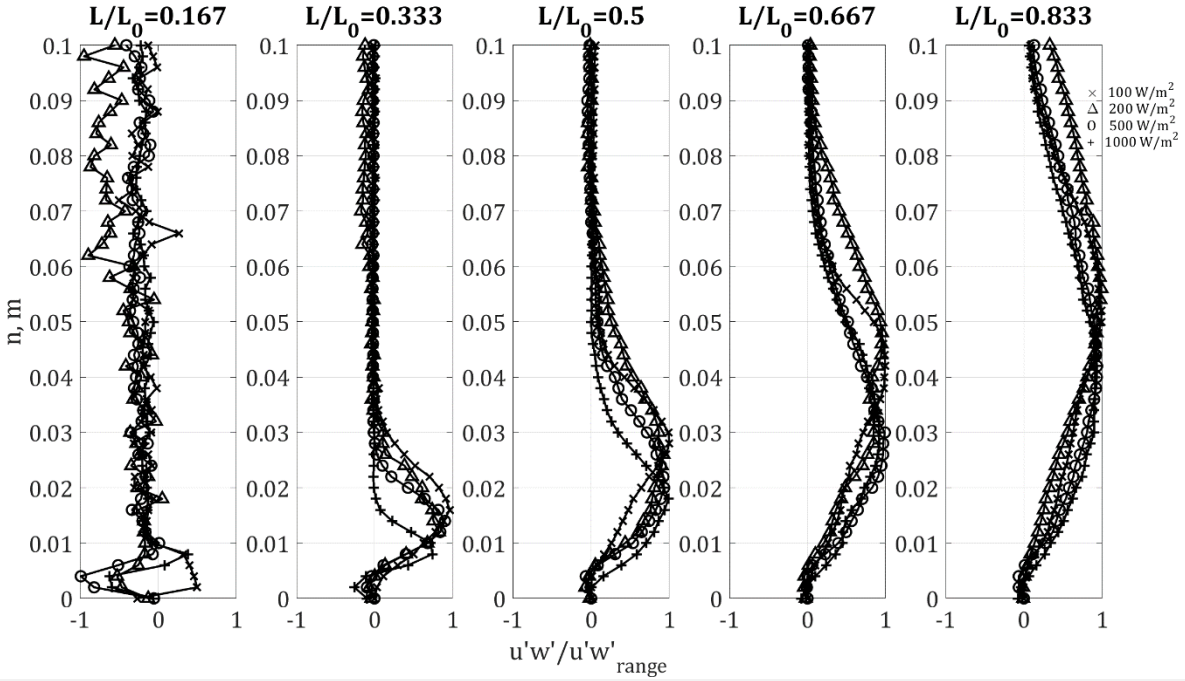

Figure 3.31 The two-hour normalized average turbulent flux $\overline{u'w'}$ profiles of the double slope configuration of $\beta = 20°$ for all heat fluxes examined.

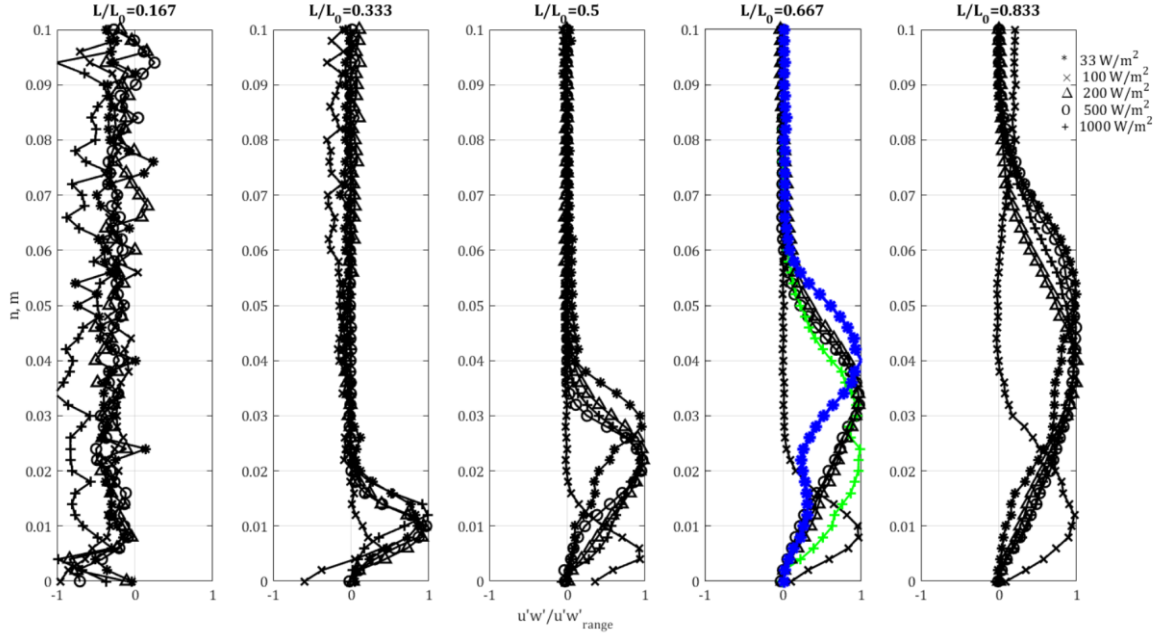

Figure 3.32 The two-hour normalized average turbulent flux $\overline{u'w'}$ profiles of the double slope configuration of $\beta = 25°$ for all heat fluxes examined. The blue and green curves correspond to *Clue#2*, representative of the "B-shaped" profile.

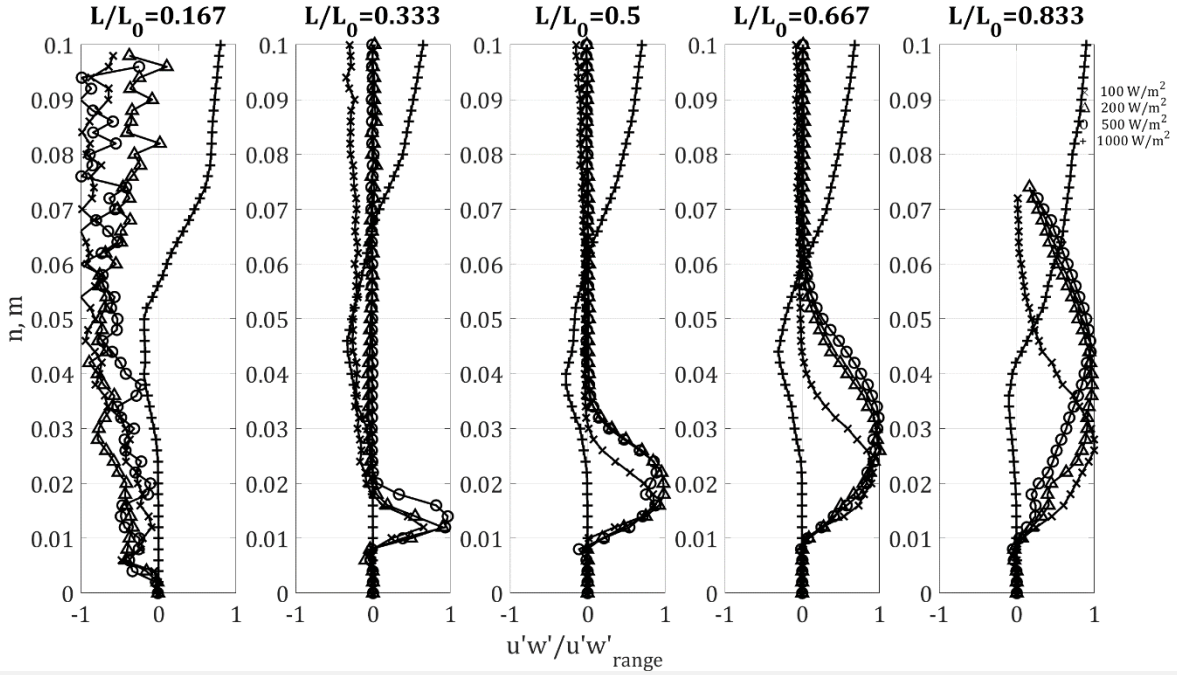

Figure 3.33 The two-hour normalized average turbulent flux $\overline{u'w'}$ profiles of the double slope configuration of $\beta = 30°$ for all heat fluxes examined.

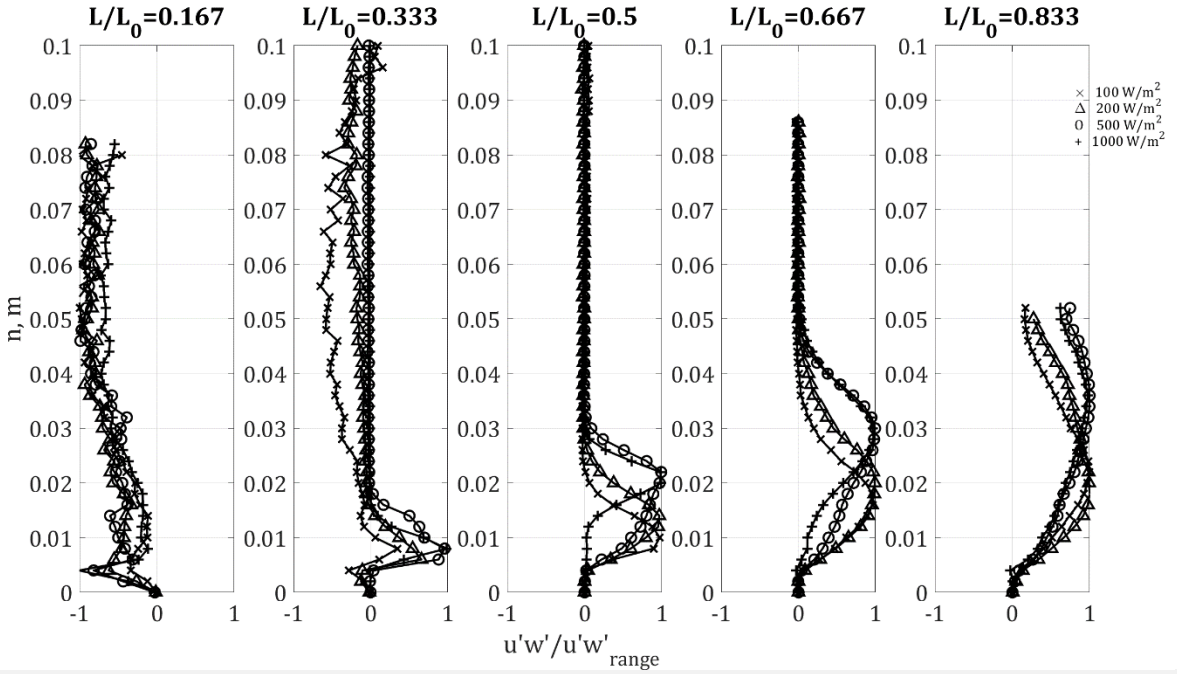

Figure 3.34 The two-hour normalized average turbulent flux $\overline{u'w'}$ profiles of the double slope configuration of $\beta = 35°$ for all heat fluxes examined.

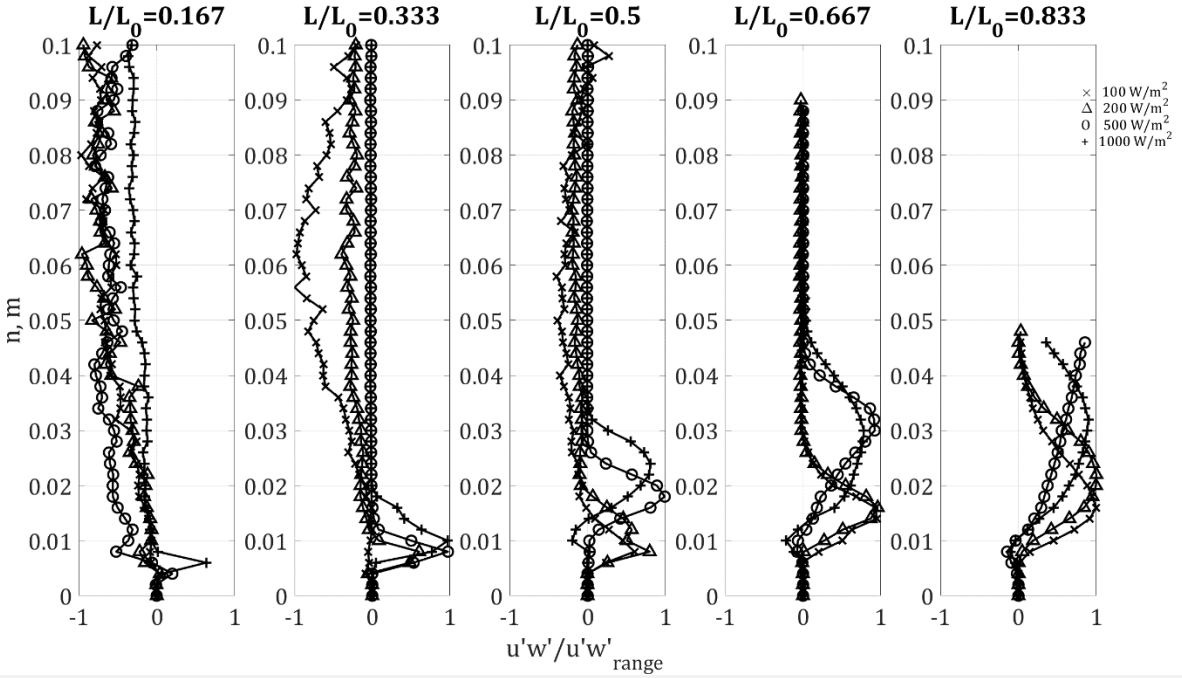

Figure 3.35 The two-hour normalized average turbulent flux $\overline{u'w'}$ profiles of the double slope configuration of $\beta = 40°$ for all heat fluxes examined.

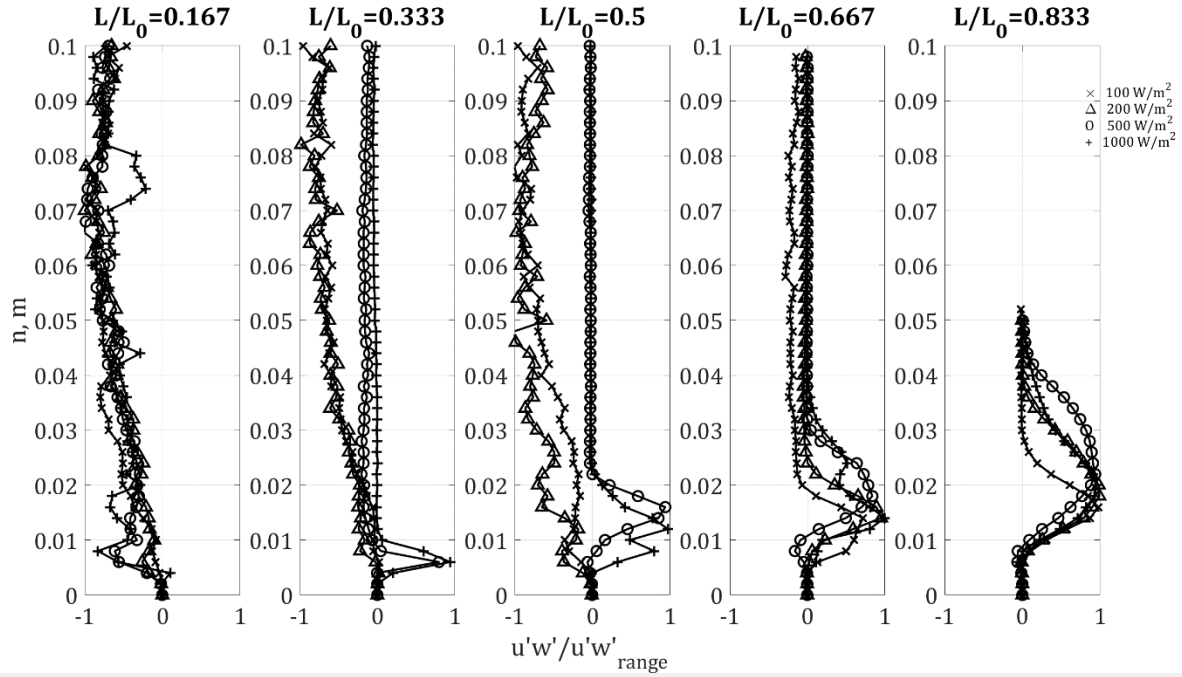

Figure 3.36 The two-hour normalized average turbulent flux $\overline{u'w'}$ profiles of the double slope configuration of $\beta = 45°$ for all heat fluxes examined.

The normalized turbulent flux profiles for this single slope configuration of $\beta = 25°$ are presented below, in Figure 3.37. It is evident that the variation between the different heat fluxes is much smaller than the double slope configurations, indicating this configuration constructs flows that are relatively steadier.

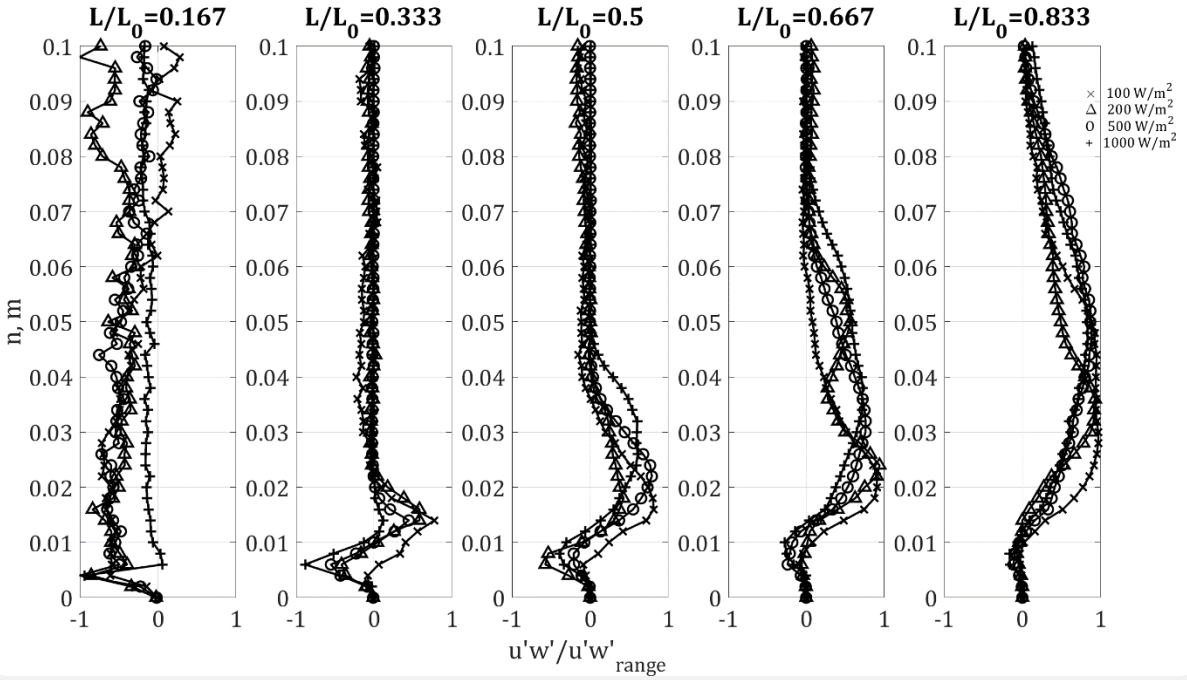

Figure 3.37 The two-hour normalized average turbulent flux $\overline{u'w'}$ profiles of the "single" slope configuration of $\beta = 25°$ for all heat fluxes examined. The single slope configuration was accomplished by using the same double slope configuration as the previously discussed experiments and adding a vertical wall at the apex, therefore preventing flow from transferring from one side to another. These experiments were conducted for a more direct comparison with the Hocut et al [11] setup.

The two sets of scaled profiles, namely the velocity-and-temperature profiles and turbulent flux profiles, present two main findings. The first is that the general shapes of the velocity profiles and temperature profiles are consistent across the different geometries and sensible heat fluxes. The second is that there were two indications of the "B-shaped" BL profile, e.g. *Clue#1* in the normalized velocity profiles in Figure 3.13 and *Clue#2* in the turbulent flux profiles in Figure 3.32. This shape resembles the digit 3 or the letter B, and we suggest that it corresponds to a

couple of intertwined and helical structures that move together coherently up the slope and at times even diagonally up the slope. This shape is different than the larger "D-shaped" BL profile describing anabatic flows that appears in the literature [5]. Additional similar clues will be presented in the following sections and finally, a qualitative video confirming the existence of the phenomenon is in the supplementary material folder (Supplementary Materials: Mendeley Data Set [55]).

To further understand the "B shaped" profile, we decided to examine the raw behavior of the tracer particles in the flow. We generated videos of artificial streaks of the particle flow by taking a set of consecutive images and extracting the maximum pixel value within each set with respect to time, forming an artificial track or streak of the brightest particles. This is a computationally cheap approach that can assist in visual understanding of the flow behavior. The Supplementary Materials: Mendeley Data Set [55] consists of several videos presenting the motion of streaks, providing another clue (*Clue#3*) revealing the presence of large movements in across the slope and enhancing the importance of the transient nature and 3D of the flow. Figure 3.38 is an example frame from one of the synthetic streak videos for a 25° slope. It demonstrates the helical structure split, and separation from its helical shape to two distinct structures, near the red arrow. The fluid from behind the laser sheet (and behind the yellow rectangle) enters the laser sheet and flows along the slope, indicated by the blue rectangle on the image. The flow is dominantly governed by the 3D behavior and this probably plays a major role in the flow intermittency. This newly observed behavior contradicts the core assumption made in [11] and therefore contradicts the previously developed model as well.

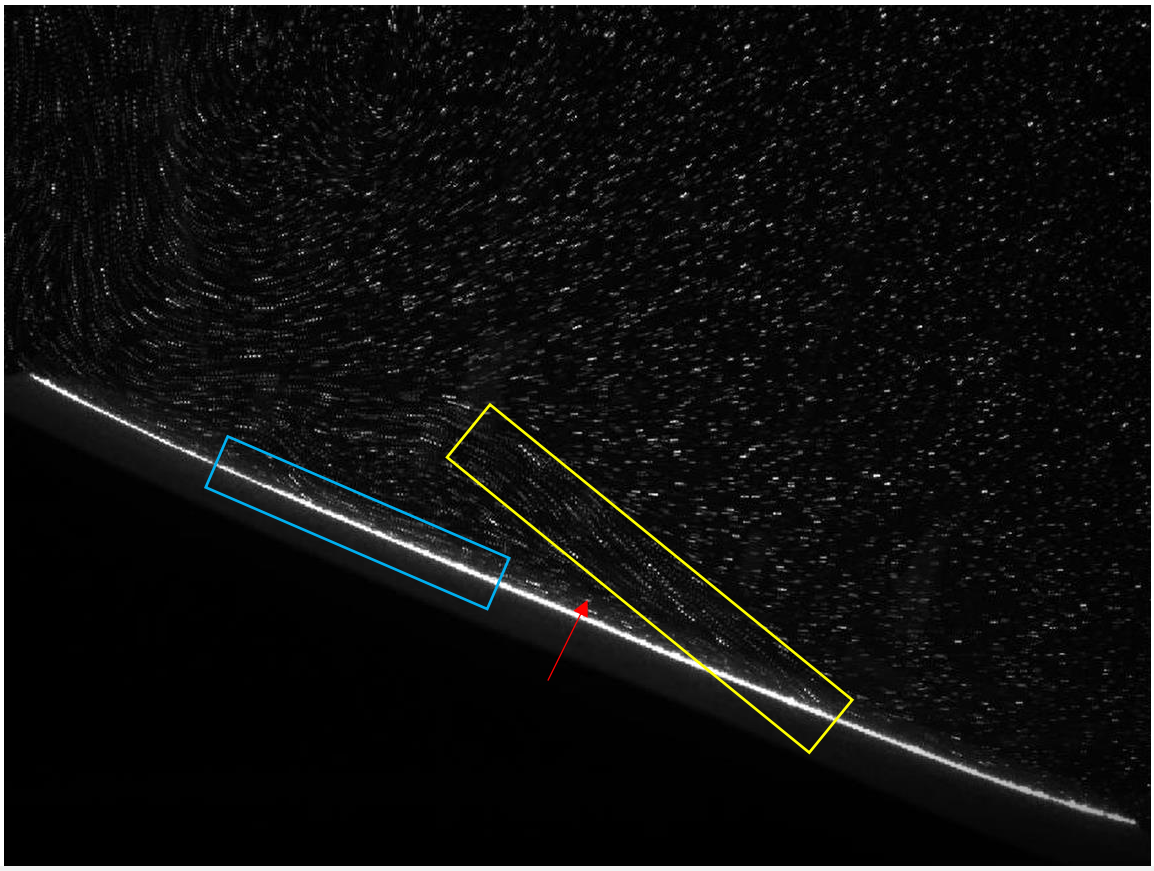

Figure 3.38 Synthetic streaks of the flow obtained by extracting the maximum brightness with respect to a time interval of one second. The yellow rectangle points out the structure that splits, i.e. the upper part of the structure separates from the slope while the blue rectangle highlights the part of the structure that remains attached to the slope. The red arrow points to a region of the flow that is entering the laser sheet from behind. The complete video is available on the Supplementary Materials: Mendeley Data Set [55].

3.2.3 Separation Detection

To determine the exact point in which the flow separates from the slope, several approaches were considered and examined. The first step was an attempt to identify backflow in the mean velocity profiles, as expected from separation of the BL in the literature and presented in Figure 2.1. This is not detected in any of the average velocity profiles examined and may be due to either the 3D structure of the flow, the transient nature of the flow, or the buoyancy flux introduced in the experiments. To further investigate this concern, the instantaneous velocity vector maps were examined visually , observing "shooting" of vortices away from the slope

on most occasions. Such "shooting" was also observed in the average vorticity maps of the flow and in the instantaneous swirling strength maps, i.e. vortex identification and their qualitative tracking.

The vorticity maps provided a clear image of the two intertwined vorticity structures along the slope. Figure 3.39 presents a sample four-minute average vorticity map along the slope. The vorticity is defined as $\omega_y = \frac{\partial w}{\partial s} - \frac{\partial u}{\partial n}$. It was computed using the second order numerical approximation of the first order derivative (taken from [53] Eq#9.8 on page 432). The BL seems to be characterized by two distinct regions. The one closest to the slope in which the mean vorticity is consistently negative, an indication of an attempt to keep the flow attached to the slope. The other, situated above, with apparently positive mean vorticity, i.e. detaching the flow from the boundary. Examination of the instantaneous vorticity maps revealed the separation of the two large structures from each other, this will also be referred to as *Clue#4*. To verify that this is indeed the phenomenon occurring along the slope, qualitative vortex identification using swirling strength was obtained. Figure 3.40 presents a representative instance of identified vortices with directionality taken from the sign of vorticity [56]. The point of the first appearance of this split along slope, or separation of two large structures, was noted for all experiments. The trend is presented in Figure 3.42, and a confirmation of this location was conducted using a qualitative vortex detection analysis manually/visually. The point in which the split of the two structures is observed is what we call the separation point; it is also the point in which the vortices from the vortex detection procedure were observed to be shooting up and away from the slope, this will be referred to as *Clue#5*. A large variation of separation point

locations along the slope is observed, calling for a more informative three-dimensional examination for the transient flow behavior.

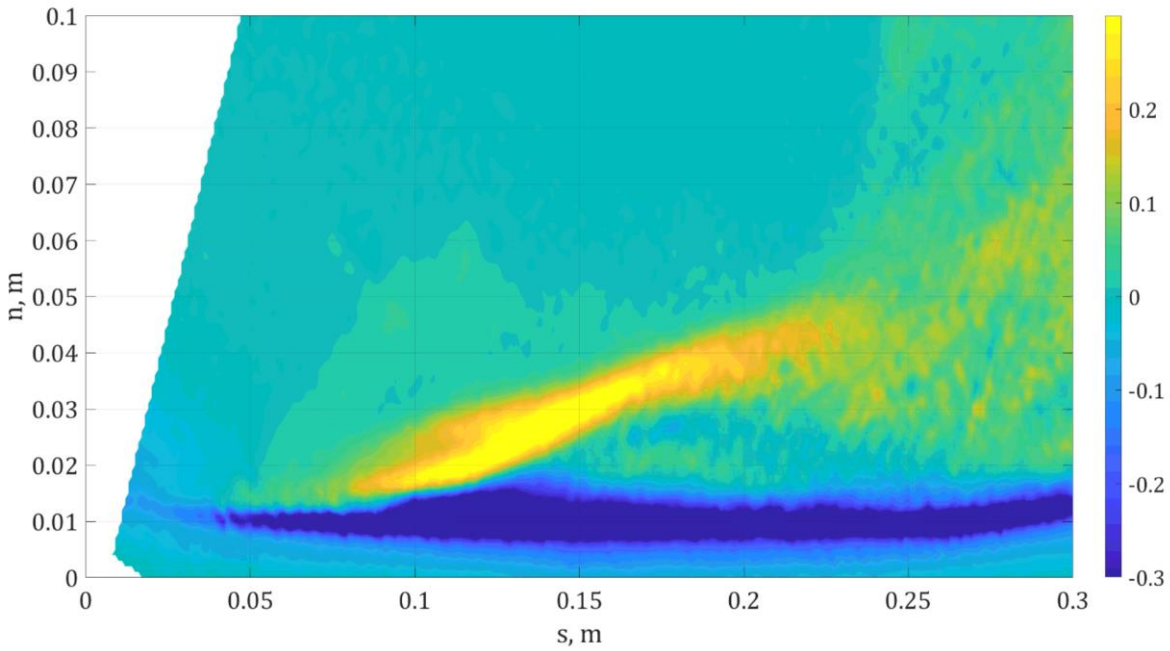

Figure 3.39 A sample four-minute average vorticity map from the double slope configuration of $\beta = 25°$ at the highest heat flux examined. The dark blue regions indicate negative vorticity, the yellow regions indicate positive vorticity, and the light turquoise regions indicate near zero vorticity.

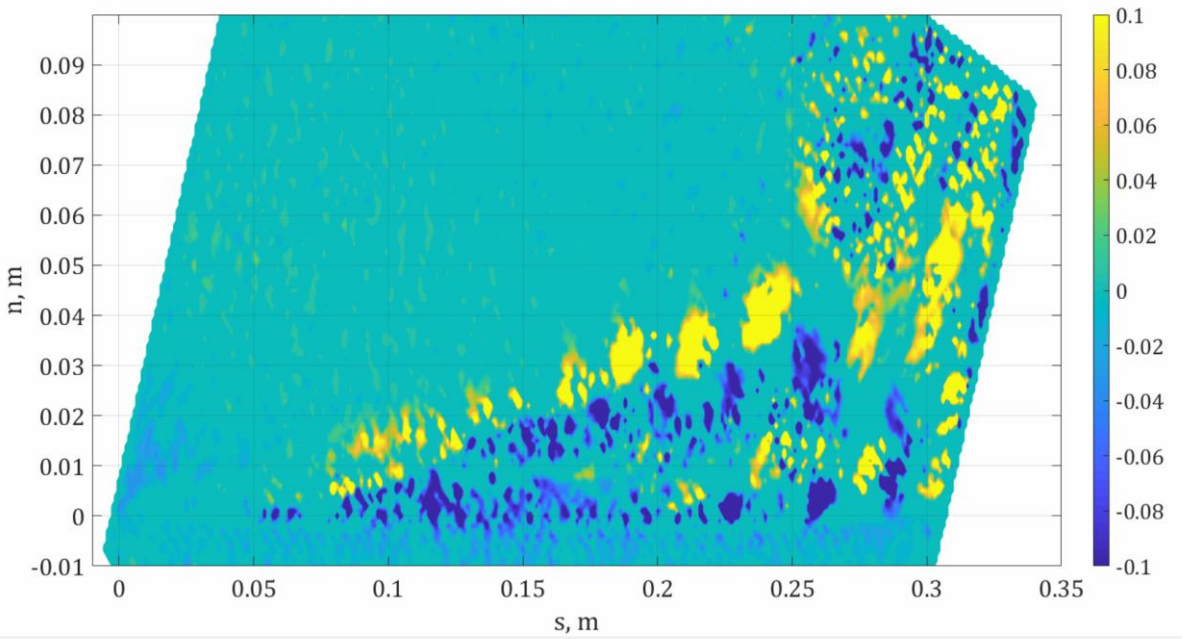

Figure 3.40 A sample one-second average swirling strength map from the double slope configuration of $\beta = 25°$ at the highest heat flux examined. The dark blue regions indicate negative rotation, the yellow regions indicate positive rotation, and the light turquoise regions indicate near zero swirling strength (i.e. no detection of a vortex). The signs/direction of rotation for this map were taken from the vorticity maps.

For a more accurate comparison with the results obtained from the previous models [11, 27], we compared the findings of the non-dimensional separation point location of the double slope configuration *with a wall* in the larger tank to the results from Hocut et al [11]. The most accurate comparison would assess the behavior in the first four-minutes of the larger model experiment to match the experimental duration of the two setups. In the smaller tank the average separation location at a 25° slope was observed to be $L_s/L_0 = 0.55$, while the larger scale experimental observations corresponded to an average of $L_s/L_0 = 0.37$. The range of the detected separation locations along the slope in the larger model was $L_s/L_0 = 0.17 - 0.44$. The size of the range is most likely due to the 3D transient nature of the flow, i.e. the

separation point observed in the laser sheet may only appear at a later point because we can only observe changes that occur in two dimensions.

The next comparison of interest is an examination of the flow behavior in the first four-minutes of all the experiments, *without the wall*, to the available model. Figure 3.41 presents the findings of the double slope experiments without the wall, where the geometric angles are used (i.e. $\beta = \beta_e$). We added two fits, a linear trend $= 0.012 \times \beta$ and one corresponding to the model with the effective angle from Equation (3.1), the new values for the constant were found to be: $\Gamma = 395$ and $\Pi = 559$. The overall non-dimensional separation locations appear to be lower than in the previous experiments, but they follow a similar increasing trend according to the model. Although the trend is similar, the comparison with the existing model is insufficient due to the new understanding of the dominance of the transient and 3D nature of the flow. The existing model is based on results obtained in a smaller tank, where the flow behavior was observed as 2D and the changes in the y-axis were negligible [11]. Here, in the larger water tank, the flow appears to have larger variations in the y-direction, causing an inconsistency with the existing model and disqualifying its validity in representing the new data.

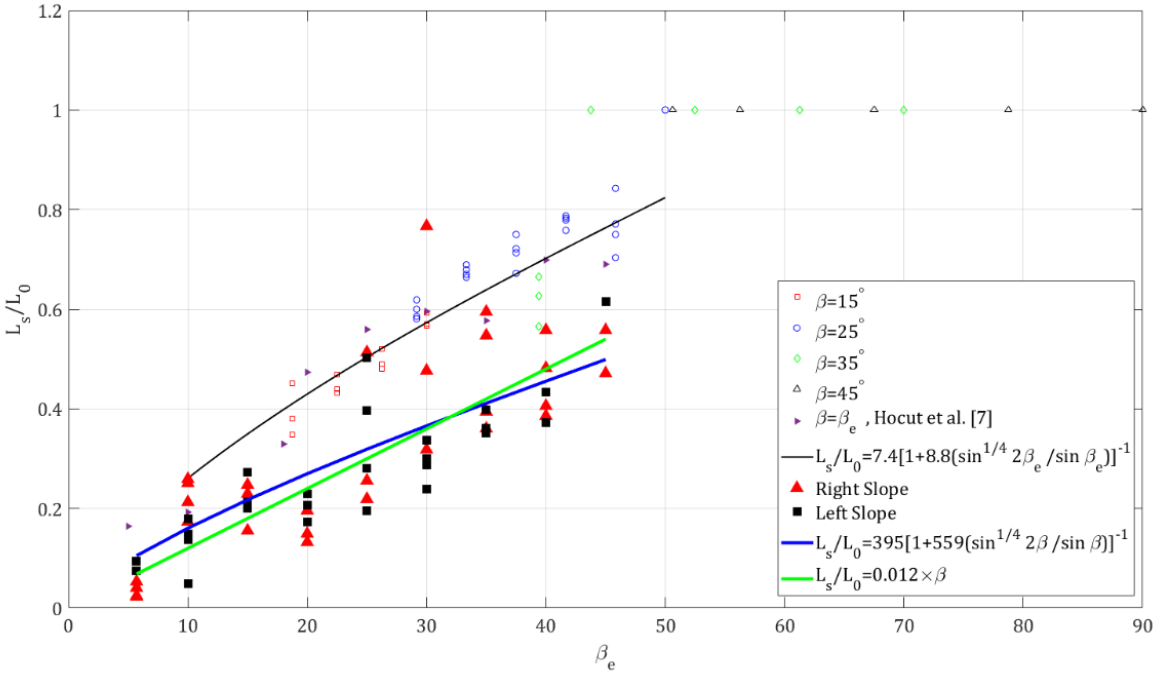

Figure 3.41 normalized separation prediction model as a function of an effective angle taken from Hilel Goldshmid et al. [27], or Figure 3.3 above. The observed separation locations for the double slope configuration are presented on top of the adapted Figure. The added results are taken from the first four-minutes of each experiment of the double slope configuration where $\beta = \beta_e$. The red triangles represent the results from the right slope. The black squares represent the left slope. The blue curve represents the new fit of the previous model with new coefficients and the green curve represents a linear fit.

Finally, the separation location for the two-hour experimental duration is examined. Figure 3.42 presents the non-dimensional separation locations for all double slope experiments. Each point represents the separation location determined form observation of the four-minute average vorticity maps. A distinction is made between the right and left slopes by color, red and black, respectively. The distributions of the separation points along the slope at each geometric configuration are presented by black curves. These curves also present a generally increasing trend with an increase in angle, but the variation at each angle is too large to provide a new prediction model. Future examination of the transient nature and three-dimensionality of the flow should be considered and incorporated into the model to obtain an accurate one.

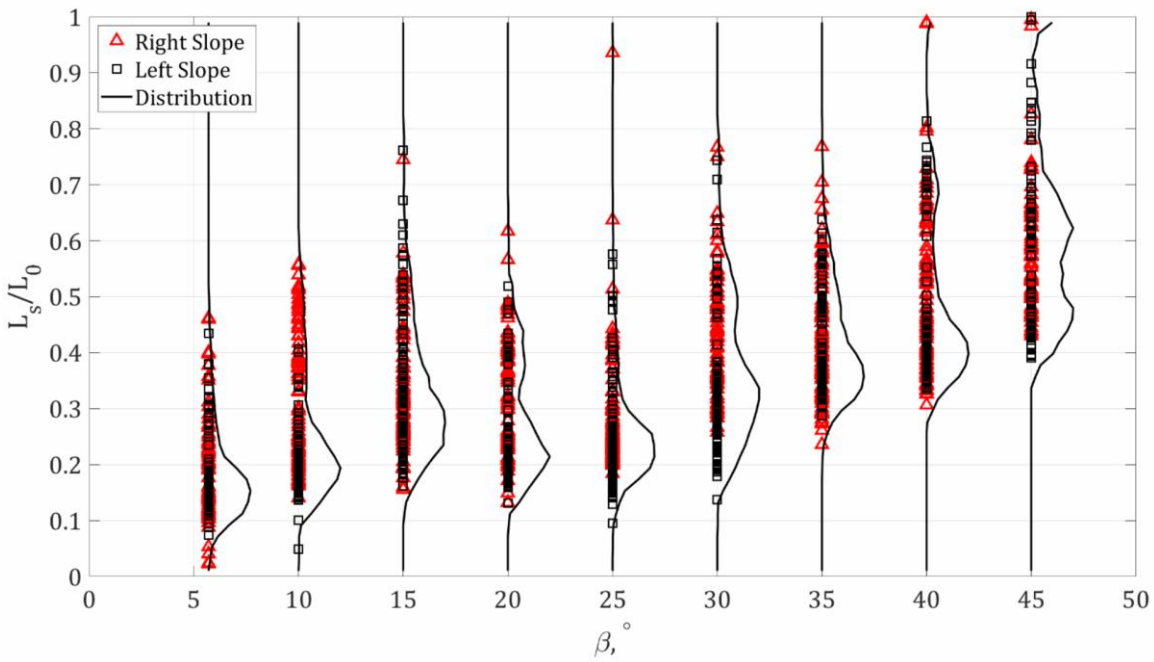

Figure 3.42 The observed separation locations for all double slope experiments at all heat fluxes. The red triangles represent the right slopes and the black circles represent the black squares. The distribution of the separation locations is presented by the black curve for each geometric configuration, i.e. β.

3.2.4 Boundary layer shape

The major conclusion that may be drawn from the previous section is that the flow does not separate from the slope itself, but that the BL splits into two structures, where one would feed the plume while the other continues to flow along the slope. After defining the point in which the boundary layer splits, the shape of the BL is examined. A curve $\delta_{ABL}(x) = a_0\sqrt{x}$ was fit along the slope on the s coordinate until the point of separation/split. Next, the shape factor was extracted for each four-minute interval of each experiment. It was computed as $H = \delta_{ABL}/\delta_{lam}$, where $\delta_{lam} = 0.664\sqrt{\nu x/u_0}$ taken from the Blasius solution [25]. The u_0 was extracted as the maximum velocity developed for each BL shape examined; it is a representative value that would characterize the expected BL mean velocity profile shape that

would develop if the fluid was ideal and irrotational flowing near a flat plate without heat transfer. The power dependence and relationship of $H(Re_x, Pr)$ was found using least squares fitting of the exponents for all data points,

$$H = Re_x^{a_1} Pr^{a_2} . \tag{3.7}$$

The coefficients from least squares fitting were found to be $a_1 = 0.38$ and $a_2 = 0.25$, the empirical relationship is presented in Figure 3.43.

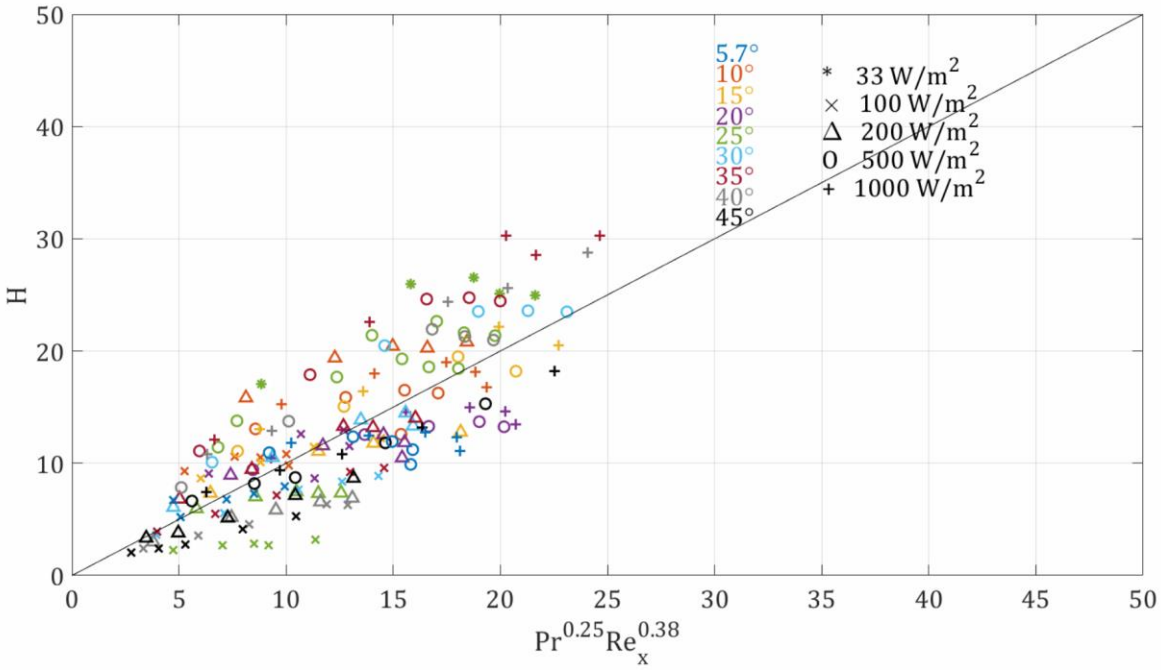

Figure 3.43 The shape factor dependence on the Prandtl and Reynolds numbers of each experiment. The exponents were obtained by curve fitting.

3.2.5 Vorticity advection and baroclinic torque

The grid of thermocouples used to obtain the temperature measurements was previously shown being not sufficiently dense to provide a detailed understanding by correlating the temperatures and velocities. The temperature profiles, however, do provide a clear picture that the bulk temperatures behave as expected from an anabatic BL flow. The study conducted by Hocut et. al. [11] presented a steady state

model that is based on the understanding that the flow would separate from the slope if the opposing vortices are of the same order. Although the presented here experimental data of much higher spatial and temporal resolutions provide evidence that the observed flow is transient, and its three-dimensionality behavior cannot be neglected. Examination of the order of magnitude of the baroclinic torque and vorticity advection along the slope is presented below.

Hocut et al [11] developed their model using the conservation of vorticity equation and the Boussinesq approximation. Under the assumptions of Reynolds similarity, fully developed flow, and 2D quasi-steady flow, the changes in vorticity with respect to time were set equal to zero as follows:

$$\frac{\partial \omega_y}{\partial t} = -\frac{\partial (b \cdot cos\beta)}{\partial s} - u_s \frac{\partial \omega_y}{\partial s} = 0. \tag{3.8}$$

The ω_y is the y-component of vorticity and the baroclinic torque is defined as $b = (\rho_0 - \rho)g/\rho_0$. The time series of the baroclinic torque (blue) and the vorticity advection (black) at all available points along and away from the slope are presented in Figures 3.44-3.48. Each figure time series of the respected quantities at all available locations above the slope, each at a specific location along the slope. It is noticeable that both the baroclinic torque and vorticity advection present significant fluctuations with zero mean. Directly correlating between the two signals would not provide useful information because of the spacing between the laser sheet and the location of the thermocouple grid. These time series do however provide an understanding of the order of magnitude of each of the properties. As we move along the slope the magnitude of vorticity advection fluctuations tends to increase until it reaches that of the baroclinic torque.

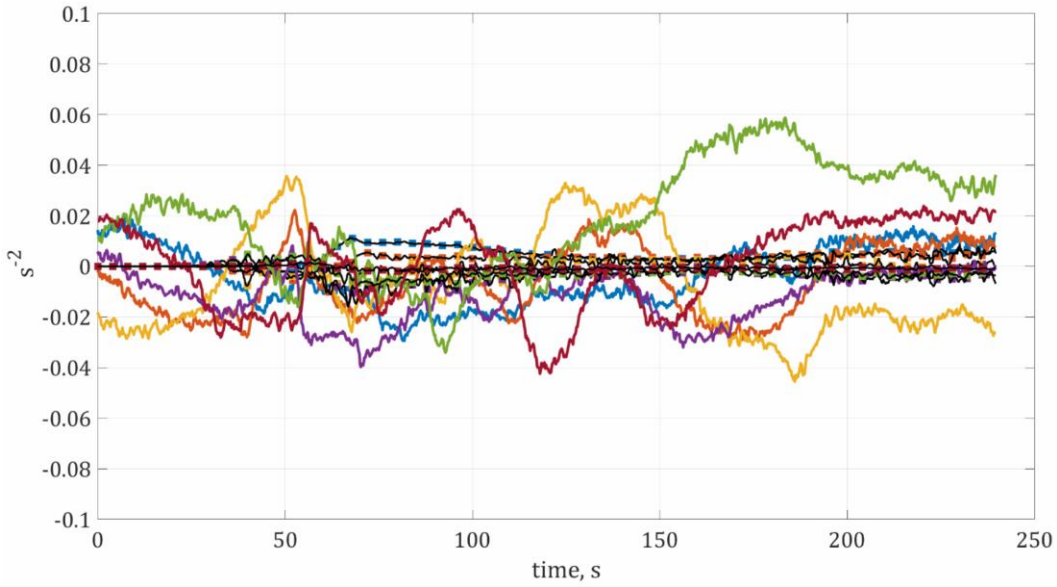

Figure 3.44 Instantaneous time series at $L/L_0 = 0.167$ on the double slope configuration with $\beta = 15°$. This is an examination of the baroclinic torque in the colorful curves and the vorticity advection in the black curves with colorful markers. The colors blue, orange, yellow, purple, green, and burgundy correspond to the points on the thermocouple grid at $n = 0.20,0.16,0.12,0.08,0.04,0\ m$, respectively.

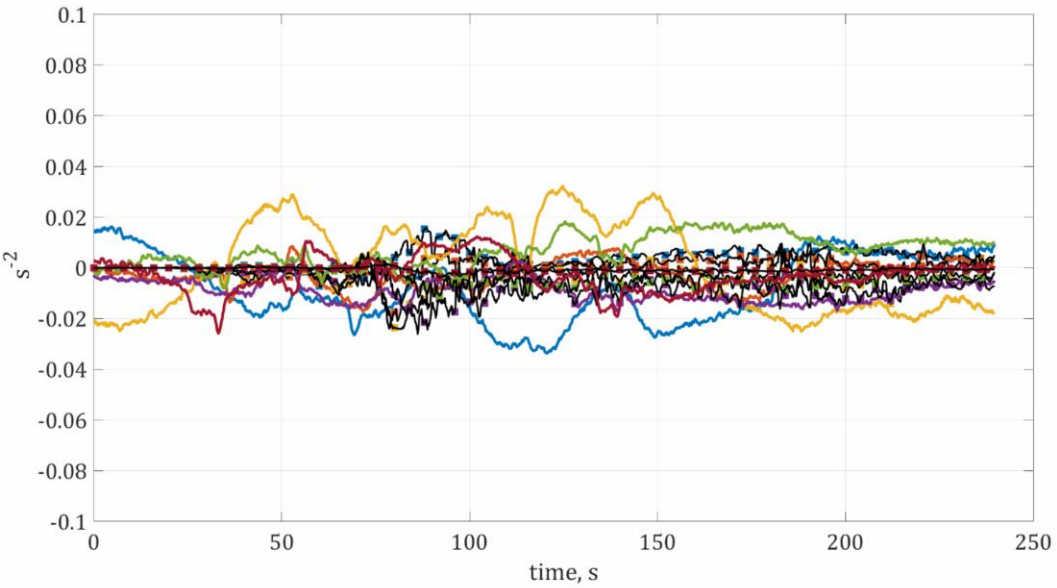

Figure 3.45 Instantaneous time series at $L/L_0 = 0.333$ on the double slope configuration with $\beta = 15°$. This is an examination of the baroclinic torque in the colorful curves and the vorticity advection in the black curves with colorful markers. The colors blue, orange, yellow, purple, green, and burgundy correspond to the points on the thermocouple grid at $n = 0.20,0.16,0.12,0.08,0.04,0\ m$, respectively.

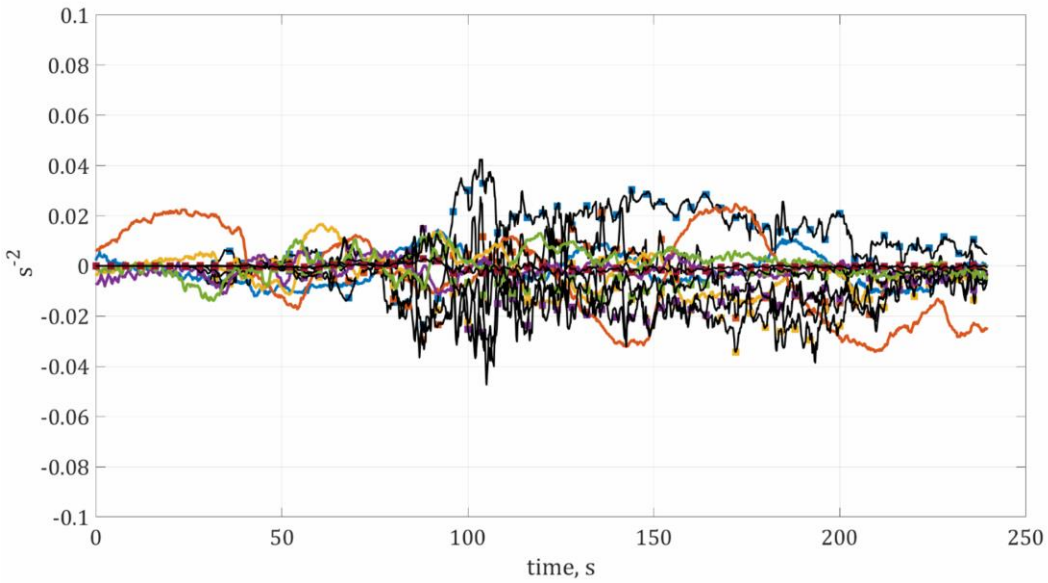

Figure 3.46 Instantaneous time series at $L/L_0 = 0.5$ on the double slope configuration with $\beta = 15°$. This is an examination of the baroclinic torque in the colorful curves and the vorticity advection in the black curves with colorful markers. The colors blue, orange, yellow, purple, green, and burgundy correspond to the points on the thermocouple grid at $n = 0.20,0.16,0.12,0.08,0.04,0\ m$, respectively.

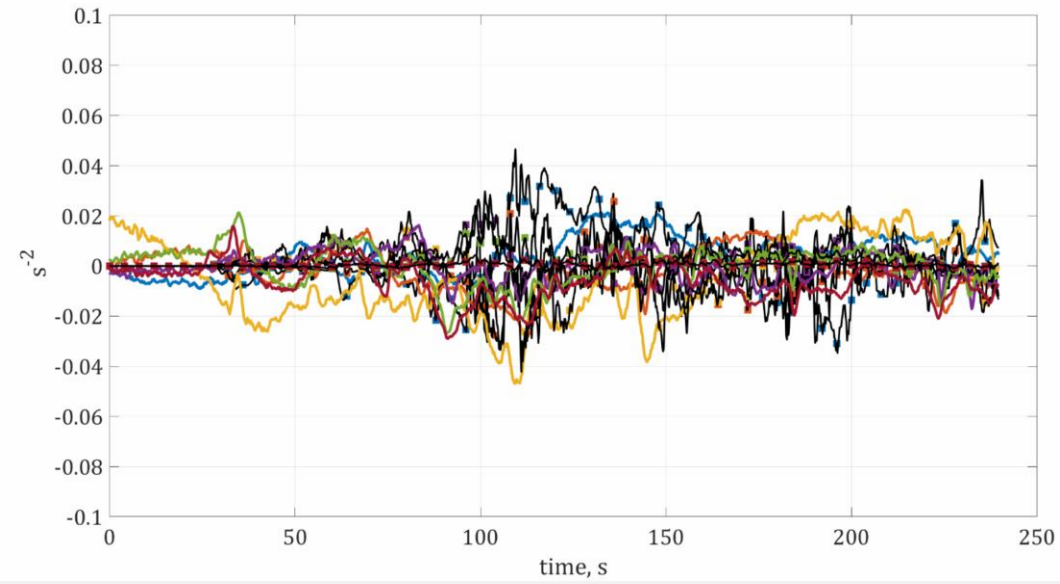

Figure 3.47 Instantaneous time series at $L/L_0 = 0.667$ on the double slope configuration with $\beta = 15°$. This is an examination of the baroclinic torque in the colorful curves and the vorticity advection in the black curves with colorful markers. The colors blue, orange, yellow, purple, green, and burgundy correspond to the points on the thermocouple grid at $n = 0.20,0.16,0.12,0.08,0.04,0\ m$, respectively.

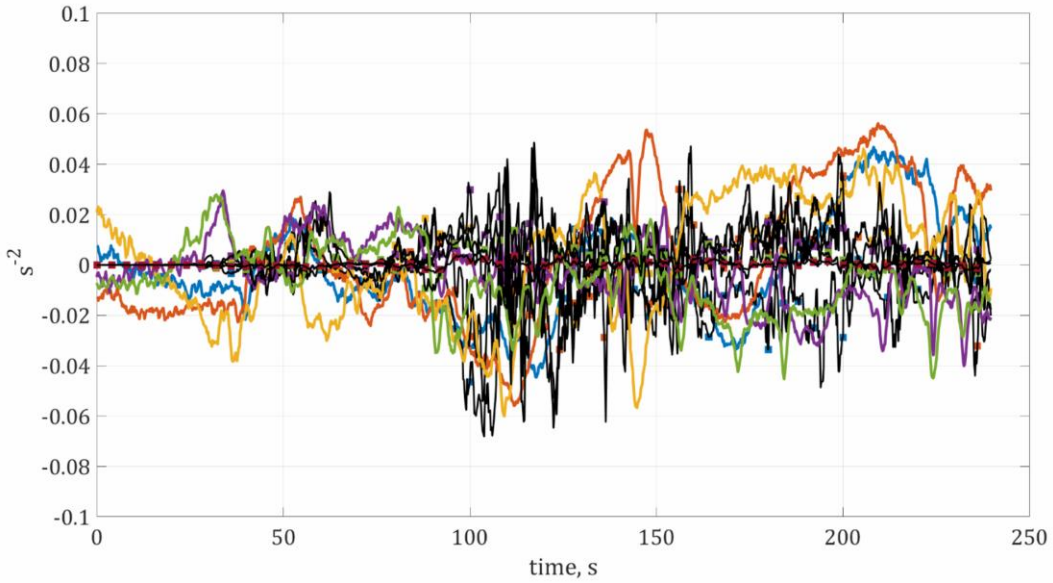

Figure 3.48 Instantaneous time series at $L/L_0 = 0.833$ on the double slope configuration with $\beta = 15°$. This is an examination of the baroclinic torque in the colorful curves and the vorticity advection in the black curves with colorful markers. The colors blue, orange, yellow, purple, green, and burgundy correspond to the points on the thermocouple grid at $n = 0.20,0.16,0.12,0.08,0.04,0\ m$, respectively.

In the lower part of the slope, where the mean velocity is low, the vorticity advection is also small. Further up the slope, the mean flow accelerated, the vorticity advection increases, attaining values comparable to those of the baroclinic torque To get a more comprehensive picture of the distribution of these two properties along the slope, probability density functions of the instantaneous values of both terms at the highest heat flux are provided for several slope angles in Figures 3.49-3.51. The baroclinic torque and vorticity advection exhibit both positive and negative values. This emerges from the time dependency of the signals, while most averages reach values close to zero. The negative baroclinic torque may be explained by the mixing and entrainment of cooler fluid by the 3D helical structures.

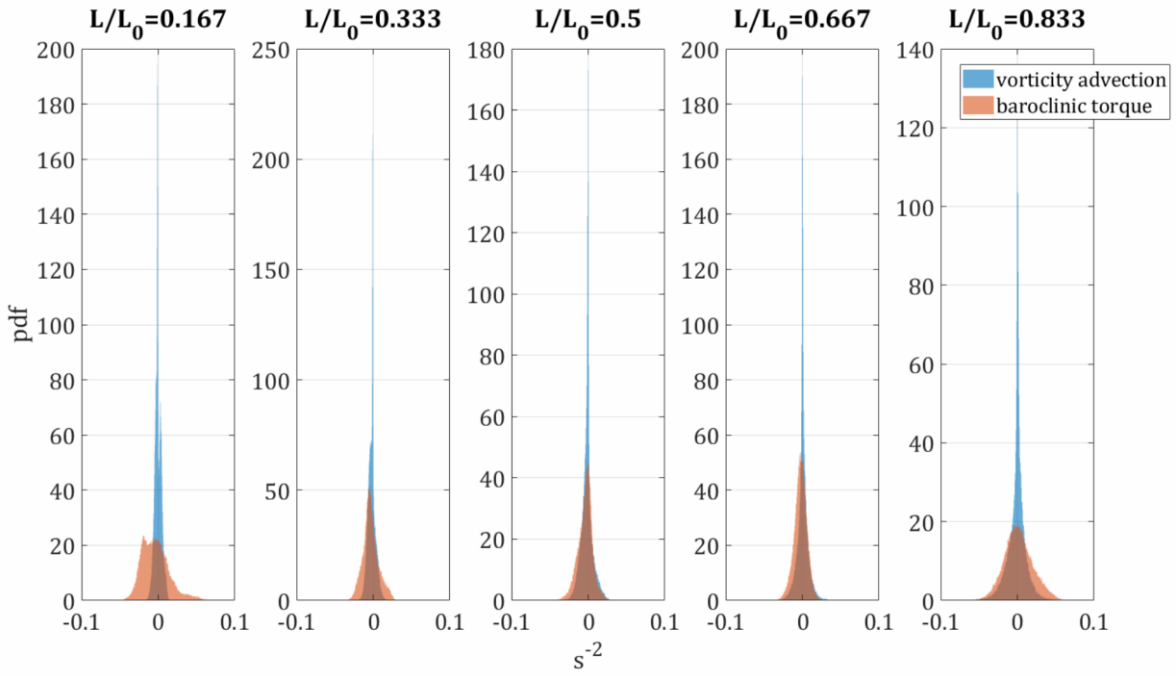

Figure 3.49 Probability density function of the distributions of the vorticity advection and baroclinic torque along the slope at $\beta = 15°$ at the highest heat flux.

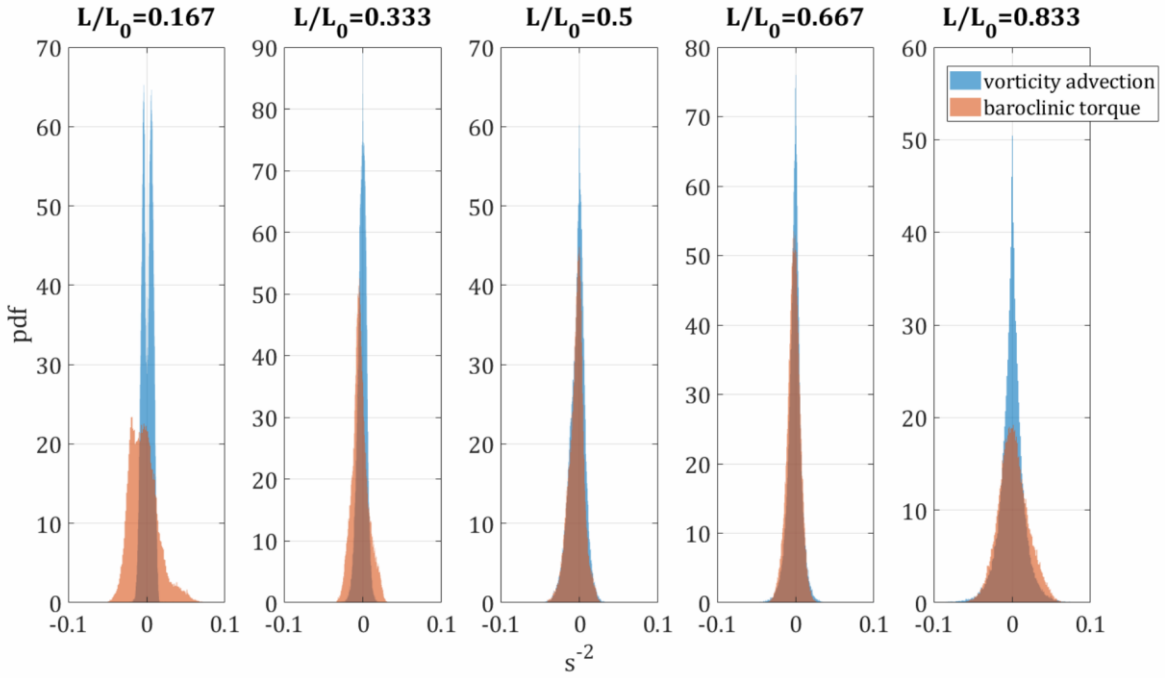

Figure 3.50 Probability density function of the distributions of the vorticity advection and baroclinic torque along the slope at $\beta = 25°$ at the highest heat flux.

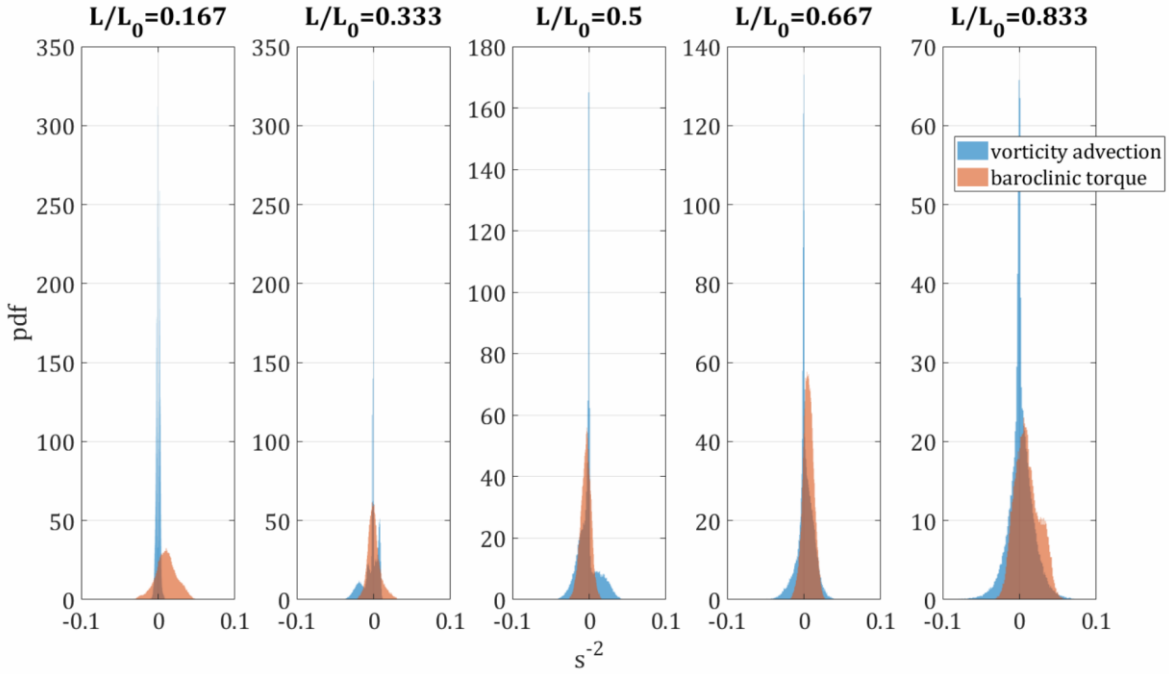

Figure 3.51 Probability density function of the distributions of the vorticity advection and baroclinic torque along the slope at $\beta = 35°$ at the highest heat flux.

3.2.6 Conclusions and limitations

Examination of anabatic BL flow developing on a larger scaled sloping model revealed the transient nature of the flow. It also highlighted the importance of the three-dimensionality of the flow leading to the recommendation that future studies of anabatic BL flow should examine the flow using 3D measurement tools such as 3D Sliced particle Image Velocimetry (3D-SPIV) or stereo-PIV. Both the transient nature and the three-dimensionality render Hocut et al. [11] model as limited only to purely 2D flow cases and probably only to the initial short-time steady period of the BL formation along the slope. Adopting similar dependencies between the governing parameters an adjusted empirical fit was derived, however the results suggest the developing anabatic BL structure and especially the point of separation do depend on the slope heat flux, again in contradiction with the previously adopted model.

The limitations of this study mainly include the resolution of both velocity and temperature measures. The velocity measurements had a large signal to noise ratio near the boundary. The use of 3D-SPIV may increase the signal to noise drastically by placing the laser sheet parallel to the slope and scanning the flow in the z-direction. The temperature measurements may be improved using a finer thermocouple grid or by using thermochromic particles. Finally, future studies should also introduce roughness and additional geometries such as slope breaks (i.e. change of slope along the mountain).

3.3 Three-dimensional helical structures

The section above revealed five clues that suggested of the presence and dominance of the three-dimensionality of the flow. *Clue#1* and *Clue#2* reveal examples of the "B-shaped" mean profiles. This shape is not present in all profiles because it can only be captured if the assumed helical structure flow intersects the stationary laser sheet. These structures do, however, also flow diagonally along the slope (this will be shown in the 3D visualizations of the flow below) explaining why the "B-shape" was not captured consistently in all experiments. *Clue#3* was simply a sample frame of one of the synthetic streaks videos that captured flow coming from the back of the laser sheet as well as two structures flowing in different directions, along and away from the slope. This will also be referred to as *Clue#4* and *Clue#5* are sample maps of vorticity and swirling strength (i.e. vortex detection) capturing the hypothesized phenomenon of the helical structure split. The five clues motivated a qualitative examination of the 3D of the flow.

3.3.1 Observation in 2D and 3D visualizations: smooth slopes

The previous section presented a visual observation of the 3D dominance of the anabatic BL flow. This was briefly presented in Figure 3.38 and more thoroughly in the Supplementary Materials: Mendeley Data Set [55]. The synthetic streaks capturing the tracer particle movements on the smooth double slope configuration revealed that particles were flowing from behind the laser sheet to the front of it and disappearing. The understanding of 3D behavior using 2D records is difficult but more achievable than point measurements that would not have been able to capture this phenomenon.

The next step for comprehending the 3D structure of the flow is visual observation without a laser sheet. The next set of qualitative experiments were

conducted in air in an enclosed Styrofoam structure of dimensions $1.2\,m\,[L] \times 0.5\,m\,[W] \times 1.45\,m\,[H]$. A Perspex sheet was fitted on one side to provide camera access and to thermally insulate the model from the environment. A large smoke machine was used to generate flow visualization particles, and settling chambers were installed on both ends of the enclosure to ensure the smoke particles enter at minimum initial momentum. Figure 3.52 shows a 3D example of the expected flow behavior (from the previous 2D experiments), confirming the presence of the helical intertwined structures forming and flowing along the slope. These were also observed to flow diagonally along the slope.

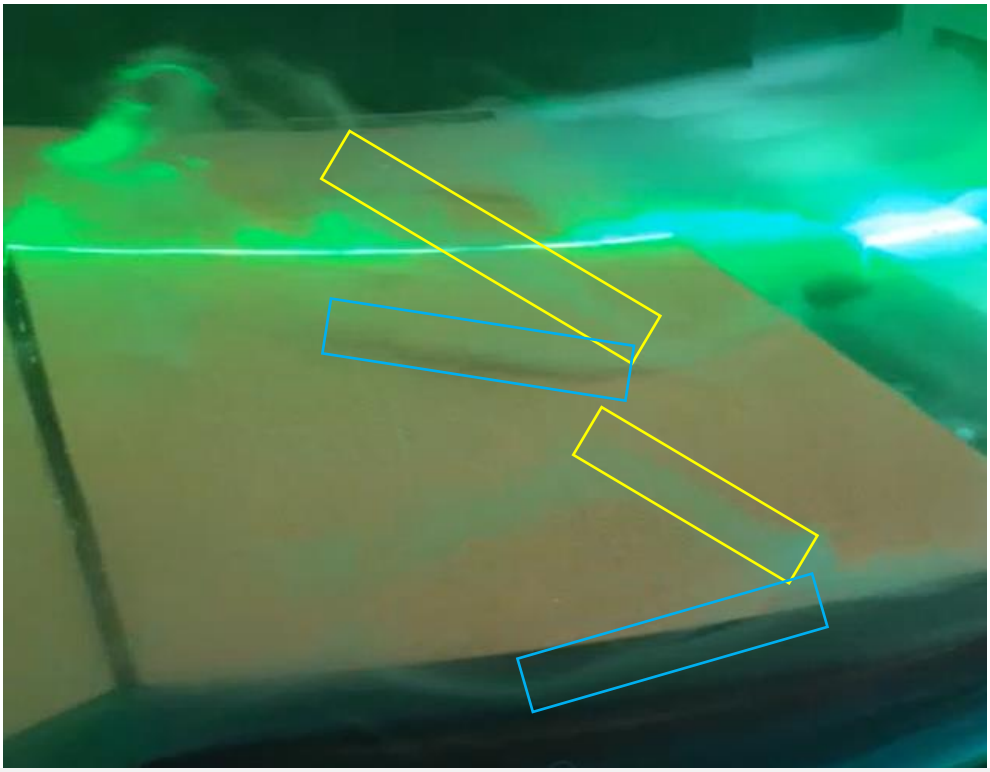

Figure 3.52 A snapshot from the 3D flow visualization on a smooth double slope configuration. The yellow rectangles present the split of the helical structure that flow away from the slope and the blue rectangles present the part of the structure that continually flows along the slope.

3.3.2 Observation in 3D visualizations: rough slopes

Smooth slopes are rarely found in nature and the ones that do exist are artificial, e.g. concrete roads, therefore not accounting for most slopes found in nature. This called for an introduction of roughness on the slope. The roughness could either have a high heat capacity, mimicking rocks/boulders on the slope, or may have a low heat capacity, mimicking patches of vegetation. Here, we introduced a homogeneous 2 *mm* grid (see Figure 3.53) with later added metal split pins distributed more densely at the bottom of the slopes, sparser in the middle, to no pins towards the apex (see Figure 3.54). Such an arrangement can correspond variability of roughness along the slope due to changing density of boulders/vegetation. A qualitative examination of the flow was conducted at a high and low heat fluxes with two different roughness arrangements along the slope. In these experiments the same helical structure splitting was observed, see Figure 3.55, calling for more comprehensive and quantitative 3D flow analysis. Additional videos were uploaded to the Supplementary Materials: Mendeley Data Set [55].

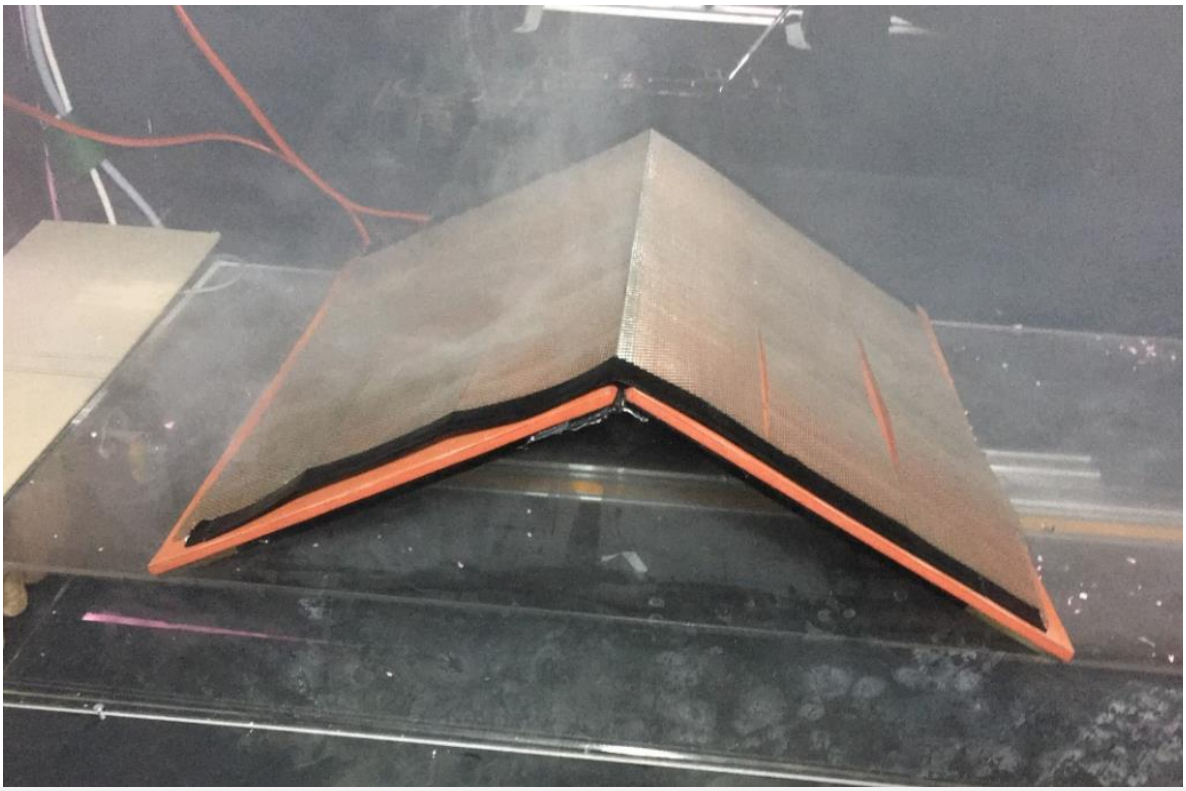

Figure 3.53 An example of the setup with uniform roughness introduced to the setup. It was accomplished using a metal mesh on the double slope configuration.

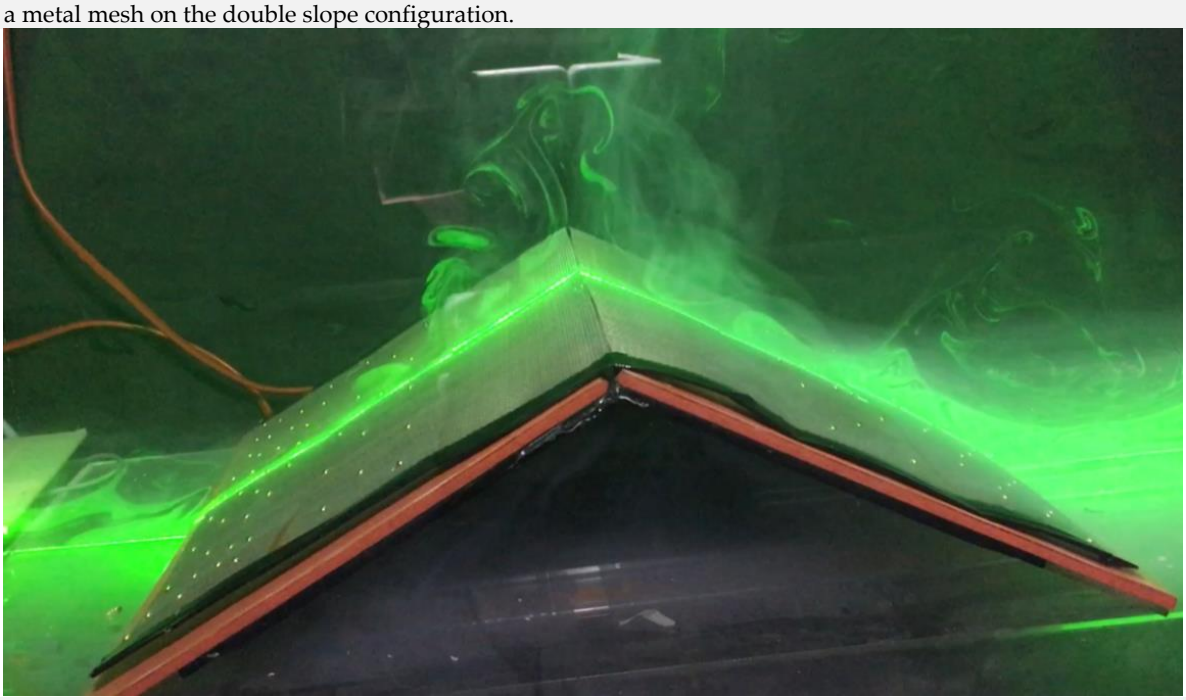

Figure 3.54 An example of the setup with gradient roughness introduced to the setup. It was accomplished using a metal mesh and split pins on the double slope configuration. The split pins added were more densely packed at the bottom of the slope, sparsely packed in the middle, and the apex did not have any.

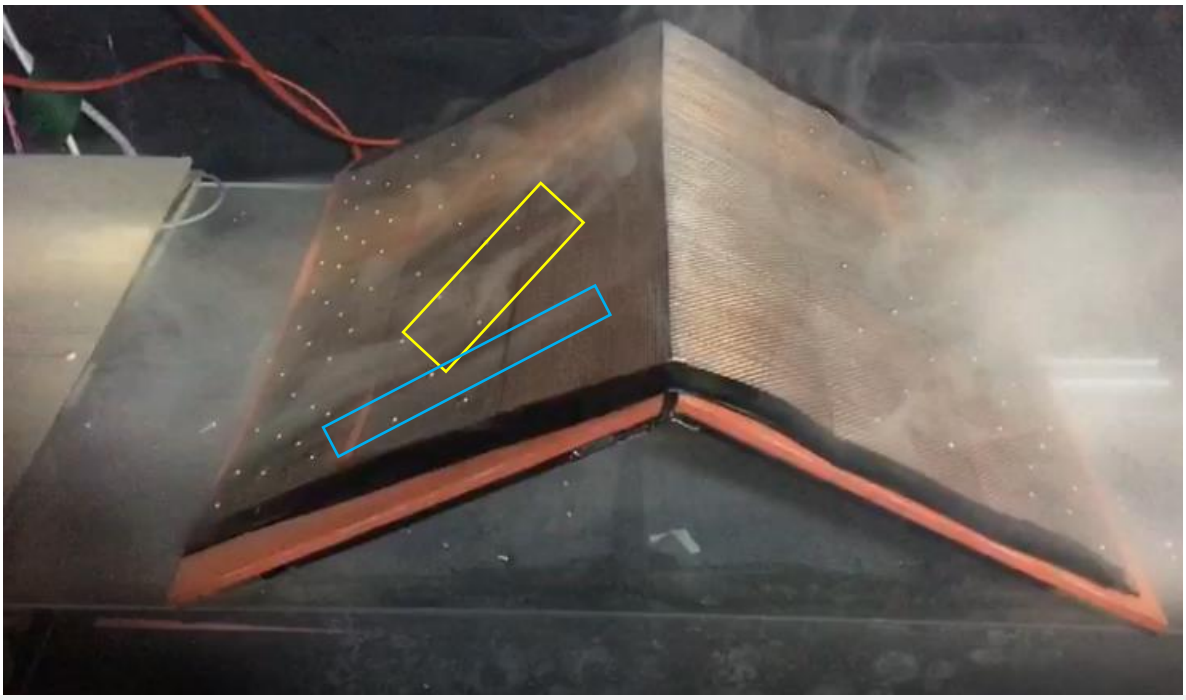

Figure 3.55 A snapshot of the helical 3D structure breakup. The setup here is with the same roughness as in Figure 3.54 above. The yellow rectangle presents the split of the helical structure that flows away from the slope and the blue rectangle present the part of the structure that continually flows along the slope.

3.3.3 Discussion and future work

Future work should capture and study the complete 3D nature of the flow. This would provide a better understanding of the anabatic BL behavior and would provide a basis for modelling such flow. The spatial and temporal resolution should be improved as well, especially near the boundary. A thermal camera or thermochromic particles should also be used to capture temperature variations at all the examined points to enable the computation of correlations with the 3D velocity field.

Chapter 4: Development of field measurement techniques

Building off the previous configuration of the combo anemometer [9], demonstrated in Figure 4.1, this chapter will detail the most recent mechanical and algorithmic advancements accomplished in improving the combo design and the associated data processing routines and algorithms.

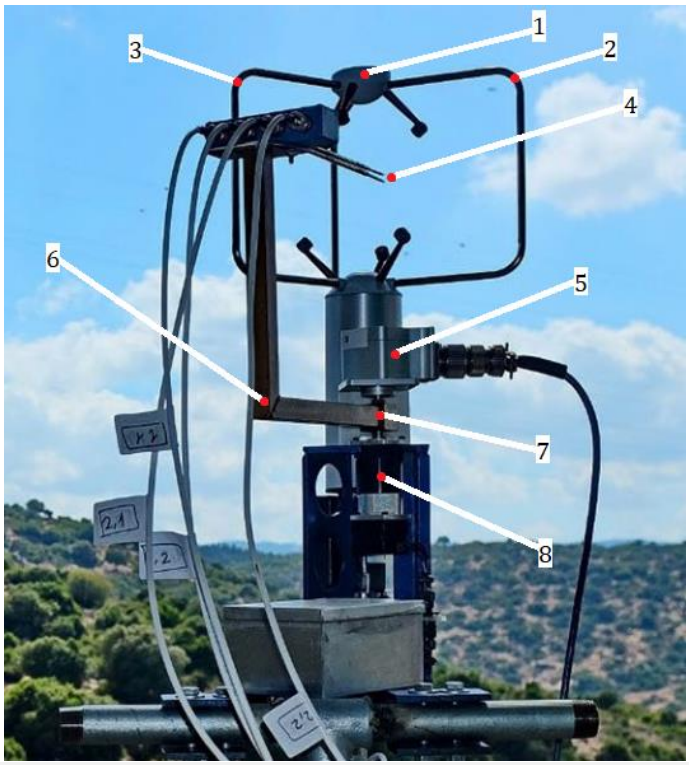

Figure 4.1 Previous configuration for the combo probe. This image is taken from the field experiment in Nofit, Israel [12]. The main components of the combo probe are 1: ultrasonic anemometer. 2-3: sonic support struts limiting the probe movement to 120°. 4: hotfilm probes. 5: absolute encoder. 6: rotating arm to align probes. 7: center of rotation of the arm. 8: motor and gearhead.

The combo anemometer is the recently developed probe capable of continuously sensing the fine-scales of turbulent fluctuations in the field—without human interaction. It consists of a collocated ultrasonic anemometer (sonic) and two

x-shaped double sensor hotfilm probes. The combo simultaneously samples the hotfilms and sonic at a high sampling frequency of several kHz. Prior to the combo, hotwire anemometry was rarely used in the field because of two major limitations: calibration complexity and requirement of probe alignment with the mean flow.

The first aspect of hotwire anemometry that proposes a challenge in field measurements is the cumbersome calibration procedure. The calibration of the wires typically involves a low turbulence flow (typically a controlled jet or a wind tunnel) and possibly a pitch/yaw manipulator to calibrate for a wide range of angles of attack. Once completed, it is only valid for nonchanging and steady environmental conditions, i.e. environment with constant ambient properties such as temperature and humidity. The calibration is no longer valid when significant enough change of conditions occurs. The combo was designed to tackle this limitation since the change of environmental conditions in the field is inevitable.

The combo utilizes an alternative approach to the traditional hotwire anemometry calibration procedure: use of the pre-calibrated sonic data for in-situ calibration of the hotfilm. The in-situ calibration procedure developed by Kit *et. al.* [9] was since then tested in several studies [12, 29, 57, 58] proving its robustness for use in various environmental conditions. It involves a careful human-decision based selection of five *representative* minutes from each hour of continuous measurements to form the training set of the artificial neural networks (NN) that would be valid for all data collected within that hour. The selected minutes are to represent the entire range of mean velocities of the hour and have high quadratic mean (rms) values to represent the velocity field fluctuations during the hour as best as possible. Two separate NN are trained for every hour, one for each x-shaped hotfilm sensor, which are used as the voltage to velocity transfer functions. After the minutes are selected,

they undergo low pass filtering down to the trusted frequency of the sonic. The filtered velocity data from the sonic are used as targets while the filtered voltage data from the hotfilms are used as inputs. Finally, the original high-frequency voltages from the hotfilms are fed into the trained NN resulting in 3D velocity field components fluctuations at high spatiotemporal resolution.

The second aspect of hotwire anemometry that poses a challenge for field measurements is the requirement that the probe remains aligned with the mean flow direction. The accuracy of the hotwires/hotfilms is proportional to the probe alignment with the mean flow, i.e. the smaller the angle of attack higher is the accuracy. Unlike in a controlled laboratory setup, the direction of the flow in the field is everchanging, preventing the angle of attack of the flow relative to the hotwire/hotfilm orientation to remain within pre-defined tight boundaries. The combo tackles this limitation by mounting the hotfilm sensors on a rotating arm and using a LabVIEW routine for periodic re-alignment of the sensors with the mean flow direction. The sonic provided velocity at the end of every measurement interval determines the new desired probe direction while a motor and encoder are used to align the probes with the direction prescribed by the sonic. In the post-processing, outlier minutes with a varying flow direction, or angles of attack larger than $\pm 10°$, are omitted.

The original design of the combo had two mechanical constraints. The first is that the hotfilm probe orientation was restricted by the sonic support struts, labels 2 and 3 from Figure 4.1, enabling limiting the re-alignment of the probe within a range of $\pm 60°$ from the initially selected orientation. The second is the location of the axis of rotation of the hotfilm probe (the two x-shaped sensors). The positioning of the motor and gearhead is several centimeters from the center of the sonic control

volume, causing the hotfilm probe to be at a different location within the control volume center at each yaw angle. While the latter limitation was shown not to cause a major reduction in accuracy, the former limitation of preselected main orientation did pose a significant constrain on the ability to monitor and record wind flow during diurnal and weekly changes in mean wind direction.

The mechanical advancements of the combo design made during this work are detailed in Section 4.1 below. These include a new and more compact design of the holding and rotating mechanism to allow accurate constant re-alignment of hotfilm probe with the mean flow. The new rotating mechanism can complete 360° turns, while assuring the hotfilm probe is always positioned at the rotation center and hence at the same location within the sonic control volume.

The following section, Section 4.2, details the algorithmic advancements of the calibration procedure, aimed to achieve a complete automation of the calibration. The automated procedure enables (almost) real-time processing, which would provide meteorological stations the ability to monitor real-time fine-scale turbulence statistics and input them into prediction models. The new procedure was tested and compared with laboratory and field obtained data. The laboratory data was acquired in a large environmental wind tunnel and the field data was acquired in the Red Sea over the water wave field. Altogether, the new mechanical design and new automated calibration procedure provide a tool to enable the combo to be used in non-stationary environments, e.g. on a boat or moving vehicle.

4.1 Mechanical evolution of the combo anemometer

Sonic anemometers are conventionally installed facing north to correspond with the manufacture's programming of the sonic. This convention is useful for

alignment of the wind direction with the real-world coordinates. The previous configuration of the combo was based on this convention and had the sonic fixed in place facing north, allowing the hotfilm probe to rotate inside the sonic control volume to follow the direction of the flow. Figure 4.1 presents the geometric constraint limiting the yaw rotation to ±60° (label 2 and label 3) from the predetermined orientation and the shift in axis of rotation of the probe relative to the sonic center. The Combo 2.0 design, presented in Figure 4.2, was devised to deal with these limitations.

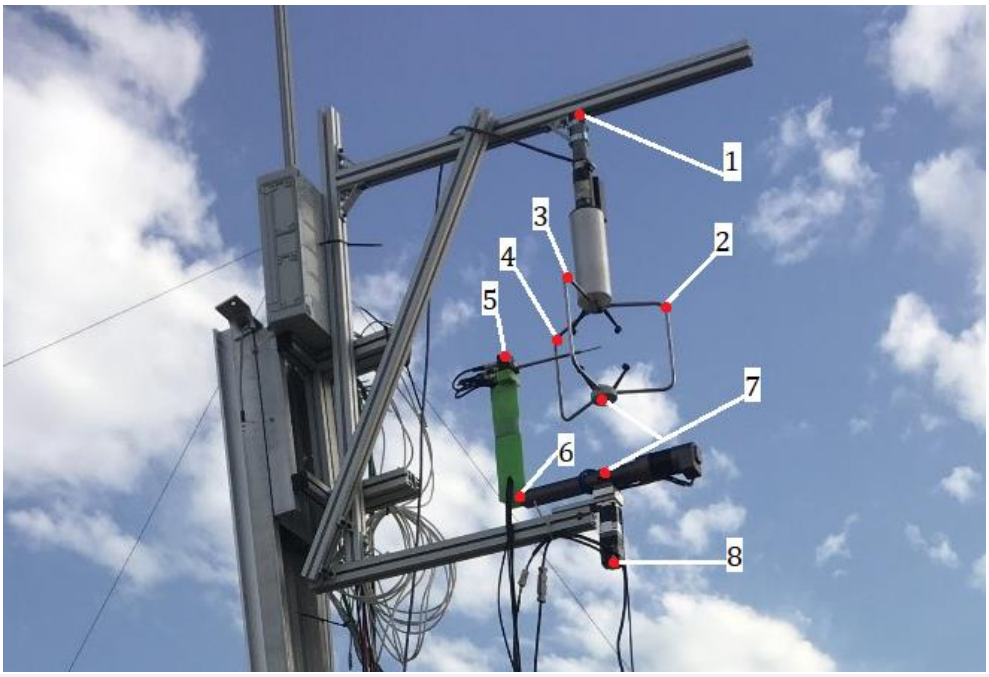

Figure 4.2 The new configuration of the combo allowing a complete 360° probe alignment with the flow direction. This version of the combo is referred to as Combo 2.0. It is composed of a sonic (labels 1-4), a hotfilm probe (label 5), an extending/retracting and rotating arm (labels 6-7), and a motor, absolute encoder, and gearhead. More specifically, 1: the sonic is fixed upside down and faces north. 2-4: sonic support struts. 5: hotfilm probe holder with two hotfilm sensors on it. 6: 3D printed structure to hold the hotfilm holder and connect it with the extending arm. 6: extending arm. 7: center of rotation of extending arm. 8: motor, encoder, and gearhead. Note: labels 1,7, and 8 share the same axis of rotation.

To attain the full 360° measurement range, we developed a new prototype (Figure 4.2). It consists of a motor, gear, encoder, and an extending/retracting arm (labels 6-7) to enable passage over the sonic support struts (labels 2-4). Using the readings from the absolute encoder, the arm is programmed to extend back when it reaches one of the support struts. The arm consists of the linear actuator and a 3D printed enclosure (the green structure—label 6) that holds the hotfilm probe and contains the cables of the hotfilm sensors in it. The sonic is fixed in place facing north and is flipped upside down to reduce the height of the arm and reach minimum torque while maintaining the same axis of rotation as the sonic. The motor rotating the hotfilm probe is placed directly below the sonic central axis, enabling the probe to have the same relative position to the sonic center at all positions. The aluminum profile frame is the external structure fixating the sonic (label 1) to the motor (label 8). This structure is large, and its presence can disrupt the flow coming behind it. This design effectively reduces the measurement range to about 270°, which is still a relative improvement from the 120° range of the previous configuration. Spoiler: the newest version of the combo elegantly reaches the 360° range without any obstructions (presented below).

Figure 4.2 above displays the deployment of Combo 2.0 on the roof of the Wolfson building at Tel Aviv University Faculty of Engineering. In this study, an attempt to examine the correlations between high frequency velocity and temperature measurements in a stable BL was made. However, due to noise problems the measurements were concluded to be insufficiently accurate and were discarded. To top it off, during the last day of the deployment, the 3D printed arm enclosure started to crack and wiggle, eventually preventing further operation. This motivated us to think about alternative solutions for the arm mechanics and

eventually led to the new concept of the combo design: we call it Combo 10.0 (Figures 4.3-4.4). The numbering of the new combo name was selected because we believe the new design skipped a few generations of mechanical development.

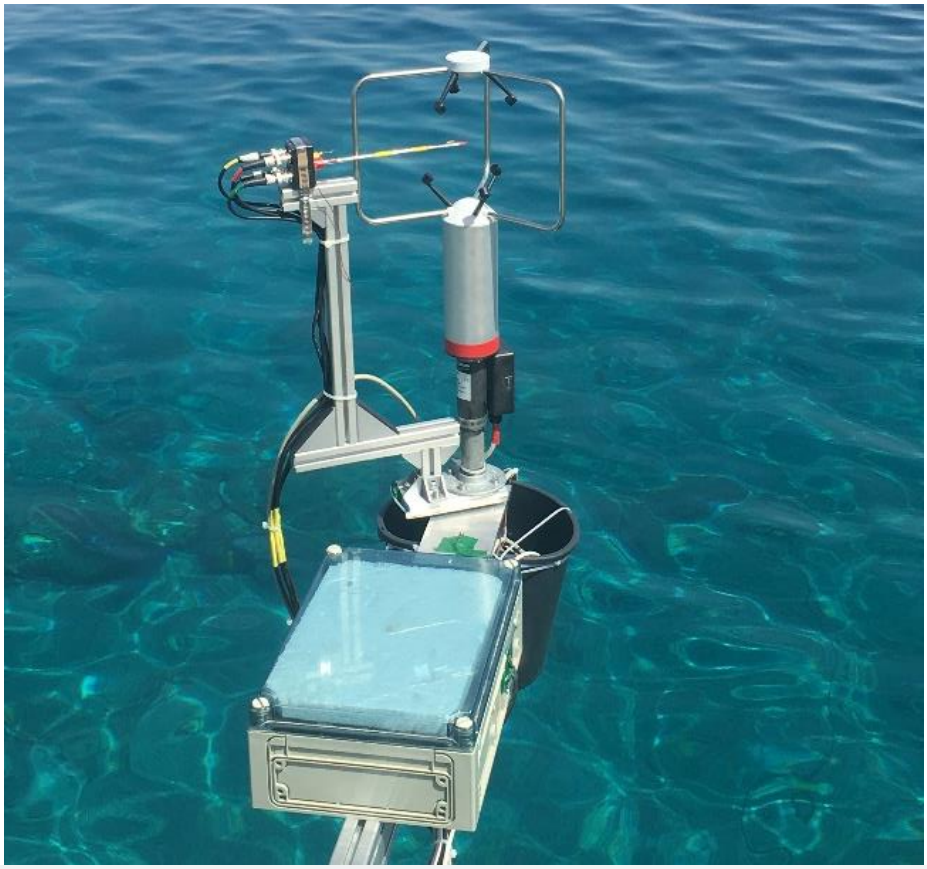

Figure 4.3 An image demonstrating the new mechanical design of the combo anemometer: Combo 10.0. Unlike Combo 2.0, the combo has no obstructions around it and can measure the complete 360° range. A more detailed image of the mechanics is presented in Figure 4.4 below.

The bulkiness, damage to the 3D printed arm, and concern that the complexity of the control program possibly causing damage the delicate hotfilm paved the path for the newer and much improved design. Instead of fixating the sonic—as per the convention—and rotating the hotfilm probe around the sonic, we propose to fixate the hotfilm probe to the sonic and rotate them both. Keeping track of the sonic and probe orientation relative to the meteorological/magnetic North is

achievable using an absolute encoder. Figure 4.4 presents the details of the elegant, more rigid, and eventually simpler both in construction and operation combo design. This design is characterized by simpler mechanics as only one rotation motor is required, the control program is also simplified, and there is a much smaller chance of error or damage to the hotfilm probes because the probes and sonic are always in the same coordinate system.

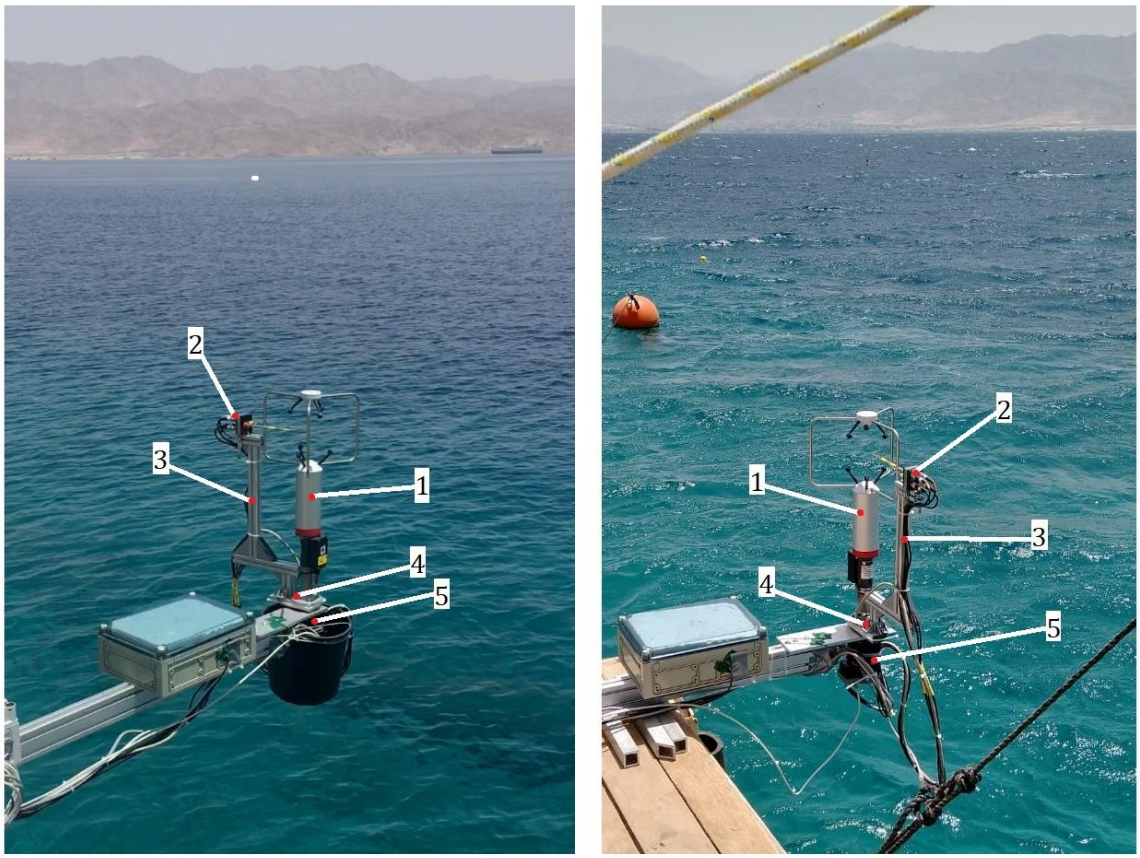

Figure 4.4 Newest version of the combo anemometer that we developed. We called it Combo 10.0. The two images are simply two angles of the same combo, the combo parts are labeled the same in both images. The entire combo (sonic and hotfilm probe) rotate as a single unit according to the direction of the flow determined by the sonic. This newest version of the combo is composed of the following 1: sonic. 2: hotfilm probe. 3: aluminum profile probe holder. 4: arm to hold the hotfilm holder. 5: motor and encoder. The image on the left has a bucket covering the motor to prevent water damage on days with higher water waves.

The Combo 10.0 was deployed for field measurements with the goals of examination of its durability and its capability of working continuously without human intervention for days or weeks at a time. The testing took place in an open sea environment at the northern tip of the Gulf of Aqaba (Red Sea) in May of 2019. The gulf hosts a lot of recreational activities due to the presence a coral reef. It is also a home of several large ports since Egypt, Israel, and Jordan all share its shoreline. Despite significant amount of wave activity and appealing topography that generates a diurnally repetitive wind flow, its wind-wave regime was never thoroughly investigated. The research goal was to assist in the understanding the fine scales of turbulent fluctuations over a water wave field. This work is also part of a project of another PhD student at T-SAIL (Almog Shani-Zerbib) [59]. This study is a more comprehensive one than the previous that was conducted in 2017 because it includes the turbulence measurements using the combo on top of the experimental setup used also in 2017; the complete description of the 2017 study can be found in [60] and the freely available data set is available on the Mendeley Data servers [61].

The measurements took place on the pier designed for marine monitoring at the Inter-University Institute for Marine Sciences (IUI) in Eilat, Israel, situated in the southmost part of Israel. Figure 4.5 presents the unique topography of the gulf that makes it an appealing location for wind-wave interaction research. It is located between relatively high mountain ridges that form an almost rectangular shape of 15 km width and is composed of relatively deep water. The rectangular shape of the gulf has a 6.5 km fetch of deep water up to the point of measurements. It also hosts a rather unique and steady diurnal wind pattern during daylight hours, characterized as approximately $10° - 20°$ northeastern wind of $8 - 12\ m/s$.

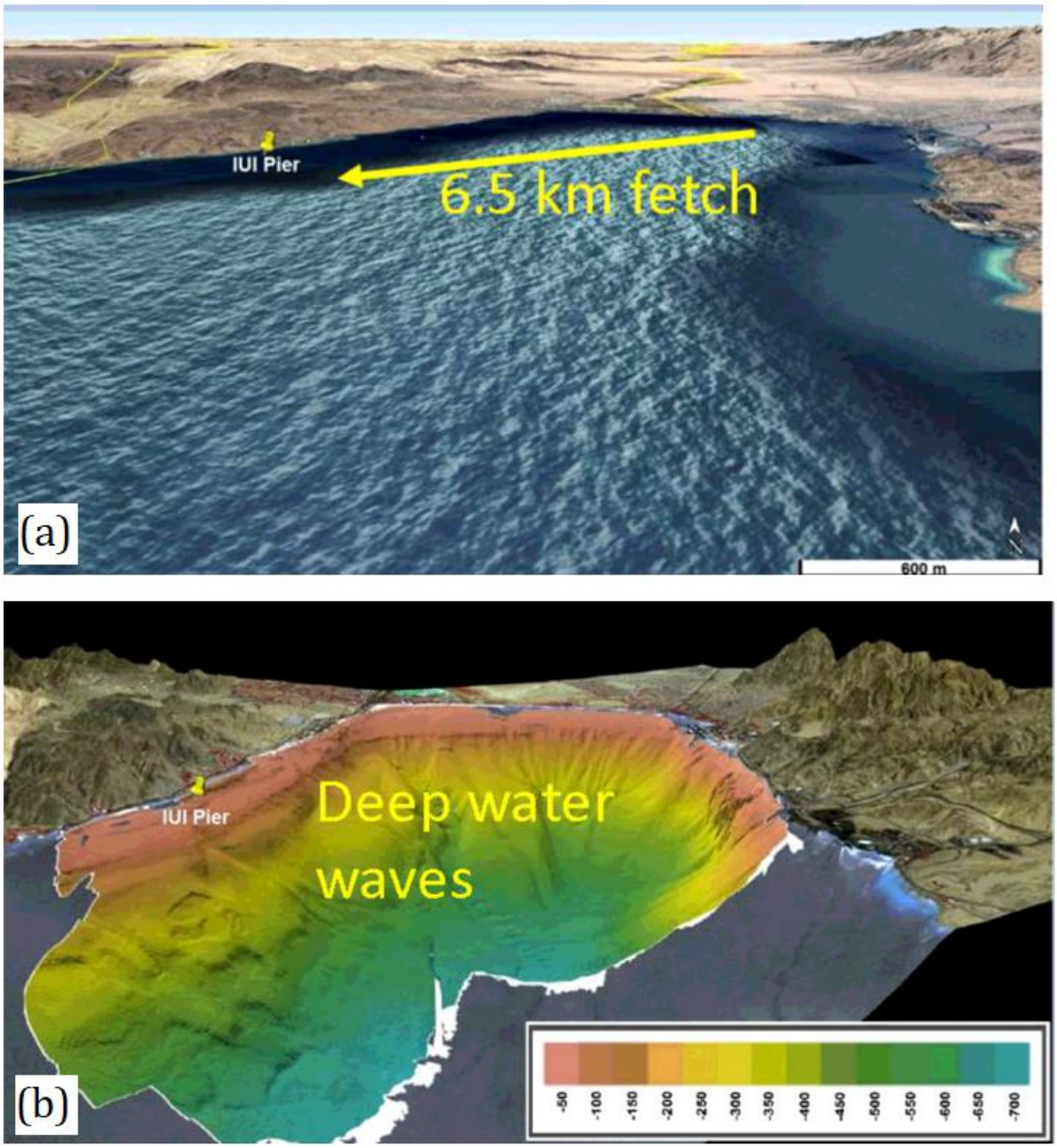

Figure 4.5 Topographic layout of the northern tip of the Gulf of Aqaba. (a) The location of the pier at the Inter-University Institute for Marine Sciences (IUI) relative to the northern part of the gulf. The 6.5 *km* fetch upstream of the pier is also presented. (b) The bathymetry of the gulf is displayed, and this confirms the deep water-wave regime in the relevant fetch.

Most elements of the experimental setup in 2019 are the same as the experiment in 2017, the only addition to this 50-hour continuous study was the re-designed combo. It provided the turbulent fluctuations of the wind velocity field components. The experimental setup was also composed of an array of five Wave Staff wave gauges to sense the wave field, two RM Young 81000 ultrasonic anemometers at two altitudes to obtain the mean wind profile, and a water pressure gauge to obtain the mean water level. A brief portion of the results is presented in Figure 4.6, the rest are under preparation for publication. The temporal evolution of four parameters presented here include the turbulence intensity, horizontal length scale, the mean wind velocity at ten meters above sea level, and the significant wave height. The turbulence intensity is defined as $TI = \sqrt{TKE}/\bar{u}$, where $\bar{u}$ is the mean velocity and the turbulent kinetic energy is defined as $TKE = (u^2 + v^2 + w^2)/2$, the u, v, w represent the fluctuations of the 3D velocity field components. The horizontal length scale is defined as $L_H = \left(\sqrt{\overline{u^2}}\right)^3/\bar{\varepsilon}$, where $\bar{\varepsilon}$ is the TKE dissipation rate and is defined in Equation (5.3) (in the next chapter). Finally, the last two parameters that will be discussed are the U_{10} and H_s; the U_{10} is the extrapolated mean velocity of the wind profile at ten meters above the water and the H_s is the significant wave height defined as the mean wave height of the top 1/3 of the highest waves.

The temporal evolution of these parameters reveals new patterns and raises several questions. Figure 4.6 reveals that the higher L_H are observed only at higher U_{10}, also accompanied by lower TI values. Additionally, the wave field appears to react to the variations in TI with an increase/decrease in L_H which precedes that of H_s. The L_H are the result of the wind BL disturbance by longer waves traveling from far, approximately 6.5 km, and the fetch appears to limit the water-wave growth. The study conducted in 2017 [60] revealed that the mean wind magnitude and

direction are both important for the local water waves field evolution, but this 2019 study reveals that also the turbulence structure is just as important. Some questions that this study raised include: is less turbulence needed to generate higher waves? What type of turbulence structure generates what type of water-wave field? What is the sensitivity of wave field to small variations in wind flow direction? These call for more detailed experiments in the Gulf of Aqaba.

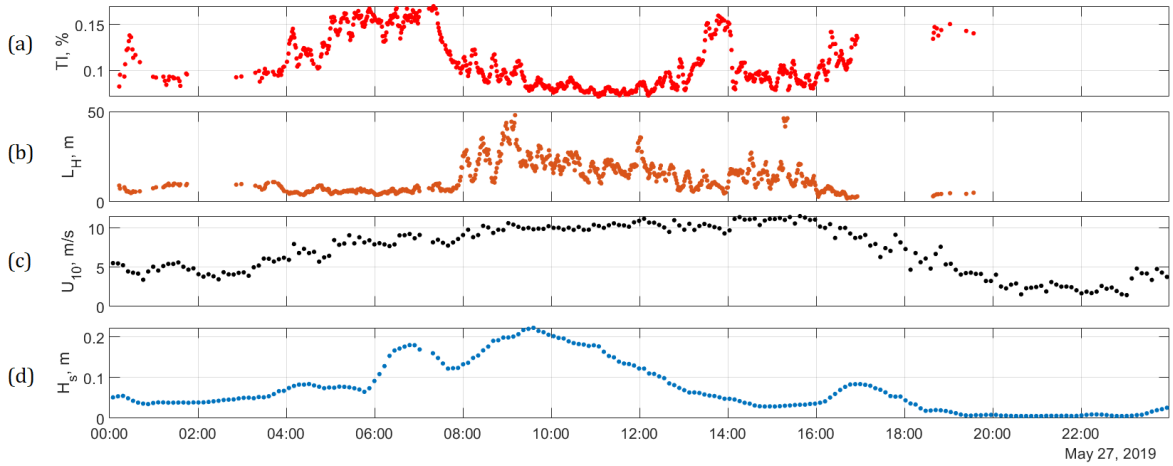

Figure 4.6 Temporal evolution from May 27th, 2019 of four important wind-wave interaction parameters. (a) turbulence intensity. (b) horizontal length scale. (c) mean wind speed at ten meters above sea level. (d) significant wave height.

This experiment not only verified the durability and working capability of Combo 10.0, but also showed its capability of working continuously without human intervention in changing field conditions. This high frequency response anemometer is useful for many types of field studies in all types of environments, both changing and not. The combo data processing advancement is presented in the next section. It will also reveal the possibility of implementing or deploying the combo on moving vehicles, such as boats, cars, or heavy lifting drones for complete BL scanning.

4.2 Automated real-time in-situ hotfilm calibration

Use of close to real-time fine-scale turbulent field measurements can assist in improving prediction/forecast models and improving the understanding of naturally occurring wind flows. The combo has demonstrated its ability of providing such scales in both stable and unstable BL flows [12, 29, 57, 58], and the last section provided evidence that Combo 10.0 can even be deployed in the open field/sea and measure the wind coming from all directions in unsteady environments. The next step is to automate the calibration procedure of the combo to enable near real-time monitoring of fine-scale turbulent fluctuations. It is especially useful with changing field conditions or non-stationary measuring stations, i.e. probes placed on moving platforms. The here proposed automated procedure was tested on field-obtained data, tested inside a wind tunnel, and compared with the "classical" hotwire calibration procedure [62, 63] using a free jet calibrator. The calibrator consists of a controlled jet and mechanical pitch and yaw manipulator. The field dataset used for comparison is the wind-wave interaction dataset conducted in the Inter-University Institute for Marine Sciences (IUI) Pier in Eilat, Israel in 2019. The laboratory dataset was collected in the Environmental Wind Tunnel available at the Faculty of Civil and Environmental Engineering at the Technion-Israel Institute of Technology.

Hotwire/hotfilm anemometry is capable of sensing small scale changes in the velocity field at high frequencies. The operating principle is sketched in Figure 4.7 and depicts how the hotwire is conceived as a cylinder sensing the cooling effect of a flow over a heated body. The wire is heated using electrical current. A servo amplifier keeps the Wheatstone bridge resistance—and therefore temperature of the sensor—in balance by controlling the current to the sensor. This loop/procedure is independent of the cooling imposed by the fluid. The Wheatstone bridge has the

benefit of isolating changes in sensor resistance from the rest of the bridge, making it independent of drift in temperature or other properties of the environment. The voltage readings from the Wheatstone bridge are recorded on an A/D card and need to be converted into the 3D velocity field components. The voltage to velocity transfer function estimation/calibration procedure are discussed in detail below.

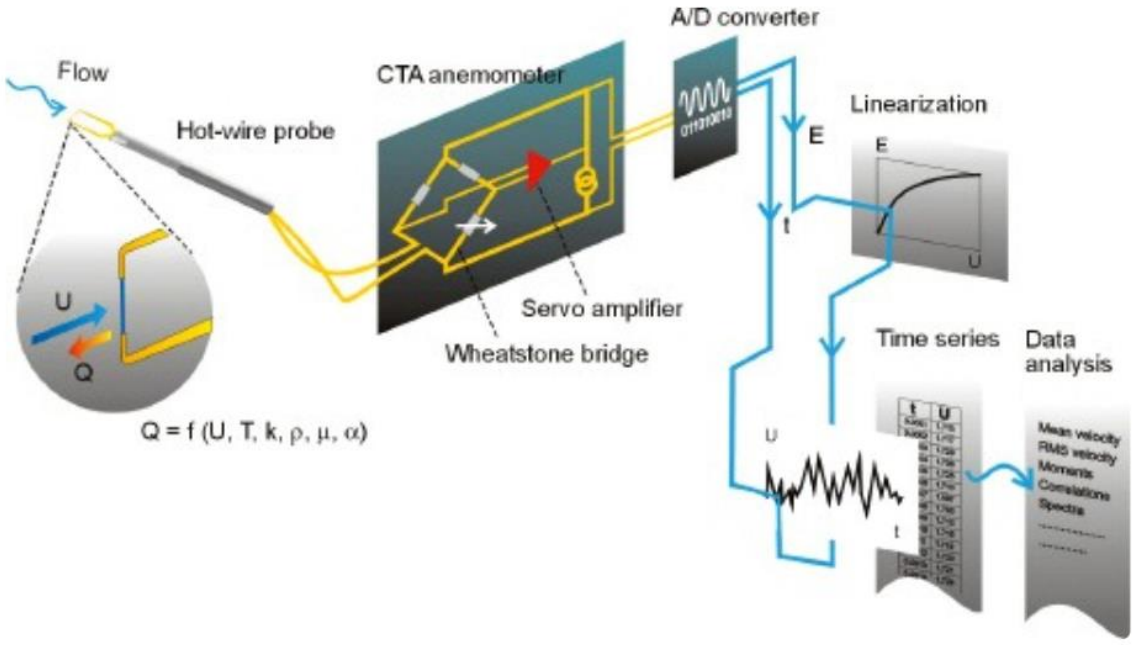

Figure 4.7 Basic measurement and operating principles of CTA (Constant Temperature Anemometer) taken from the Dantec Dynamics website. Left to right: hotwire exposed to fluid flow, Wheatstone bridge and servo amplifier for maintenance of constant resistance and monitoring of fluid velocity fluctuations, A/D card to capture the voltage change, and finally a representation of the voltage-to-velocity transfer function estimate.

The voltage to velocity transfer function is traditionally estimated using a calibrator, often made up of a controlled jet with low a turbulence intensity. An example calibrator is the Dantec directional calibrator for hot-wire probes (Figure 4.12); it includes a controlled jet and a motorized mechanical manipulator to adjust the angle of attack of the flow to the probe. The transfer function can be estimated using several methods. The most common ones in the laboratory are the least-

squares polynomial fitting using King's law and the lookup table method [63]. These are unpractical in the field, and the in-situ calibration method was proposed as an alternative by Oncley et. al. [64, 65]. It was later implemented by Kit et. al. [9], where they presented the ability to use the simultaneously measured low frequency signal form the ultrasonic anemometer to calibrate the high frequency signal of the hotfilm using artificial neural networks (NN).

Previously, the field calibration procedure included a delicate selection of five representative minutes from the hour to train a NN that would be valid for that hour. These minutes needed to both cover the entire range of velocities and have a high rms value to cover as many variations of fluctuations as possible. However, this manual selection is time consuming and is human decision based. Advances in AI research teach us that in order to achieve better training of NNs, larger data training data sets of broad range of varying values are required [66]. We, therefore, propose to use all low-pass filtered data from a representative hour (or period with constant ambient properties) as a training set. The best representation of the hour is all the points available during that hour, however when expanding the training set significantly (by at least an order of magnitude) we might have to consider expanding the network size to avoid underfitting.

In fact, the selection of an hour was previously chosen arbitrarily. The real requirement is for the background flow conditions to remain constant, i.e. temperature, pressure, and humidity. The automated process should include a maximum duration and a range in which these properties are considered relatively constant. The low pass filtering frequency should be chosen independently for each minute based on the mean velocity of that minute. The empirical relationship of the

upper sonic trusted frequency to the mean velocity is given by $f = \bar{u}/2\pi L$ [67], where L is the acoustic fly path of the sonic in use, here $L = 0.15\ m$.

The testing of the automated calibration method was conducted in two types of environments, a controllable and non-controllable one. Section 4.2.1 details the experimental setup in the laboratory and the BL properties of the examined flow, including the power density spectra of velocity fluctuations using the lookup table method. Section 4.2.2 presents the turbulence results obtained in the wind tunnel using the automated in-situ calibration method, and Section 4.2.3 presents the method testing on field data.

4.2.1 Experimental setup in the wind tunnel

The laboratory experimental setup took place in the Environmental Wind Tunnel at the Civil and Environmental Engineering Faculty of the Technion-Israel Institute of Technology. This wind tunnel (Figure 4.8) has a 12 m long test section that operates using a powerful blower in an open-circuit flow-suction mode that can produce velocities up to 14 m/s. The cross section is a square of 1.75 m on each side and the roof is adjustable to enable control of pressure gradients in the streamwise direction. The leading edge of the wind tunnel has a flow straightening honeycomb that is 15 cm long and consists of cylinders with a 5 cm diameter.

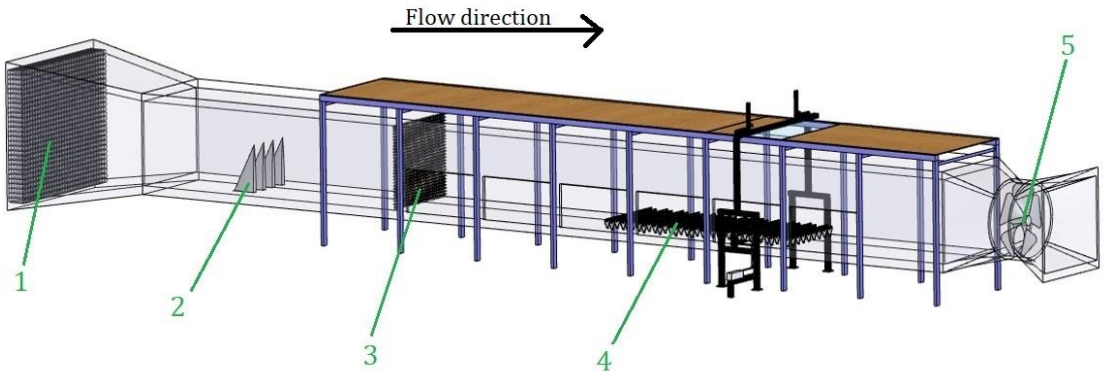

Figure 4.8 A sketch of the Environmental Wind Tunnel at the Civil and Environmental Engineering Faculty of the Technion-Israel Institute of Technology. This a suction type wind tunnel. 1: settling chamber. 2: vortex generating spires. 3: shear generating grid. 4: model canopy. 5: powerful blower with velocity up to 10 m/s.

The wind tunnel is currently in use of for another project that examines the effect of spanwise landscape heterogeneities on the vegetation canopy evapotranspiration in the atmospheric boundary layer flow. We used their setup to compare the hotwire calibration procedures by deploying the combo in the wind tunnel; the hotwires were installed 55 cm from the floor inside the sonic control volume. The construction of the BL was established by a PhD candidate at T-SAIL (Ewelina Winiarska) and was designed based on literature reviews and some trial and error. The final design is presented in Figure 4.9; it included a grid with various densities to generate shear flow and artificially increase the BL height—it is most dense at the bottom and least dense at the top. The grid is positioned between the vortex generating spires and the model canopy, while gravel is spread in the entire area leading to the model canopy to provide surface roughness.

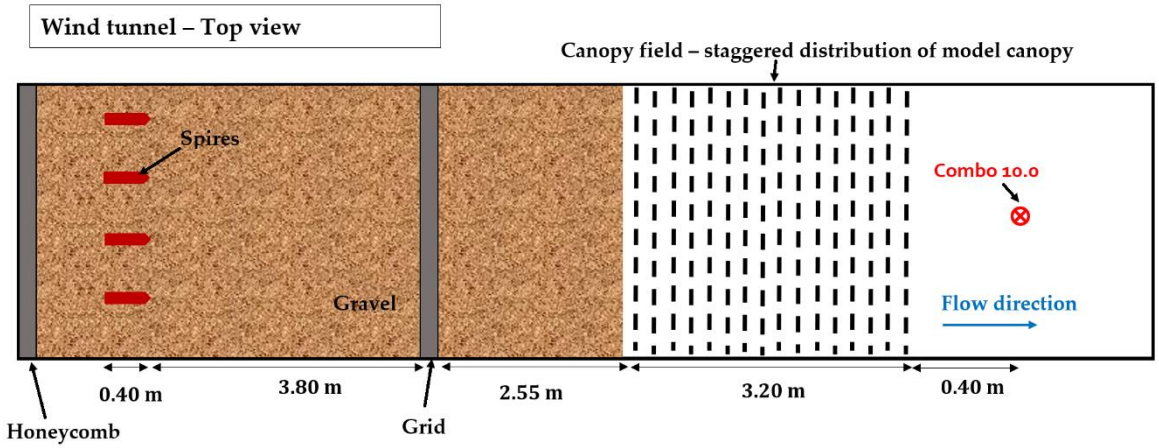

Figure 4.9 Experimental setup of the artificially designed BL. The tools used to design the artificial BL from left to right are honeycomb, gravel, spires, and the grid. The staggered canopy model is displayed to the right and finally the placement of the combo.

Scanning of the velocity profiles at the combo location was also conducted using pitot tubes to measure the BL thickness and confirm correct placement of the hotfilm inside the BL. The profiles for high and low blower frequency of all examined experimental setups are presented in Figure 4.10. The velocity profiles make it evident that the hotfilm were indeed inside the BL for all experimental regimes; the placement of the hotfilm relative to the wind tunnel is depicted by the red circle with an x inside. The length of the sonic acoustic fly path is 15 cm, and the BL height is about 70 cm. The ratio of the sonic length to the height of the BL is not negligible in this case (as it would be in the field). This is important because the sonic averages velocities over different regions in this BL inherently introducing errors in the sonic readings. The three types of experimental setups considered for our purpose were as follows: (1) the complete setup described in Figure 4.9 and referred to as YGYC, which stands for yes-grid-yes-canopy; (2) the same setup as before but without the canopy model and referred to as YGNC, which stands for yes-grid-no-canopy; finally, (3) the same as before but excluding the grid, i.e. only the gravel,

spires, and honeycomb and referred to as NGNC, which stands for no-grid-no-canopy. Table 4-1 below summarizes the three configurations examined.

Table 4-1 Experimental configurations and naming of wind tunnel testing

Experiment name	Grid installed	Canopy	Honeycomb, spires, and gravel
NGNC	No	No	Yes
YGNC	Yes	No	Yes
YGYC	Yes	Yes	Yes

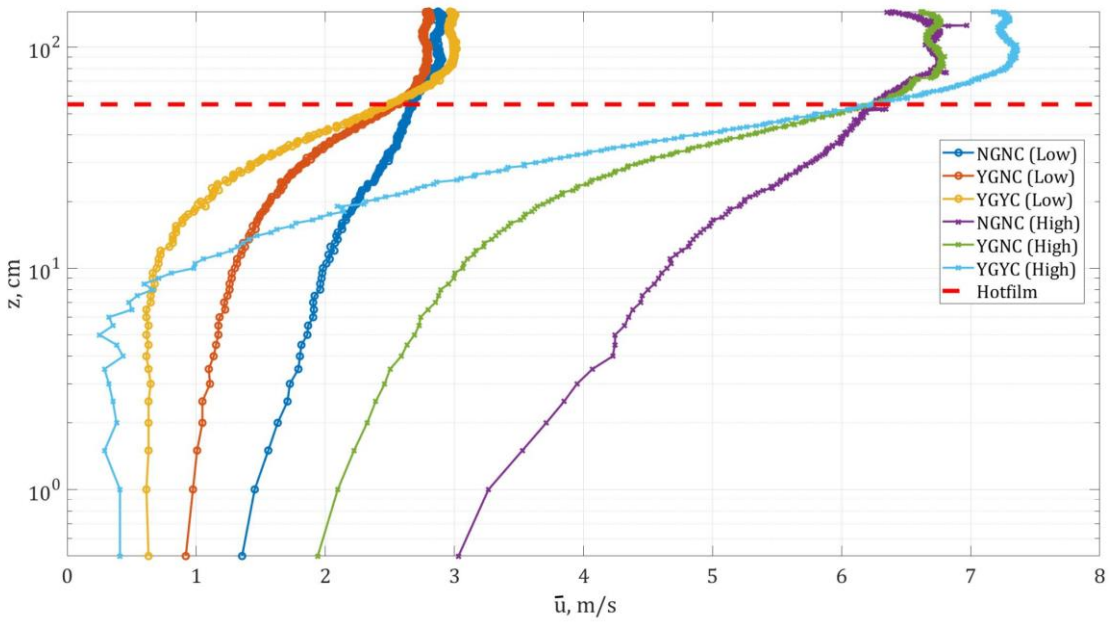

Figure 4.10 The velocity profiles of high and low blower frequencies for all three configurations examined using the combo.

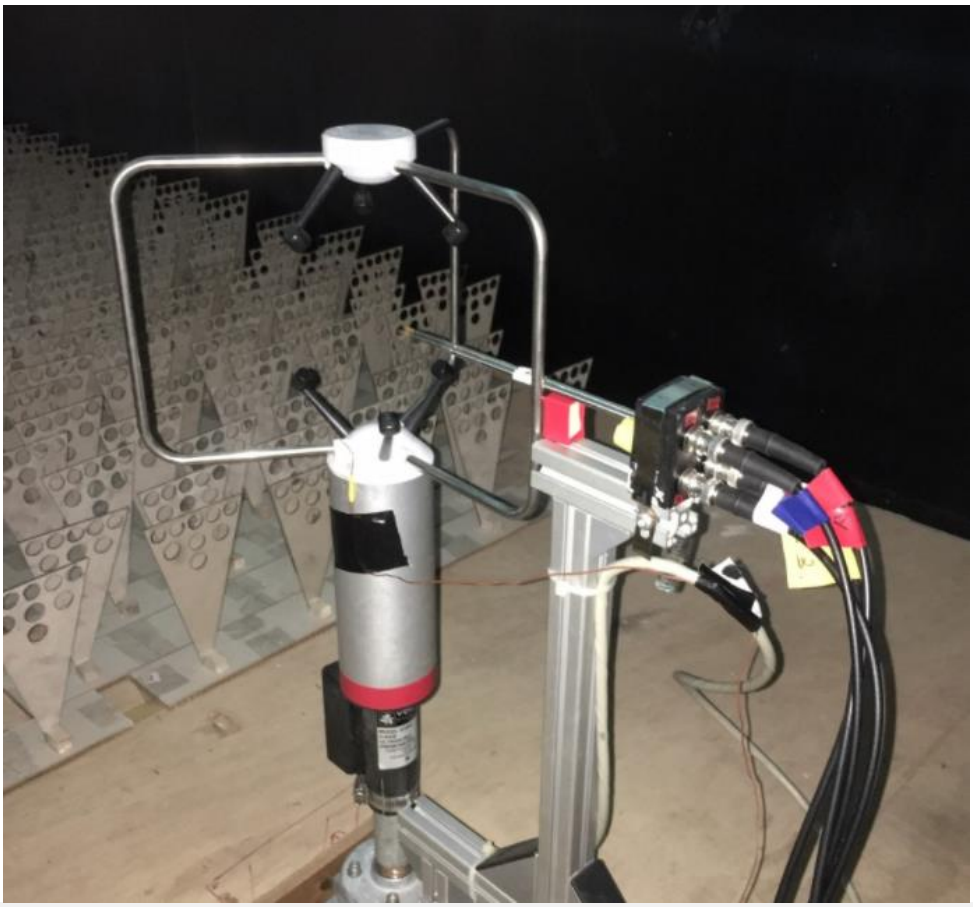

Figure 4.11 Combo 10.0 placed in the wind tunnel after the model canopy.

After examining the mean properties of the experimental configurations, the fine scale turbulent properties are considered. The hotfilm calibration was performed using an automated manipulator fabricated by Dantec Dynamics presented in Figure 4.12, which consists of a controlled jet with a pitch and yaw manipulator. The Dantec provided program for calibration was insufficient for our purposes. The manufacturer's program is designed to produce a sequence of velocities of interest and then select a velocity in the middle of the range and perform the pitch and yaw manipulations on it. Their program was also limited to only two or three wires on the probe. This means we would need to repeat the calibration several times to obtain the desired dataset for our 4-wire probe. It would include

repeating each velocity at all angles twice (once for each x-probe) which would be unreasonably time consuming and may even cause the calibration to become invalid if the environmental conditions change between the runs. The motivation of the selection of two x-probes is mostly economical and is based on [68], where two x-probes are oriented 90 degrees from each other to provide the complete 3D flow components. Each x-probe captures two components of the velocity field, and since they are oriented at a 90° (in the roll axis) relative to each other, all three components are captured. One probe provides the u, v and the other provides the u, w components. The redundant u component is eventually averaged. The use of two x-probes compensates some spatial resolution but has the benefit of better resolving the streamwise component. We, therefore, needed to write (and wrote) an in-house MATLAB® program to control the jet and manipulator to examine all angles at all velocities of interest for all four wires simultaneously, saving valuable time.

Figure 4.12 Dantec Dynamics calibrator with the two x-probe holder.

The jet-based calibration was performed twice, before and after the measurements took place inside the wind tunnel. The calibration was in the shape of a wide cone covering changes in azimuth and elevation in the range of $-45° \div +45°$ with increments of 7.5° on each axis and covered a range of velocities of $0 \div 15\ m/s$, each point was sampled at 6000 Hz and averaged over 5 seconds. As for the measurements themselves, the combo obtained data was saved in chunks of 52 seconds. The background temperature range of the calibration and flow was between $20 - 26°C$. The transfer function estimates were obtained using the lookup

table method, as it was suggested to be the most accurate up-to-date [63]. The calibrated velocities from each calibration set (before and after the measurements) were averaged to correct for drift.

The spectral shapes, turbulence intensities, and length scales are presented in Figures 4.13-4.14. The turbulence intensity, (TI), is as defined above, the horizontal length scale (L_H) is also as defined above, the Taylor length scale is defined as $\lambda = \sqrt{\overline{u^2}/\overline{\left(-\frac{1}{\bar{u}}\frac{\partial u}{\partial t}\right)^2}}$, and finally the Kolmogorov length scale $\eta = (\nu^3/\bar{\varepsilon})^{1/4}$. The u and $\bar{u}$ are the streamwise component fluctuating and mean decompositions, and $\bar{\varepsilon}$ is the turbulent kinetic energy dissipation rate, as defined in Equation (5.3) (next chapter). The spectral shapes and length scales presented below confirm that the BL behavior was well captured, the probe size selection was sufficient, and that the measurements were conducted properly. The spectra present the three expected energy cascade ranges: the energy containing range, the inertial subrange ($-5/3$ slope), and the dissipation range. Flattening out of the spectral shapes indicated that the signal to noise is very low at the specific frequency. It suggests that that there are either no more turbulent fluctuations or that the probe is not sensitive enough at that range. The flattening is observed at different frequencies, ranging from $500\ Hz - 3000\ Hz$, depending on the flow regime and mean velocity. For example, the YGYC at the high blower frequency presents the dissipation range from $2000 - 3000\ Hz$, meaning that an increase in the sampling frequency should be considered. All of this suggests that the overheat ratio of 1.7 is sufficient, the sampling frequency of $6000\ Hz$ should be increased to capture the entire dissipation rage, and the compensation of the spatial resolution due to the use of two independent x-probes together did not affect the measurements.

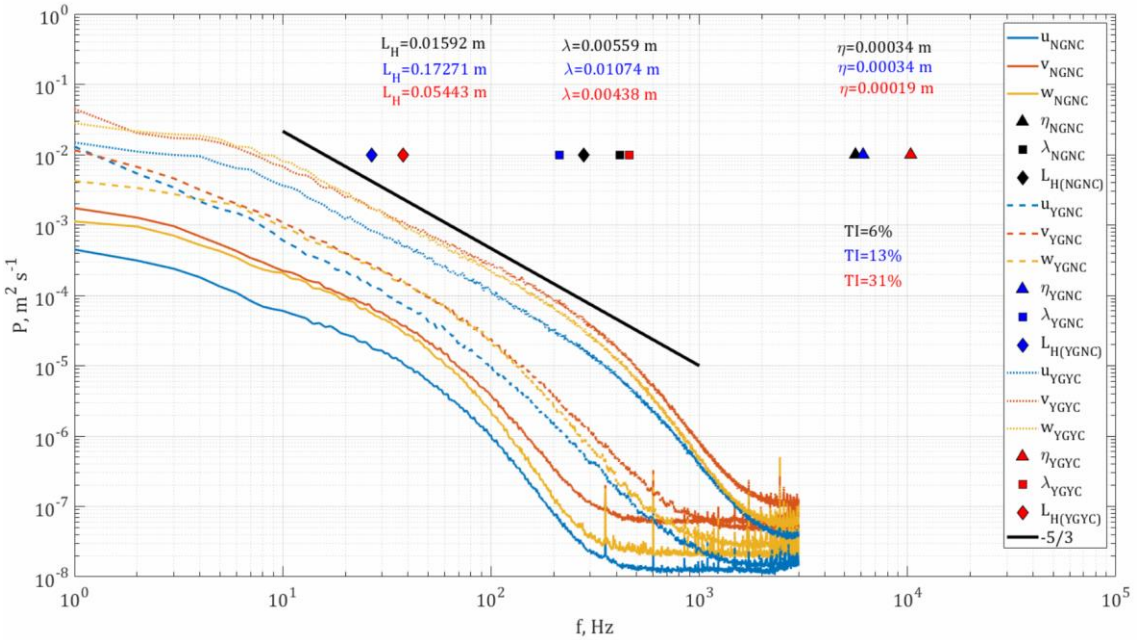

Figure 4.13 The power density spectral shapes of velocity fluctuations with the *low* blower frequency examined. The results presented here provide the three experimental setups of YGYC, YGNC, and NGNC. The turbulence intensity, horizontal length scale, Taylor length scale, ad Kolmogorov length scale are presented for each of the experimental configurations as well.

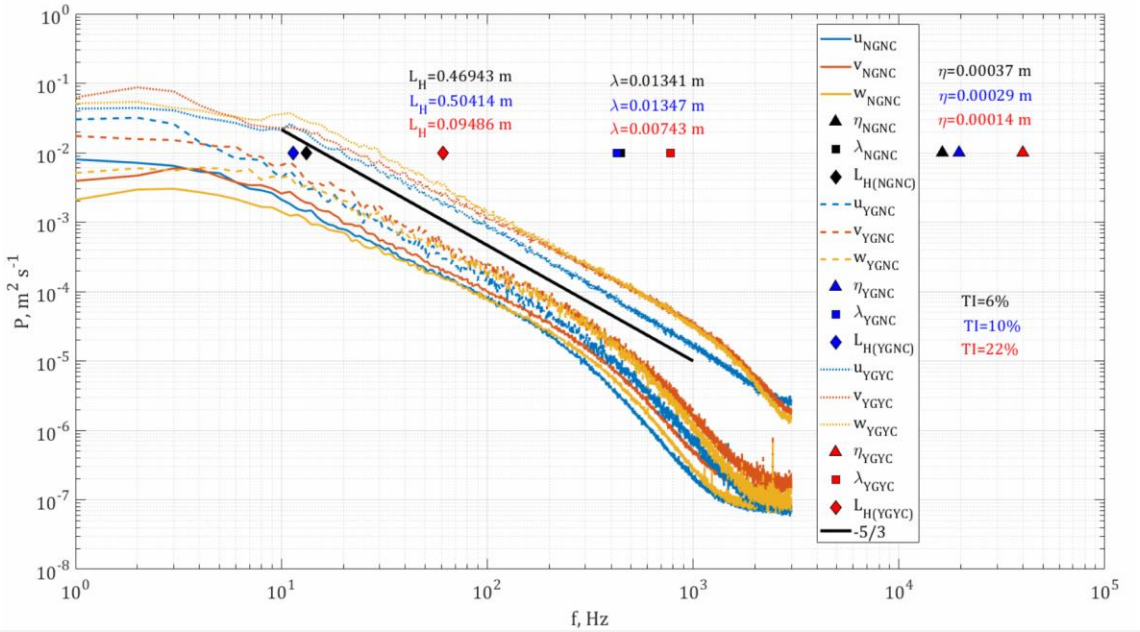

Figure 4.14 The power density spectral shapes of velocity fluctuations with the *high* blower frequency examined. The results presented here provide the three experimental setups of YGYC, YGNC, and NGNC. The turbulence intensity, horizontal length scale, Taylor length scale, ad Kolmogorov length scale are presented for each of the experimental configurations as well.

As the flow becomes more complex the dissipation range continues to higher frequencies, or smaller scales continue to coherently exist in the flow and are not dissipated by viscosity. The black $-5/3$ line is drawn in the same place of both Figures above, indicating the fluctuations are also intensified with the increased flow complexity. The length scales of both flow regimes without the model canopy appear to exhibit similar length scales, yet when the canopy is introduced the length scales appear smaller. As expected, the Taylor length scales appear to exist in the inertial subrange. The Kolmogorov length scales are the largest scales in which the viscous dissipation dominates the turbulent kinetic energy and converts the energy into heat. It appears that as the flow becomes more complex, the turbulent fluctuations sustain their coherence down to smaller scales, similar to the observations on the spectra.

4.2.2 Automated procedure: laboratory testing

The Combo 10.0 described earlier in the chapter was developed to increase the range of measuring capability to complete the 360° turn. The new design also makes the combo more rigid and provides more consistency in the measurements—accomplished by fixating the hotwire probes in the sonic control volume. This section will detail the next achieved advancement related to the combo (or to hotwire field measurements): the automated calibration procedure of the combo. This section details the calibration procedure performance by comparison with the "classical" calibration procedure using a jet and a mechanical pitch-and-yaw manipulator. To correct for drift in the measurements, we performed the calibration twice; we have a pre-measurement and post-measurement calibration sets that are

used to construct two independent transfer function estimates. The outputs from these two are eventually averaged to reduce the drift error.

The two most used methods for estimating the velocity-voltage transfer function are the lookup table method and the polynomial fit method. According to Van Dijk (2004) [63] the most trustworthy estimation method is the lookup table because it does not oversimplify (or underfit) the transfer function. Historically, it was not preferred because it was time consuming for computation, but modern computers computational power makes this method much simpler to implement, i.e. using the *griddedinterpolant* MATLAB® function [69]. We use the lookup table as the ground truth (GT) reference and compare our findings with it.

We defined the GT here similarly to the results from the previous section: using the lookup table method and averaging the derived time series from the two sets of calibrations (pre-measurement and post-measurement calibration). This GT set is also referred to as $TJ3$; the T stands for Table, J stands for Jet, and the 3 stands for the three velocity components obtained using a single model/function. The velocities here were composed of averaging four sub-probes from the 4-wire hotfilm set [63, 68, 69]:

$$uvw_{sub1} = f\left(E_{1,1}, E_{1,2}, E_{2,1}\right) \tag{4.1}$$

$$uvw_{sub2} = f\left(E_{1,1}, E_{1,2}, E_{2,2}\right) \tag{4.2}$$

$$uvw_{sub3} = f\left(E_{2,1}, E_{2,2}, E_{1,1}\right) \tag{4.3}$$

$$uvw_{sub4} = f\left(E_{2,1}, E_{2,2}, E_{1,2}\right) \tag{4.4}$$

and finally,

$$uvw = \frac{\left(uvw_{sub1} + uvw_{sub2} + uvw_{sub3} + uvw_{sub4}\right)}{4} . \tag{4.5}$$

Two studies [63, 68] showed an alternative approach of averaging two sub probes that were defined a bit differently, yet neither was shown to be superior to the other. They defined them as the two x-probes they are, $uw_{sub1} = f(E_{1,1}, E_{1,2})$ and $uv_{sub2} = f(E_{2,1}, E_{2,2})$, and averaging only the u component of the sub probes. In the text, we refer to this method as TJ_2; the T stands for Table, J stands for Jet, and the 2 stands for the two velocity components obtained using a single model/function. Since the lookup table interpolates between known values and does not use a fitting method such as least square polynomial fitting, error minimization/elimination is only achievable by averaging as many results as possible. This is the reason that we selected TJ_3 to be the GT reference, it would most likely reduce possible noise.

The other classical method commonly used for hotwire calibration is the polynomial fitting using the least-squares method. This is based on King's Law that relates the heat transfer coefficient to the fluid velocity using a polynomial approximation whose coefficients are obtained using calibration. Van Dijk (2004) [63] has shown that this approximation is too simple to represent the heat transfer coefficient relationship to velocity, and suggested for future (and past) studies to consider only the lookup table method. When we attempted to examine this claim using our wide attacking angle calibration sets, we noticed that using 1000 different initial guesses for the least squares fit numerical algorithm provided 1000 different solutions. This most likely means that the fit converges to a local minimum with each guess. We even calculated the self-reconstruction errors of more than 100,000 solutions and found that a global minimum can be reached. The computational costs, however, are tremendously high making it an inefficient approach. In this chapter we refer to this method as $PJ3$, where the P stands for polynomial fit, J stands

for Jet, and the 3 stands for the three velocity components obtained using a single model/function.

Artificial neural networks (NN) have also successfully been used for complex function approximations. Several studies have shown that regression NN are capable of capturing the velocity voltage relationship estimates strikingly well in hotwire anemometry [12, 57, 58, 68, 70]. In these studies, the training set used for each model was based on delicately selected minutes that contained mean velocities that covered the entire range of interest and high rms values of velocity fluctuations. Elimination of this manual selection procedure will fully automate the in-situ NN based calibration of combo data and enable the fine scale measurements to be obtained in the field independently of human decision. Instead, we suggest using all low-pass filtered data points within an hour (or duration with constant ambient properties) as the training set.

Table 4-2 presents all transfer function estimate methods we have examined. More specifically, the last three methods are NN based methods and they include the SH_3 which stands for shallow NN (2 layers) with 100 hidden neurons and handpicked training set. The selection of the training set was conducted separately for each flow type (NGNC, YGNC, and YGYC), allowing a separate model to be trained. The second shallow NN method we examine is the SA_3which stands for a shallow NN (2 layers) with 100 hidden neurons and an automated training set using all data points. This is an extreme case because three different flow types are examined together and constructed using the same model. Finally, the third NN model type we examine is a deep NN model named DA_3. This model has 15 layers of 100 hidden neurons each and the training set is also selected using all data points from all three flow types. Selection of 15 layers was dictated by the memory limits of the used PC.

Table 4-2 Examined calibration approaches. The boxed cell is the selected setup that was used as the ground truth.

Method name		Inputs	Outputs	Jet	In-situ
Lookup table		$E_{1,1}\ E_{1,2}\ E_{2,1}\ E_{2,2}$	u, v, w	TJ_3	TI_3
		$E_{1,1}\ E_{1,2}$ $E_{2,1}\ E_{2,2}$	u, w u, v	TJ_2	TI_2
Polynomial curve fitting		$E_{1,1}\ E_{1,2}\ E_{2,1}\ E_{2,2}$	u, v, w	PJ_3	-
Shallow Neural Network	Handpicked training set	$E_{1,1}\ E_{1,2}\ E_{2,1}\ E_{2,2}$	u, v, w	-	SH_3
	all data for training set (automated)	$E_{1,1}\ E_{1,2}\ E_{2,1}\ E_{2,2}$	u, v, w	-	SA_3
Deep Neural Network	all data for training set (automated)	$E_{1,1}\ E_{1,2}\ E_{2,1}\ E_{2,2}$	u, v, w	-	DA_3

Our initial suggestion for automation of the in-situ NN based training is in increasing the training set size by using all low pass filtered data. The motivation is to have the best possible representation of the "unseen" high frequency data in the data set itself. Figure 4.15 presents an example [66] of why an increase in the training set size can sometimes not be sufficient to obtain the desired performance and an increase in the complexity of the network should be considered as well. This is also known as the bias vs variance tradeoff in AI. The two most common sources of possible errors in NN training are bias and variance [66] as seen in Figure 4.16. The variance (associated with overfitting) of a trained NN is how much worse the model performs on unseen data than it did on the training set. If the variance is high, it is

commonly helpful to increase the training set size. Bias (associated with underfitting) is the embedded error in the training set and is broken down to avoidable and unavoidable bias. An example of unavoidable bias is the sonic measurement limitation, while an example of avoidable bias is a simplified model to represent a complex relationship, Kings law in our case. The avoidable bias can be eliminated by increasing the size of the model (i.e. adding more neurons and layers). Theoretically, when the bias is small, but the variance is large, adding more training data will probably help close the gap between test set error and training set error. Eventually we increased both the training set size and the model complexity, and we show the effect of each of the steps.

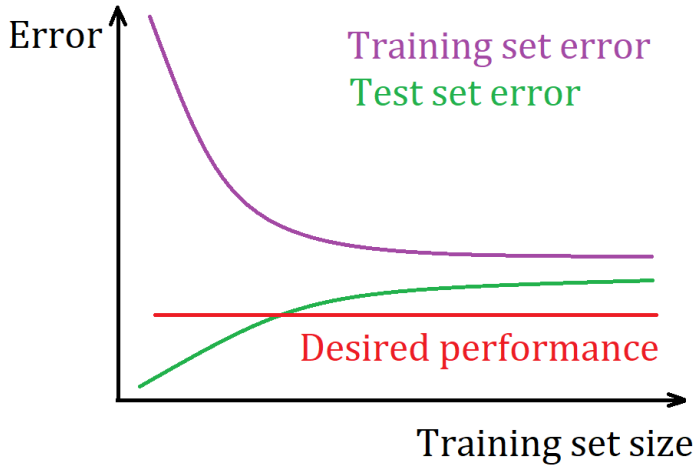

Figure 4.15 Example error diagnosis of training a NN model with respect to training set size [66]. An increase in the size of the training set will not necessarily provide the desired performance.

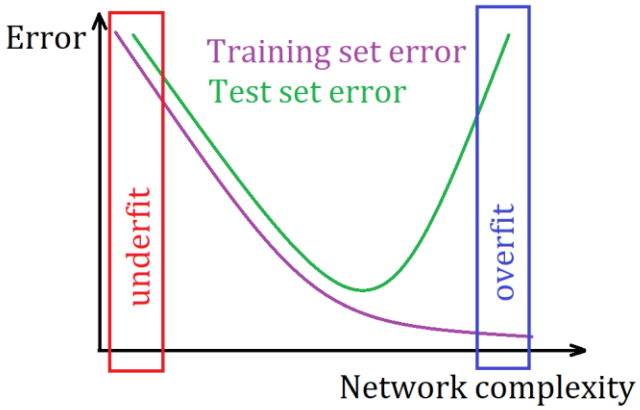

Figure 4.16 Error diagnosis example of bias vs variance in training a NN model. The underfitting or overfitting (bias vs variance) of a model can be modified based on the network complexity.

We did not perform a complete learning curve analysis on this set because it would not be useful to implement across different flows when attempting to automate the calibration procedure. The other reason is that we do not have a real ground truth for reference and our training set has an embedded unavoidable error in it. What do we mean by a real ground truth? Say we were attempting to train a model to identify cats in images, the training set for such a model can be developed by humans and would have an expected error that is almost zero. Here, we have the sonic data as a training set, while sonic sensed velocity field are of finite accuracy, set by the manufacturer calibration correcting for the presence of struts and the use of sophisticated electronics to resolve the acoustic signal Doppler effect measurements. Moreover, the sonic provides spatially averaged measurements, depending on their acoustic signal fly path length, in the case of the used here wind tunnel measurements the ratio of the sonic acoustic fly path to the BL height is about 20%. While in the field it would be at least 1-2 orders of magnitude smaller. In the case of the used here wind tunnel measurements, the sonic data originated bias is particularly significant, because the ratio of height of the sonic acoustic fly path to

the BL height is about 20% and in the field it would be at least 1-2 orders of magnitude smaller.

To eliminate avoidable errors, we train 10 separate NN models with similar hyperparameters and average their results—this is true for all NN results we discuss in this study. The only difference between the 10 NN models is the random selection of the training/testing/validation data points from the training set. Since the main goal here was the automation of the NN training procedure, we performed some trial and error analysis using various hyperparameters, based on machine learning theory [66], and also examined the impact of increasing the network complexity. When we examined the outputs of the 10 separately trained NN we noticed that the large scales velocity fluctuations were captured somewhat differently in each network. This was observed before [68] and a correction was suggested using the large scales from the sonic. This difference is exhibited as a constant shift of the power density spectrum of velocity fluctuations, although the shape remains the same. When averaging the 10 NN together, it was noticed that the deviation of the large scales from those provided by the sonic became smaller. It was suggested that the final averaged time-series should be shifted to correspond with the trusted large scales of the sonic.

The inconsistency between the 10 NN raised a question of whether this might possibly be an avoidable bias that we can correct for. After noticing that the polynomial fits using various initial guesses converged to various solutions (probably reaching of local minima), we suspected that the NN might be doing the same thing. An attempt to tackle this was made using the training of a deep NN. It is suggested [71] that deep NN are highly unlikely to have local minima, instead saddle points are more expected and the global minimum is more susceptible to be

found when a solution is reached. Indeed, after training the deep NN the variety of large scales between the solutions was avoided. This might point to the fact that the shallow NN was too simple to represent the complex transfer function of hotfilm sensor.

The rest of the section discusses quantification of each calibration method results in comparison with the set ground truth (lookup table). We examine the various calibration methods performance in terms of comparing the small scales, the large scales, and turbulence statistics. We also raise a question of whether the hotfilm can capture the large scales more accurately than the sonic. If so, the correction that was previously suggested [68] might no longer be necessary.

The first step is a visual observation of the power density spectra of minutes that were measured under the same flow characteristics. After the flow was stabilized in the NGNC and YGYC regimes, we took all minutes at the highest blower frequency and compared their spectral shapes. Figures 4.17-4.18 present the streamwise (u) component of velocity fluctuations of the NGNC and YGYC flow regimes at the highest blower frequency. The same minutes were calibrated using the two different procedures, TJ_3 and DA_3, and because they represent the same flow, the spectral shapes for all of these minutes should be the same. The spectral calculation was computed using one second windows, resulting in 1 Hz spectral resolution. Each curve represents a different minute and all minutes represent identical flow conditions. The colors of the curves indicate different transfer function approximation procedures. Three interesting things can be observed here. The first is that both spectral shapes obtained using the two calibration methods exhibit a similar shape—a sanity check. Next, it appears that the spectral shapes computed using both approximation methods have the same range of variation between the

minutes. If anything, it seems as though the DA_3 model results resemble each other slightly more than TJ_3. More specifically the larger scales of the DA_3 expand over a smaller range than the TJ_3, and the same is true for the small scales. Finally, the larger scales of the sonic are approximately in the same range as both methods.

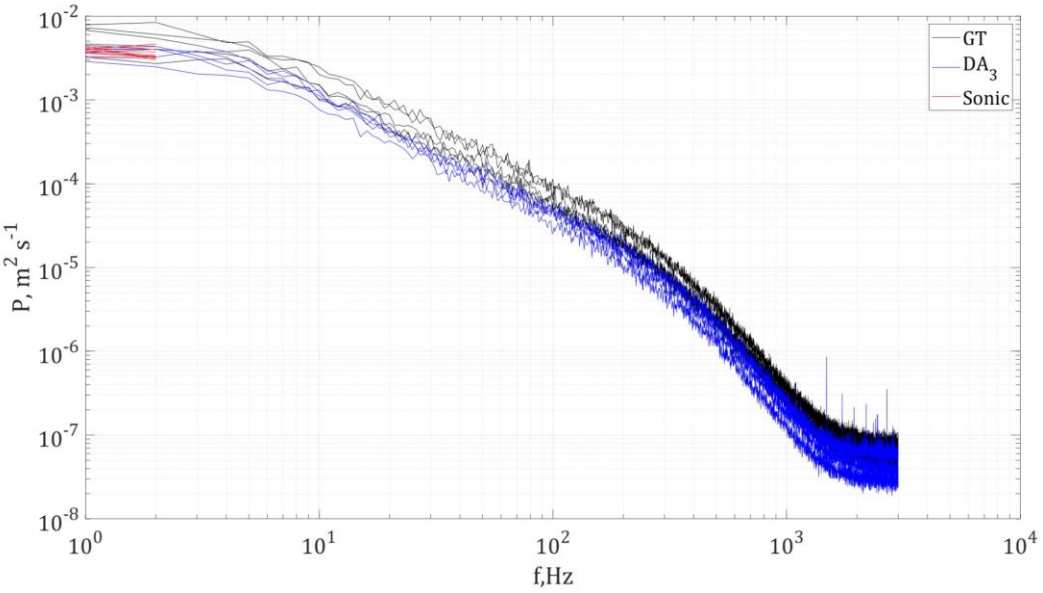

Figure 4.17 The streamwise component of five minutes recording a similar flow regime—NGNC—at the highest blower frequency. Each curve represents a different minute, while all minutes represent identical flow conditions. The black curves represent the spectral shapes approximated using the calibrator and the lookup

table method, TJ_3. The blue curves represent the spectral shapes approximated using the sonic and the deep NN method, DA_3. The red lines represent the trusted frequency of the sonic output.

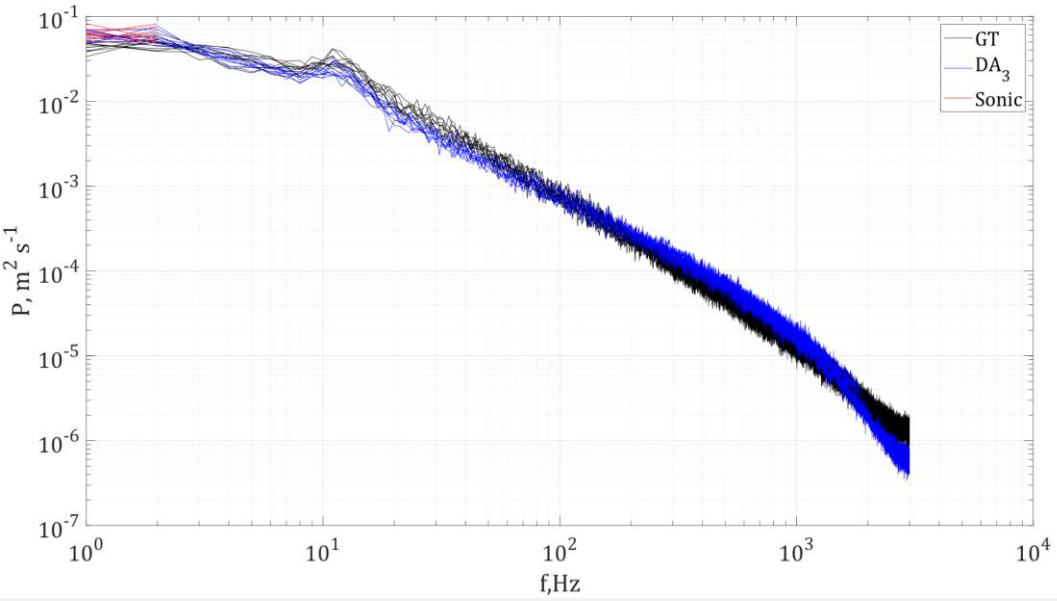

Figure 4.18 The streamwise component of five minutes recording a similar flow regime—YGYC—at the highest blower frequency. Each curve represents a different minute, while all minutes represent identical flow conditions. The black curves represent the spectral shapes approximated using the calibrator and the lookup table method, TJ_3. The blue curves represent the spectral shapes approximated using the sonic and the deep NN method, DA_3. The red lines represent the trusted frequency of the sonic output.

To compare the results using all the different transfer function approximation methods more accurately, an average of all minutes of the similar flow regimes of the highest blower frequency were taken. These are presented separately for each velocity component. Figures 4.18-4.21 represent the streamwise (u) component at the highest blower frequency of the three examined flow regimes, NGNC, YGNC, and YGYC respectively. Figures 4.22-4.24 represent the longitudinal (v) component of the three flow regimes, and 4.25-4.27 represent the transverse (w) component. There seems to be some variation between the two types of lookup table approximation procedures GT and TJ_2. The small scales of the in-situ calibrated lookup table method (TI_2, TI_3) and the jet calibrated polynomial seem to suffer from excessive noise, consistently appearing more elevated than the GT and neural network counterparts. The DA_3 might have been able to capture the dissipation

range in the range of $2000 - 3000\ Hz$, where the GT method seems to have captured noise because it flattens horizontally on the high frequencies (see Figure 4.21 and Figure 4.24).

Finally, the large scales of the sonic relative to the different methods are examined quantitatively. The blue $-5/3$ curve is placed on the same location in all figures to help see the increase in intensity fluctuations between the types of flows. The fact that the there is a significant change in the average intensities between the flows indicates that the hotwires can differentiate between the different flows examined using *all* calibration procedures. In practice, this is the key/critical point that is sought for in the experiments. The aim is to capture the absolute quantities as best as possible, but even more important are the changes between different flows and the ability to differentiate between different flow regimes and turbulent characteristics.

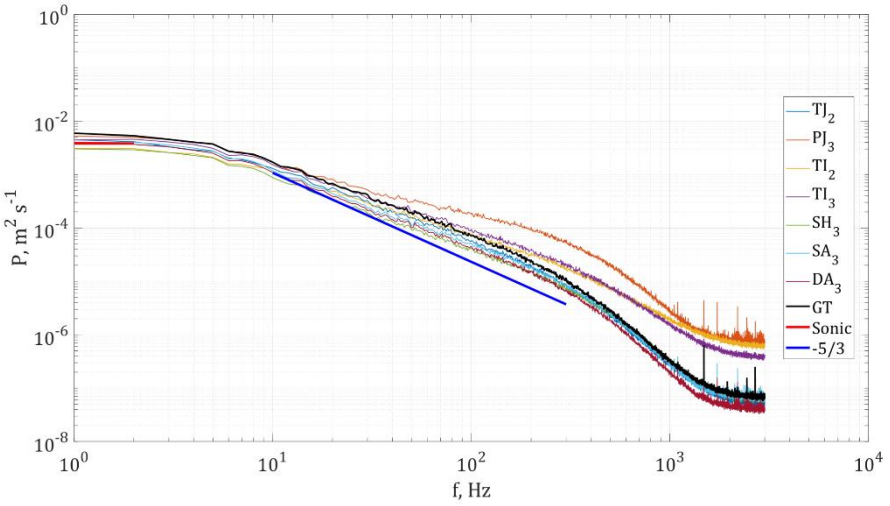

Figure 4.19 Average spectral shapes approximated for the streamwise (u) component of all data obtained at the highest blower frequency of the NGNC flow regime.

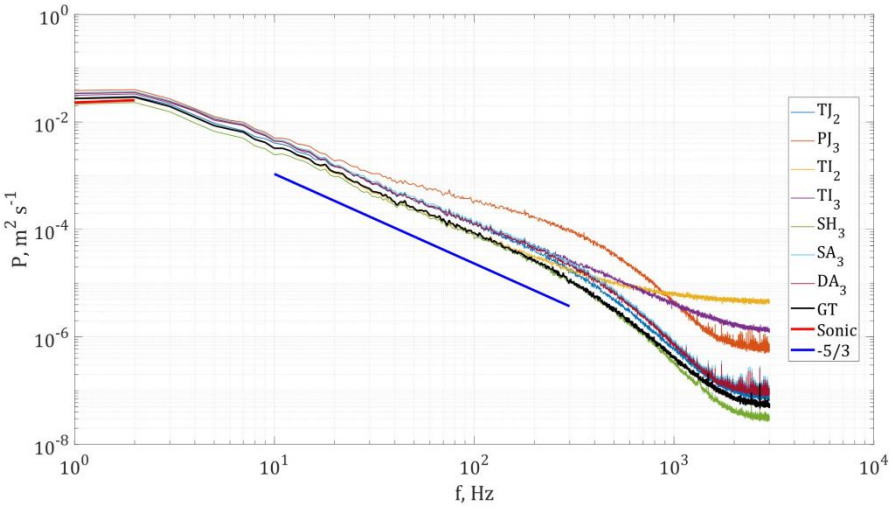

Figure 4.20 Average spectral shapes approximated for the streamwise (u) component of all data obtained at the highest blower frequency of the YGNC flow regime.

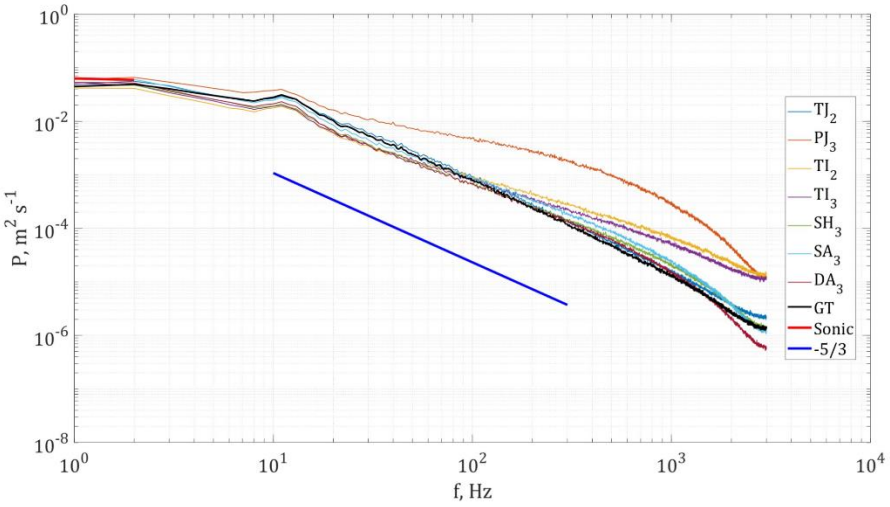

Figure 4.21 Average spectral shapes approximated for the streamwise (u) component of all data obtained at the highest blower frequency of the YGYC flow regime.

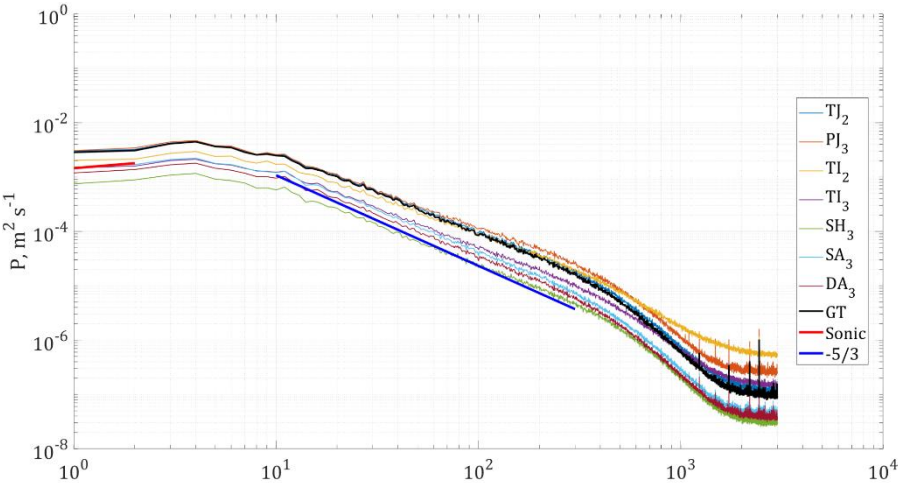

Figure 4.22 Average spectral shapes approximated for the longitudinal (v) component of all data obtained at the highest blower frequency of the NGNC flow regime.

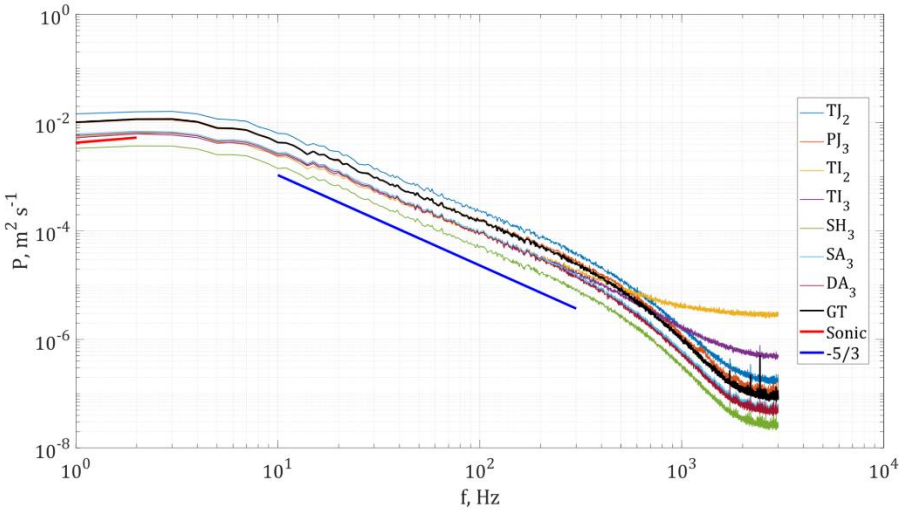

Figure 4.23 Average spectral shapes approximated for the longitudinal (v) component of all data obtained at the highest blower frequency of the YGNC flow regime.

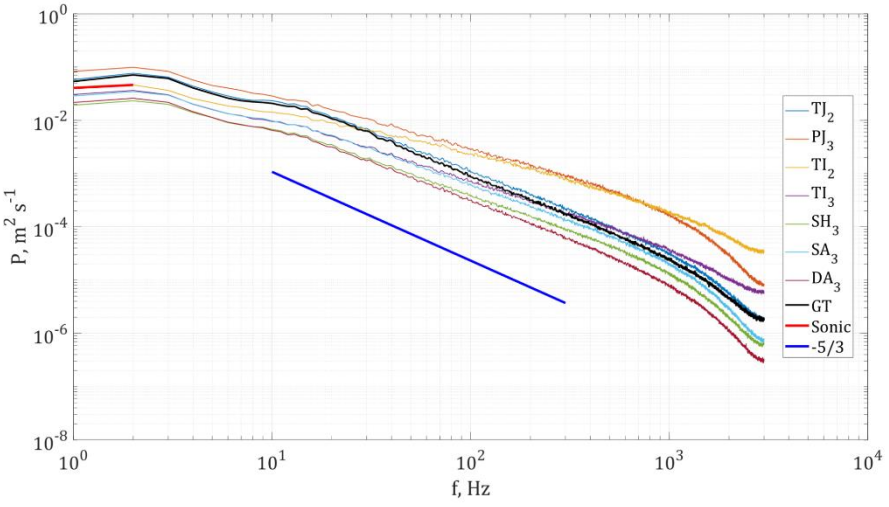

Figure 4.24 Average spectral shapes approximated for the longitudinal (v) component of all data obtained at the highest blower frequency of the YGYC flow regime.

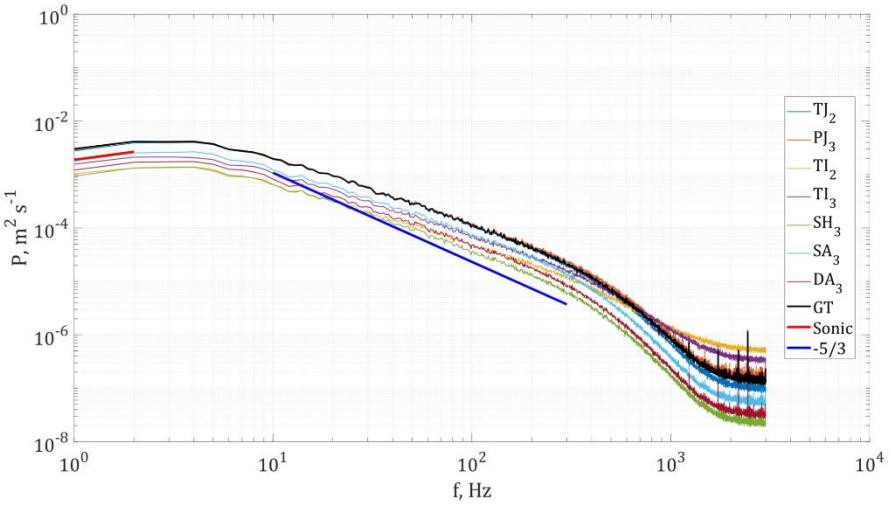

Figure 4.25 Average spectral shapes approximated for the transverse (w) component of all data obtained at the highest blower frequency of the NGNC flow regime.

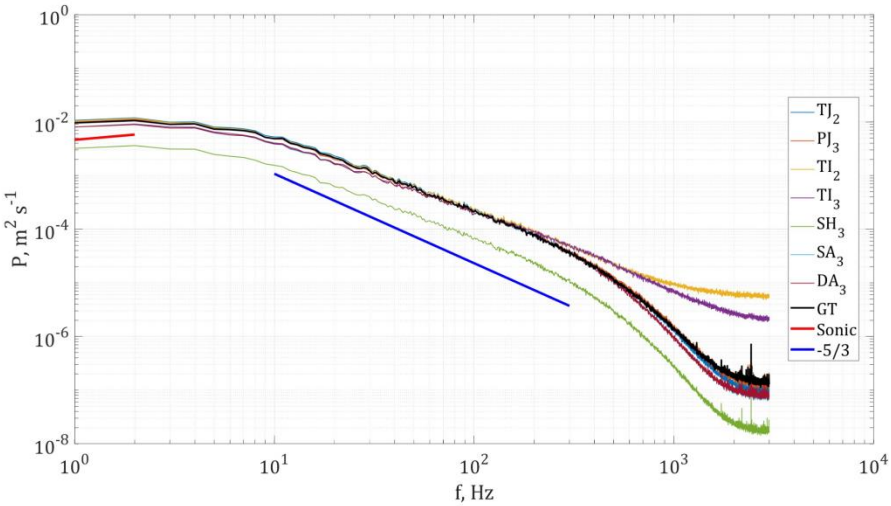

Figure 4.26 Average spectral shapes approximated for the transverse (w) component of all data obtained at the highest blower frequency of the YGNC flow regime.

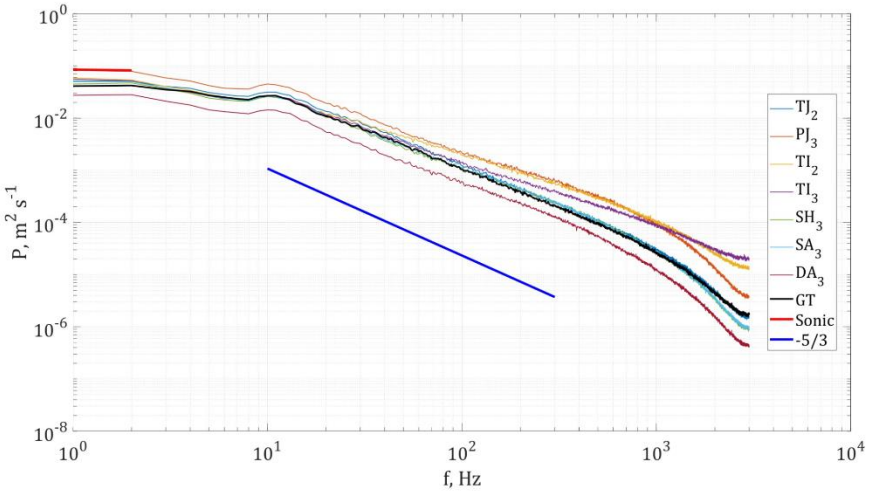

Figure 4.27 Average spectral shapes approximated for the transverse (w) component of all data obtained at the highest blower frequency of the YGYC flow regime.

The next step of the calibration methods comparison analysis is to quantify the small scales in a similar manner to the previous studies [10, 68]. Which will be followed by similar comparison of the large scales and turbulence statistics. The average delta error is defined as the average of all deltas derived from each of the three velocity components,

$$\bar{\delta} = \frac{\delta_u + \delta_v + \delta_w}{3} \,. \tag{4.6}$$

The delta error is defined as the normalized to the rms and therefore non-dimensional error parameter [10, 68], defined for each velocity component separately

$$\delta_u = rms(\tilde{u} - \tilde{u}_{GT}) \,, \tag{4.7}$$

$$\delta_v = rms(\tilde{v} - \tilde{v}_{GT}) \,, \tag{4.8}$$

$$\delta_u = rms(\tilde{w} - \tilde{w}_{GT}) \,. \tag{4.9}$$

The tilde hat is a normalization procedure for any property ψ. In this case it will be the velocity component fluctuations (u, v, w) of the streamwise, longitudinal, and transverse directions, respectively. The GT refers to the ground truth, and the normalization is defined as

$$\tilde{\psi} = \frac{\psi}{rms(\psi)} \,. \tag{4.10}$$

The average delta error values are compared in Figure 4.28 for all methods as a function of the mean streamwise velocity. The mean delta error when comparing the two lookup table methods with the jet (TJ_2 vs GT) is indeed the smallest, as expected; reminder: GT was selected to be TJ_3. It is noticeable that the delta error generally decreases with an increase in the mean velocity except for the sonic dependent

approximation methods that do not have a noise reduction procedure, especially TI_2 and TI_3.

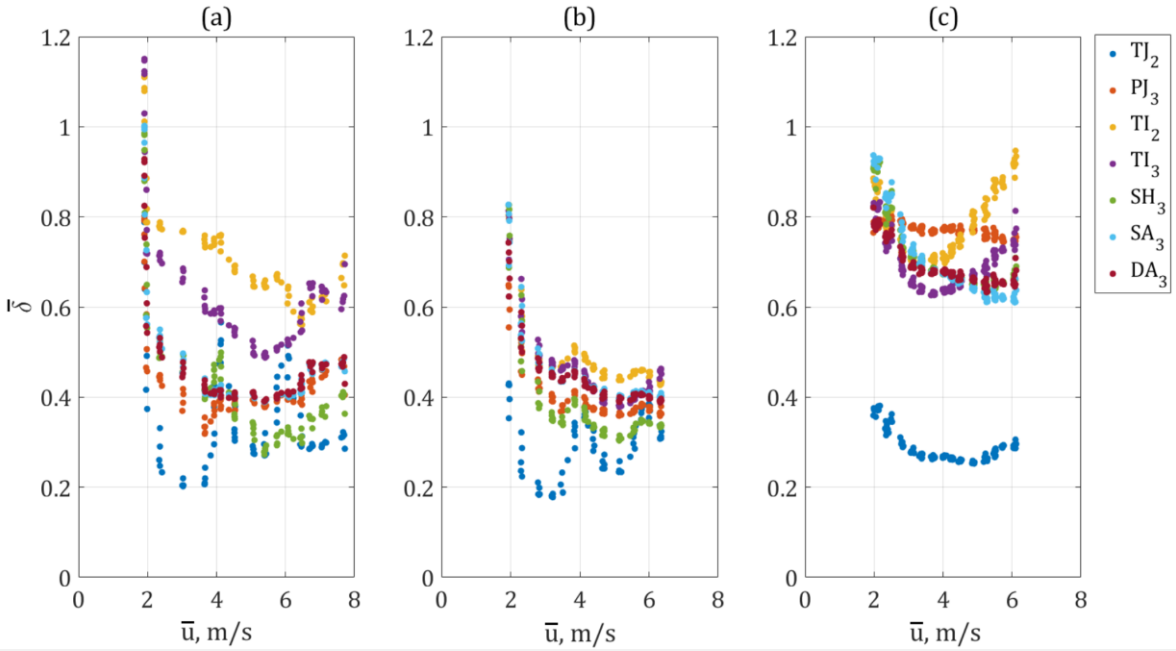

Figure 4.28 Average delta error for all calibration procedures examined here as a function of the mean streamwise velocity. These delta errors are all with respect to the previously decided ground truth TJ_3. These are broken down by the flow regime examined (a) NGNC, (b) YGNC, and (c) YGYC.

The delta error components are also presented separately for each flow regime and for each calibration procedure separately in Figures 4.29-4.35. The in-situ NN calibration delta errors show a decrease with an increase in mean velocity, as expected because the sonic performs better when the velocity is higher, unless small scale noise (e.g. TI_2, TI_3) is dominant.

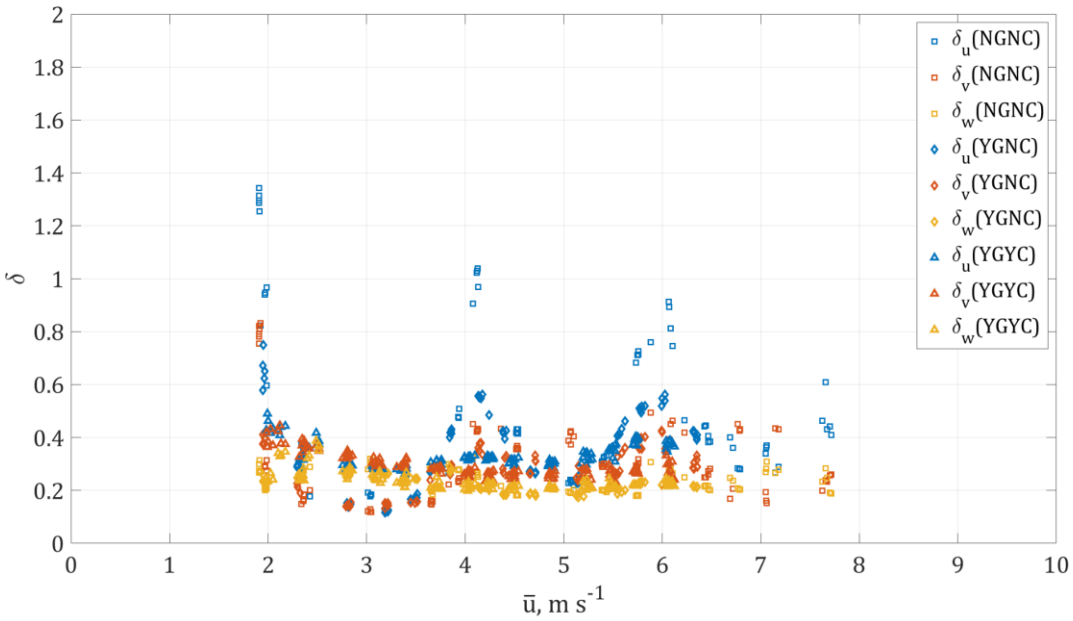

Figure 4.29 Delta error analysis with respect to the mean streamwise velocity component for the TJ_2 calibration procedure. The blue, orange, and yellow represent δ_u , δ_v , δ_w components, respectively. The shapes represent the flow regime examined: squares, diamonds, and triangles represent NGNC, YGNC, and YGYC, respectively.

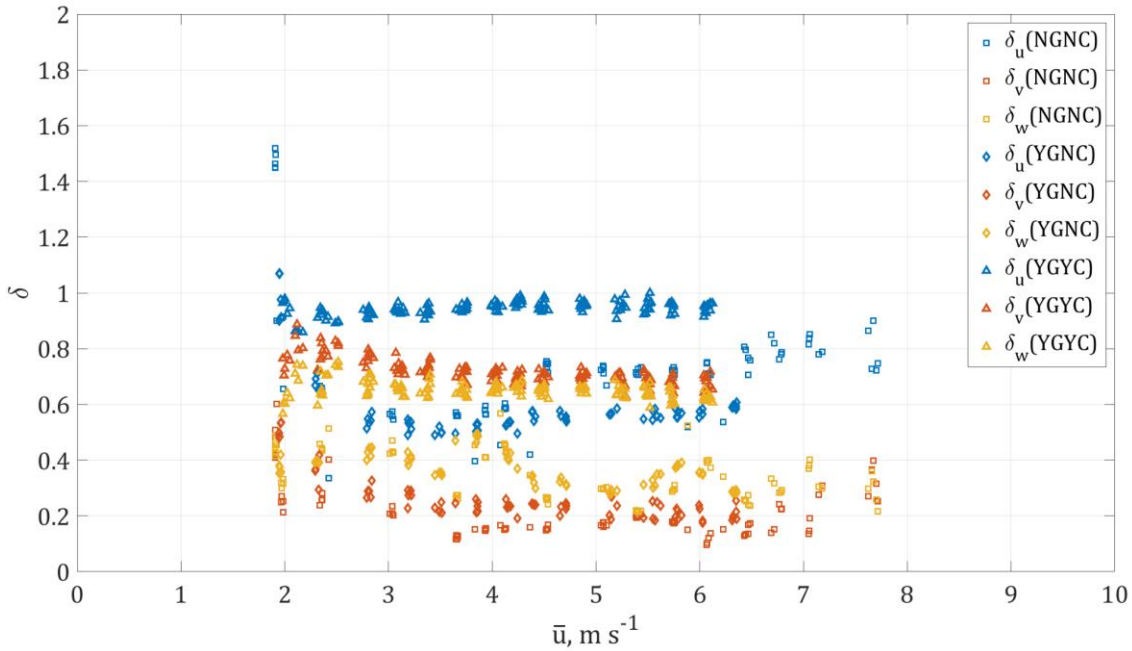

Figure 4.30 Delta error analysis with respect to the mean streamwise velocity component for the PJ_3 calibration procedure. The blue, orange, and yellow represent δ_u , δ_v , δ_w components, respectively. The shapes represent the flow regime examined: squares, diamonds, and triangles represent NGNC, YGNC, and YGYC, respectively.

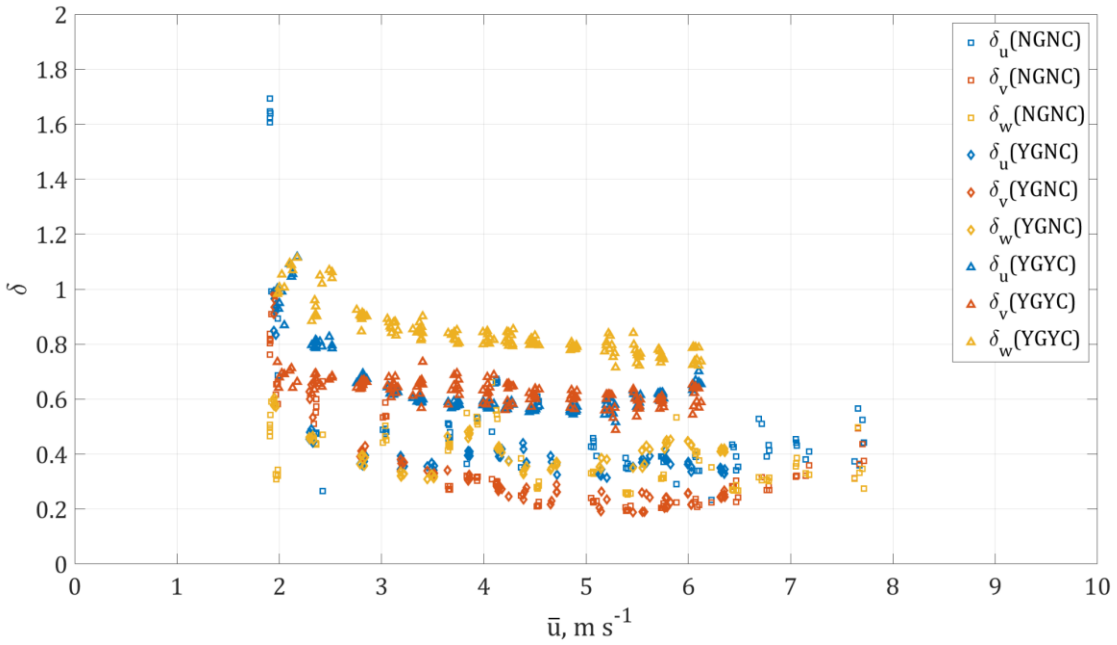

Figure 4.31 Delta error analysis with respect to the mean streamwise velocity component for the SH_3 calibration procedure. The blue, orange, and yellow represent δ_u , δ_v , δ_w components, respectively. The shapes represent the flow regime examined: squares, diamonds, and triangles represent NGNC, YGNC, and YGYC, respectively.

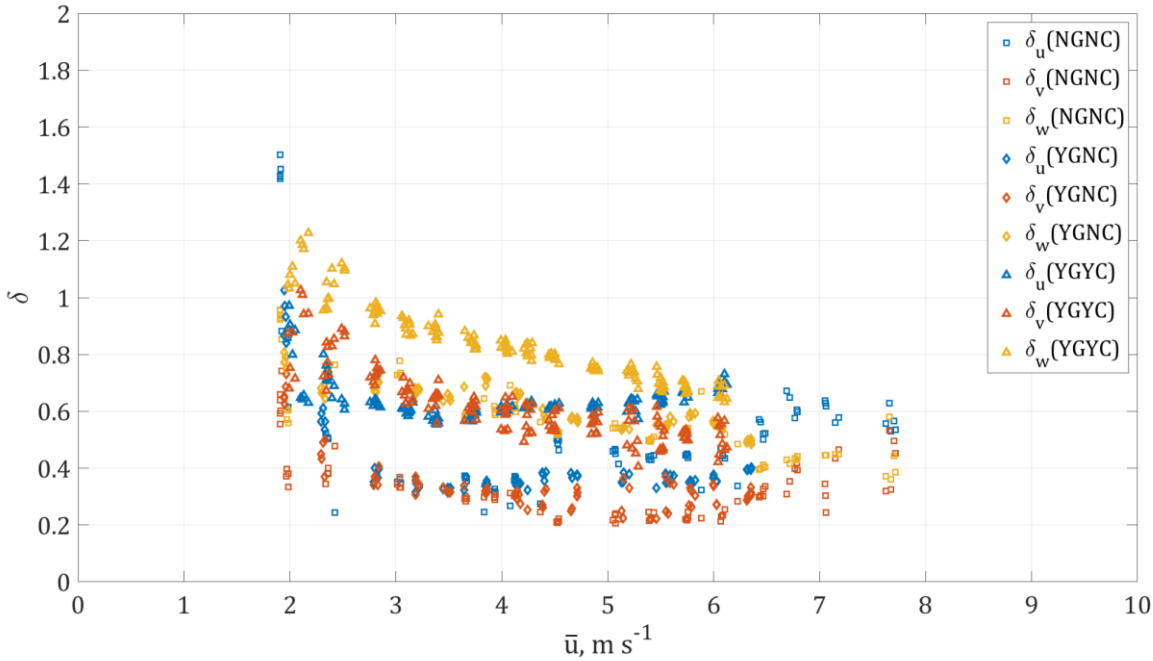

Figure 4.32 Delta error analysis with respect to the mean streamwise velocity component for the SA_3 calibration procedure. The blue, orange, and yellow represent δ_u , δ_v , δ_w components, respectively. The shapes represent the flow regime examined: squares, diamonds, and triangles represent NGNC, YGNC, and YGYC, respectively.

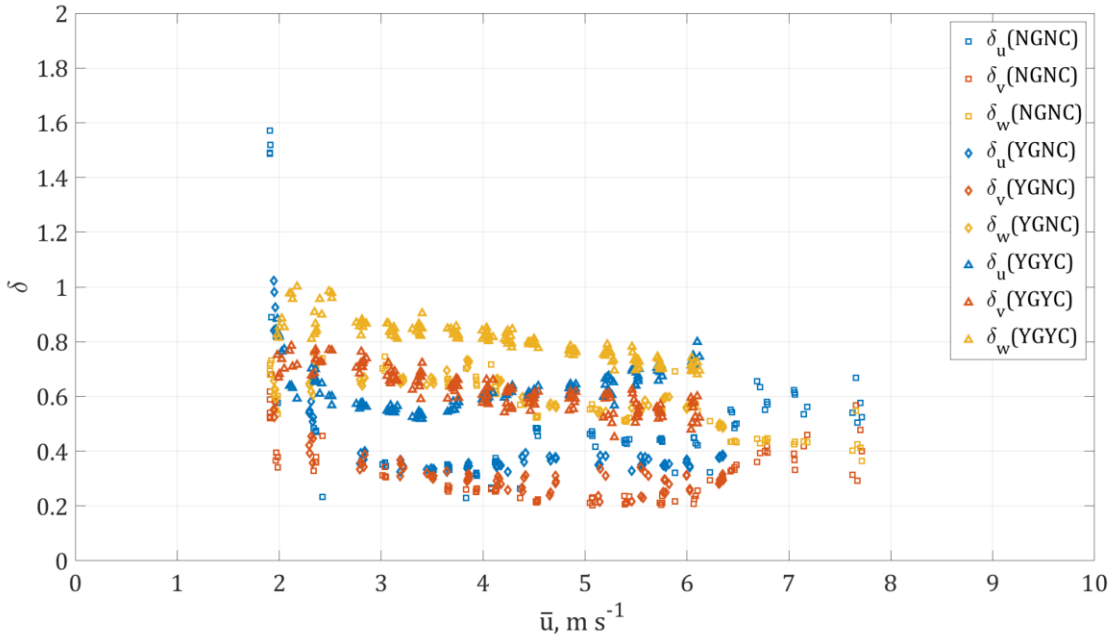

Figure 4.33 Delta error analysis with respect to the mean streamwise velocity component for the DA_3 calibration procedure. The blue, orange, and yellow represent δ_u , δ_v , δ_w components, respectively. The shapes represent the flow regime examined: squares, diamonds, and triangles represent NGNC, YGNC, and YGYC, respectively.

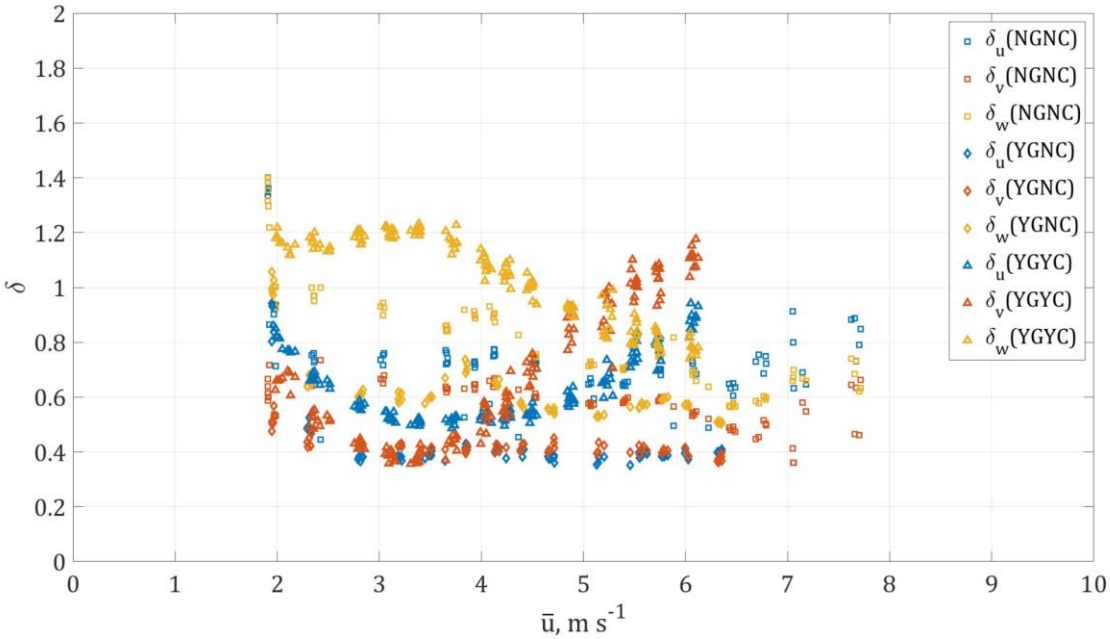

Figure 4.34 Delta error analysis with respect to the mean streamwise velocity component for the TI_2 calibration procedure. The blue, orange, and yellow represent δ_u , δ_v , δ_w components, respectively. The shapes represent the flow regime examined: squares, diamonds, and triangles represent NGNC, YGNC, and YGYC, respectively.

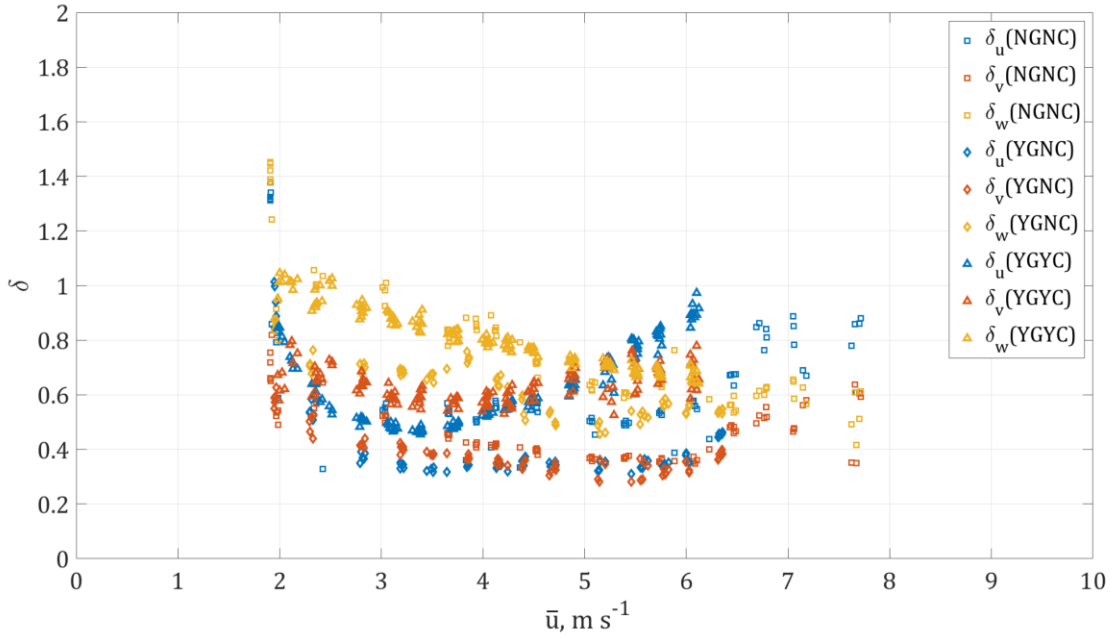

Figure 4.35 Delta error analysis with respect to the mean streamwise velocity component for the TI_3 calibration procedure. The blue, orange, and yellow represent δ_u , δ_v , δ_w components, respectively. The shapes represent the flow regime examined: squares, diamonds, and triangles represent NGNC, YGNC, and YGYC, respectively.

Theoretically, the NN model should only capture the coherence of a signal and miss/omit any white noise. Therefore, there is the possibility that the hotwires are solving the larger scales more precisely than the sonic. Since we do not have any additional reference to compare with, such as PIV or a pitot tube, no concrete conclusions can be drawn here, but we do want to raise this question and point out that this should be examined further in future studies. We do this by examining the spectral shapes and quantifying the large-scale deviation relative to those of the GT. Originally, we claimed and selected the most "trusted" method as the standard calibration method using the automatic calibrator and the transfer function using the lookup table (TJ_3). Here, we will compare the absolute difference of the sonic large scales to those of the ground truth. Then we will compare how those differences relate to the raw output provided by the NN based models. These normalized differences are defined as:

$$\Delta P_{Sonic} = \frac{|P_{Sonic} - P_{GT}|}{P_{GT}}, \quad (4.11)$$

$$\Delta P_{NN} = \frac{|P_{NN} - P_{GT}|}{P_{GT}}. \quad (4.12)$$

For consistency, the comparison is made up to $2Hz$ since it is the highest trusted frequency of the sonic at the lowest mean velocity examined in this study. The comparison is only made with the NN methods because these were previously recommended to undergo a correction based on the sonic reading of the large scales [68]. The same results are presented twice: Figures 4.36-4.38 present the different flow regimes separately while Figures 4.39-4.41 present the three types of NN models separately. In the case that the correction would be unarguably necessary, the cloud of points should have been densely stacked in the southwest corner of all figures. Since this is not the case, the possibility that the hotwires resolve the large scales more accurately than the sonic should be considered. When comparing the three NN models large scale performance, it appears that the deep NN has slightly smaller differences than the shallow NN models. All methods, however, fall close to the 1: 1 ratio line. We are, essentially, comparing the large scales of the sonic to the large scales of the NN derived signals that are based on the sonic data. The comparison and normalization of both are based on the GT large scales; these signals are calibrated using the jet and are unrelated to the sonic signals. Since there are not many points that lie below the 1: 1 line, it appears that the uncorrected NN large-scale signals (using the sonic data) ultimately have smaller differences from the GT than the sonic raw large-scale signals.

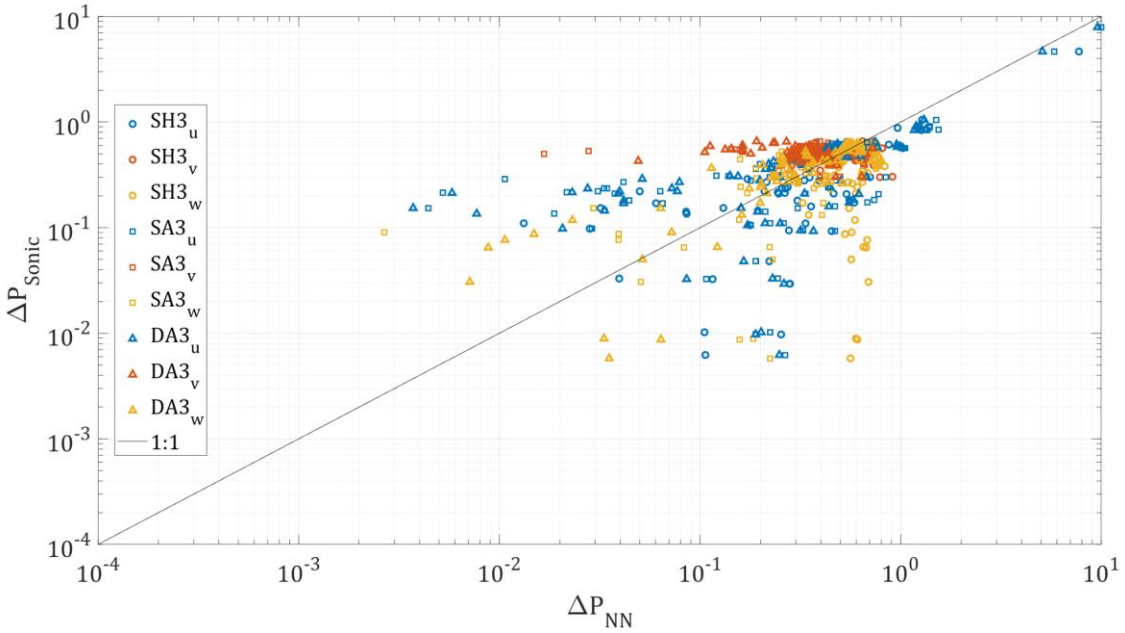

Figure 4.36 The NGNC flow regime large scale normalized deviation of the NN methods relative to those of the sonic. These are all compared with the defined GT data. The circles, squares and triangles represent SH_3, SA_3, DA_3. The blue, orange, and yellow represent the u, v, w components.

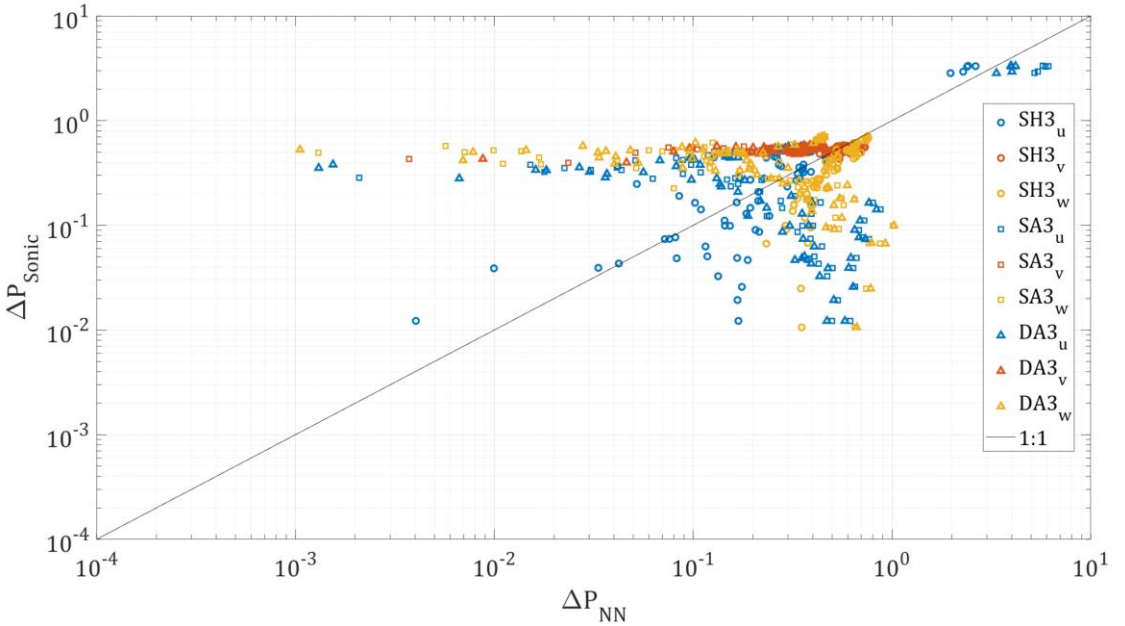

Figure 4.37 The YGNC flow regime large scale normalized deviation of the NN methods relative to those of the sonic. These are all compared with the defined GT data. The circles, squares and triangles represent SH_3, SA_3, DA_3. The blue, orange, and yellow represent the u, v, w components.

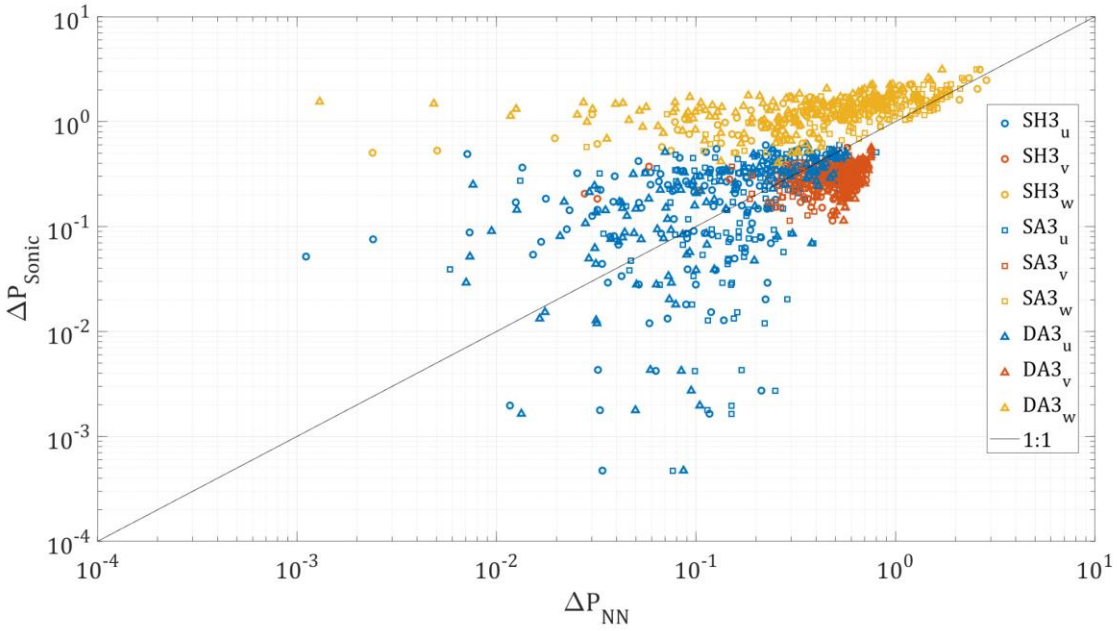

Figure 4.38 The YGYC flow regime large scale normalized deviation of the NN methods relative to those of the sonic. These are all compared with the defined GT data. The circles, squares and triangles represent SH_3, SA_3, DA_3. The blue, orange, and yellow represent the u, v, w components.

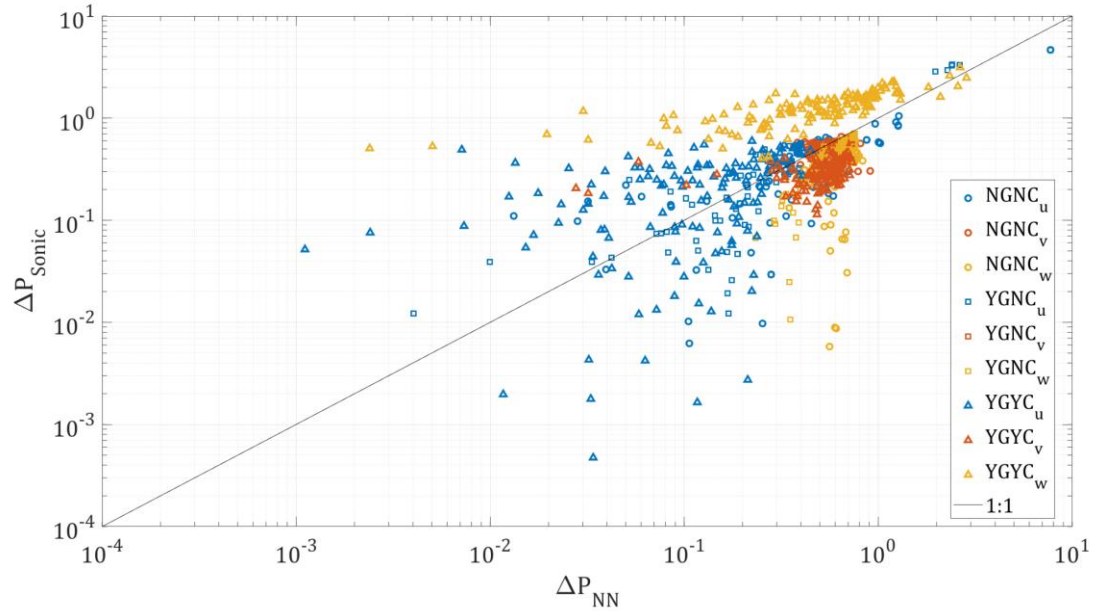

Figure 4.39 The large scale normalized deviation of the SH_3 NN methods relative to those of the sonic. These are all compared with the defined GT data. The circles, squares and triangles represent different flow regimes: NGNC, YGNC and YGYC. The blue, orange, and yellow represent the u, v, w components.

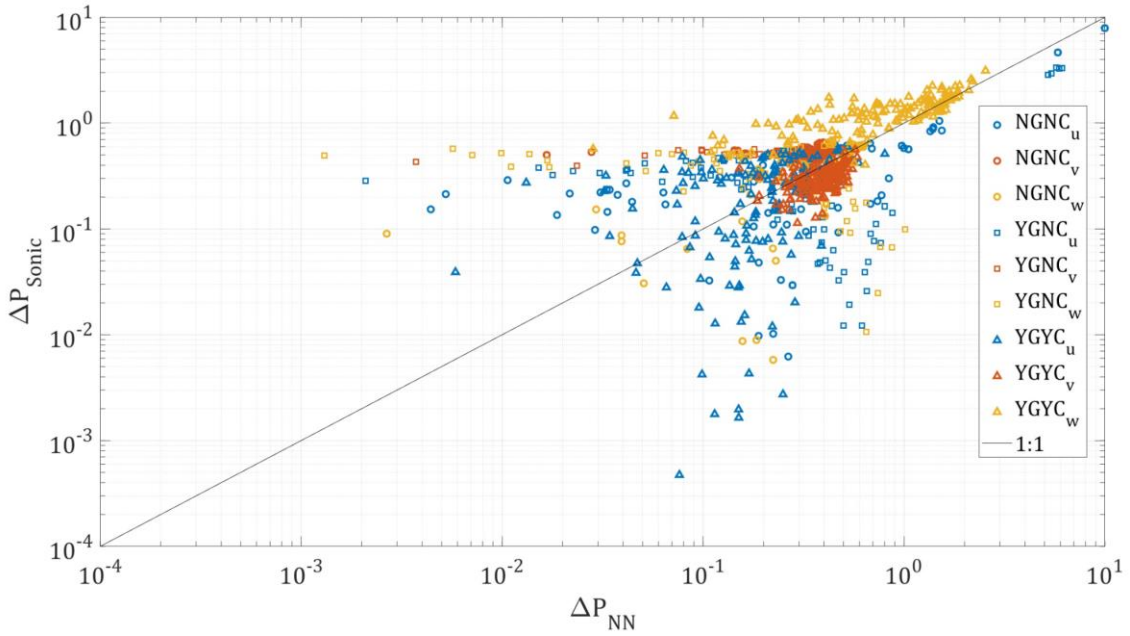

Figure 4.40 The large scale normalized deviation of the SA_4 NN methods relative to those of the sonic. These are all compared with the defined GT data. The circles, squares and triangles represent different flow regimes: NGNC, YGNC and YGYC. The blue, orange, and yellow represent the u, v, w components.

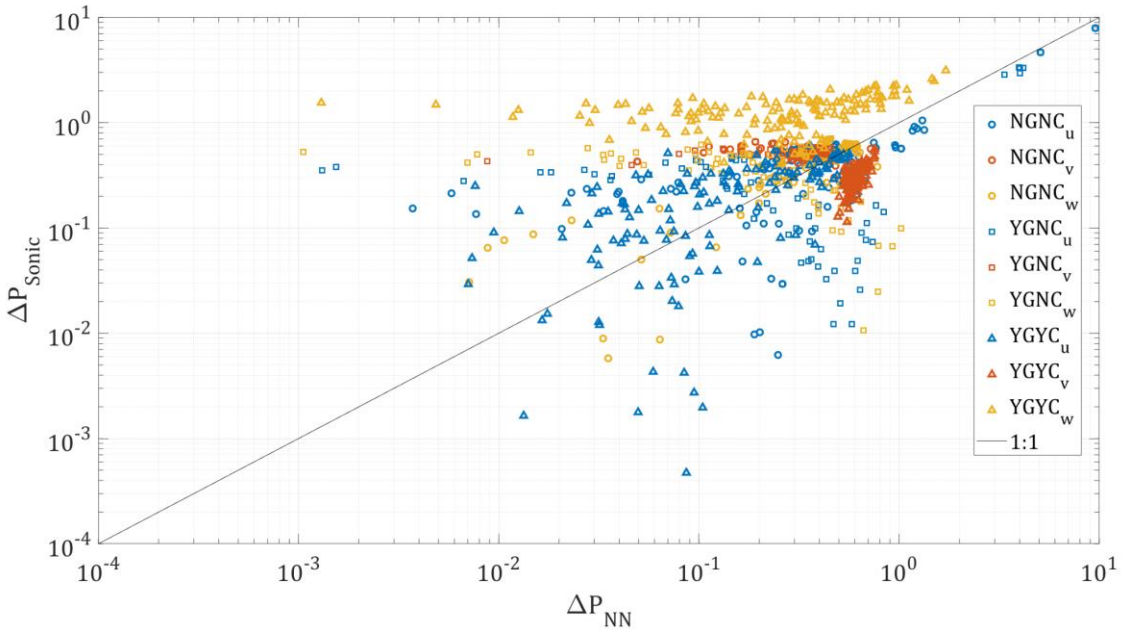

Figure 4.41 The large scale normalized deviation of the DA_3 NN methods relative to those of the sonic. These are all compared with the defined GT data. The circles, squares and triangles represent different flow regimes: NGNC, YGNC and YGYC. The blue, orange, and yellow represent the u, v, w components.

Finally, a comparison is made for all turbulence statistics relative difference from the GT based statistics. Due to the findings from the previous paragraph, these results are presented without the suggested spectral shift according to the sonic (for all 3 types of NN based calibration procedures). Figures 4.42 -4.47 present the relative difference of the following statistics and length scales: $TKE, TI, \bar{\varepsilon}, L_H, \lambda, \eta$. The most noticeable difference is the polynomial fit, with has the highest deviation from all methods. The deep NN automated model seems to consistently lie in the lower range of Δs and is also of a similar order of magnitude as the Δ of TJ_2 (also derived using the calibrator). This is remarkable given the extreme conditions that this network was required to deal with. It was trained using a training set of three different flow regimes together. This suggests that in the field, even if the conditions do change drastically, the network is expected to perform just as well as the most accurate jet calibration. In Figure 4.45, the horizontal length scale at the lowest blower frequency, $\bar{u} = 2\ m/s$, has a distinguishable behavior than the rest of the velocities, but this appears to be more negligible in the YGYC flow regime—pointing towards a lower signal to noise ratio.

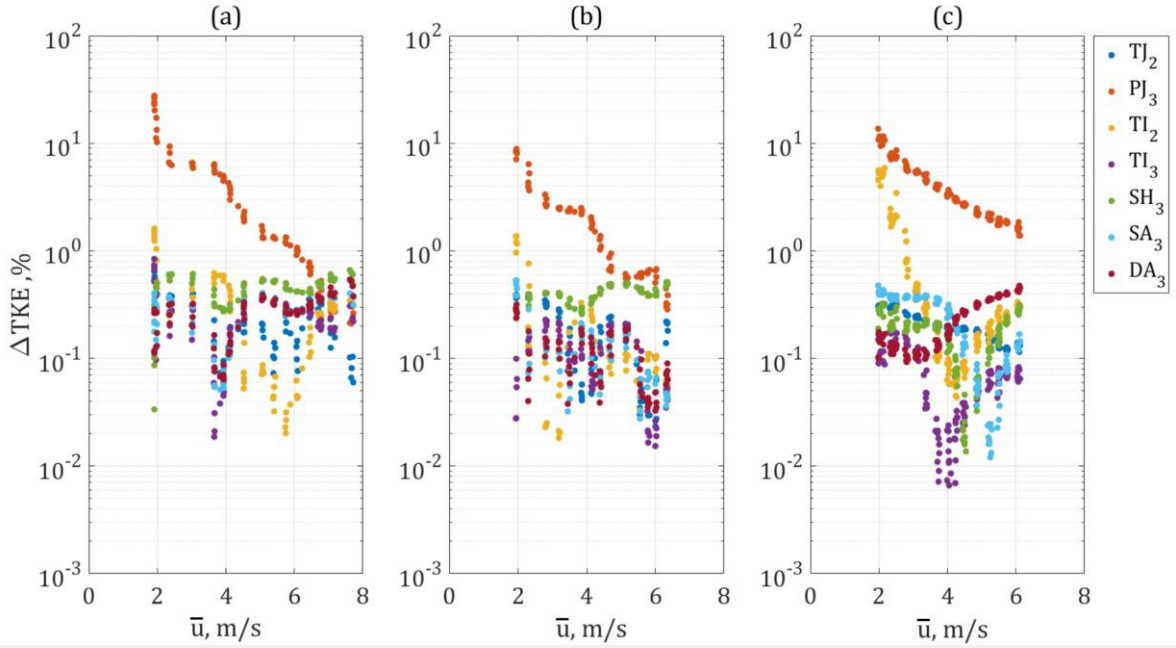

Figure 4.42 Comparison of the TKE error relative to the GT with respect to the mean streamwise velocity. The different calibration procedures are compared and are presented with respect to the different flow regimes NGNC, YGNC, and YGYC in (a), (b), and (c), respectively.

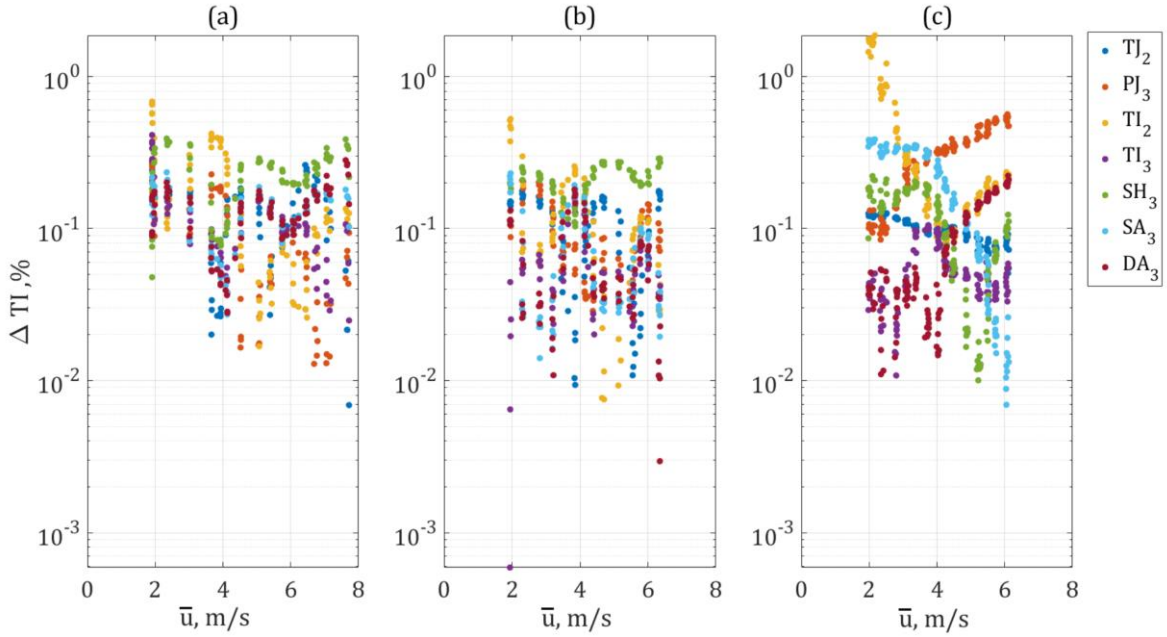

Figure 4.43 Comparison of the TI error relative to the GT with respect to the mean streamwise velocity. The different calibration procedures are compared and are presented with respect to the different flow regimes NGNC, YGNC, and YGYC in (a), (b), and (c), respectively.

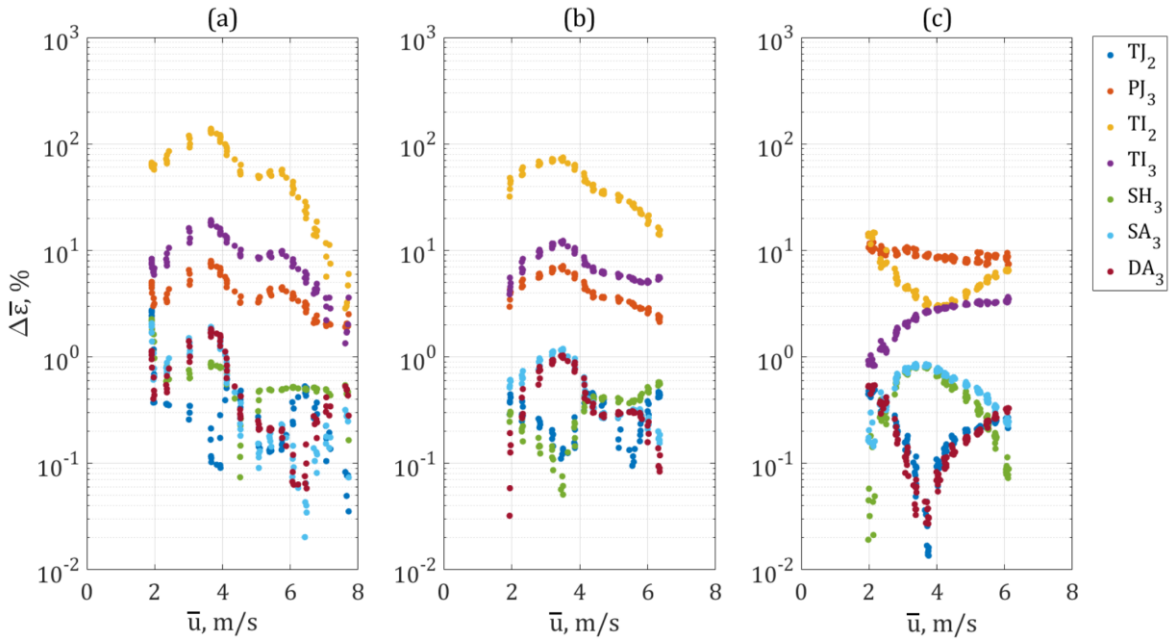

Figure 4.44 Comparison of the $\bar{\varepsilon}$ error relative to the GT with respect to the mean streamwise velocity. The different calibration procedures are compared and are presented with respect to the different flow regimes NGNC, YGNC, and YGYC in (a), (b), and (c), respectively.

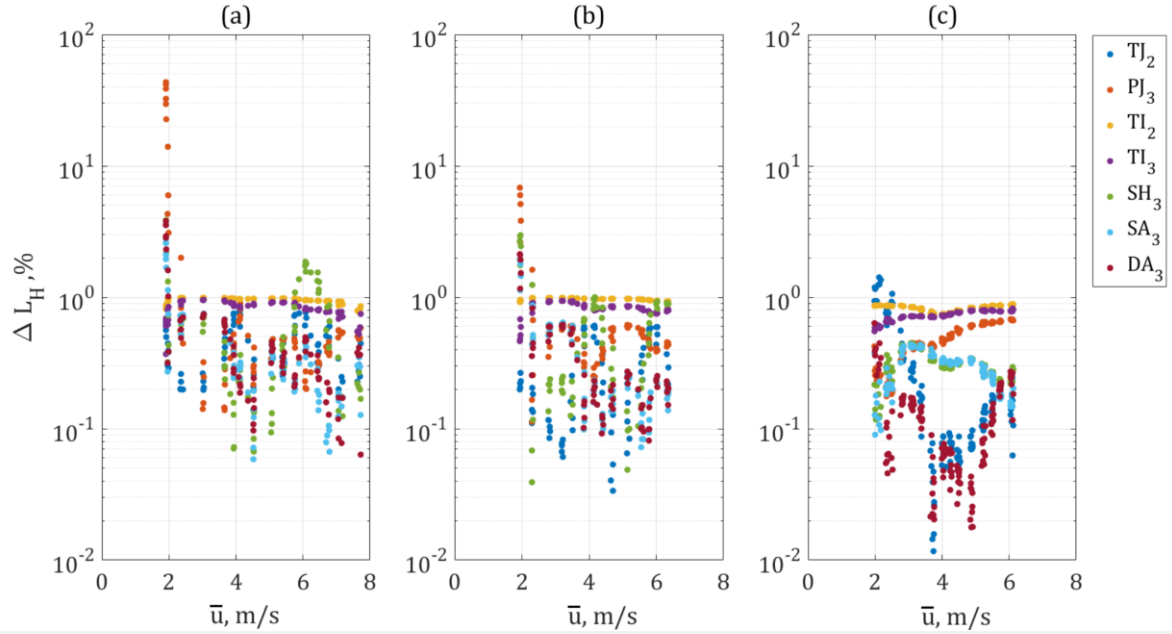

Figure 4.45 Comparison of the L_H error relative to the GT with respect to the mean streamwise velocity. The different calibration procedures are compared and are presented with respect to the different flow regimes NGNC, YGNC, and YGYC in (a), (b), and (c), respectively.

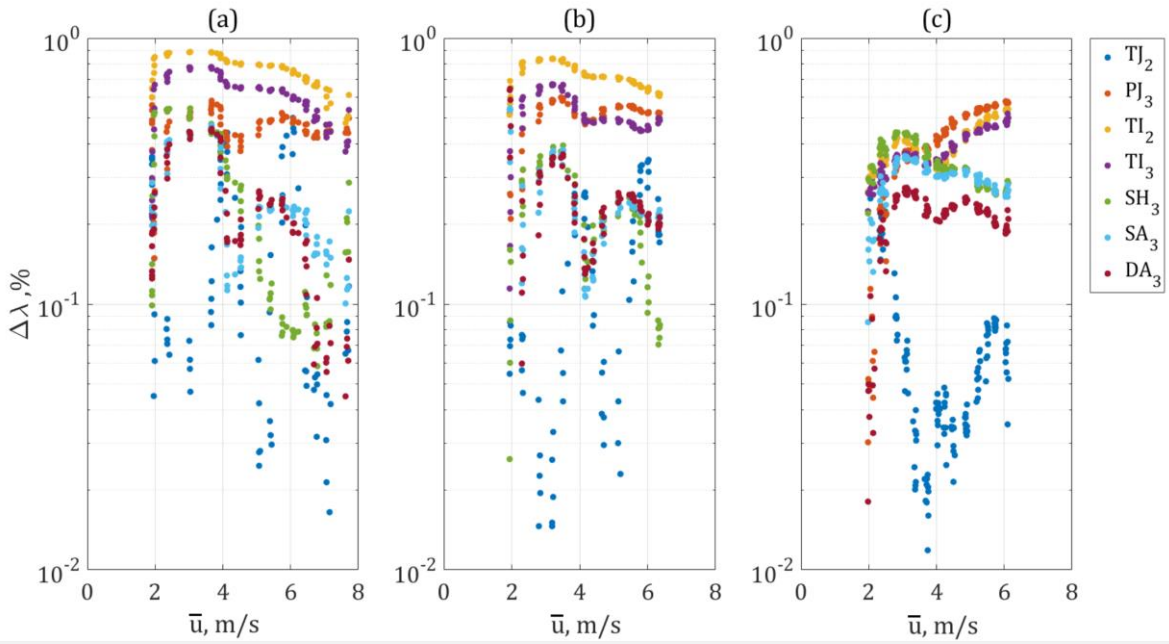

Figure 4.46 Comparison of the L_T error relative to the GT with respect to the mean streamwise velocity. The different calibration procedures are compared and are presented with respect to the different flow regimes NGNC, YGNC, and YGYC in (a), (b), and (c), respectively.

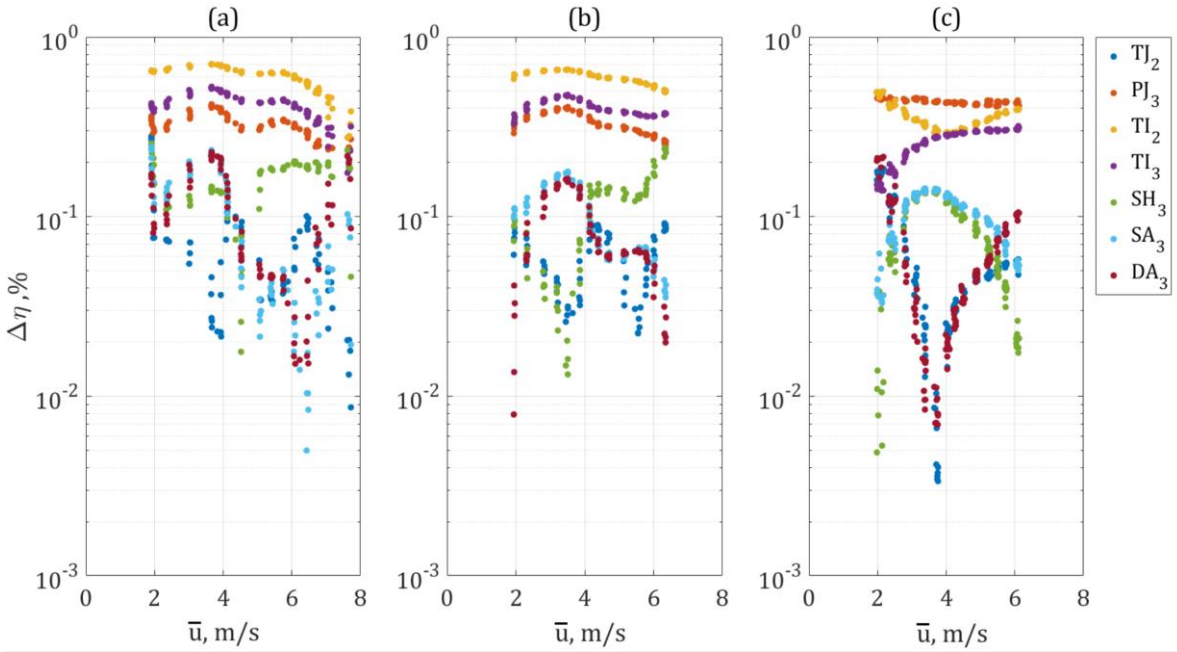

Figure 4.47 Comparison of the η error relative to the GT with respect to the mean streamwise velocity. The different calibration procedures are compared and are presented with respect to the different flow regimes NGNC, YGNC, and YGYC in (a), (b), and (c), respectively.

4.2.3 Automated procedure: field testing

The suggested automated in-situ NN based calibration procedure was also tested on the dataset from the Red Sea, detailed above. The results presented above were obtained using the previous calibration procedure using handpicked minutes for the training set, SH_3. This was used as the GT for comparison with the automated procedure DA_3. The comparison of the results from a sample hour of measurements is presented in Figures 4.48 and 4.49. The delta errors are of the same range as we observed in the previous section and in the previous study [68]. The relative difference in turbulence statistics also falls in the same range as observed above, concluding this method is indeed acceptable for use in the field given the range of variation from the previously accepted approach.

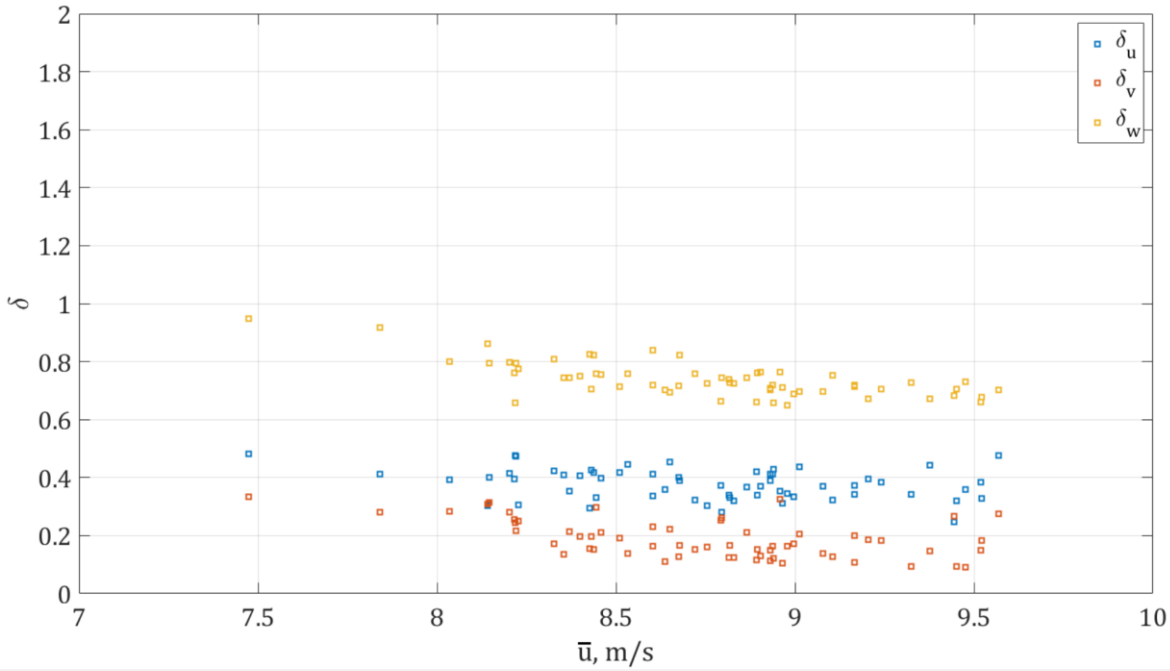

Figure 4.48 The delta error for all three velocity components with respect to the mean streamwise velocity in a representative hour at 9 am on May 27th, 2019.

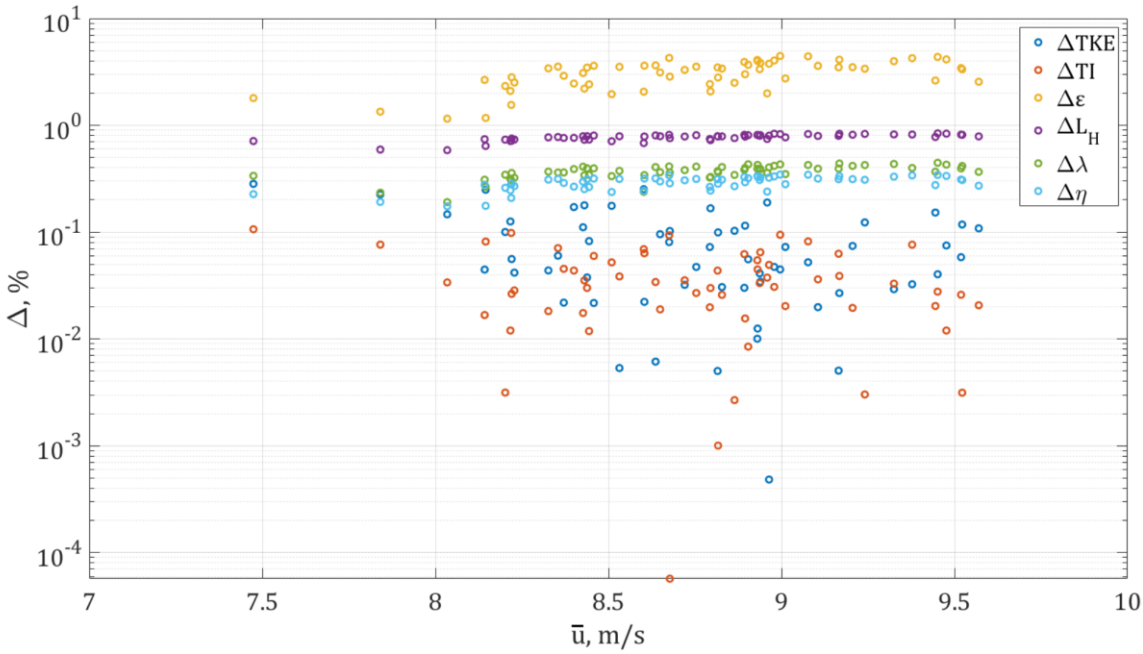

Figure 4.49 The relative turbulence statistics difference with respect to the mean streamwise velocity in a representative hour at 9 am on May 27th, 2019.

4.3 Concluding remarks

Prior to the combo, hotwire anemometry was rarely used in the field because of the cumbersome calibration procedure necessary to operate the hotwires and because of the requirement for alignment with the mean wind direction. The combo was previously shown to tackle these limitations [12, 29, 57, 58] using the collocated ultrasonic anemometer (sonic) with two x-shaped double sensor hotfilm probes. It is capable of continuously sensing the fine-scales of turbulent fluctuations in the field. This chapter presented the most recent mechanical and algorithmic developments of the combo design and its associated data processing routines and algorithms.

Prior to our developments, the combo had a sensing limitation of 120°, and studies that required a wider range than the one available installed several combos at different orientations [57, 58]. Our mechanical development is based on fixating the hotfilms to the sonic and rotating them together. This enables the capture of all 360° around the probe and minimized the obstructions made to the flow. To examine the durability of the design, the combo was deployed in an open sea environment for several days. This experiment confirmed that the combo operates properly and has the capability of working continuously without human intervention for days or weeks at a time.

Just to clarify, the data collection prior to this study did not require any human intervention, but the calibration procedure itself was human decision based. The next accomplishment we presented in this chapter is the automation of the combo calibration procedure to enable near real-time monitoring of fine-scale turbulent fluctuations. The automation procedure proposed was tested on both the open sea dataset and inside a wind tunnel using the classical calibration procedure consisting of a low turbulence intensity jet and a mechanical manipulator. The

automated procedure included the use of a deep NN, instead of the previously used shallow NN, and the use of all low pass filtered data (of the sonic and hotfilms) of steady ambient conditions for the training set.

The automated calibration in the wind tunnel was used to represent an extreme case of significant variations in wind magnitude and turbulence characteristics during the span of a measurement. Here three different flow regimes used together to train one transfer function. The observed results confirmed that the combo can tolerate even extreme changes in the flow conditions. The resulting length scales, derived using the different transfer function estimating techniques, exhibited values in the expected range (relative to the ground truth obtained by controlled jet and lookup tables calibration). The same was observed for the turbulence intensity and the turbulent kinetic energy dissipation rate. More specifically, the NN based approaches exhibited a variation from the ground truth ($GT = TJ_3$) that resembled the one observed between the TJ_2 and TJ_3. The latter two use the same jet-based calibration set but have a different averaging procedure of the so-called sub-probes. The deep NN appears to have much better frequency response and hence better capture the finest scales, as it exhibited a continued dissipation rage at much higher frequencies instead of flattening. As for the field comparison, the results exhibited the same range of differences between the automated procedure using deep NN and the human-decision based calibration method using shallow NN.

We originally began this testing with a range of acceptable uncertainty. We are aware that the estimates for the transfer function will vary up to a certain degree depending on which method we chose to use. For example, the lookup table method using two or four sub probes exhibit some difference in their results. By introducing

automated training our attempt is to avoid as much avoidable (human based) bias as possible. Here, we also presented an extreme case where we threw all data, taken from three different flow regimes, in for the training of one transfer function. In the field, in practice, when the conditions change this much, a new model would be trained, but we do show here that the networks manage to find the coherence even in highly variable flow conditions. Our results do not allow a conclusion regarding the ultimately most accurate method, but we can say with certainty that the deviation between the commonly used methods and the newly proposed methods are of the same range. Meaning hotwires *can* and *should* be implemented in the field and the automatic calibration using deep NN is preferable.

The combined results of this chapter show that capturing turbulent flow measurements in the field are now more achievable than ever before. The new and compact combo design makes this possible in all 360°. The goal of any turbulent flow monitoring is to identify relative changes in turbulent properties, regardless of the selected procedure for estimating the voltage-to-velocity transfer function. The combo and the automated calibration procedure have shown to manage this task well. This anemometer of high spatio-temporal resolution is useful for many types of field studies in various types of environments, both steady and highly variable in terms of mean flow parameters and turbulence characteristics. The automated procedure enables almost real-time processing, which would provide stationary meteorological stations the ability to monitor real-time fine-scale turbulence statistics, a useful feature for on-site close to real time temperature and pollution transfer monitoring and for use in prediction/forecast models. This is especially useful with changing field conditions and consequently with non-stationary

measuring stations, such as probes placed on moving platforms such as moving vehicles, boats, and drones that can be used to scan the entire boundary layer.

Chapter 5: Automated detection of turbulent bursting periods

Inaccuracies in numerical weather prediction models (NWP) and global climate models (GCM) are partially a result of insufficient real-time estimates of the total energy budget in the atmosphere, i.e. lack of accurate initial condition inputs to the models [72]. Inclusion of more complex physical parametrization of processes that occur on a sub grid scale can improve model accuracy [20, 73]. For example, small scale turbulent bursting periods—bursts—remain an unresolved phenomenon that lacks proper modeling to be incorporated in numerical/forecasting models [58, 74, 75]. The CASES-99 study of the nocturnal boundary layer (BL) emphasizes the importance of intermittent turbulence modeling after observing multiple occurrences at night time [76]. The study suggests that the flow is not statistically steady, contrary to the major assumptions of the used Reynolds-Averaged form of the Navier-Stokes equations, which impedes correct representation of the stable BL and limits the capabilities of NWP and GMC [77]. Bursts are considered an additional turbulent kinetic energy (TKE) generation mechanism, and can be explained by coherent structure breakup assisting in turbulent production/maintenance of turbulence [78–82]. Often referred to as the 'bottleneck effect,' turbulence statistics that include bursting periods present a significant deviation from those corresponding canonical turbulence, appearing as a bump on the slope of the velocity fluctuation power density spectra [12, 58]. Therefore, experimental characterization of this phenomenon is crucial for deriving physical parametrizations that would assist in obtaining more accurate forecasting results [83].

As the name suggests, the bursting periods are the eruption of TKE in the flow; these are characterized by a short-lived *relative* increase in the turbulent velocity fluctuation density, accompanied by elevated TKE dissipation rates, ε. A variety of definitions for the bursting phenomenon and the nature of burst generation mechanisms exist in the literature. In BL flows, these include "intermittent periods of considerable activity" [84], "intermittent turbulence" [85, 86], "violent ejection events" [87], "lifted wall streaks" [88–91], and "a sudden loss of stability in a rising fluid and a more erratic motion ensues" [78]. Additionally, Kim *et. al.* [79] defined these periods as the "entire process which carries the flow from a relatively quiescent wall-model structure to a more random chaotic turbulent character," while Willmarth *et. al.* [91] further defined bursting as "special events when large contributions to turbulent energy and Reynolds stress occur. They (are) hypothesized to be abrupt breakages or ejections of fluid from stretching of hairpin vortices that are very intense and intermittent." These definitions are all vague on the *relativity* aspect, raising questions such as: what threshold defines a relatively considerable activity? Is there a threshold variation that should be considered for different flows? Do initial/boundary conditions affect the threshold? To address these questions, a clear definition of turbulent bursting must first be specified and a distinction between the observed phenomena and the generation mechanism must be clear.

Modern field instrumentation—including ultrasonic anemometers (sonics), radars, and LIDARS—are implemented in atmospheric BL observations to produce real time estimates of the initial conditions for prediction models. All of which have low spatiotemporal frequency response making bursts undetectable in real time acquisition. Sonics, for example, have a long acoustic fly path $O(0.1\,m)$ over which

velocities are averaged, thereby lowering the frequency response to several Hz, especially at low mean velocities [67]. Several papers do report on bursting periods captured using sonics, but they use large scale intermittent turbulence phenomenon interchangeably with turbulent bursting periods, which are of much smaller scales [92–94]. An example of intermittent turbulence is the commonly observed phenomenon in stable BL, where the turbulence is constantly suppressed by the strong thermal stability and appears sporadically in time and space [18]. When the background/surrounding flow is not turbulent, capturing intermittent turbulence intervals is achievable. Reina and Mahrt [92] reported on the use of overlapping window averaging of normalized Reynolds stresses to detect such instances. The otherwise quiescent background flow made the capture and identification of intermittent turbulence possible using ultrasonic anemometers alone. However, when the background flow field is itself turbulent everything changes. The distinction of short periods of more intense velocity fluctuations *relative* to the turbulent background fluctuations, often referred to as turbulent bursts or bursting periods, is substantially more challenging. Violent ejections accompanied by bursting periods were first observed in the laboratory in BL flows using the hydrogen bubble technique [80], and later using dye injected flow visualization [87]. Hotwire anemometry in laboratory studies also captured the phenomenon [18, 80, 84, 87, 95, 96], and only recently it was captured in the field using a novel collocated sonic-hotfilm probe, combo probe [12, 58].

This Chapter reports on a new method for detection of *short bursting periods* in a turbulent flow. These are defined as *periods where an increase in the velocity fluctuation density is observed relative to that of the background turbulence*. Bursting periods are identifiable in visual examination of the velocity component fluctuation

time series; however, the literature does not offer a universally quantified measure and threshold to detect the beginning and end of such periods. Making a clear distinction between the phenomenon and the generation mechanism responsible for its creation, we offer a method for the phenomenon detection. And hence, a tool for future studies to investigate generation mechanisms by conducting analysis of various flow field characteristics, separately for bursting and burst-free time periods.

To obtain a general framework of a turbulent bursting generation mechanism, one can imagine an unbounded, homogeneous, and isotropic turbulent flow with an upstream obstacle generating vortex shedding. The generated vortices will break down at some point due to their inability to sustain their original shapes, hence creating time intervals of increased turbulent fluctuation density. More generally, any turbulence generation mechanism may cause intermittent bursting periods that may live in a turbulent, transitioning, or laminar background flow. As for BL turbulent flows, these are several bursting phenomenon generation mechanisms observed/proposed over the years:

1. The overturning of small-scale internal waves was observed to intermittently generate turbulence, i.e. turbulent bursting periods [97].
2. Shear instability caused by a low level jet that flows in a BL with strong stratification stability [18, 85, 86, 95, 98, 99].
3. The Kelvin-Helmholtz instability on the interface between two distinct densities of the fluid may generate turbulent bursting periods. These separated vortices are foreign to the background flow and may appear as an intermittent increase in fluctuation density in point measurements [100, 101].

4. Fluid ejections, in which low-speed streaks are rising from the boundary and oscillating, suddenly finding themselves in higher speed background with the potential for abrupt breakage causing an intermittent increase in the velocity fluctuation density. Such ejection processes may also be strengthened by buoyancy [102, 103]. Identification of violent ejections near the boundary, often assisted by flow visualization, is then used to detect the bursts [87–91, 104, 105].
5. Bursting generation mechanism associated with passing of outer region intermittent structures was proposed by Offen and Kline [90] using space time correlation and conditioning of turbulent vs non-turbulent observed periods [79, 80, 106], additionally derived mathematically by Lohse and Grossmann [107]. The problems encountered with correlation derivations originated from the fact that these were made using the entire turbulent time series and not the bursting events alone [96].

The variety of generation mechanisms proposed for the bursting phenomenon in the literature should be considered when attempting to characterize the events. Justifying/correlating the flow with any of the possible mechanisms is most accurate if the bursting periods are accurately identified and examined separately from the background flow.

The transient nature of bursting periods makes their identification in available velocity fluctuation time series a nontrivial and cumbersome task, and over the years the proposed techniques focused on the generation mechanism rather than on the observed bursting phenomenon itself. The identification of violent ejections has been studied extensively, but remains a challenge, especially if flow visualization is not available (such as in the case of conventional atmospheric field

studies). The obtained results are not consistent between the detection methods due to the presence of background turbulence [84, 87]. Bogard and Tiederman [87] compared several suggested methods including quadrant analysis (i.e. conditional sampling using QII), certain streamwise conditions, rate of change of the velocity components, and correlation with visual observations made using simultaneously sampled data and flow visualization. Pointing out a wide discrepancy between the detection methods, they conclude the Quadrant technique with its proposed threshold of Lu and Willmarth [88] yields the best results when compared to flow visualization.

To the best of our knowledge, the method proposed by Kit *et. al.* [58] is currently the only one available in the literature that is capable of directly detecting bursting periods, independent of knowledge or identification of the underlying generation mechanism. In their method, they proposed using a minimal threshold of varying TKE dissipation (ε) values, obtained at one-second long ensemble averages, determining if each selected ensemble of velocity fluctuation records contains bursting periods or is burst-free. The threshold was selected in a similar manner to the other methods [87, 108]. When an ensemble contains values of ε that are at least an order of magnitude larger than the mean value, it is claimed that the ensemble consists of at least one burst. This detection method, tagging each ensemble as containing bursts or being burst-free, is however not capable of detecting the beginning and end of respective bursting periods within the ensembles. Development of a new method for accurate identification of turbulent bursting periods, hence allowing discriminative analysis of bursts and the background flow, is of high importance to a variety of turbulence-related research fields. Beside the immediate benefit of the added ability to investigate the bursting

generation mechanisms, such identification will allow a more detailed examination of turbulent flow characteristics in general, of scalar transport related phenomena, of heat transfer rates, and more. All of which are heavily influenced by the magnitude and frequency of bursting events [109]. The investigation of such phenomena can unfold novel physical models to advance the state-of-the-art weather/climate forecasting algorithms.

Here a new automated bursting identification technique is described. It was developed to enable detection of turbulent bursting periods in unstably stratified upslope BL flow reported in Hilel Goldshmid and Liberzon [12] and to allow examination of turbulent bursting characteristics separately from and in comparison with the background turbulence. The method presented here relies on short term sliding window averaging and appropriate normalization of the velocity component instantaneous fluctuations. The suggested normalization of instantaneous TKE dissipation rate eliminates the need for obtaining flow-specific thresholds, hence offering the possibility for the new technique implementation across various turbulent flows. We provide an analysis of the detection method sensitivity to the user specified, data examination based, input-parameter of averaging non-dimensional window-size, τ^*. The analysis is followed by data-specific optimal selection of input-parameters and a set of guidelines for their optimal selection in future studies. Results of turbulent burst detection using the method suggested here and data from Hilel Goldshmid and Liberzon [12] are also reported alongside statistical analysis of the low resolution temperature (scalar) dissipation rate in the duration of turbulent bursting periods that were separated from the background flow. Finally, a recipe is provided to enable application of the new identification method on data of various turbulent velocity fields. All of this chapter is taken from

my most recent publication in the Journal of Measurement Science and Technology [29] and we also provided all of the calculational routines freely at [110].

5.1Experimental dataset

The dataset used for examination of the proposed method was obtained during my master's degree program. In this section we demonstrate the use of ε_N variations for identification of short bursting periods in data collected during a field experiment reported in Hilel Goldshmid and Liberzon [12]. An anabatic BL flow (upslope) was investigated in Nofit, a communal village in Israel, for eight consecutive days during the warm summer days of August 2015. The investigated flow developed on a moderate, 5.7°, slope on the southwestern part of the hill. The fine scales of velocity fluctuations were captured using the recently developed combo anemometer [9, 10, 57, 58], composed of collocated ultrasonic anemometer (sonic) and two x-shaped double sensor hotfilm (hotfilm) probes. The calibration procedure developed by Kit *et. al.* [9] was followed. Briefly, the low pass filtering of both the carefully selected slow sonic records and of the simultaneously recorded fast hotfilm records provided training sets for neural networks. Trained networks were then fed the original hotfilm voltages and provided the *in-situ* calibrated 3D velocity field components. The complete experimental setup and calibration procedure are available in §3 of Hilel Goldshmid and Liberzon [12].

The data used in this study are the same 560 data blocks with a sampling frequency of 2 kHz from Hilel Goldshmid and Liberzon [12]. Each block includes four 60-second-long ensembles: the three already calibrated velocity components u, v, w in the streamwise, longitudinal, and transverse directions respectively, and the sonic provided temperature T. A visual examination of the time series enabled

Boolean tagging of each minute long ensemble as containing burst or being burst-free [12]. The period of the Taylor length scale for ensembles that were observed as containing bursts were $\tau_\lambda = 0.003 - 0.03\,s$. Leading to selection of the sliding averaging non-dimensional window length to be at least $\tau^*_{min} = 0.5$, ensuring averaging over well more than ten periods. Additionally, all approximated burst lengths (τ_{ATB}) were observed to be longer than half a second by a visual examination of the data. Identification of bursting periods in the described data, using the above elaborated procedure, was performed. In the next section, we present the results obtained for various τ^* values to unfold the method sensitivity to the averaging window size selection. Due to negligible changes under the experimental conditions, the values for the kinematic viscosity and thermal diffusivity were assumed to be constant and taken to be equal to $\nu = 1.6 \times 10^{-5}\ m^2\ s^{-1}$ and $\alpha = 2.3 \times 10^{-5}\ m^2\ s^{-1}$. Discriminating the velocity field records into bursting and burst-free periods was followed by derivation of relevant turbulence statistics, comparison between bursting and non-bursting intervals and statistical analysis of temperature fluctuations.

5.2Automated burst detection procedure

An automated procedure is necessary when attempting to identify turbulent bursting periods within a turbulent background flow. However, such a task is nontrivial because the bursting period occurrence is not predictable and because the bursting period characteristics may vary depending both on the burst generation mechanism and on the background flow parameters. Recently, Kit *et. al.* [58] proposed using the TKE dissipation rate, ε, variations to flag pre-determined time intervals as bursting or burst-free ensembles for stable atmospheric BL flow.

Averaging over one-second intervals allowed representative ε values for each second in the examined ensemble to be obtained, observing a flow specific pattern of variations. The ε was at least one order of magnitude higher when an interval partially consisted of a bursting period. This allowed selection of a specific threshold to distinguish between bursting and burst-free containing ensembles, however, the exact identification of the burst period starting and ending times was impossible. It was suggested that future studies should aim at identifying ensembles consisting of 100% turbulent bursting periods and comparing them with those 100% burst-free to investigate the burst related phenomena and characteristics of the flow.

Here, we suggest a different approach: implementing moving and overlapping window averaging to obtain variations of the TKE dissipation rate. This allows identification of the bursting period beginning and ending times within an examined data ensemble with sufficient accuracy, leading to an automated burst identification. To allow implementation in a variety of flows and over various characteristics of similar flows, a proper normalization of the examined averaged TKE dissipation rate is additionally required. We suggest selecting a short enough window to capture the phenomenon, as the window length is proportional to the smallest detectable burst length, and using a sliding window with a step size corresponding to the velocity record sampling frequency to obtain the instantaneous variations of the TKE dissipation rate, ε. The instantaneous TKE dissipation rate is then normalized by the ratio between the ensemble averaged ε and the corresponding root mean square (rms) value, as described in Equations (5.3)-(5.8).

Invoking Taylor's frozen turbulence hypothesis allows one to convert a single-point measurement to spatial gradients

$$\frac{\partial \psi}{\partial t} = -\left(\bar{u}\frac{\partial \psi}{\partial x} + \bar{v}\frac{\partial \psi}{\partial y} + \bar{w}\frac{\partial \psi}{\partial z}\right), \tag{5.1}$$

where ψ is any point measured quantity of the flow. Here, we examine variations of the velocity field TKE dissipation rate and later the temperature dissipation rate. Two distinct types of averages are used here for the sake of automated identification (Table 5-1); all of which are computed from the velocity fluctuation time-series. The first is a moving average, denoted hereinafter by an overbar $\bar{\psi}$, and representing a sliding window median. The second is an ensemble average, denoted hereinafter by angle brackets $\langle\psi\rangle$, and representing the ensemble median. The median was selected for averaging (of the velocity fluctuations) purposes to avoid biases resulting from outliers expected within bursting periods present in the flow. The instantaneous fluctuations relative to each of the averages are denoted as ψ' when removing the moving average, and as ψ'' when removing the ensemble average. Finally, the rms of the fluctuations is denoted as $\tilde{\bar{\psi}}$ for the sliding window rms, and as $\{\psi\}$ for the ensemble rms.

Table 5-1 Nomenclature of notations for averaging and rms calculations

	Sliding window	Ensemble
Average (mean or median)	$\bar{\psi}$	$\langle\psi\rangle$
Fluctuations	ψ'	ψ''
Root mean square (rms)	$\tilde{\bar{\psi}}$	$\{\psi\}$

To begin calculating the normalized instantaneous ε, variations of which will be used to identify the bursts, a moving-average window length, τ, must be selected.

The upper bound of this length should first be determined by preliminary data examination, and hence will depend on the examined flow field. A visual observation of the time series will approximate the typical turbulent bursting length, τ_{ATB}. Here, it was selected to be $\tau_{ATB} = 1\ s$. The lower bound must be long enough to allow averaging over several typical relevant length scales of the turbulent flow. The length scale of choice for our data set is the Taylor microscale, λ, because it is a commonly used length scale that lies in the inertial subrange at which the eddy dissipation rate is still not dominated by viscosity. It is defined as

$$\lambda = \sqrt{\frac{\{u''\}^2}{\left\langle \left(-\frac{1}{\langle u \rangle}\frac{\partial u''}{\partial t}\right)^2 \right\rangle}}\ , \tag{5.2}$$

where u is the streamwise component [105, 111]. This scale should be calculated prior to implementation of the identification method for each velocity record ensemble to be examined. The corresponding time period is then obtained by $\tau_\lambda = \lambda/\langle u \rangle$ [18] (from equation 1.4c). Finally, the averaging window length, τ, is to be selected in the range of $10\tau_\lambda < \tau \leq 2\tau_{ATB}$ to allow both averaging over several periods of the Taylor scale vortices representative of the flow and to remain small enough to identify the bursting phenomenon. Finally, the non-dimensional window length, $\tau^* \equiv \tau/\tau_{ATB}$, is defined. This, in turn, provides a corresponding non-dimensional range to consider for the accepted sensitivity $10(\tau_\lambda/\tau_{ATB}) < \tau^* \leq 2$.

Once the window length is selected, the average instantaneous TKE dissipation rates, ε, are computed as the mean of three TKE dissipation terms:

$$\varepsilon = \frac{\varepsilon_u + \varepsilon_v + \varepsilon_w}{3}, \tag{5.3}$$

where ε_u is an estimate of the TKE dissipation rate using the streamwise velocity component (defined below), ε_v and ε_w are the TKE dissipation rate estimates using the longitudinal and transverse velocity components, respectively, and ν is the kinematic viscosity.

$$\varepsilon_u = 15\frac{\nu}{\bar{u}^2}\overline{\left(\frac{\partial u'}{\partial t}\right)^2}, \tag{5.4}$$

$$\varepsilon_v = 7.5\frac{\nu}{\bar{u}^2}\overline{\left(\frac{\partial v'}{\partial t}\right)^2}, \tag{5.5}$$

$$\varepsilon_w = 7.5\frac{\nu}{\bar{u}^2}\overline{\left(\frac{\partial w'}{\partial t}\right)^2}. \tag{5.6}$$

The corresponding instantaneous fluctuations of the TKE dissipation rate are then defined as

$$\varepsilon'' = \varepsilon - \langle\varepsilon\rangle. \tag{5.7}$$

To allow comparison across various flows, these are to be normalized by the fluctuation rms over the entire ensemble,

$$\varepsilon_N = \frac{\varepsilon''}{\{\varepsilon''\}}, \tag{5.8}$$

providing a normalization of the signal relative to the background flow. A MATLAB® script detailing the computation of ε_N from velocity fluctuation time series is available in the Appendix I and the complete dataset along with the MATLAB® code for reproduction of all the figures presented here are available online [110]. Variations of ε_N are used to identify bursting periods along each ensemble. Time intervals during which the value of ε_N exceeds a preselected threshold value (ε_T) are detected as bursting. The use of a threshold of ε_N variations, a normalized signal inherently independent of the background flow properties, paves the way to possible generalization to bursting event detection in other flows.

Its potential generalization lies in its independence of the physical properties of the flow, i.e. it does not depend on flow-specific dimensions, boundary conditions or forcing of the observed flow. Here, we examined a threshold value $\varepsilon_T = 2$ signifying a substantial (i.e. two-fold or a 200%) increase relative to that of the background turbulent flow, indicative of a bursting period presence. The threshold is somewhat arbitrary—it is very conservative and round number and any value larger than 1 would signify a deviation from the expected background turbulence variations—yet a selection of $\varepsilon_T = 1.8$ or $\varepsilon_T = 2.2$, for example, would provide similar results for the examined here data set. This threshold can, and sometimes should, be modified based on the nature of the examined flow field and especially the available experimental data, such as flow visualization of fast enough measurements of scalars. Future modification of the threshold can be achieved following the same statistical examination we provide below (i.e. Figure 5.5).

5.3Discussion of detection method

To test the stability and consistency of the results obtained using the proposed method, automatic detection of bursting periods is performed using the procedure described above with varying non-dimensional window lengths, τ^*. This test examines the proposed method sensitivity to the averaging window size selection. At the longest possible non-dimensional averaging window length of 60, limited by the ensemble length, the obtained results are compared with the method proposed by Kit *et. al.* [58] described below. After detecting bursting periods, the fluctuations of the temperature variance dissipation rate in the duration of bursting periods were considered and compared with those of non-bursting periods described below.

5.3.1 Window size sensitivity analysis

To define bursting periods, the procedure and threshold described above are used. Invoking a threshold of $\varepsilon_T = 2$, defines periods with $\varepsilon_N \geq 2$ as 100% *turbulent bursting* periods, periods with $\varepsilon_N \leq 1$ as 100% burst-free periods and hereinafter are referred to as *background turbulence* periods, and finally periods with $1 < \varepsilon_N < 2$ as *intermediate* periods. The latter are periods in which the TKE dissipation rate is elevated relative to that of the background flow, but is still smaller than the set bursting threshold, therefore the period is not guaranteed to be of bursting nature.

An additional condition for minimal non-dimensional bursting period length was invoked, based on the Taylor time scale values noted previously, and set to be $\tau^*_{min} = 0.5$. Moreover, consecutively detected bursting periods separated by a non-bursting period shorter than τ^*_{min} are considered as one continuous bursting period.

To examine the method sensitivity to window size selection, the automatic detection algorithm was applied to the entire dataset using a range of averaging non-dimensional window sizes, τ^*. Window sizes in the range of $0.5 \leq \tau^* \leq 30.0$, were applied with $\Delta\tau^* = 0.1$, and with a coarser step size, $\Delta\tau^* = 1.0$, in a second range of $31.0 \leq \tau^* \leq 60.0$. The second range was computed to compare the results with the Kit *et. al.* [58] method in which averaging over the whole length of the ensemble ($60\ s$) is applied.

Details of the first mapping of the method dependence on τ^* are presented in Figures 5.1-5.3. Parts (a) of the Figures display representative examples of the three velocity-components time series; parts (b) display the corresponding ε_N variations obtained using $\tau^* = 0.5,1.0,2.0,3.0$; and parts (c) display a map corresponding to background turbulence, intermediate, and turbulent bursting periods as a function

of τ^* from 0.5 to 30.0. The ε_N signals presented in (b) are consistent with the general trend of regions with elevated fluctuation intensity thereby consistently marking regions with the observed phenomenon. The curves present a sharp increase in ε_N, indicating the ability to capture the instantaneous change in the flow properties. The maps in Figures 5.1-5.3(c) demonstrate the reduction of accuracy of the beginning and end of bursting interval detection with an elongation of the averaging window.

For example, using averaging windows longer than about $\tau^* = 12$ in Figure 5.1(c) results in inclusion of the two separate bursting events occurring at 30 s and 40 s in one window, as these times are included on both ends of the window. The result is a single event marked in the center of the averaging window at about 35 s. This is still a true detection but of a coarser and insufficient resolution. To better demonstrate this, Figure 5.1(c) includes two green lines at the edges of the detected burst period on the $\tau^* = 20$ result line. When comparing this detected region to the time series, it displays that both bursting periods are indeed a part of the coarse resolution result. In Figure 5.2(c) and Figure 5.3(c) a shift in the detection region is observed at $\tau^* = 19$ and 7 respectively. This shift only indicates the center of the window thereby including the half of τ^* on each end of window center location and would consistently include the actual burst independent of window size. Such visual examination of the time series is made as a 'sanity check' when selecting a window size. Selection of a small enough window is hence essential for accurate capturing of the beginning and end of the phenomenon, presenting several events merging, or shifting off the detected bursting event time.

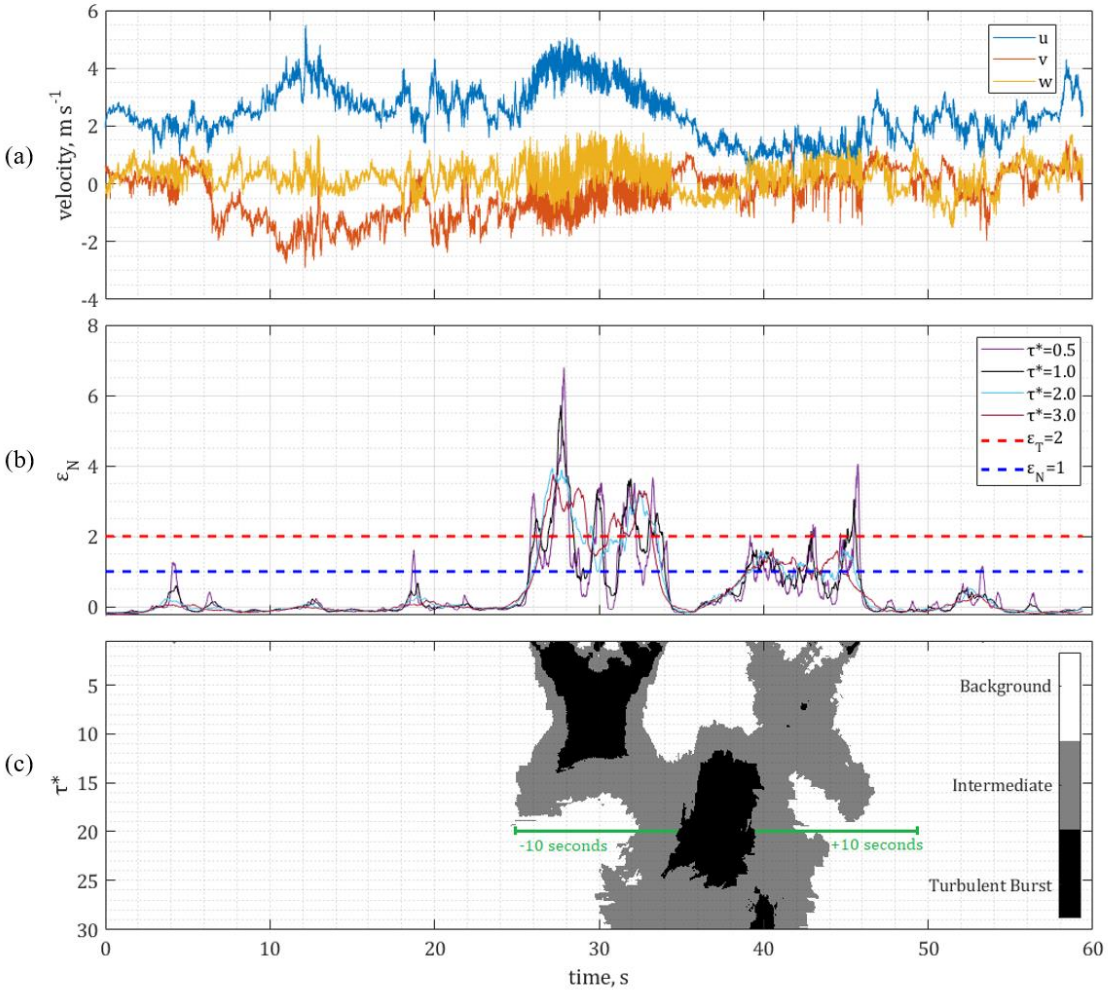

Figure 5.1 (a) Time series of instantaneous velocity components (u, v, w) in blue, orange, and yellow, obtained on 08-Aug-2015 at 11:56; (b) normalized instantaneous TKE dissipation rates (ε_N) derived using $\tau^* = 0.5, 1.0, 2.0, 3.0$ in purple, black, blue and red respectively. The red dashed line represents the maximum threshold for background turbulence periods, the area between the red dashed line and the blue dashed line represents the intermediate range, and the area above the blue dashed line represents the turbulent bursting range; (c) Displays a map of detected background turbulence, intermediate, and turbulent bursting periods in white, grey and black. These are a function of time and τ^* ranging from $0.5 - 30.0$ with $\Delta\tau^* = 0.1$. The green lines represent the size of the sensing window at $\tau^* = 20.0$. This depicts that a coarse resolution of τ can cause a merge of two separate bursting events into one due to the decreased sensitivity.

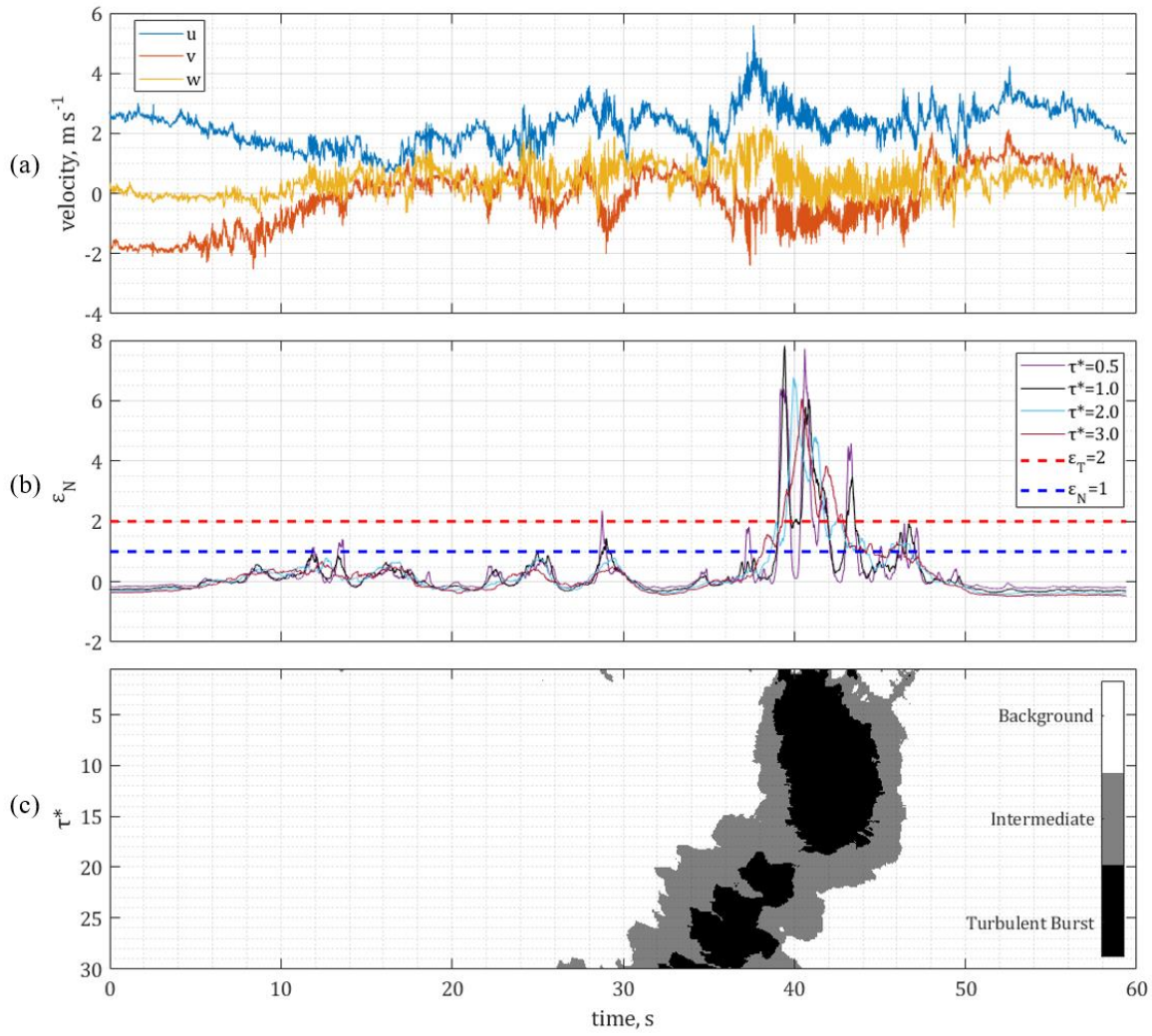

Figure 5.2 (a) Time series of instantaneous velocity components (u, v, w) in blue, orange, and yellow, obtained on 08-Aug-2015 at 12:28; (b) normalized instantaneous TKE dissipation rates (ε_N) derived $\tau^* = 0.5, 1.0, 2.0, 3.0$ in purple, black, blue and red respectively. The red dashed line represents the maximum threshold for background turbulence periods, the area between the red dashed line and the blue dashed line represents the intermediate range, and the area above the blue dashed line represents the turbulent bursting range; (c) Displays a map of detected background turbulence, intermediate, and turbulent bursting periods in white, grey and black. These are a function of time and τ^* ranging from $0.5 - 30.0$ with $\Delta\tau^* = 0.1$.

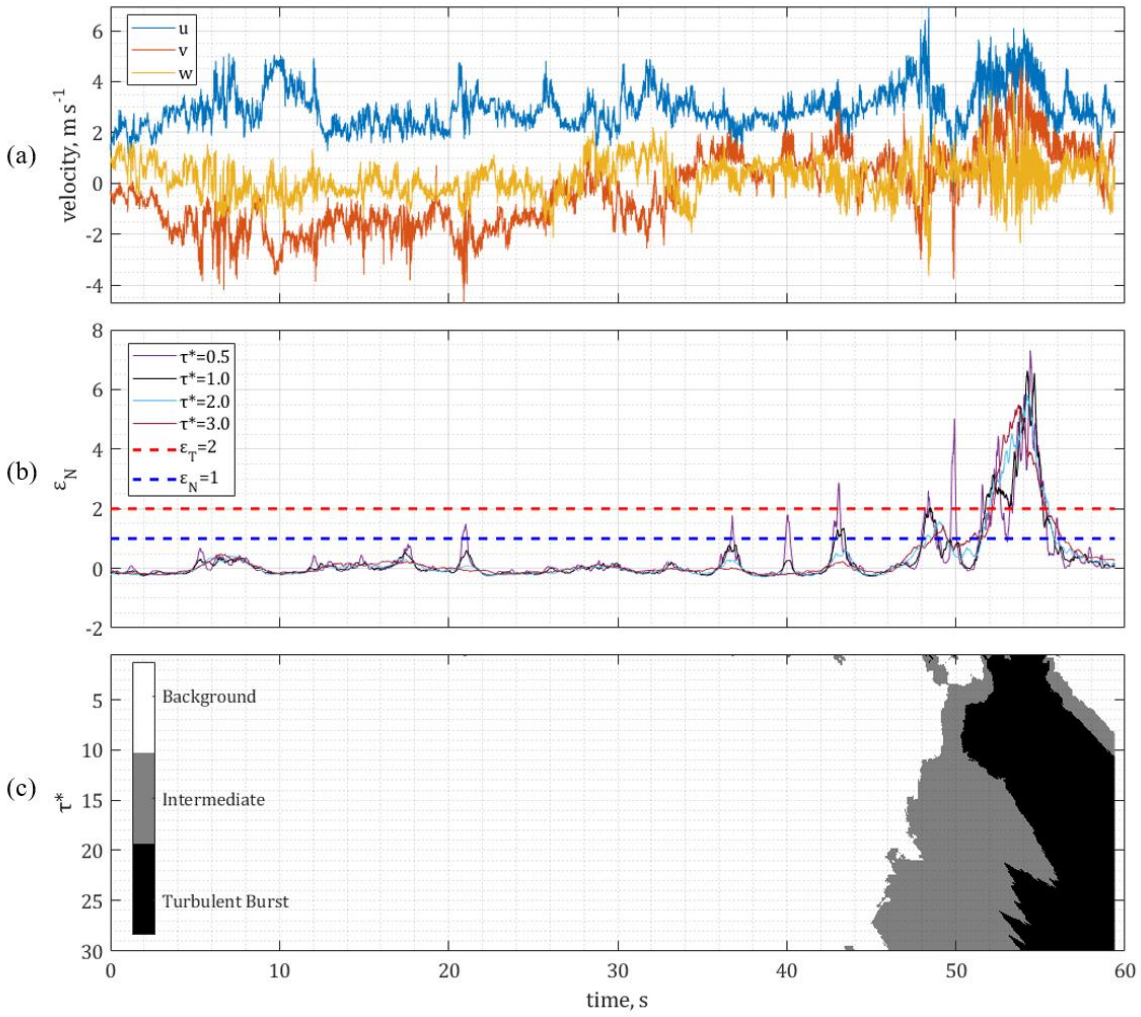

Figure 5.3 (a) Time series of instantaneous velocity components (u, v, w) in blue, orange, and yellow, obtained on 09-Aug-2015 at 14:20; (b) normalized instantaneous TKE dissipation rates (ε_N) derived using $\tau^* = 0.5, 1.0, 2.0, 3.0$ in purple, black, blue and red respectively. The red dashed line represents the maximum threshold for background turbulence periods, the area between the red dashed line and the blue dashed line represents the intermediate range, and the area above the blue dashed line represents the turbulent bursting range; (c) Displays a map of detected background turbulence, intermediate, and turbulent bursting periods in white, grey and black. These are a function of time and τ^* ranging from $0.5 - 30.0$ with $\Delta\tau^* = 0.1$.

After observing the general trends of the detection algorithm dependence on τ^*, total counts of detected burst-periods and of one-minute long ensembles containing bursts were obtained and are displayed in Figure 5.4 as a function of the averaging non-dimensional window size, τ^*. The ensemble count obtained for a $\tau^* = 60.0$ long window is also compared with results calculated following the Kit *et. al.* [58] method. The total burst count curve is observed to peak at $\tau^* = 1.0$, accompanied by the start of a short plateau observed in the ensembles count curve. The latter begins to decrease as the window size increases above $\tau^* = 5.0$, signifying loss of valuable instantaneous information derivable in shorter windows. The ensembles count curve reaches a minimum at $\tau^* = 40$ and the noticeable increase (which meets the Kit *et. al.* [58] values) is clear due to inclusion of the start and end of a minute effects.

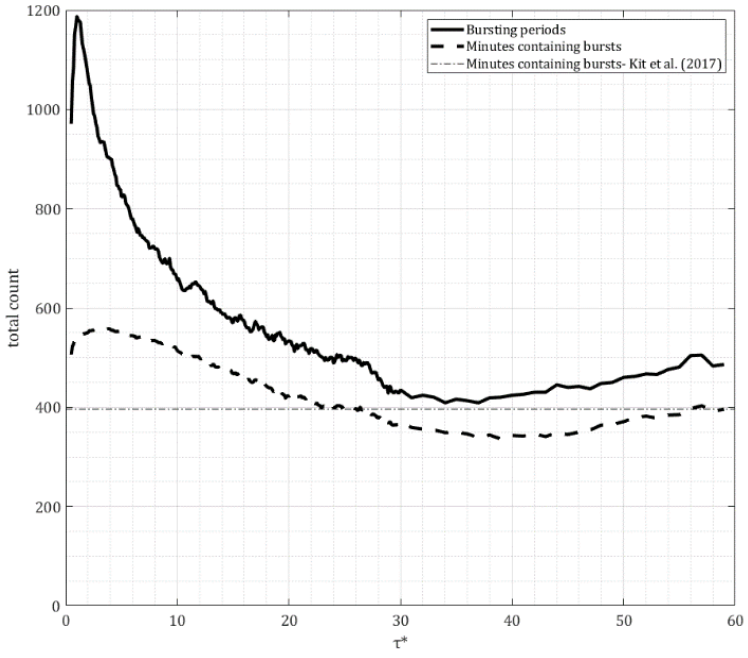

Figure 5.4 Count of detected bursting periods as a function of non-dimensional window size τ^*. The black curve represents the total number of turbulent bursts detected. The dashed curve displays the number of one-minute long ensembles that were tagged with at least one bursting period. The grey dashed line $(- \cdot)$ represents a direct comparison with the work of Kit et al [3] where one minute long ensemble average is used.

Detecting turbulent bursting periods also allowed obtaining conditional statistics. Values of the ensemble average normalized TKE dissipation rates, ε_N, were calculated for each detected bursting period, thereby obtaining a representative $\langle\varepsilon_N\rangle_{TB}$ value for each bursting period. The distribution of these values is displayed in Figure 5.5 as probability density functions (PDF) for all examined window sizes, $\tau^* \leq 3.0$. The non-dimensional window size limit of 3.0 was arbitrary selected as large enough value, but not too large to fall into reduced accuracy detection range. The location of the peaks of all PDF distribution curves is greater than three and the areas under the curves in the range of $\langle\varepsilon_N\rangle_{TB} \geq 3$ are significantly larger than those of $\langle\varepsilon_N\rangle_{TB} \leq 3$; both observations indicate that the $\varepsilon_T = 2$ threshold is a sufficiently conservative selection. While selection of any threshold value close to 2, i.e. $\varepsilon_T = 1.8$ or $\varepsilon_T = 2.2$, would yield very similar results, which can be examined using the code [110] and modifying the threshold value. For each examined data set of turbulent velocity field fluctuations, the threshold value should be individually selected or even fine-tuned if additional types of measurements are available, e.g. flow visualization with PIV.

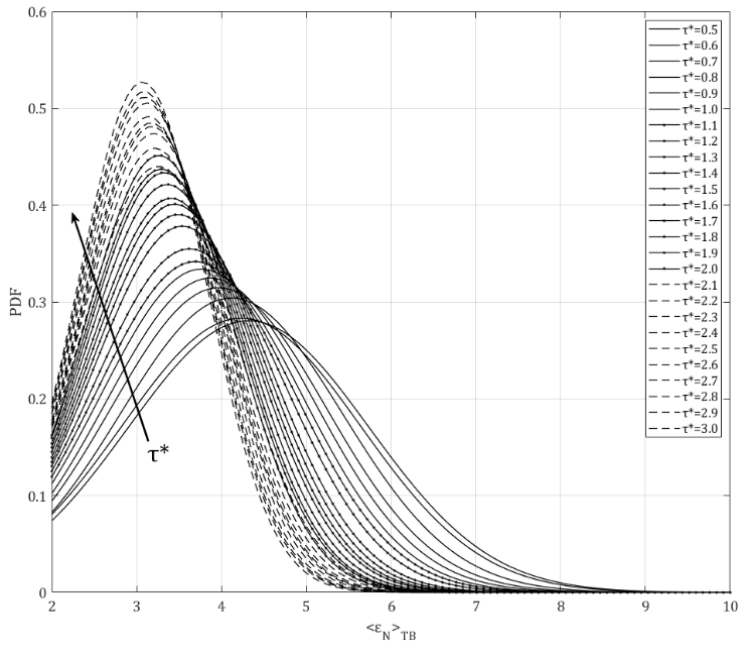

Figure 5.5 Probability density functions of all detected bursting period $\langle\varepsilon_N\rangle_{TB}$ values. Each curve represents a distribution of all $\langle\varepsilon_N\rangle_{TB}$ values obtained from all detected bursts corresponding to a specific averaging non-dimensional window size τ^*, while $\tau^* \leq 3.0$, as presented in the legend.

Distribution of the non-dimensional detected burst duration, τ^*_{TB}, was examined next (using a scaling similar to τ^*, i.e. scaled with τ_{ATB}). The use of the observation-based scaling of the method sensitivity (τ^*) and of the detected turbulent bursting period lengths (τ^*_{TB}) simplifies the interpretation of the obtained results and enables scalability for future studies. The exceedance probability EP, is an integral measure of the PDF describing the probability of an occurrence of a given value or higher. All τ^*_{TB} were ranked and the EP, with 1 being the largest possible value, was calculated by

$$EP = \frac{m_0}{n_0 + 1} \quad , \tag{5.9}$$

where m_0 represents the rank and n_0 represents the total number of τ^*_{TB} events [112]. Figure 5.6 displays the exceedance probability of τ^*_{TB}, where again, different curves represent different window sizes, τ^*. A decrease in an order of magnitude in the exceedance probability signifies that essentially all values beyond that range are not representative but rather are extreme cases. It is observed that for all τ^*, the range of non-dimensional detected burst lengths is indeed greater than 0.5 ($\tau^*_{TB} \geq \tau^*_{min}$ as conditioned), while the maximum length of most bursting periods is between $1.5 \leq \tau^*_{TB} \leq 2.25$, just as anticipated using the visual observations and the Taylor time scales based section of the averaging window size. The short duration of the events is expected as these are transient events, not representing the background turbulent fluctuations, but representing a short-lived increase in kinetic energy due to momentum injection from some source.

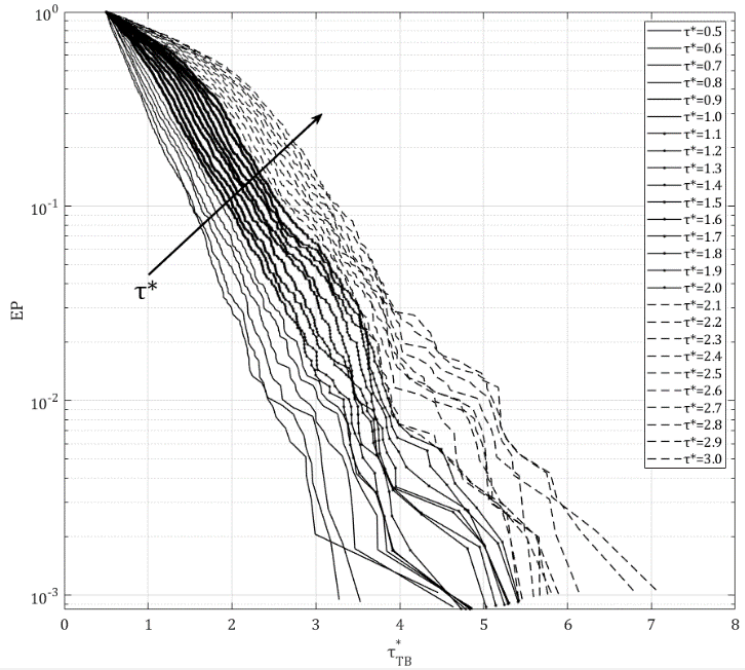

Figure 5.6 Exceedance probability curves of all non-dimensional detected bursting period lengths, τ^*_{TB}. Each curve represents a specific averaging window size τ^* examined, as presented in the legend.

An additional confirmation of successful identification of bursting periods, and the now acquired ability to examine the turbulent flow characteristics separately for bursting periods and for burst-free background flow, is provided by the means of conditional spectral analysis. When bursting periods are part of a turbulent background flow, the bottleneck effect is observed in the power density spectra of velocity fluctuations [12, 58]. The velocity fluctuation power density spectra of all background turbulence, intermediate, and turbulent bursting periods were calculated separately using Fourier Transforms; window averaging was implemented using one-second long windows resulting in $1\,Hz$ frequency resolution. This was performed separately for each ensemble and examination of the obtained spectral shapes showed similar findings, hence averaging for each of the three defined periods was implemented. The burst-free background turbulence period spectral shapes closely follow the Kolmogorov $-5/3$ slope in the inertial subrange. The other two cases deviate from the $-5/3$; the *turbulent bursting* periods having a notably milder slope and the *intermediate* periods have a slope in between. Figures 5.7-5.10 show the spectral shapes obtained with $\tau^* = 0.5, 1.0, 2.0, 3.0$, respectively. The spectral shapes show that the bursting periods are characterized by higher power density of velocity fluctuations at all scales, exhibiting the smallest increase relative to the background turbulence at the larger scales, and deviating more significantly at the smaller scales. This observation corresponds to the observations of the time series plots (Figures 5.1-5.3) where the velocity fluctuation intensity during the bursts appears elevated across various scales. However, the magnitude of the elevated fluctuations is much higher at higher frequency scales. The spectral shape of the intermediate range computed with $\tau^* = 0.5$ (Figure 5.7)

did not converge due to the small total number of intermediate range periods at the spectral resolution of 1 Hz.

Next, values of the Taylor microscale distribution for the various period types are displayed in Figure 5.11 (a)-(d). The average Taylor scales of the turbulent bursting periods, λ_{TB}, were observed to be smaller than those of the background flow turbulence λ_B, while those of the intermediate periods, λ_I, were in between. These representative average values are presented in Figure 5.11; they were obtained from fitting the data with exponentially modified normal distributions. This indicates the bursting periods were able to reach even smaller scales before viscous dissipation interfered, and this observation is consistently independent of the τ^* selection. The second statistical parameter observed in Figure 5.11(e)-(h) is the streamwise velocity derivative skewness Sk, using $\tau^* = 0.5, 1.0, 2.0, 3.0$. Bursting-period Sk (Sk_{TB}) exhibit a scatter centred around values closer to zero, indicating these values deviate significantly from the value of -0.4 observed in wind tunnel studies of grid generated homogeneous turbulence [69, 113–115]. This behavior is consistent regardless of τ^*, indicating it is representative of the bursting events. The background turbulence period Sk values, (Sk_B), are scattered more densely near -0.4, closely resembling the aforementioned value from wind-tunnel studies of homogeneous turbulence [69, 113–115]. The deviation of the bursting periods from this value may indicate a deviation from the Kolmogorov theory and from the assumption that energy is supplied solely at larger scales [116–118]. This can possibly indicate that energy may also enter the system at smaller scales, or at specific bursting length scale. This claim should be examined further, in view of possible bursts generation mechanism specific for the examined flow.

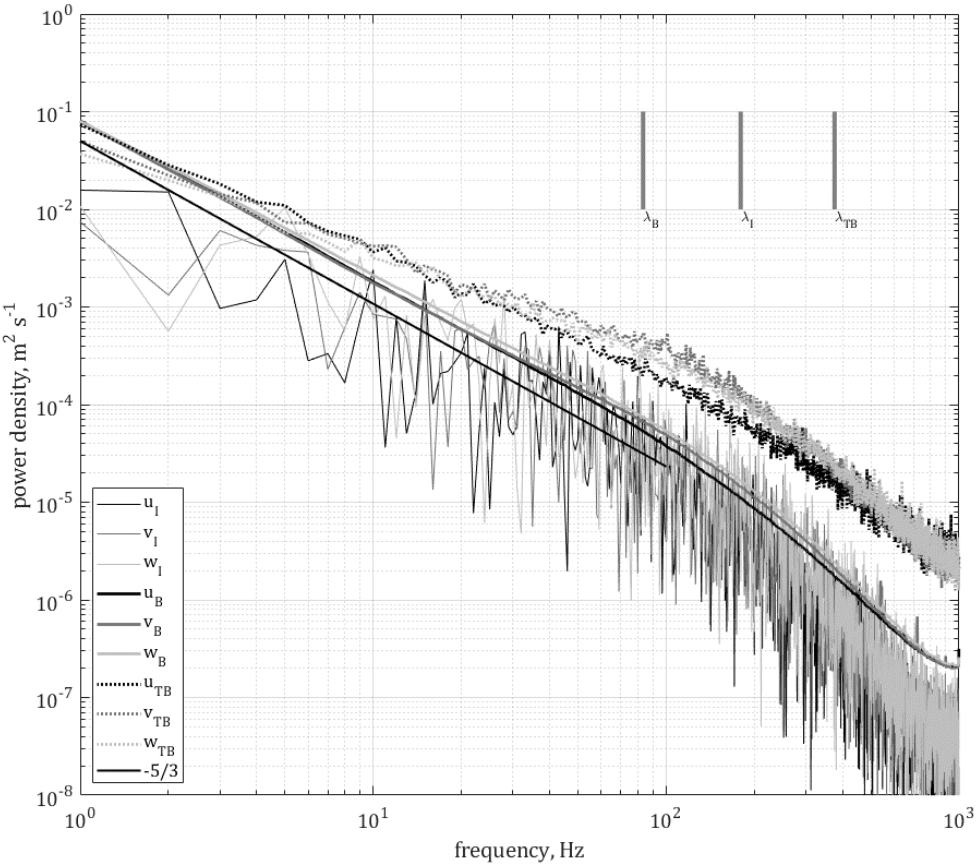

Figure 5.7 Mean power density spectra of velocity fluctuations of all minute-long ensembles. The colors black, dark grey, and light grey represent u, v, w respectively. The curves types represent different period types in the ensembles obtained with $\tau^* = 0.5$: thick, thin, and dotted curves represent background turbulence, intermediate, and turbulent bursting. The grey vertical lines represent the Taylor scale corresponding mean frequency for background turbulence (λ_B), intermediate(λ_I), and turbulent bursting (λ_{TB}) periods.

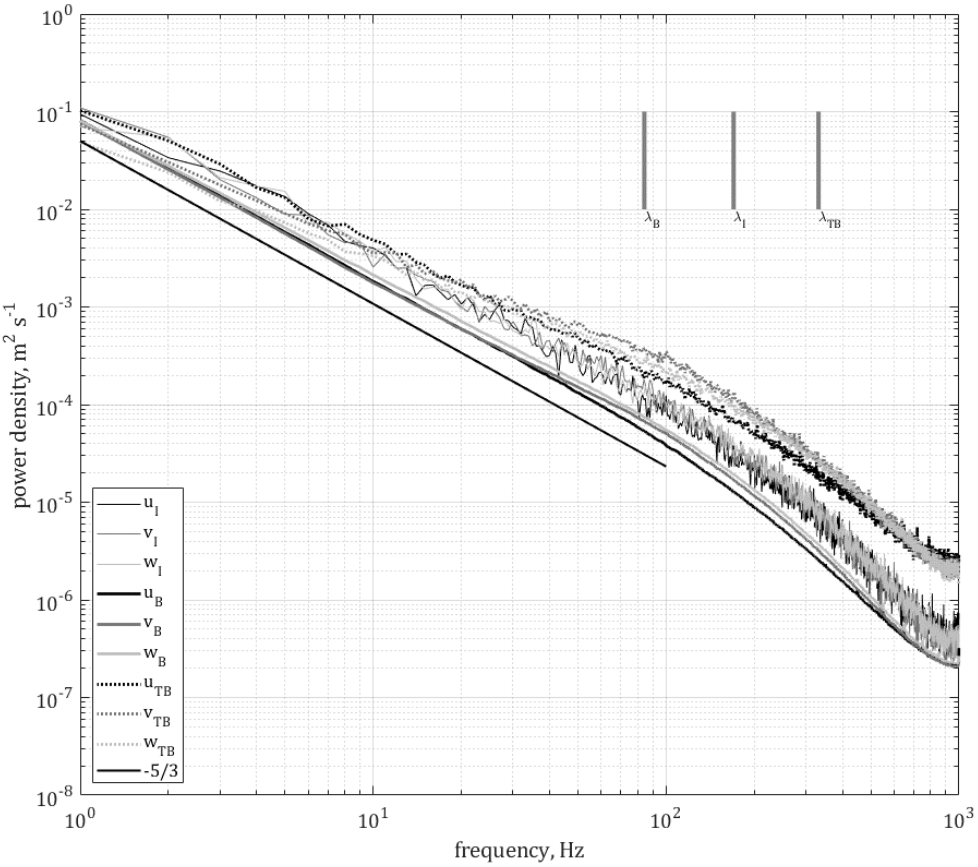

Figure 5.8 Mean power density spectra of velocity fluctuations of all minute-long ensembles. The colors black, dark grey, and light grey represent u, v, w respectively. The curves types represent different period types in the ensembles obtained with $\tau^* = 1.0$: thick, thin, and dotted curves represent background turbulence, intermediate, and turbulent bursting. The grey vertical lines represent the Taylor scale corresponding mean frequency for background turbulence (λ_B), intermediate(λ_I), and turbulent bursting (λ_{TB}) periods.

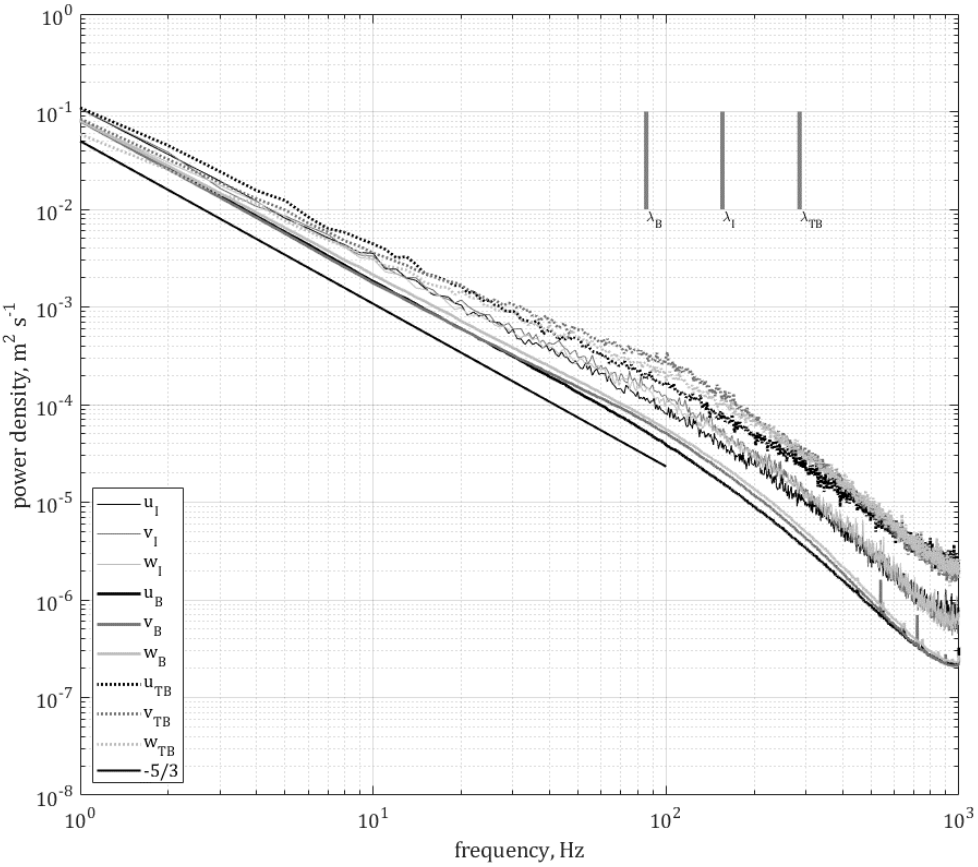

Figure 5.9 Mean power density spectra of velocity fluctuations of all minute-long ensembles. The colors black, dark grey, and light grey represent u, v, w respectively. The curves types represent different period types in the ensembles obtained with $\tau^* = 2.0$: thick, thin, and dotted curves represent background turbulence, intermediate, and turbulent bursting. The grey vertical lines represent the Taylor scale corresponding mean frequency for background turbulence (λ_B), intermediate(λ_I), and turbulent bursting (λ_{TB}) periods.

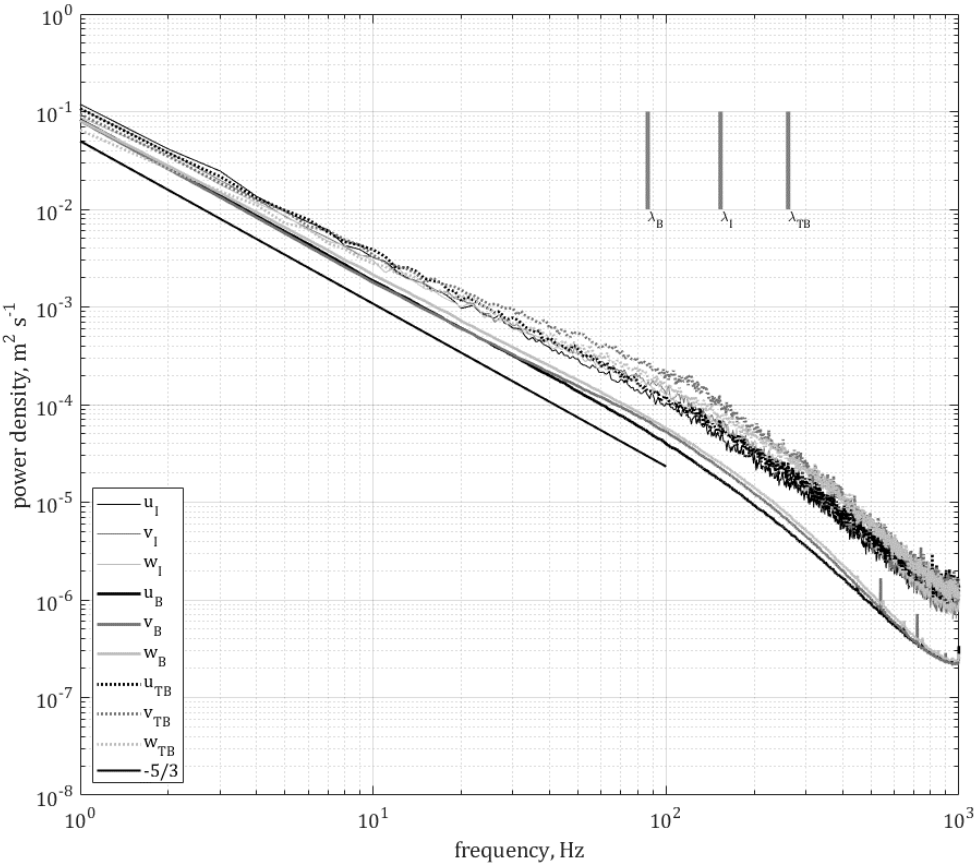

Figure 5.10 Mean power density spectra of velocity fluctuations of all minute-long ensembles. The colors black, dark grey, and light grey represent u, v, w respectively. The curves types represent different period types in the ensembles obtained with $\tau^* = 3.0$: thick, thin, and dotted curves represent background turbulence, intermediate, and turbulent bursting. The grey vertical lines represent the Taylor scale corresponding mean frequency for background turbulence (λ_B), intermediate(λ_I), and turbulent bursting (λ_{TB}) periods.

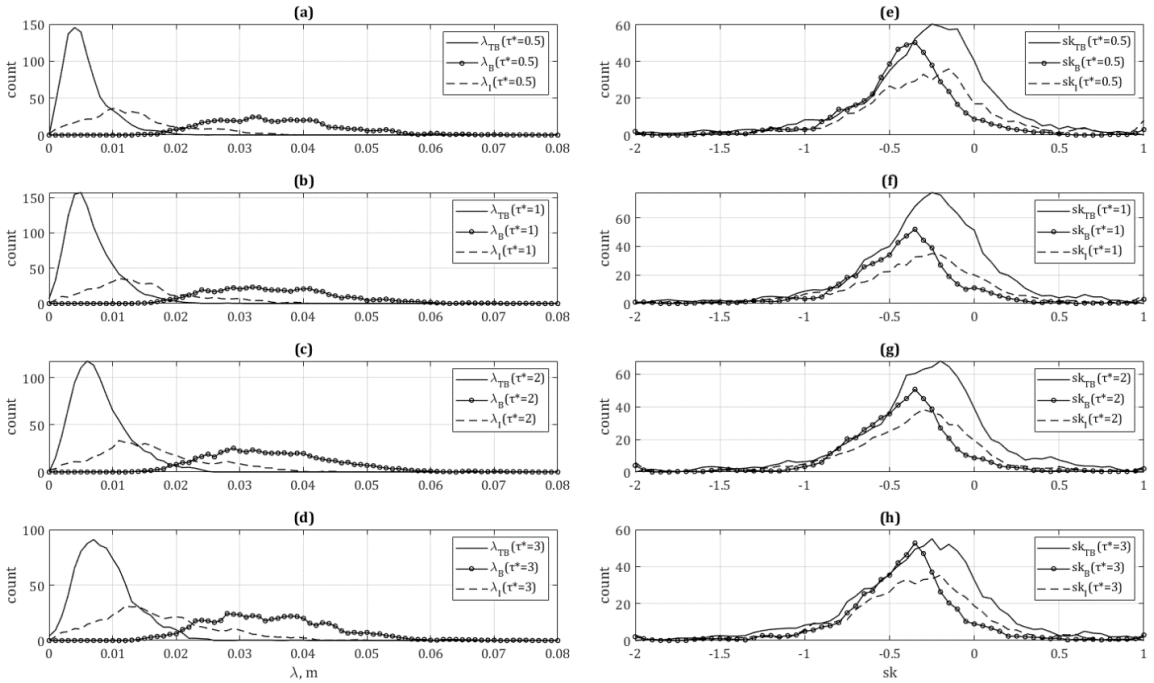

Figure 5.11 Distribution of Taylor microscale, λ, and velocity derivative skewness, Sk, in the streamwise direction are presented at various τ^* values. The distinction between periods was made using $\tau^* = 0.5, 1.0, 2.0, 3.0$ for background turbulence, intermediate, and turbulent bursting periods, in black curves, in black curves with a circle, and in black dashed curves respectively. These distributions were additionally fit with an exponentially modified normal distribution to obtain the following representative peaks: (a) $\tau^* = 0.5$ with peaks corresponding to $\lambda_B = 0.036\,, \lambda_I = 0.014, \lambda_{TB} = 0.0053\,m$; (b) $\tau^* = 1.0$ with peaks corresponding to $\lambda_B = 0.035, \lambda_I = 0.015, \lambda_{TB} = 0.0066\,m$; (c) $\tau^* = 2.0$ with peaks corresponding to $\lambda_B = 0.035, \lambda_I = 0.016, \lambda_{TB} = 0.0077\,m$; (d)$\tau^* = 3.0$ with peaks corresponding to $\lambda_B = 0.035, \lambda_I = 0.017, \lambda_{TB} = 0.0087\,m$;(e) $\tau^* = 0.5$ with peaks corresponding to $Sk_B = -0.38, Sk_I = -0.29, Sk_{TB} = -0.24$; (f) $\tau^* = 1.0$ with peaks corresponding to $Sk_B = -0.40, Sk_I = -0.29, Sk_{TB} = -0.27$; (g) $\tau^* = 2.0$ with peaks corresponding to $Sk_B = -0.41, Sk_I = -0.31, Sk_{TB} = -0.29$; (h) $\tau^* = 3.0$ with peaks corresponding to $Sk_B = -0.39, Sk_I = -0.32, Sk_{TB} = -0.31$;

To conclude the window size sensitivity analysis, we recommend the use of the statistical and conditional spectral analysis presented above for confirmation of the threshold value ε_T selection and the non-dimensional averaging window length τ^*. The parameters selected here, while shown to be justified for the examined data set, most certainly will need an adjustment for use with different turbulent flow fields. Depending on various turbulent characteristics of the flow and the relevant burst generation mechanism.

5.3.2 Temperature dissipation rate during bursting periods

The ability to accurately detect periods of turbulent bursts in the velocity field measurements naturally calls for investigation of burst generation mechanism, preferably incorporating a flow visualization technique. Such an investigation can also be supported by examination of the various flow field scalar dissipation rates—such as the temperature, pressure, water vapor or some contaminant concentration, depending on the nature of a flow. Producing correlations between the scalar dissipation rates and those of the turbulent bursting and background velocity field requires obtaining the records of the relevant scalar fluctuations at resolution like that of the velocity field. Here we explore the temperature dissipation rate statistics aligned with detected bursting periods. While measured at much lower spatiotemporal resolution by the sonic, the observed trends of the temperature dissipation rates serve as an example of scalar investigation in view of bursts and demonstrate the technique for proper normalization.

Using the same procedure and thresholds as above, the *turbulent bursting*, *intermediate and background turbulence* periods were identified in all available ensembles and examined separately. Of interest, while examining a buoyancy-driven BL flow, were the possible changes in the temperature (T) behavior across the turbulent bursting periods. Changes in T gradient variance are expected due to increased mixing during bursting events. And indeed, a significant decrease in T variations was first noted by visual examination of the time series in the duration of a bursting period indicating uniform mixing.

Eradication of the temperature gradient variance in the duration of bursting periods (i.e. the mixing of the fluid) can be quantified using the scalar (temperature in our case) dissipation rate (θ) along with proper normalization, for comparison with the normalized TKE dissipation rate variations. Each sonic-temperature time

series of one-minute long ensemble was originally sampled at 2 kHz to correspond with the sampling frequency of the hotfilm records and ensure synchronization between the two instruments recordings. Here, we down sampled the sonic provided temperature to 32 Hz, its declared frequency response, using sliding window averages. The instantaneous temperature dissipation rate is calculated as [119]:

$$\theta = \frac{3\alpha}{\bar{u}^2}\overline{\left(\frac{\partial T'}{\partial t}\right)^2}, \tag{5.10}$$

where α is the thermal diffusivity of the fluid.

Next, these instantaneous temperature dissipation rates were normalized similarly to the instantaneous TKE dissipation rate fluctuations, producing variations of

$$\theta_N = \theta''/\{\theta''\}, \tag{5.11}$$

while,

$$\theta'' = \theta - \langle\theta\rangle. \tag{5.12}$$

A MATLAB® script detailing the computation of θ_N is also provided in the Appendix.

Unlike in the case of previously described TKE dissipation rate fluctuations, here the mean was used for calculation of averages. As per the sonic-limited frequency response, outliers were not expected here, any observed statistical variations may only be of large scales. The spatial derivatives from [119] are converted to temporal derivatives using the Taylor hypothesis resulting in Equation (5.10), with smaller values indicating the scalar is well mixed. The gradients are squared yielding only positive values that are to be averaged over time. In Equation (5.12), the mean of the signal is removed and in Equation (5.11) these new 'instantaneous variations' of the temperature dissipation rate are normalized using

their respective rms. Therefore, negative θ_N values indicate periods during which the temperature mixing is at higher level compared to that of the background turbulence.

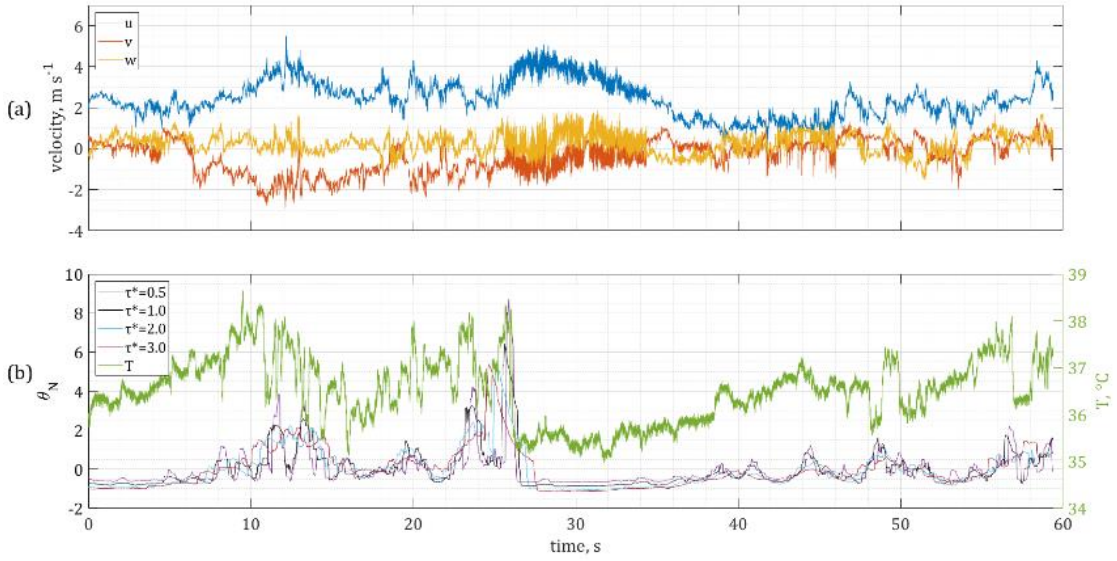

Figure 5.12 (a) Time series of instantaneous velocity components (u, v, w) in blue, orange, and yellow, obtained on 09-Aug-2015 at 14:20; (b) The left axis displays θ_N as obtained using $\tau^* = 0.5, 1.0, 2.0, 3.0$ in purple, black, blue and red, respectively. The right axis displays the original oversampled temperature signal obtained by the sonic.

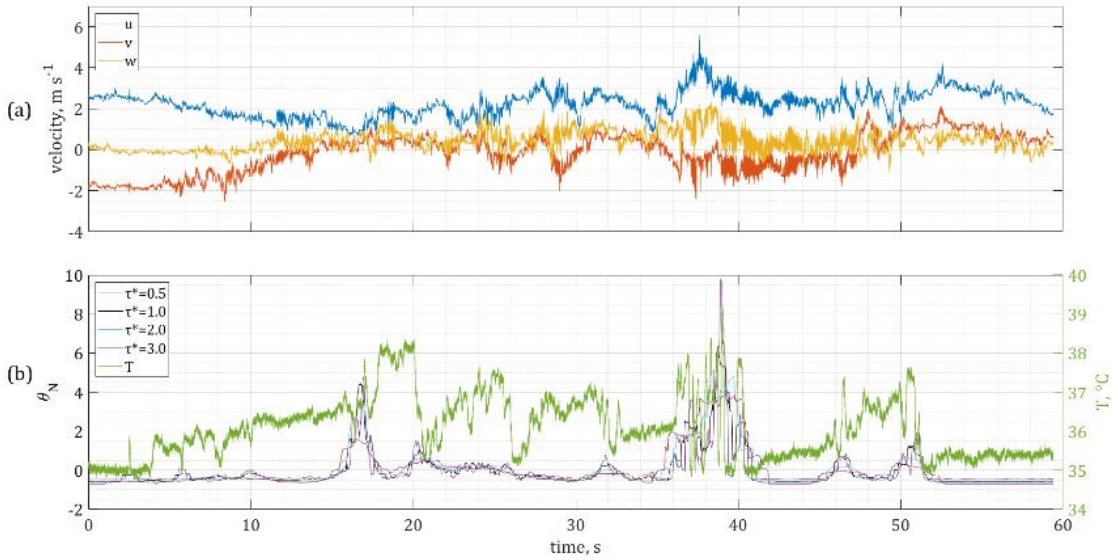

Figure 5.13 (a) Time series of instantaneous velocity components (u, v, w) in blue, orange, and yellow, obtained on 08-Aug-2015 at 12:28; (b) The left axis displays θ_N as obtained using $\tau^* = 0.5, 1.0, 2.0, 3.0$ in purple, black, blue and red, respectively. The right axis displays the original oversampled temperature signal obtained by the sonic.

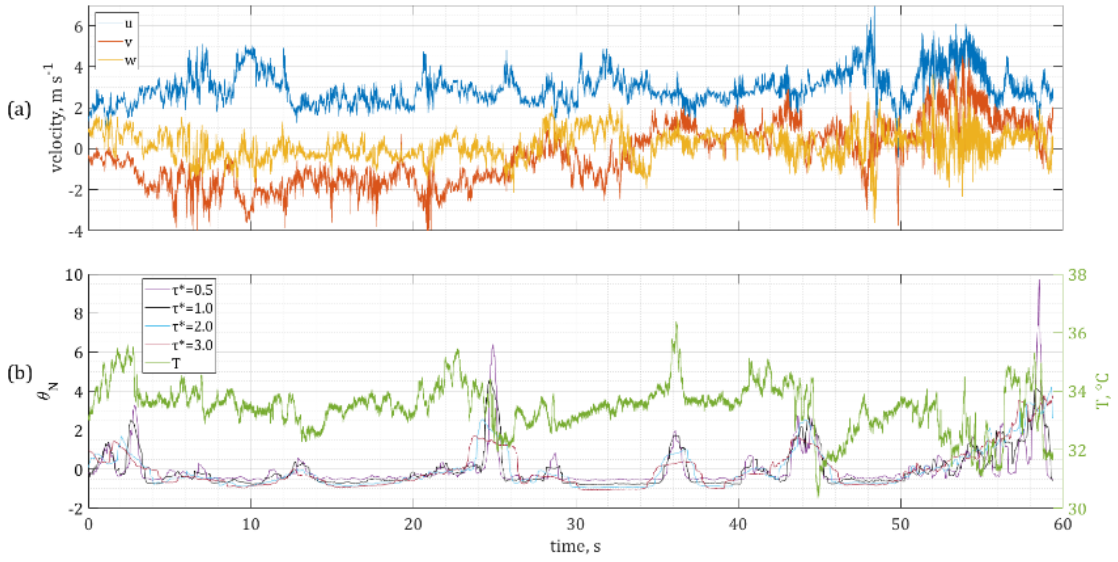

Figure 5.14 (a) Time series of instantaneous velocity components (u, v, w) in blue, orange, and yellow, obtained on 09-Aug-2015 at 14:20; (b) The left axis displays θ_N as obtained using $\tau^* = 0.5, 1.0, 2.0, 3.0$ in purple, black, blue and red, respectively. The right axis displays the original oversampled temperature signal obtained by the sonic.

During (or immediately following) bursting events, a decay of temperature dissipation rate, θ, is expected. Variations of θ_N derived using $\tau^* = 0.5, 1.0, 2.0, 3.0$

are presented in Figures 5.12-5.14 along with the corresponding time series of the temperature fluctuations obtained using the sonic. These Figures correspond to the same representative minutes displayed in Figures 5.1-5.3. Temperature dissipation rates during bursting events were found to exhibit a significantly different behavior from no-burst periods and the trend of the temperature gradient variance suppression was investigated further.

To examine the correlation between the appearance of bursting periods and the decrease in θ_N, the following processing was implemented on the entire data set. An ensemble average value $\langle\theta_N\rangle_{TB}$ representing each bursting period was derived separately for $\tau^* = 0.5, 1.0, 2.0, 3.0$; while bursting period identification for each was performed using the same values of τ^*. Figure 5.15 presents the histograms of $\langle\theta_N\rangle_{TB}$ values for the four τ^* values. The distributions were fit with an exponentially modified normal distribution, obtaining statistical parameters representative of the examined periods. The fit-obtained averages, μ, ranging between -0.61 to -0.80 and standard deviation of $\sigma = 0.1 - 0.23$, i.e. most $\langle\theta_N\rangle_{TB} \leq -0.4$. The results indicated that the temperature dissipation rate experiences a significant decrease during most bursting periods, indicating higher level of scalar mixing and supporting the observations made by visually examining the time series.

The suppression of the temperature dissipation rate relative to those characterizing the background turbulent flow shows a significant statistical variation, but—given the limited frequency response of the sonic—no physical interpretations can be made based on this data set beyond the demonstration of the ability to detect such variations using the new method. Taking these findings into consideration, for future studies it is recommended to perform a series of higher spatiotemporal resolution observations of a scalar of interest, e.g. using cold wires

for temperature measurements, along with flow visualization techniques to better understand the physics of the flow.

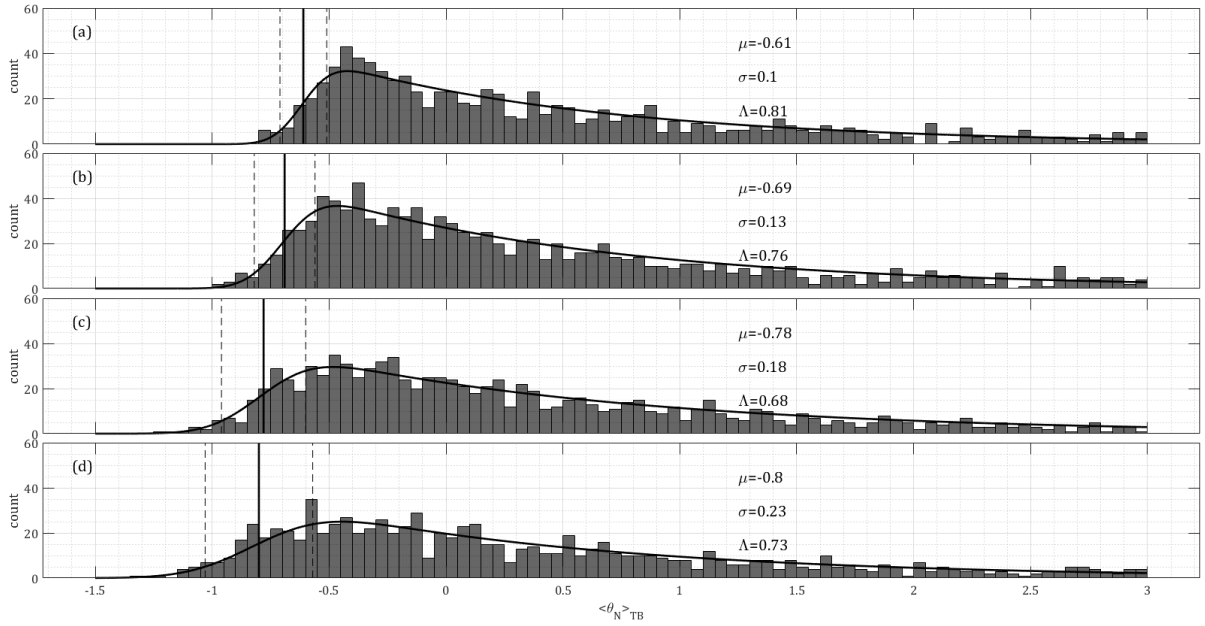

Figure 5.15 Distribution of average $\langle\theta_N\rangle_{TB}$ for each identified bursting period for a given a τ^* value. The black curve represents the exponentially modified Gaussian fit of the distribution with the derived average μ, standard deviation σ, both plotted on the distribution as the black full and dashed vertical lines, respectively. The mean exponential component of the distributions is Λ. (a) Results for (a) $\tau^* = 0.5$; (b)$\tau^* = 1.0$; (c) $\tau^* = 2.0$; (d) $\tau^* = 3.0$.

5.4 Expected contribution and concluding remarks

Motivated by the importance of gaining a better understanding of turbulent flows, and especially the need to resolve the smallest scales of turbulent fluctuations correctly, a new detection method allowing identification and quantification of elevated velocity fluctuation density, i.e. bursting periods, was presented. Addressing one of the most complex problems of identification of bursts in turbulent background flow, the new automated method is shown to be able to detect turbulent bursting periods in turbulent velocity field fluctuation records both accurately and automatically after proper selection of an appropriate threshold (ε_T) and resolution

(τ^*) based on the initial assessments using the velocity time series. Building upon the method of Kit *et. al.* [58], the identification of bursts is achieved by marking the time periods of elevated instantaneous TKE dissipation rate levels obtained using sliding window averaging. The non-dimensional window length (τ^*) is prescribed by the turbulent flow characteristics obtained in pre-processing of the velocity field data: the Taylor microscale and the typical minimal burst period length. The ensemble is then appropriately normalized providing a discrimination (a two-fold increase of the normalized instantaneous TKE dissipation rate) between bursting and burst-free periods within the turbulent velocity fluctuation ensembles.

A step-by-step guide of the automated procedure is provided below. Two input parameters should be selected prior to automation; the first is τ^* and the second is ε_T.

1. Visually examine the time series of velocity fluctuations and estimate the typical bursting interval length (τ_{ATB}).
2. Calculate the Taylor time scale, τ_λ, of each ensemble. Alternatively, a different characteristic time scale can be used (Kolmogorov or Horizontal time scale), with the selection based on the nature of the examined flow.
3. Select a value of τ^* from $10(\tau_\lambda/\tau_{ATB}) < \tau^* < 2$ to obtain statistics averaged over sufficiently long periods.
4. Compute the normalized instantaneous TKE dissipation rate (ε_N) from Equations (5.3)-(5.8) and visually examine the variations of ε_N.
5. Select an appropriate threshold value ε_T. A good starting point would be selecting a two-fold increase from background turbulence values, $\varepsilon_T = 2$. Adjust the actual threshold value after examining the detected bursts

maps as in Figures 5.1-5.3 and additional statistics and spectra as in Figures 5.4-5.11.

6. Identify turbulent bursting periods and calculate the appropriate statistics.

The developed method was tested and its implementation was demonstrated using velocity field records from a field study of turbulent, thermally driven, upslope BL flow experiencing diurnal fluctuations due to solar heating of the slope [12, 110]. Sensitivity to the selected averaging non-dimensional window size τ^* was examined, and it was shown that within the selected range the actual window size is of lesser importance. The results were also shown to converge with the Kit e*t. al.* [58] results for the window size corresponding the total velocity record ensemble length. Statistical examination of the results, including exceedance probability function and spectral analysis of bursting and burst-free periods, strongly supported the selection of a two-fold threshold for the normalized instantaneous TKE variations for detection of bursting periods in the examined data. Spectra of burst-free periods showed characteristics closely resembling those of Kolmogorov's theory, while the bursting periods demonstrated significant deviations. We have presented the distribution of the Taylor microscale and the velocity derivative skewness for each period separately as empirical evidence for the change in flow behavior in the duration of turbulent busting events. The burst-free periods were characterized by the velocity derivative skewness values resembling that of -0.4, as observed in wind tunnel studies of homogeneous freely decaying turbulence. Moreover, the Taylor microscale average values during bursting periods were observed to be approximately twice smaller than those during burst-free periods.

All together these findings indicated a successful identification and distinction between bursting periods and burst-free background turbulence.

For future implementation, it is recommended to apply the above mentioned statistical analysis of window size sensitivity and the conditional spectral analysis for selection of the best suitable threshold and window size values, in view of the turbulent flow characteristics and the nature of burst generation mechanism of any examined flow field.

Implementation of the new method ensued successful identification of bursting periods longer than $\tau^*_{min} = 0.5$ and allowed investigation of the temperature dissipation rate behaviour in correlation with the occurrence of bursts. A significant decrease in the temperature gradient variance was found to accompany most of the bursting periods indicating the better-mixed nature of the flow in the duration of a bursting event relative to the background turbulence.

Implementation of the averaging window size selection, based on the flow parameters and proper normalization of the TKE dissipation rate variations, render the presented bursting period identification method as potentially suitable for implementation in records across different flows, including flows characterized by significantly varying mean velocity, background turbulence intensity, and forcing conditions. Proper normalization of the TKE dissipation rate allows automated identification of bursts without the need of selection of physics-based thresholds and manual identification of suitable ensembles. Based on analysis of velocity field fluctuations obtained in a single point, this method is suitable for use with data produced in laboratory, field experiments, and that of detailed direct numerical simulations. The new method opens the possibility to produce analysis of new and existing data for the purpose of investigating possible burst generation mechanisms,

instabilities, scalar transport, and more to assist in improving NWP and GCM. In this work, we have also demonstrated the possible technique for producing correlations between the scalar dissipation rate and the occurrence of bursts. A proper normalization of scalar dissipation rate was suggested for future studies to better compare with the bursting period duration.

Chapter 6: Conclusions

6.1 Concluding remarks

More than 70% of urban areas are characterized by complex terrain which greatly influences the weather, microclimates, and pollution transfer or lack thereof. The complexity of the terrain along with the diurnal solar cycle introduce diurnal wind patterns. The physical understanding of these flows can be used for several engineering solutions. In the past decades, a great progress was made on understanding synoptic scale flow and valley flows, but much less research was conducted on slope flows. Of the research that was conducted, the majority focused on katabatic flows (down-slope).

This experimental study was conducted both in the laboratory and the field and mainly focuses on anabatic flows. These are upslope flows that occur on mountains and hills and are driven by the diurnal heating cycle. Anabatic flows are highly turbulent and unstable, which makes their investigation cumbersome relative to the other slope and valley flows in nature. The current state of field measuring instrumentation available includes low spatial and temporal resolution instruments, and the large dimensions of mountainous regions prevent the capturing of the mean picture describing the entire boundary layer (BL) behavior. This study presents laboratory scaled experiments to capture the mean BL behavior and advancements to field measuring techniques and their data analysis routines.

The first part (Chapter 3) of this dissertation detailed the highly controlled laboratory model experiments. The second part (Chapter 4) focused on the development of field measurement techniques. Finally, the third part (Chapter 5) presented a newly developed automated method of detection of turbulent bursting

periods, allowing effective separation and individual examination of the background turbulence and the intermittent turbulent bursts in anabatic and other turbulent BL flows.

Building off the most recent laboratory study examining upslope flow on a single smooth slope in a water tank, an added complexity was introduced to the model: a heated plateau at the apex of the slope resembling the shape of a truncated pyramid [27]. The model was uniformly heated to mimic solar radiation and a range of slope angles and plateau widths were examined. Particle Tracking Velocimetry (PTV) and Feature Tracking Visualization (FTV) were used to detect the upslope flow separation point and mean upslope velocity at the point of separation. The finite width of the plateau (D) and the geometric slope angle were expressed into an effective angle that was used for the BL separation prediction model. For effective angles of $17° < \beta_e < 45°$, the separation length was found to increase with the effective angle, yet when the effective angle was larger than 45°, the flow did not separate and was independent on the plateau width. In the sub-flow regime of $\beta \sim 15°$, the relationship between the separation length and the width of the plume for this case is observed to be $L_s/L_w \approx 0.29$. As expected, it was found that the mean upslope velocity at the point of separation (U_s) is dependent on the buoyancy flux, the effective slope angle, and the separation length and corresponded with the velocity scale proposed by Hocut et al. [7]. After presenting the empirical findings of thermally driven upslope flow in the presence of a plateau, the next step we took was to expand the laboratory scale modelling to a much larger volume, to observe much longer experimental durations, the three dimensionality of the flow, and the effect of roughness on the slopes.

The next set of laboratory experiments were conducted in a much larger tank and examined the flow behavior on a symmetric double slope configuration with various slope angles ranging from 5.7° to 45° at various heat fluxes in the range of $Q = 40 - 1000\ W/m^2$. These heat fluxes correspond to buoyancy fluxes in the range of $2 \times 10^{-8}\ m^2 s^{-3}\ to\ 5 \times 10^{-7}\ m^2 s^{-3}$. All experiments were run for two-hours with a sampling frequency of 5 Hz to examine the mean BL flow behavior. The along slope velocity profiles, the temperature profiles, and the Reynolds stress profiles are presented for all experiments. The shapes of most normalized profiles closely resemble each other. The examination of the shorter averaged profiles revealed the transient nature of the flow and highlighted the importance of the three-dimensionality of the flow.

The three-dimensionality of the flow revealed that the separation of the flow did not appear as the "classical" separation since it did not include backflow. Instead, it appeared as a breakup of the helical structure into two separate strands as if the flow does not separate from the slope itself, but that the BL splits into two structures. One that feeds the plume while the other continues to flow attached along the slope. We do, however, call it separation because the BL separates into two pieces, one of which that feeds the apex plume. The separation location was manually recorded using average vorticity maps. The variability was large for every angle, but a generally increasing trend of separation length was observed with an increase of the slope angle. It was concluded that this is due to the dominance of the three-dimensionality of the flow. Future examination of the transient nature and three-dimensionality of the flow should be considered and incorporated into the separation prediction models. The BL shapes were also examined and an empirical relationship of the shape factor as a function of Re and Pr was derived. Finally, the

relationship between two main driving forces of the flow were examined, the baroclinic torque and the vorticity advection. Both were found to present significant fluctuations with zero mean. Negative vorticity is just indicating the flow rotation direction, while negative baroclinic torque may be explained by the mixing and entrainment of cooler fluid by the 3D helical structures forming on the slope. The magnitude of vorticity advection fluctuations tends to increase along the slope, until it reaches that of the baroclinic torque. Consequently, in the lower part of the slope, where mean velocity is lower, the vorticity advection is small. It is observed to increase along the slope until it reaches values comparable to those of the baroclinic torque. Given the importance of the three-dimensionality of the flow, future studies of anabatic BL flow should examine the flow using 3D measurement tools.

As for the field measurements, two advancements of the up-to-date available fine-scale field measurement instrumentation and techniques were made: the new combo probe design and an automated calibration procedure. The previous design of the combo probe was geometrically constrained to a yaw-rotation range of 120°. The new design of the combo probe (Combo 10.0) enables the combo to realign the hotwires in any desirable angle of attack, or the complete 360°. The new design improves the rigidity of the probe and provides more consistency in the measurements because the probes are always in the same position inside the sonic control volume. It was deployed in the field (in an open sea environment) and was shown to be capable of operating properly and independently for weeks or months at a time.

Since the operation of the combo does not require any human intervention, we decided to automate the calibration procedure as well. Previously, the calibration procedure using artificial neural networks (NN) was based on hand-picking several

minutes to represent the entire set of measurements collected in an hour and to serve as the NN training set after low-pass filtering. We showed that using all low-pass filtered data from the sonic and hotwires to construct the training set and increasing the complexity of the NN provided acceptable results while fully automating the calibration process. The method testing was conducted in two types of environments, a controllable and non-controllable one. The controllable environment was a wind tunnel and the non-controllable environment is the data collected in the open sea. The examination of the new calibration method has an acceptable range of expected uncertainty. The voltage to velocity transfer function estimates are expected to vary up to a certain degree depending on the method chosen for approximation. The examples we presented include the "classical" calibration procedures using the calibrator data with the lookup table method and with the polynomial fitting method. Two separate computational procedures were presented for the lookup table alone, using four and two sub-probe configurations of the 4-wire hotfilms. The polynomial fitting approach was presented and was found to converge to different solutions (local minima) depending on the initial guess used.

After examining the variability between the "classical" transfer function evaluation procedures, we compared our proposed method to one of these classical methods. Our deep NN model that was trained with an extreme case of three types of flow regimes was shown to provide velocity fluctuation estimates resembling those from the lookup table. In some cases, it was shown to capture the coherence of the signal even better at a lower signal to noise ratio, while the lookup table captured all the noise. This implies that this method is robust enough to resolve turbulent measurements in varying field conditions. Although no conclusion can be

drawn on which transfer function calculation method is more accurate, we showed with certainty that the deviation between the commonly used methods and the newly proposed methods are of the same range. This simply means that hotwires *can* and *should* be implemented in the field along with the automatic calibration procedure.

The last part of the dissertation focuses on development of an automated method for detection of turbulent bursting phenomenon in complex turbulent flows. The accurate detection of bursting periods allows for effective distinction between the bursts and the background turbulence. The accurate detection of the phenomena enables independent analysis of both flow regimes and investigation of the burst generation mechanisms. Our developed method was built upon that of Kit et. al. [58], and the results obtained in both methods were found to correspond. The identification of bursts is accomplished by proper normalization of the 'instantaneous' TKE dissipation rate and identification of periods that exceed a pre-selected threshold. The threshold selection is not a physics-based selection. This study presented the findings of a 200% increase of the TKE dissipation rate relative to the background flow, enabling the use across different flow regimes without modifications. We tested the automated method on a field obtained dataset that examined anabatic flow using the combo [12], and provided the step-by-step guide and the complete code [110] for future studies to use. In addition to the bursting detection procedure, we demonstrated the possible technique for producing correlations between the scalar dissipation rate and the occurrence of bursts using proper normalization of the scalar dissipation rate to better compare with the bursting period duration.

6.2 Contributions and future research

The significance of this research lies in its expected contribution toward increasing the performance and accuracy of weather prediction models and possibly future pollution mitigation engineering solutions. We conducted an experimental investigation of the developing turbulent anabatic BL under various forcing and conditions in the laboratory. We made progress in improving the measuring capabilities of the combo probe, we automated the calibration procedure of the combo probe, and we developed an automated fine-scale turbulent bursting detection method. These, together, provide a comprehensive understanding of the anabatic BL flow behavior and expand the tool set that can be used to further examine and study these flows both in the labs and in the field. Some examples include:

1. Use of close to real-time fine-scale turbulent field measurements can assist in improving prediction/forecast models and in improving the understanding of naturally occurring wind flows. It is especially useful with changing field conditions or non-stationary measuring stations, i.e. probes placed on moving platforms such as moving vehicles, boats, drones.
2. An experimental dataset of anabatic flow that can be used for comparison with numerical simulations. This dataset provided empirical relationships that can contribute to the ability of producing more accurate weather forecast models, investigation of climate processes, and understanding of the processes governing pollution transport in complex terrains.
3. The development of an automated turbulent bursting detection method can assist in gaining a better understanding of turbulent flows, and especially the need to resolve the smallest scales of turbulent fluctuations correctly. The new method opens the possibility to analyze new and existing data and attempt to

investigate burst generation mechanisms, instabilities, scalar transport, and more. Eventually this can assist in improving numerical weather prediction models and climate change forecasting models as well.

Future works are encouraged to focus on the transient nature of anabatic flows, more specifically their three-dimensionality. While the current study had insufficient temperature measurements, the thermocouple grid was too coarsely spaced and did not cover the entire boundary layer in some experiments, we recommend deploying dense grids of temperature sensors or use non-contact methods. Velocity measurements near the boundary had a relatively low signal-to-noise ratio and future studies should use slope parallel laser sheets to avoid that. An increase in the spatial and temporal resolution of the PIV is also recommended. Finally, future studies should introduce uniform and gradually varying slope roughness, and additional geometries such as slope breaks (i.e. change of slope along the mountain). Together, these would provide a better understanding of the anabatic BL behavior and would provide a broader basis for modelling of such flow.

Appendix

Below is a list of appendices referenced in the text.

Appendix I: MATLAB® code for automated burst detection

```
function [EpsilonN,ThetaN] = GettingNormCurves(u,v,w,T,Fs,Tau,TauATB,nu,alpha)
%       MATLAB® code written in version 2018b.
%u      instantaneous streamwise velocity component, m/s
%v      instantaneous longitudinal velocity component, m/s
%w      instantaneous transverse velocity component, m/s
%T      instantaneous temperature, degrees Celsius
%Fs     sampling frequency, Hz
%Tau    non-dimensional window size
%TauATB approximated bursting period length from visual observation, s
%nu     kinematic viscosity, m^2/s
%alpha  thermal diffusivity of the fluid, m^2/s
%EpsilonN   Normalized instantaneous TKE dissipation rate
%ThetaN    Normalized instantaneous temperature (scalar) variance dissipation rate

N=round(Fs*Tau*TauATB,0); %must have an integer for a window size

%% Defining normalized TKE dissipation rates
um=movmedian(u,N,'omitnan');
vm=movmedian(v,N,'omitnan');
wm=movmedian(w,N,'omitnan');
ut=u-um;
vt=v-vm;
wt=w-wm;

% Equations (4)-(6) from the text
eu=(15*nu./um(1:end-1).^2).*movmedian((diff(ut).*Fs).^2,N,'omitnan');
ev=(7.5*nu./um(1:end-1).^2).*movmedian((diff(vt).*Fs).^2,N,'omitnan');
ew=(7.5*nu./um(1:end-1).^2).*movmedian((diff(wt).*Fs).^2,N,'omitnan');
% Equation (3) from the text
epsilon_m=(eu+ev+ew)./3;
% Equation (7) from the text
epsilon_m_t=(epsilon_m-nanmedian(epsilon_m));
% Equation (8) from the text
EpsilonN=epsilon_m_t./rms(epsilon_m_t);

%% Defining normalized scalar (temperature) variance dissipation rate
Tm=movmean(T,N,'omitnan');
Tt=T-Tm;
%define the instantaneous temperature variance dissipation rate
[Tx,~]=gradient(Tt);
% Equation (10) from the text
Theta=(3.*alpha./um.^2).*movmean((Tx.*Fs).^2,Num,2,'omitnan');

% Equation (12) from the text
Thetat= Theta-nanmean(Theta,2);
% Equation (11) from the text
ThetaN= Thetat./rms(Thetat,2);

end
```

References

1. Baines PG, Manins PC (1989) The principles of Labratory Modeling of Stratified Atmospheric Flows over Complex Terrain. J Appl Meteorol 28:1213–1225
2. Baines PG (1995) Topographic effects in stratified flows. Cambridge University Press
3. Belcher SE, Hunt JCR (1998) Turbulent Flow Over Hills and Waves. Annu Rev Fluid Mech 30:507–538. https://doi.org/10.1146/annurev.fluid.30.1.507
4. Boyer DL, Davies PA (2000) Labratory studies of orographic effects in rotating and stratified flows. Annu Rev Fluid Mech 32:165–202
5. Whiteman CD (2000) Mountain Meteorology: Fundamentals and Applications. Oxford University Press, New York
6. Princevac M, Fernando HJSS (2007) A criterion for the generation of turbulent anabatic flows. Phys Fluids 19:1051021–1051027. https://doi.org/10.1063/1.2775932
7. Geerts B, Miao Q, Demko JC (2008) Pressure Perturbations and Upslope Flow over a Heated, Isolated Mountain. Mon Weather Rev 136:4272–4288. https://doi.org/10.1175/2008MWR2546.1
8. Zardi D, Whiteman CD (2012) Diurnal mountain wind systems. In: Mountain Weather Research and Forecasting. Berlin, pp 35–119
9. Kit E, Cherkassky A, Sant T, Fernando HJS (2010) In Situ Calibration of Hot-Film Probes Using a Collocated Sonic Anemometer: Implementation of a Neural Network. J Atmos Ocean Technol 27:23–41. https://doi.org/10.1175/2009JTECHA1320.1
10. Vitkin L, Liberzon D, Grits B, Kit E (2014) Study of in-situ calibration performance of co-located multi-sensor hot-film and sonic anemometers using a 'virtual probe' algorithm. Meas Sci Technol 25:75801. https://doi.org/10.1088/0957-0233/25/7/075801
11. Hocut CM, Liberzon D, Fernando HJS (2015) Separation of upslope flow over a uniform slope. J Fluid Mech 775:266–287. https://doi.org/10.1017/jfm.2015.298
12. Hilel Goldshmid R, Liberzon D (2018) Obtaining turbulence statistics of thermally driven anabatic flow by sonic-hot-film combo anemometer. Environ Fluid Mech. https://doi.org/10.1007/s10652-018-9649-x
13. Deardorff JW, Willis GE (1987) Turbulence within a baroclinic laboratory mixed layer above a sloping surface. J Atmos Sci 44:772–778
14. Chen R, Berman N, Boyer D, Fernando HJS (1999) Physical model of nocturnal drainage flow in complex terrain. Contrib to Atmos Phys 72:219–242
15. Long RR (1955) Some Aspects of the Flow of Stratified Fluids. Tellus 7:341–357
16. Fultz D, Long RR, G. O, et al (1959) Studies of Thermal Convection in a Rotating Cylinder with Some Implications for Large Scale Atmospheric Motions. Literary Licensing, LLC, Whitefish
17. Incropera FP, DeWitt DP, Bergman TL, Lavine AS (2007) Fundamentals of Heat and Mass Transfer. Water 6th:997. https://doi.org/10.1016/j.applthermaleng.2011.03.022
18. Stull RB (1988) An Introduction to Boundary Layer Meteorology. Kluwe. Academic Publishe.s, Netherlands
19. Incorpera FP, Dewitt D., Bergman TL, Lavine A. (2007) Fundmentals of Heat and Mass Transfer
20. Chow FK, De Wekker SFJ, Snyder (2015) Mountain Weather and Research Forecasting
21. Incropera FP, DeWitt DP, Bergman TL, Lavine AS (2007) Introduction to Heat Transfer
22. Kays WM, Crawford ME (1980) Convective Heat and Mass Transfer

23. Osborne DG, Incropera FP (1985) Experimental study of mixed convection heat transfer for transitional and turbulent flow between horizontal, parallel plates. hf J Hear Mass Trmfer 28:1337–1344. https://doi.org/10.1016/0017-9310(85)90164-4
24. Hunt JCR, Fernando HJS, Princevac M (2003) Unsteady Thermally Driven Flows on Gentle Slopes. J Atmos Sci 60:2169–2182. https://doi.org/10.1175/1520-0469(2003)060<2169:UTDFOG>2.0.CO;2
25. Schlichting H, Shapiro A (1968) Boundary layer theory
26. Chen R-RR, Berman NS, Boyer DL, Fernando HJS (1996) Physical Model of Diurnal Heating in the Vicinity of a Two-Dimensional Ridge. J Atmos Sci 53:62–85. https://doi.org/10.1175/1520-0469(1996)053<0062:PMODHI>2.0.CO;2
27. Goldshmid RH, Bardoel SL, Hocut CMM, et al (2018) Separation of upslope flow over a plateau. Atmosphere (Basel) 9:. https://doi.org/doi:10.3390/atmos9050165
28. Hilel R, Liberzon D (Advisor) (2016) Turbulence of anabatic (up-slope) thermally driven flow. Thesis (Master's)--Technion - Isr. Inst. Technol. Fac. Civ. Environ. Eng.
29. Goldshmid RH, Liberzon D (2020) Automated identification and characterization method of turbulent bursting from single-point records of the velocity field. Meas Sci Technol 31:105801. https://doi.org/10.1088/1361-6501/ab912b
30. Zardi D, Whiteman CD, Zardi D, Whiteman CD (2012) Diurnal mountain wind systems. In: Mountain Weather Research and Forecasting. Berlin, pp 35–119
31. Fernando HJS (2010) Fluid Dynamics of Urban Atmospheres in Complex Terrain. Annu Rev Fluid Mech 42:365–389. https://doi.org/10.1146/annurev-fluid-121108-145459
32. Mayr GJ, Armi L, Gohm A, et al (2007) Gap flows: Results from the Mesoscale Alpine Programme. Q J R Meteorol Soc 133:881–896. https://doi.org/10.1002/qj.66
33. Lu R, Turco RP (1994) Air Pollutant Transport in a Coastal Environment. Part I: Two-Dimensional Simulations of Sea-Breeze and Mountain Effects. American Meteorological Society
34. Crook NA, Tucker DF (2005) Flow over heated terrain. Part I: Linear theory and idealized numerical simulations. Mon Weather Rev 133:2552–2564. https://doi.org/10.1175/MWR2964.1
35. Banta RM (1984) Daytime Boundary-Layer Evolution over Mountainous Terrain. Part 1: Observations of the Dry Circulations. American Meteorological Society
36. Chao WC (2012) Correction of excessive precipitation over steep and high mountains in a GCM. J Atmos Sci 69:1547–1561. https://doi.org/10.1175/JAS-D-11-0216.1
37. Fast JD, De Foy B, Rosas FA, et al (2007) A meteorological overview of the MILAGRO field campaigns. Atmos Chem Phys 7:2233–2257. https://doi.org/10.5194/acp-7-2233-2007
38. Whiteman CD, Zhong S, Bian X, et al (2000) Boundary layer evolution and regional-scale diurnal circulations over the Mexico Basin and Mexican plateau. J Geophys Res Atmos 105:10081–10102. https://doi.org/10.1029/2000JD900039
39. Kleinman LI, Springston SR, Daum PH, et al (2008) The time evolution of aerosol composition over the Mexico City plateau. Atmos Chem Phys 8:1559–1575. https://doi.org/10.5194/acp-8-1559-2008
40. de Foy B, Caetano E, Magaña V, et al (2005) Mexico City basin wind circulation during the MCMA-2003 field campaign. Atmos Chem Phys 5:2267–2288. https://doi.org/10.5194/acp-5-2267-2005
41. Raga GB, Baumgardner D, Kok G, Rosas I (1999) Some aspects of boundary layer evolution in Mexico City. Atmos Environ 33:5013–5021. https://doi.org/10.1016/S1352-2310(99)00191-0
42. Baumgardner D, Raga GB, Kok G, et al (2000) On the evolution of aerosol properties at a

mountain site above Mexico City. J Geophys Res Atmos 105:22243–22253. https://doi.org/10.1029/2000JD900299

43. Reuten C, Steyn DG, Strawbridge KB, Bovis P (2005) Observations of the relation between upslope flows and the convective boundary layer in steep terrain. Boundary-Layer Meteorol 116:37–61. https://doi.org/10.1007/s10546-004-7299-7
44. Reuten C, Steyn DG, Allen SE (2007) Water tank studies of atmospheric boundary layer structure and air pollution transport in upslope flow systems. J Geophys Res Atmos 112:1–17. https://doi.org/10.1029/2006JD008045
45. De Wekker SFJ (2008) Observational and numerical evidence of depressed convective boundary layer heights near a mountain base. J Appl Meteorol Climatol 47:1017–1026. https://doi.org/10.1175/2007JAMC1651.1
46. Serafin S, Zardi D (2010) Daytime heat transfer processes related to slope flows and turbulent convection in an idealized mountain valley. J Atmos Sci 67:3739–3756. https://doi.org/10.1175/2010JAS3428.1
47. Serafin S, Zardi D (2010) Structure of the Atmospheric Boundary Layer in the Vicinity of a Developing Upslope Flow System: A Numerical Model Study. J Atmos Sci 67:1171–1185. https://doi.org/10.1175/2009JAS3231.1
48. Fernando HJSS, Lee SM, Anderson J, et al (2001) Urban Fluid Mechanics: Air Circulation and Contaminant Dispersion in Cities. Environ Fluid Mech 1:107–164. https://doi.org/10.1023/A:1011504001479
49. Liberzon D, Shemer L (2011) Experimental study of the initial stages of wind waves' spatial evolution. J Fluid Mech 681:462–498. https://doi.org/10.1017/jfm.2011.208
50. Kline SJ, McClintock F. (1953) Describing uncertainties in single-sample experiments - Technion Israel Institute of Technology. Mech Eng 75:3–8
51. Chen CC, Labhabi A, Chang HC, et al (1991) Spanwise pairing of finite-amplitude longitudinal vortex rolls in inclined free-convection boundary layers. J Fluid Mech 231:73–111. https://doi.org/10.1017/S0022112091003324
52. Rouse H, Yih CS, Humphreys HW (1952) Gravitational Convection from a Boundary Source. Tellus 4:201–210. https://doi.org/10.3402/tellusa.v4i3.8688
53. Adrian RJRJ, Westerweel J (2011) Particle Image Velocimetry
54. Raffel M, Willert CE, Wereley ST, Kompenhans J Particle Image Velocimetry
55. Goldshmid RH, Liberzon D (2020) Experimental data revealing the 3D behavior of anabatic flow
56. Wu Y, Christensen KT (2006) Population trends of spanwise vortices in wall turbulence. J Fluid Mech 568:55–76. https://doi.org/10.1017/S002211200600259X
57. Fernando H, Pardyjak ER, Di Sabatino S, et al (2015) The materhorn : Unraveling the intricacies of mountain weather. Bull Am Meteorol Soc 96:1945–1968. https://doi.org/10.1175/BAMS-D-13-00131.1
58. Kit E, Hocut C, Liberzon D, Fernando H (2017) Fine-scale turbulent bursts in stable atmospheric boundary layer in complex terrain. J Fluid Mech 833:745–772. https://doi.org/10.1017/jfm.2017.717
59. Shani-Zerbib A, Goldshmid R, Liberzon D (2019) Observations of water waves and wind-wave interactions in the Gulf of Aqaba (Eilat). In: 72nd Annual Meeting of the APS Division of Fluid Dynamics
60. Shani-Zerbib A, Rivlin A, Liberzon D (2018) Data Set of Wind–Waves Interactions in the Gulf of Aqaba. Int J Ocean Coast Eng 01: https://doi.org/doi.org/10.1142/S2529807018500033

61. Shani-Zerbib A, Liberzon D (2018) Data set of wind-waves interactions in the Gulf of Eilat (IUI), June 2017
62. Bruun HH (1995) Hot wire anemometry : principles and signal analysis. Oxford University Press
63. Van Dijk A, Nieuwstadt FTM (2004) The calibration of (multi-)hot-wire probes. 2. Velocity-calibration. Exp Fluids 36:550–564. https://doi.org/10.1007/s00348-003-0676-z
64. Oncley SP, Friehe CA, Larue JC, et al (1996) Surface Layer Fluxes Profiles and Turbulence Measurements over Uniform Terrain under Near Neutral Conditions. J Atmos Sci 53:1029–1044
65. Poulos GS, Semmer S, Militzer J, Maclean G (2006) A NOVEL METHOD FOR THE STUDY OF NEAR-SURFACE TURBULENCE USING 3-D HOT-FILM ANEMOMETRY: OTIHS. In: 17th Symp. on Boundary Layers and Turbulence. Amer. Meteor. Soc., P2.3., San Diego, CA
66. Ng A (2018) Machine Learning Yearning
67. Kaimal JC, Finnigan JJ (1994) Atmospheric boundary layer flows: their structure and measurement. New York
68. Kit E, Liberzon D (2016) 3D-calibration of three- and four-sensor hot-film probes based on collocated sonic using neural networks. Meas Sci Technol 27:95901. https://doi.org/10.1088/0957-0233/27/9/095901
69. Tsinober A, Kit E, Dracos T (1992) Experimental investigation of the field of velocity gradients in turbulent flows. J Fluid Mech 242:169–192. https://doi.org/10.1017/S0022112092002325
70. Kit E, Grits B (2011) In situ calibration of hot-film probes using a collocated sonic anemometer: Angular probability distribution properties. J Atmos Ocean Technol 28:104–110. https://doi.org/10.1175/2010JTECHA1399.1
71. Kawaguchi K (2016) Deep learning without poor local minima. Adv Neural Inf Process Syst 586–594
72. Van de Wiel BJH, Moene AF, Ronda RJ, et al (2002) Intermittent turbulence and oscillations in the stable boundary layer over land. Part II: A system dynamics approach. J Atmos Sci 59:2567–2581. https://doi.org/10.1175/1520-0469(2002)059<2567:ITAOIT>2.0.CO;2
73. Panofsky HA (1969) Internal Atmoshperic Turbulence. Bull Am Meteorol Soc 50:539–543
74. Uriel Frisch (1998) Advanes in Turbulence VII
75. Rorai C, Mininni PD, Pouquet A (2014) Turbulence comes in bursts in stably stratified flows. Phys Rev E - Stat Nonlinear, Soft Matter Phys 89:1–8. https://doi.org/10.1103/PhysRevE.89.043002
76. Poulos GS, Blumen W, Fritts DC, et al (2002) CASES-99: A comprehensive investigation of the stable nocturnal boundary layer. Bull Am Meteorol Soc 83:555–581. https://doi.org/10.1175/1520-0477(2002)083<0555:CACIOT>2.3.CO;2
77. Holtslag AAM, Svensson G, Baas P, et al (2013) Stable atmospheric boundary layers and diurnal cycles: Challenges for weather and climate models. Bull Am Meteorol Soc 94:1691–1706. https://doi.org/10.1175/BAMS-D-11-00187.1
78. Davidson PA (2004) Turbulence an introduction for scientists and engineers. Oxford University Press
79. Kim H, Kline S, Reynolds W (1971) The production of turbulence near a smooth wall in a turbulent boundary layer. J Fluid Mech 50:133–160
80. Kline SJ, Reynolds WC, Schraub FA, Runstadler PW (1967) The Structure of Turbulent Boundary Layers. J~Fluid Mech 30:741–773
81. Blackwelder RF, Eckelmann H (1979) Streamwise vortices associated with the bursting

phenomenon. J Fluid Mech 94:577. https://doi.org/10.1017/S0022112079001191
82. Blackwelder RF, Kaplan R. (1976) On the wall structure of the turbulent boundary layer. Math Proc Cambridge Philos Soc 47:375–395. https://doi.org/10.1017/S0305004100026724
83. Ramage CS (1976) Prognosis for weather forecasting. Bull Am Meteorol Soc 57:
84. Rao KN, Narasimha R, Narayanan M a. B, et al (1971) The 'bursting' phenomenon in a turbulent boundary layer. J Fluid Mech 48:339–352. https://doi.org/10.1017/S0022112071001605
85. Ohya Y, Nakamura R, Uchida T (2008) Intermittent bursting of turbulence in a stable boundary layer with low-level jet. Boundary-Layer Meteorol 126:349–363. https://doi.org/10.1007/s10546-007-9245-y
86. Mahrt L, Vickers D (2003) Formulation of turbulent fluxes in the stable boundary layer. J Atmos Sci 2538–2548. https://doi.org/http://dx.doi.org/10.1175/1520-0469(2003)060<2538:FOTFIT>2.0.CO;2
87. Bogard DG, Tiederman WG (1986) Burst detection with single-point velocity measurements. J Fluid Mech 162:. https://doi.org/10.1017/S0022112086002094
88. Lu SS, Willmarth WW (1973) Measurements of the structure of the Reynolds stress in a turbulent boundary layer. J Fluid Mech 60:481–511. https://doi.org/10.1017/S0022112073000315
89. Jackson RG (1993) Sedimentological and fluid-dynamic implications of the turbulent bursting phenomenon in geophysical flows. 118:1490–1507
90. Offen GR, Kline SJ (1975) A proposed model of the bursting process in turbulent boundary layers. J Fluid Mech 70:209–228. https://doi.org/10.1017/S002211207500198X
91. Willmarth WW, Lu SS (1972) Structures of Reynolds stress near the wall. J Fluid Mech 55:56–92
92. Reina N, Mahrt L (2005) A study of intermittent turbulence with cases-99 tower measurements. Boundary-Layer Meteorol 114:367–387. https://doi.org/10.1007/s10546-004-0857-1
93. Sun J, Burns SP, Lenschow DH, et al (2002) Intermittent turbulence associated with a density current passage in the stable boundary layer. Boundary-Layer Meteorol 105:199–219. https://doi.org/10.1023/A:1019969131774
94. Sun J, Lenschow DH, Burns SP, et al (2004) Turbulence in Nocturnal Boundary Layers. Boundary-Layer Meteorol 110:255–279
95. Mahrt L (1999) Stratified atmospheric boundary layers. Boundary-Layer Meteorol 90:375–396. https://doi.org/10.1023/A:1001765727956
96. Blackwelder RF, Kovasznay LSG (1972) Time Scales and Correlations in a Turbulent Boundary Layer. Phys Fluids 15:1545. https://doi.org/10.1063/1.1694128
97. Koop CG (1981) A Preliminary Investigation Of The Interaction Of Internal Gravity Waves With A Steady Shearing Motion
98. Waleffe F (1997) On a self-sustaining process in shear flows. Phys Fluids 9:883–900. https://doi.org/10.1063/1.869185
99. Greenspan HP, Benney DJ (1963) On shear-layer instability, breakdown and transition. J Fluid Mech 15:133–153. https://doi.org/10.1017/S0022112063000112
100. Fritts DC (1979) The excitation of radiating waves and Kelvin-Helmholtz instabilities by the gravity-wave critical-level interaction. J Atmos Sci 36:
101. Cadet D (1977) Energy dissipation within intermittent clear air turbulence patches. J Atmos Sci 34:137–142

102. Fukui K, Nakajima M, Ueda H (1983) A laboratory experiment on momentum and heat transfer in the stratified surface layer. Q J R Meteorol Soc 109:661–676. https://doi.org/10.1002/qj.49710946114
103. Ueda H, Mitsumoto S, Komori S (1981) Buoyancy effects on the turbulent transport processes in the lower atmosphere. Quarr J R Met Soc 107:561–578
104. Holmes P, Lumley JL, Berkooz G, Rowley CW (1998) Turbulence, Coherent Structures, Dynamical Systems and Symmetry
105. Pope SB (2000) Turbulent flows. Cambridge University Press, New York
106. Laufer J (2003) New Trends in Experimental Turbulence Research. Annu Rev Fluid Mech 7:307–326. https://doi.org/10.1146/annurev.fl.07.010175.001515
107. Lohse D, Grossmann S (1993) Intermittency in turbulence. Phys A Stat Mech its Appl 194:519–531
108. Genevieve Comte-Bellot, Sabot J, Saleh I (1978) Detection of intermittent events maintaining Reynolds stress. In: Proceedings of the Dynamic Flow Conference. pp 213–229
109. Narasimha R, Kailas S V. (1990) Turbulent bursts in the atmosphere. Atmos Environ Part A, Gen Top 24:1635–1645. https://doi.org/10.1016/0960-1686(90)90497-B
110. Goldshmid RH, Liberzon D (2020) Anabatic flow field measurements and the detection algorithm of turbulent bursting periods. Mendeley Data
111. Taylor GI (1935) Statistical Theory of Turbulence. Proc R Soc London Ser A - Math Phys Sci 151:421 LP – 444
112. Galambos J, Lechner J, Simiu E (1994) Extreme Value Theory and Applications. In: Macri N (ed). Kluwer Academic Publishers
113. Batchelor GK, Townsend AA (1947) Decay of vorticity in isotropic turbulence. 534–550
114. Krogstad P-Å, Davidson P (2011) Freely-Decaying, Homogeneous Turbulence Generated by Multi-scale Grids. J Fluid Mech 417–434. https://doi.org/10.1088/1742-6596/318/3/032042
115. Krogstad PA, Davidson PA (2012) Near-field investigation of turbulence produced by multi-scale grids. Phys Fluids 24:. https://doi.org/10.1063/1.3693132
116. Pope SB (2000) Turbulent flows. Cambridge University Press, New York
117. A.N.Kolmogorov (1961) A refinement of previous hypotheses concerning the local structure of turbulence in a viscous incompressible fluid at high Reynolds number. Jfm 82–85
118. Richardson LF (1922) Weather prediction by numerical process
119. Zhou T, Antonia RA (2000) Approximations for turbulent energy and temperature variance dissipation rates in grid turbulence. Phys Fluids 12:335–344. https://doi.org/10.1063/1.870312

מחקר ניסויי של זרימות עולות מונעות מעבר חום

חיבור על מחקר לשם מילוי חלקי של הדרישות לקבלת התואר
דוקטור לפילוסופיה

רוני גולדשמיד

הוגש לסנט הטכניון- מכון טכנולוגי לישראל
תשרי תשפ"א ,חיפה ,ספטמבר 2020

המחקר נעשה בהנחיית
פרופסור חבר דן ליברזון
בפקולטה להנדסה אזרחית וסביבתית

אני מודה לטכניון- המכון הטכנולוגי לישראל,
לקרן הדו-לאומית לחינוך למדע ארה"ב-ישראל,
ולקרן הלאומית למדע
על התמיכה הכספית הנדיבה בהשתלמותי

תקציר

זרימות עולות על מדרון, או בשמם המדעי זרימות אנאבטיות, הינן גורם משמעותי ביצירת סביבות מיקרו-אקלים בשטח מורכב והן אחראיות להסעת סקלרים כמו אבק וזיהום אויר. ולכן, זרימות אילו משפיעות באופן ישיר על הפעילות היומיומית של האדם המתגורר בקרבת גבעות והרים. זרימות עולות על מדרון מאופיינות כזרימות טורבולנטיות בשכבת הגבול, ובהעדר אילוץ סינופטי, הן מונעות באופן בלעדי על ידי חימום וקירור של המדרונות במחזור יומי. אפיון של זרימות אלו מורכב בגלל האופי הארעי שלהן, מה שמסביר את המספר המצומצם של מחקרים בתחום זה. דיווח זה מפרט מחקר ניסויי אשר נערך במעבדה ובשדה שמטרתו הייתה לאפיין את הסקאלות הגדולות והקטנות של זרימה אנאבטית.

במעבדה, ערכנו ניסויים שתוכננו לדמות את הזרימות כפי שהן מופיעות בטבע. הניסויים נערכו על מדרונות במספר זוויות שונות ומספר עוצמות שטף חום, תוך שימוש בשני סוגי גיאומטריה: מדרון בודד בעל רמה שטוחה בחלקו העליון, ושני מדרונות צמודים סימטרית. ראשית, הרחבנו את המודל שפותח ע"י Hocut et al. (2015), המודל התמקד בחיזוי נקודת התנתקות הזרימה ממדרון חלק, והוספנו את השפעת קיום הרמה. הניסויים נערכו במיכל מים מלבני בעל ריבוד יציב והזרימה הותנעה ע"י חימום המשטחי המדרון והרמה. הניסויים בחנו השפעה של מספר רב של פרמטרים: זוויות, עוצמות חימום, ורוחבי רמה. אנליזה של הזרימה הראתה דמיות כמותית למודל הקודם לאחר שהגדרנו זווית אפקטיבית המכלילה את רוחב הרמה ואת השיפוע הגיאומטרי. שנית, אפיינו את הסקאלות הגדולות של שכבת הגבול של הזרימה האנאבטית שהתפתחה על מדרון סימטרי. הגדלנו משמעותית את המדיום הניסויי והניסויים שוב נערכו במים. בחינת הצורה של פרופיל המהירות הממוצעת, פרופיל מאמצי ריינולדס, והתנהגות אומדן הערבוליות של הזרימה חשפה את האופי הארעי והתלת ממדי של זרימה הנחקרת. בחינה מעמיקה יותר של ההתנהגות הרגעית של הזרימה הדגישה את החשיבות של האופי התלת ממדי, תוך ציון מגבלות המודל הדו ממדי שפותח לפני כן. בנוסף, גזרנו והצגנו את הקשר האמפירי של צורת שכבת הגבול בעזרת קבוצות חסרות ממד נפוצות. ולסיום, ערכנו מספר ניסוי תצפית לחקירת האופי התלת ממדי של הזרימה. הפעם השתמשנו באוויר כזורם והוויזואליזציה נעשתה בעזרת מכונת עשן. בתצפיות זהינו מבנים תלת ממדיים קוהרנטיים בנויים בצורת סלילים שמטפסים לאורך המדרון, לעתים במסלול אלכסוני. התצפיות הנוספות אימתו את החשדות לקיומם של מבנים אילו שעלו מהניסויים הדו ממדים, והדגישו את הצורך לחקור את האופי התלת ממדי של זרימות אנאבטיות.

עבודה ניסויית בשדה עסקה בעיקר בפיתוח שיטות מדידה עבור זרימות עולות וזרימות טורבולנטיות בכלל. עיקר המחקר עסק במכשיר הקומבו - מכשיר חדשני המשלב חוטי להט עם מד מהירות רוח אולטרסוני. לאחרונה, מספר מחקרים הציגו וביססו את היכולת של הקומבו לספק מדידות על פני כל ספקטרום הסקלות של זרימת רוח טורבולנטית בתנאי שדה. לקומבו המקורי הייתה מגבלת מדידה אחת משמעותית: טווח

גזרת הרוח שהמכשיר מסוגר לכסות הייתה מוגבל ל- 120 מעלות. כאן פיתחנו תצורה מכנית חדשה המאפשרת לקומבו לכסות את זרימת הרוח בזווית אפשריות, 360 מעלות. בחינת התצורה החדשה של הקומבו נעשתה בניסוי ים, והראנו את היכולת של המכשיר לבצע מדידות באופן אוטונומי למשך פרקי זמן ממשוכים, מספר ימים או שבועות, ברצף. בנוסף שיפרנו את שיטת עיבוד הנתונים של הקומבו שהייתה תלוית החלטת אנוש בתהליך כיול in-situ. את תהליך זה הפכנו לאוטומטי ע"י שימוש ברשתות נוירונים עמוקות והכללת כלל הנתונים של הסקלות הגדולות באימון רשתות אלה.

החלק האחרון של מחקר זה עסק בפיתוח שיטה כמעט אוטומטית לזיהוי התפרצויות טורבולנטיות בשדה מהירות. הנתונים ששימשו אותנו לפיתוח זה היו נתוני מהירות רוח שנמדדו בעזרת הקומבו בניסויי שדה שחקר זרימות עולות על מדרון מתון. השיטה החדשה מתבססת על זיהוי פרקי זמן המאופיינים בעליה משמעותית של קצב דעיכת אנרגיה טורבולנטית קינטית, הצפויה בזמני התפרצות עוצמת תנודות המהירות. הראנו איך השיטה החדשה מפרידה בצורה יעילה את פרקי הזמן בהן מתקיימות התפרצויות טורבולנטיות מזרימת רקע טורבולנטית מורכבת. שיטה חדשה זו תאפשר חקירה מעמיקה של תופעה פיזיקלית מורכבת של הופעת פרצי מהירות טורבולנטיים, ותוכל לסייע בהשגת דיוק רב יותר במודלים נומריים עליהם מתבססת הפקת תחזיות.